

Investigation of Thermally-Actuated Pumping During Pool Boiling of a Dielectric Liquid on an Asymmetric Microstructured Silicon Heat Sink

by

Naveenan Thiagarajan

A dissertation submitted to the Graduate Faculty of
Auburn University
in partial fulfillment of the
requirements for the Degree of
Doctor of Philosophy

Auburn, Alabama
December 14, 2013

Keywords: reentrant cavities, pool boiling, FC72, microgravity, anemometry

Copyright 2013 by Naveenan Thiagarajan

Approved by

Sushil H. Bhavnani, Chair, Professor of Mechanical Engineering
Roy W. Knight, Assistant Professor of Mechanical Engineering
Jeyhoon Khodadadi, Professor of Mechanical Engineering
Daniel Mackowski, Associate Professor of Mechanical Engineering
Narendra Govil, Professor of Mathematics and Statistics

Abstract

Developments in the field of electronics fabrication have led to significant miniaturization of devices. Such a reduction in foot-print of the electronic devices coupled with increased capabilities, such as computing power, have offered numerous advantages to human comfort in the form of connectivity and portability. But these developments have also resulted in a bottle-neck which is the demand to dissipate the resulting high heat densities in the electronic packages. With heat dissipation demands exceeding more than 1000 W/cm^2 , traditional air cooling techniques and even evaporative liquid cooling techniques like heat pipes have been pushed to their limits of operation. Future high powered, micro-electronics, thermal management could potentially migrate to liquid cooling involving phase change which is considered as one of the potential solutions for high heat dissipation demands. While a technique such as flow in microchannels with phase-change has proven to meet the demands, it comes with the cost of power required to pump the fluid through narrow passages. With modern electronics getting leaner in power consumption, an ideal cooling technique would be one that while dissipating a large volume of heat, also self-propels the fluid to enhance the heat transfer characteristics. Such a cooling system with a pump-less flow loop will be power-free, compact and self-regulating. The system proposed will also be applicable to thermal management of space electronics, where power is a precious commodity. The study conducted by the author in collaboration with a heat transfer research group from Oregon State University, investigates the liquid self-propulsion effects during pool boiling of a dielectric liquid on asymmetric surfaces.

The study describes a novel silicon heat sink with an asymmetric saw-tooth cross-sectioned surface structure, which has the potential to be translated into a liquid propulsion system while dissipating heat efficiently. The heat sink was fabricated using a combination of

gray-scale lithography, deep reactive ion etching and wet etching techniques. The novelty of the heat sink lies in the ability to effect lateral motion of bubbles due to nucleation from re-entrant cavities fabricated on the shallow slope of the saw-toothed surface. The asymmetric nucleation, growth and departure of bubbles leads to an angular momentum imparted to the liquid, thereby resulting in a net lateral flow. The study investigates the ability of surface structure to propel the liquid in its immediate vicinity under a variety of test conditions. The tested conditions include heat flux in the range of 0-4 W/cm², liquid subcooling ranging from 0-20°C, and gravity ranging from 0-1.8g.

Due to the unique profile of the surface, the bubble characteristics are very different from those reported in the literature for common surfaces and fluids. One of the primary objectives of the study is the characterization of bubble dynamics from such a surface. In the experiments conducted, bubble growth and departure from re-entrant cavities on the asymmetric structures were studied using high speed photography and image processing techniques. The asymmetry in shape of the ratchet and location of re-entrant cavities resulted in nucleation only from the shallow slope of the ratchets. Interestingly, the bubbles were “light-bulb” shaped which otherwise would be more circular for a highly wetting fluid such as FC-72. It was observed that the bubble growth and departure were normal to the shallow slope of the ratchet surface structure. Bubble dynamics such as growth rate, bubble departure diameter and frequency were studied as a function of heat flux and subcooling. Asymptotic growth relationships were expressed as $D = At$ and $D = \beta t^m$ for the inertia and heat transfer controlled regimes respectively. The values of A, varying between ≈ 48 -181, increased with increasing heat flux and decreasing subcooling. Similarly, in the heat transfer controlled growth regime, the value of β , termed as the growth constant, was observed to increase between ≈ 0.25 -0.3 with increasing heat flux and decreasing subcooling. Subcooling or heat flux did not affect the value of m significantly which varied between 0.20 - 0.25, compared to the value of 0.5 that has been widely reported in the literature. The bubble departure frequency was estimated to be increasing between ≈ 0 - 60 with increasing heat flux

and decreasing subcooling. However, under the tested conditions bubble departure diameter was not found to be affected significantly with heat flux or diameter.

A similar saw-toothed surface was tested at microgravity to understand the effects of gravity on bubble dynamics and self-propelled bubble motion across the surface. Pool boiling experiments were conducted aboard NASA's reduced gravity flight. In FC-72, vapor bubbles six times larger in diameter compared to $1g$ were observed, due to lack of buoyancy. Interestingly, bubbles were observed to be sliding across the asymmetric surface at velocities as high as 27.4 mm/s. This motion was observed at all tested conditions. Pool boiling on a plain surface would result in stagnant, surface residing vapor bubbles that would affect the heat transfer characteristics adversely causing burn-out of the chip being cooled. The ability to move the bubble along the surface at high velocities prevented any heat transfer deterioration, and actually leads to an enhancement. The sliding motion was attributed to pressure differences in the thin liquid film existing between the saw-toothed surface and the vapor bubble. A model has been proposed based for the sliding velocity of bubbles, which proves that the force due to pressure differences in the liquid film is a potential driving force for the bubbles among other forces.

Acknowledgments

The author would like to extend his sincere thanks to his advisory committee, chaired by Prof. Sushil H. Bhavnani, and comprising Prof. Jeyhoon Khodadadi, Prof. Roy W. Knight, Prof. Daniel Mackowski and Prof. Narendra Govil for their contributions and time. Special thanks are extended to Prof. Roy Hartfield for serving as the external reader.

The author gratefully acknowledges the support of sponsors, NSF and NASA, for the opportunity to work in this field of research. Words cannot express the joy and pride that this research has brought along, especially, in the form of microgravity testing.

The author would like to sincerely thank his adviser and committee chair Prof. Sushil H. Bhavnani for being a constant source of inspiration and motivation through a lot of difficult times, and for all the opportunities provided. Sincere thanks and appreciation are extended to Prof. Vinod Narayanan and his graduate students, Florian Kapsenberg and Logan Strid, for the guidance and ideas provided.

The author is also thankful to AMSTC, especially Mr. Charles Ellis, for providing the facilities and knowledge for the fabrication of test devices. The author would like to acknowledge the guidance and assistance provided by Dr. Shakib Morshed, and Dr. Tamara Isaacs-Smith in fabricating the test sections. Thanks are extended to Mr. Travis Wheeler for his precious assistance during microgravity testing. Much gratitude is extended to my colleagues at the Heat Transfer Research laboratory for their help, support, and company.

Above all, the author would like to thank his parents and sister for their endless love, support, encouragement and sacrifices.

Table of Contents

Abstract	ii
Acknowledgments	v
List of Figures	ix
List of Tables	xix
List of Abbreviations	xx
1 Introduction	1
1.1 Thermally actuated pumping systems: Literature review	7
1.1.1 Self-propulsion in single phase liquids	7
1.1.2 Self-propelled flow in phase change systems	9
1.1.3 Fabrication of re-entrant cavities and sloped surfaces: Background	14
1.1.4 Bubble dynamics in pool boiling on plain and enhanced surfaces	19
1.1.5 Bubble dynamics under reduced gravity	23
2 Fabrication of Silicon Test Devices	32
2.1 Fabrication of silicon ratchet array	35
2.2 Fabrication of re-entrant cavities	39
2.3 Fabrication of heater	40
2.4 Bonding of saw-tooth ratchet wafer to the heater wafer	46
3 Terrestrial Experiments	52
3.1 Experimental Setup	52
3.2 Results and Discussion	55
3.2.1 Bubble Dynamics using High Speed Photography	55
3.2.2 Bubble growth - Experiments	56
3.2.3 Bubble departure frequency and diameter	67

3.2.4	Bubble growth - Comparison of experimental data with models . . .	70
3.2.5	Heat Dissipation	74
3.2.6	Lateral Liquid Velocity Measurements Using Hot Wire Anemometer: Parametric Effects	76
3.3	Summary	82
4	Microgravity Experiments	84
4.1	Experimental Setup	84
4.2	Results and Discussion	87
4.2.1	Bubble Dynamics	88
4.2.2	Bubble Transit Hypothesis	96
4.2.3	Heat Dissipation	104
5	Conclusions and Recommendations	106
5.1	Bubble dynamics: Terrestrial experiments	106
5.2	Net lateral liquid velocity under terrestrial gravity	108
5.3	Bubble dynamics: Microgravity	108
5.4	Recommendations	109
	Appendices	118
A	Thermophysical Properties of FC-72 and Water	119
B	Preliminary Closed Loop Experiments Under Terrestrial Gravity Using FC-72 .	120
C	Calibration of Sensors	124
C.1	Calibration of thermistor and thermocouple	124
C.2	Calibration of test section heater	125
C.3	Calibration of hot wire anemometer	126
D	Empirical Model for Lateral Liquid Velocity in Nucleate Boiling	128
E	Particle Image Velocimetry (PIV)	131
F	Microgravity Experiments: Test Equipment Data Package (TEDP)	137
G	Microgravity Experiments: Sample Calculations for the Bubble Velocity Model .	186

List of Figures

1.1	Evolution of supercomputers since its introduction illustrating the increase in number of Floating point operations per second (Flops) and the reduction in cost per operation. The corresponding evolution of cooling systems used in these supercomputers from a simple liquid cooling system such as in car radiators to advanced phase change cooling systems is illustrated. A popular current laptop is used for comparison which is much faster than the supercomputers in 1985.	2
1.2	Chart illustrates the adaptation of advanced cooling techniques for high heat density applications compared to the simple, lower heat transfer air cooling techniques for low power, low heat density applications	3
1.3	Schematic diagram of the concept under 1g showing the cross-section of the saw-toothed structure. Bubbles grow and depart from the re-entrant cavities at an angle that is normal to the surface. This is hypothesized to result in a net lateral velocity.	6
1.4	Schematic diagram of the concept under 0g showing the larger size of the bubble due to lack of buoyancy. Bubble slides from left to right due to pressure difference in the liquid film underneath, between the crest and trough, that arises due to differences in radii of curvature (r)	6
1.5	(a) Image illustrates the local convective flow at the liquid surface and the resulting convective cells (b) The surface tension gradients due to alternating difference in temperatures of warmer and cold liquids cause deflection of the free surface. Image was acquired from Carey [6].	8

1.6	(a) Oval flow loop with saw-toothed heated ratchet sections used by Jo [1] (b) Asymmetric temperature gradients induced by the shape of the ratchet profile, which leads to surface tension gradients leading to liquid movement. The direction of liquid movement is marked in (a)	10
1.7	Flow pattern in oil observed by Stroock et al. [3] over asymmetric mini-ratchets at velocities up to 2mm/min.	10
1.8	Surface tension induced flow towards the trough of a symmetrical triangular groove which is marked by the movement of glass particles. Alexeev et al. [2] reported that this results in liquid flow towards the wall at the trough and away from the wall at the crest, thus setting up a vortex flow.	10
1.9	(a) Leidenfrost droplet motion over a saw-toothed surface demonstrated by Linke et al. [8] (b) Droplet propelled by pressure gradients in the thin liquid layer induced by the differences in radii of curvature of liquid-vapor interface (c) The direction of liquid movement due to the pressure gradient is shown. R-134a droplet velocities of up to 5 cm/s were reported	13
1.10	Bubble based micropumps that rely on asymmetry in surface structure, surface wetting characteristics and heater locations. (i) Meng and Kim [10] demonstrated preferential gas bubble motion due to surface asymmetry in the form of a neck in the microchannel structure as seen in (a). The gas bubble translation was promoted due to a hydrophilic-hydrophobic junction causing bubble translation to the right as seen in (b). Liquid flow rates of up to 65 nL/s were reported. (ii) Jun and Kim [11] demonstrated bubble motion due to surface tension gradients induced by sequential powering of the heaters. Liquid (isopropanol) velocities of up to 160 $\mu\text{m/s}$ were observed.	13

1.11 (a) Pyramidal re-entrant cavities used in immersion cooled surfaces studied by Nimkar et al. [14]. Such re-entrant cavities are formed by anisotropic potassium hydroxide etch (b) Bulb shaped re-entrant cavity used in immersion cooled heat sinks by Baldwin et al. [13] and Bhavnani et al. [17]	16
1.12 (a) Artificial cavities for nucleation formed by punch marks that were used in microchannel heat sinks by Kandlikar et al. [15] (b) Inter-connected re-entrant cavities to form slots that were used in silicon microchannel heat sinks by Koşar et al. [16]	16
1.13 Steps involved in deep reactive ion etching (DRIE) (a) Formation of a photomask using photolithography (b) Etching of silicon using a plasma containing SF_6 (c) Passivation cycle involving the deposition of a polymer material which protects the side walls from being etched in the subsequent etching cycles (d) Etching cycle is repeated.	18
1.14 Steps involved in gray-scale lithography as illustrated in Waits et al. [23] (a) Design of gray-scale mask (b) Exposure and development of photoresist to obtain a gradient height in photoresist (c) DRIE to obtain a gradient height (slope) in silicon.	18
1.15 Types of bubble growth models (a) Uniform superheat theory, involving spherical vapor growth in an uniformly superheated liquid (b) Bubble growth in non-uniform temperature field; temperature highest at the wall[25].	21
1.16 Regimes of bubble growth illustrated as shown in Carey [6] (a) Ambient cooler liquid is brought in to contact with the heater surface (b) Growth of boundary layer (c) Bubble nucleation and inertia controlled regime (d) Relaxation micro-layer thickness decreases (d) Bubble departure.	22

1.17	Bubble growth process from a cylindrical cavity on a silicon surface using FC-72 - Hutter et al. [34]	24
1.18	Bubble growth rate from a cylindrical cavity on a silicon surface using FC-72 - Hutter et al. [34]. The asymptotic growth relationship is marked as the equation of fit in the figure.	24
1.19	(a) Parabolic trajectory of a C-9B flight and the achieved reduced gravity periods (b) G-jitters in a parabolic flight due to disturbances such as air turbulence - Straub [37].	26
1.20	Large bubble of diameter ≈ 2.5 mm in pool boiling of FC-72 under reduced gravity at a wall superheat of 30°C - Kim and Benton[38].	28
1.21	(a) Lower heat transfer observed under microgravity in pool boiling of FC-72 at higher wall superheat. Critical heat flux (CHF) also reduced compared to earth gravity - Kim and Benton[38] (b) Heat transfer increases with increasing heater sizes and liquid subcooling - Henry and Kim [41]	29
1.22	Large hovering bubble in R-113; smaller adjacent bubbles near the larger bubble were noticed to migrate towards the larger bubble at high subcooling - Lee and Merte Jr. [43].	30
2.1	Illustration of steps involved in fabrication of the silicon test devices to be used in the large and small array experiments	34
2.2	Steps involved in the fabrication of silicon saw-tooth ratchets	36
2.3	Illustration of DRIE parameters discussed in Table 2.1	37
2.4	SEM image of the ratchets with an angle 19° . The inset shows an SEM image of silicon nano-structures, known as “silicon grass”, formed during the DRIE process with Recipe A.	38

2.5	Cross-section of a ratchet array with a nominal saw-tooth angle of 24°	38
2.6	Illustration of fabrication steps involved in etching re-entrant cavities from the back side of saw-teeth to form trapezoidal cavity mouths only on the shallow slope	41
2.7	Isometric and back side view illustrations of small and large array cavities on the shallow slope of saw-toothed surface	42
2.8	SEM image showing the top view of saw teeth and cavity mouth measurements in the test device with a saw-tooth angle of 24°	42
2.9	Sketch of aluminum serpentine heaters used in large and small array experiments that were fabricated on silicon. The width and thickness of heater traces are $500\ \mu m$ and $2\ \mu m$ respectively. The electrical contact pad configuration is labeled in the figure. The arrangement of electrical contact pads for the small array heater is based on the arrangement of electrical contacts in the wafer fixture.	44
2.10	Fabrication of aluminum serpentine heaters used in large and small array test devices.	45
2.11	Fabrication of isolation trenches on the back side of heater footprint and reduction of wafer diameter to 3 inches. Silicon nitride was coated to eliminate reflection of radiation during infrared measurements made during the small array experiments at OSU.	46
2.12	Images of fabricated aluminum serpentine heaters used in large and small array experiments. The diameter of heater wafer for the large and small array test experiments are 4 inches and 3 inches respectively.	47
2.13	Illustration of fusion bonding process used to bond the large array of silicon saw-teeth to the heater wafer.	48

2.14	Illustration of gold eutectic bonding process used for bonding the small array saw-tooth ratchets to the 3 inch heater wafer	50
2.15	X-ray image showing the bond quality of gold eutectic bonding process	50
3.1	Silicon test device	53
3.2	Boiling chamber assembly	53
3.3	Image showing bubble departure from re-entrant cavities at an angle normal to the sloped surface of saw-teeth during saturated pool boiling at a heat flux of $q'' = 2.20 W/cm^2$	56
3.4	Bubble growth and departure from re-entrant cavities at $q'' = 2.0W/cm^2$ and saturated pool conditions. Bubbles nucleating from neighbouring cavities are marked with a different color. Relative time stamps are marked at the bottom right of each image.	57
3.5	Ebullition cycle of a bubble at $q'' = 1.6 W/cm^2$ and 21°C subcooling	59
3.6	Image processing steps of a single bubble frame at 178.44 ms in Fig. 3.5	60
3.7	Estimated bubble growth for images shown in Fig. 3.5 at $q''=1.6 W/cm^2$ and 21°C subcooling	61
3.8	Effect of heat flux on bubble growth at a liquid subcooling of 21°C	64
3.9	Effect of subcooling on bubble growth at a nominal heat flux of $1.0 W/cm^2$	64
3.10	Growth constant from experiments at a liquid subcooling of 0-20°C. The figure shows a linear curve fit used to approximately express the growth constant. The equations 3.3 and 3.5 used for comparison from the studies Fritz and Ende [52] and Cole and Shulman [29] respectively, were calculated for saturated pool conditions.	66

3.11	Effect of heat flux on bubble growth at a liquid subcooling of 20°C	68
3.12	Effect of subcooling on bubble growth at a nominal heat flux of 1.0 W/cm^2	68
3.13	Effect of subcooling and heat flux on bubble departure frequency	69
3.14	Effect of subcooling and heat flux on bubble departure diameter	69
3.15	Comparison with existing models for bubble growth	73
3.16	Effect of subcooling on pool boiling curve for the test device with a saw-tooth angle of 24°	76
3.17	(a) and (b) TSI constant temperature anemometer and power supply used for liquid velocity measurements. Electrical circuit and connections are shown in (c) and (d) [55]	78
3.18	Illustration of the probe set up over the test device with a saw-teeth angle of 24°	79
3.19	Raw and temperature corrected voltage measurements using hot wire anemometer over the test device with a saw-tooth angle of 24°	81
3.20	Temperature corrected liquid velocity measurements using hot wire anemometer over the test device with a saw-tooth angle of 24°	82
4.1	Zero gravity flight used for parabolic maneuvers - (a) A NASA Zer0-g flight on it upward ascent. Boeing 727 was used for the flight experiments (b)-(c) Gravity profile and recorded accelerometer readings of the achieved parabolic maneuvers	85

4.2 Experimental setup for reduced gravity experiments - (a) 31° test device with two re-entrant cavities per saw-tooth (b) Assembled test device with the polycarbonate flow channel. Co-ordinate system shows the orientation of the test device with respect to the aircraft. (c) Boiling chamber used for the reduced gravity experiment. Bellows assembly with double containment is used to maintain a constant chamber pressure. 88

4.3 Assembled view of the experimental structure used for microgravity experiments. Details of the individual components in the structure and the related structural analysis are provided in Appendix F. 89

4.4 Bubble dynamics in water and FC-72 under μg (a) Vapor bubble 10 times larger than at 1g was observed at microgravity. Image inset shows vapor nucleation from re-entrant cavities, under the foot print of the larger bubble, illustrating the presence of a liquid film. (b) Sliding motion of vapor bubbles at a velocity of ≈ 10 mm/s, across the saw-teeth (left to right in images) at $q'' = 0.5$ W/cm². Sliding motion was observed at all tested conditions. (c) Sliding motion of vapor bubbles (left to right in the images) at $q'' = 1.4$ W/cm². 91

4.5 Bubble dynamics in FC-72 under 1.8g. Bubble departure diameters are very small compared to those at 1g ($\approx 0.25 D_{1g}$). Bubbles were observed to grow and depart at an angle normal to the shallow slope of the saw-teeth, a phenomenon that was previously demonstrated under 1g. 92

4.6 Comparison of experimental data with departure diameter estimated using Equation 4.1 for water and FC-72 under μg 93

4.7 Sliding velocity of bubbles in FC-72 under μg . Uncertainty in bubble velocity is $\pm 0.5\%$ 95

4.8	Schematic diagram of bubble motion over a saw-tooth in FC-72 under μg (not to scale). The arrows marked between the saw tooth and the vapor bubble indicate the direction of forces acting on the bubble due to pressure differences.	97
4.9	Liquid-vapor interface of a sliding vapor bubble in FC-72 under μg	98
4.10	Estimated bubble sliding velocities for liquid film thickness varying from 0-25 μm . The experimental bubble velocity of 27.4 mm/s is predicted closely for a H value of 17 mm. From bubble images, a value of H	104
4.11	Boiling curves for large array experiments with FC-72 under μg and $1g$. $\Delta T_{sub} = T_{sat} - T_{pool}$. Both experiments were performed with a highly subcooled pool and pool temperature was not controlled. Uncertainties in q'' and $(T_w - T_{sat})$ are $\pm 1\%$ and $\pm 0.3\%$ respectively.	105
B.1	Bottom plate used in the closed loop experiments with FC-72. The “race-track” is the flow channel in which flow is intended to occur in the clockwise direction.	120
B.2	Assembly of the closed loop experimental set up showing the polycarbonate flow loop and the assembly of the test device.	121
B.3	Schematic representation of the closed flow loop used in the study.	122
B.4	Schematic representation of the net flow effected mainly by the condenser location.	123
C.1	Calibration of Omega ON44007 thermistor and a K-type thermocouple using a NIST certified thermistor as a standard	124
C.2	Calibration of test section heater using a NIST certified thermistor as a standard	125
C.3	Flow loop for the calibration of hot wire probe	126
C.4	Flow loop for the calibration of hot wire probe	127

D.1	Illustration of the angular momentum imparted by a growing bubble normal to the shallow slope, leading to a net lateral liquid velocity	129
D.2	Control volume defined for estimation of resulting net lateral liquid velocity due to bubble growth at an angle normal to the shallow slope of the ratchet	129
E.1	Illustration of a PIV system showing the laser sheet that is used to illuminate the particles. The image of the particles is recorded at two time instances using a camera to measure velocity [59]	131
E.2	Assembled view of the PIV chamber - basic parts include borosilicate glass chamber, and a top polycarbonate lid with ports for sensors	133
E.3	Exploded view of the PIV chamber showing the assembly of the copper heating block, borosilicate glass chamber, and a top polycarbonate lid with ports for sensors	133
E.4	Velocity vectors obtained from a PIV experiment that are overlaid on top of the captured image. In this image, the shallow long slopes of the saw teeth face towards the left side of the image, and any expected flow due to asymmetric bubble growth will be from right to left in the image. Vectors colored in green and yellow represent measured and interpolated velocities, respectively.	134
E.5	Magnitude of velocity vectors obtained from the PIV experiment. Color chart indicates liquid velocities of up to 17 mm/s, although scattered in different directions	135

List of Tables

2.1	DRIE etch parameters and resulting saw-tooth angle	37
2.2	Characteristics of different types of test sections fabricated	51
3.1	Summary of curve fitting parameters from Fig. 3.8 and Fig. 3.9	65
3.2	Summary of available models and experimental data for bubble growth during inertia controlled (IC) and heat transfer controlled (HTC) regimes.	70
A.1	Thermophysical properties of FC-72 and saturated water at 1 atm	119

List of Abbreviations

Acronyms

CVD Chemical Vapor Deposition

CHF Critical Heat Flux

DAQ Data Acquisition System

DRIE Deep Reactive Ion Etching

HWA Hot Wire Anemometry

LUT Look Up Table

MABE Microheater Array Boiling Experiment

PECVD Plasma Enhanced Chemical Vapor Deposition

PID Proportional Integral Differential Controller

PAE Phosphoric Acid and Acetic Acid Etchant

PIV Particle Image Velocimetry

TEDP Test Equipment Data Package

Symbols

A constant in Eq. 3.7, mm/s

A area, m^2

C_p specific heat, J/kgK

C_D	drag co-efficient
D	diameter, m
F	Force, N
g	gravity, m/s^2
H	height, m
h_{lv}	latent heat of vaporization, J/kg
I	supply current, A
Ja	Jacob number, m
k	thermal conductivity, W/mK
L	length, m
m	mass, kg
m	exponent in power law curve fit (Table 3.1)
P	pressure, Pa
P	momentum, $kg.m/s$
Pr	Prandtl number
q	power supplied to the heater, W
q''	heat flux, W/cm^2
q_{loss}	heat lost to the ambient, W
R	radius, m
r	radius of curvature, m

Re Reynolds number, m

R_h heater resistance, Ω

t time, s

T temperature, $^{\circ}\text{C}$

v velocity, m/s

V voltage, V

Greek symbols

α thermal diffusivity, m^2/s

β growth constant

ΔP pressure drop, kPa

ΔT_{sub} inlet subcooling, $^{\circ}\text{C}$

μ dynamic viscosity, Nsm^{-2}

ν kinematic viscosity, m^2/s

ρ density, kg/m^3

σ surface tension, N/m

θ saw tooth angle, *degree*

τ shear stress, N/m^2

Subscripts

∞ ambient

c cavity

<i>h</i>	heater
<i>l</i>	liquid
<i>le</i>	equilibrium liquid superheat
<i>p</i>	particle
<i>sat</i>	saturation
<i>w</i>	saw tooth surface
<i>v</i>	vapor

Chapter 1

Introduction

Advances in electronics processing and fabrication techniques have led to significant miniaturization, allowing manufacturers to pack a billion transistors, carrying out a billion calculations into an area smaller than a thumbnail. Consequently, current supercomputers, which are indispensable for storm tracking, DNA mapping, social networking, and numerous other scientific research applications, are more than 20 billion times faster than the first ones built in 1960s. During the same period, the cost per million operations in a supercomputer has reduced by more than a billion fold. Central to these developments has been the evolution in cooling technologies for the dissipation of resultant high heat densities. Liquid-vapor phase change (boiling) of dielectric fluids has been at the forefront of cooling techniques starting with the immersion cooling technique employed in Cray 2 supercomputers to the flow boiling technique used in the current TITAN supercomputers. These advances in computing technologies aided largely by miniaturization are not limited to supercomputers, but have translated to laptops and hand-held devices. The microprocessors used in the latest computers are much faster than the supercomputers in 1960s and often uses a combination of air cooling and liquid cooling techniques such as forced convection heat sinks and heat pipes, respectively, to dissipate the resulting high heat density. A summary of this evolution in advances in computing power and cooling techniques is shown in Fig. 1.1 and 1.2. To further reduce the footprint of the billions of transistors, significant advances are required in the field of electronics cooling to push the limits of super-computing and bring even more powerful computing to desks and palms. Such advances in electronics cooling, especially liquid cooling, will also be essential and critical to modern space electronics, like Martian rovers, and critical electronics including life support systems in space.

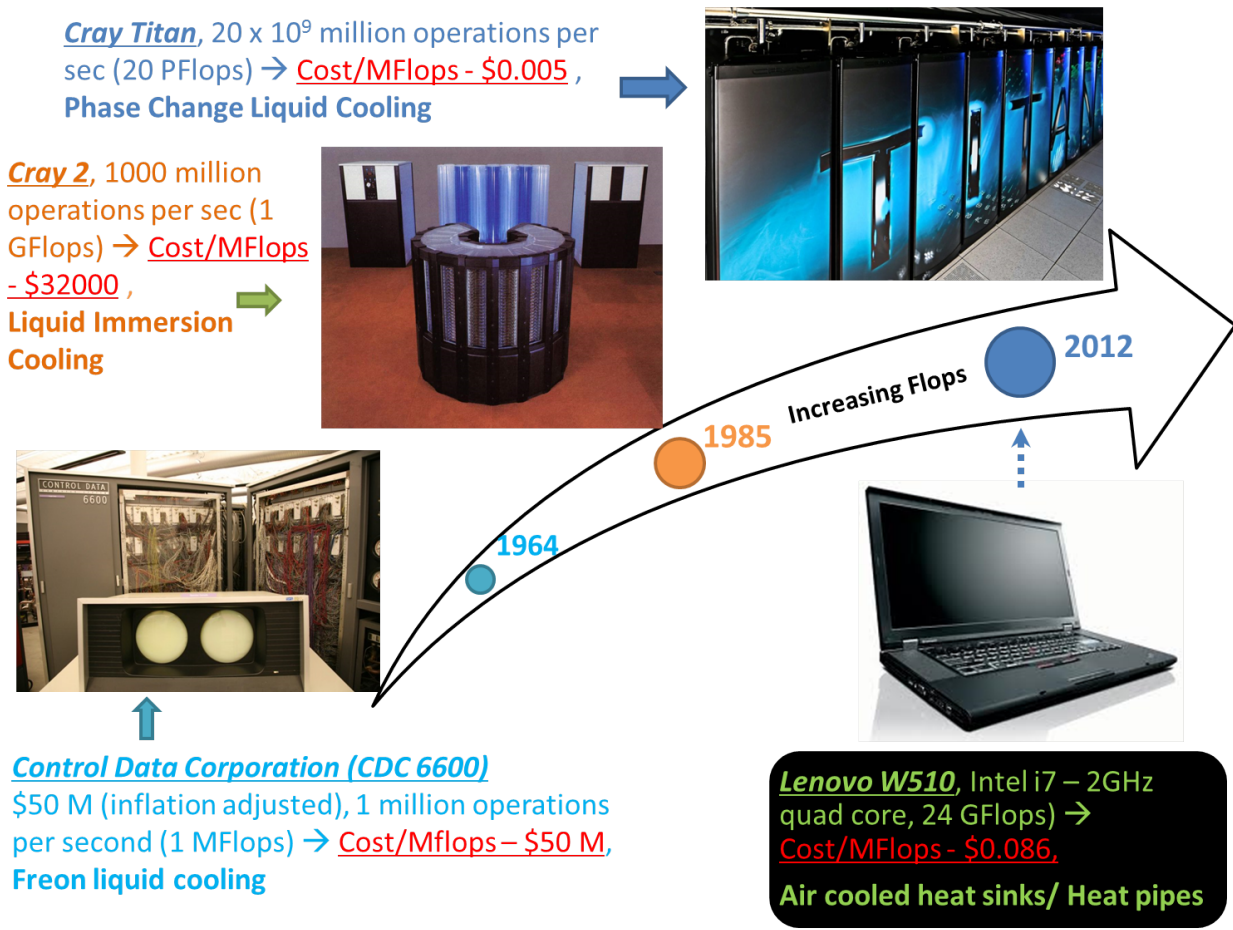


Figure 1.1: Evolution of supercomputers since its introduction illustrating the increase in number of Floating point operations per second (Flops) and the reduction in cost per operation. The corresponding evolution of cooling systems used in these supercomputers from a simple liquid cooling system such as in car radiators to advanced phase change cooling systems is illustrated. A popular current laptop is used for comparison which is much faster than the supercomputers in 1985.

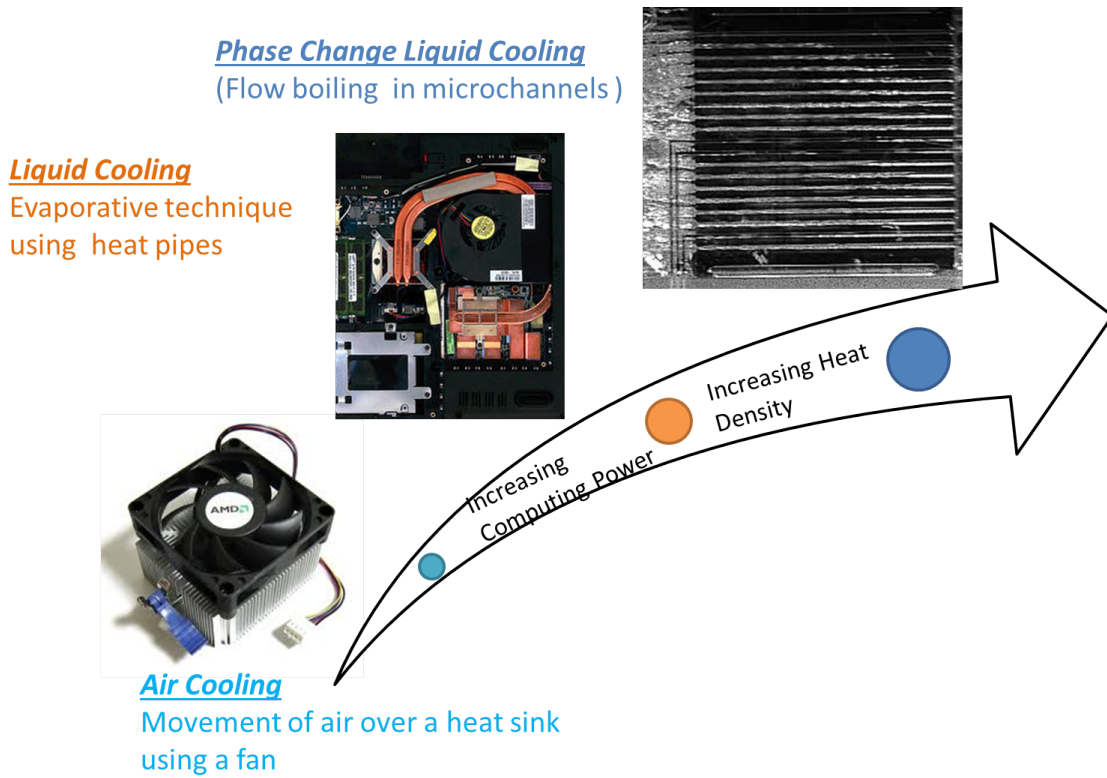


Figure 1.2: Chart illustrates the adaptation of advanced cooling techniques for high heat density applications compared to the simple, lower heat transfer air cooling techniques for low power, low heat density applications

Boiling or liquid-vapor phase change, as a mode of high heat flux dissipation technique can be realized in two different ways, namely, pool boiling or flow boiling. Pool boiling involves immersing the electronics in a dielectric fluid with a low boiling point, like in the early supercomputers such as Cray 2. The heat from the microprocessor converts the liquid to vapor providing very high heat removal rates. These rates are increased even further if the liquid is flowing such as in flow boiling. Flow boiling involves heat rejection to a liquid flowing in a closed loop causing phase change to vapor as shown in Fig. 1.2. Such a cooling technique offers a number of advantages over single phase flow of liquid such as higher heat transfer, lower flow rates required for the same heat transferred, and chip temperature uniformity. The heat transfer rate involved in phase change liquid cooling is also dependent on the regime of boiling. The highest heat transfer rates in boiling are associated with the lower surface temperature nucleate boiling regime which involves the cyclic nucleation, growth and departure of individual vapor bubbles. In contrast, a film boiling regime, which involves the formation of a thin vapor layer between the surface and liquid, results in lower heat transfer compared to nucleate boiling but higher heat transfer than natural convection, at temperatures high enough to cause failure of any electronic components.

Such advanced cooling techniques, however, consume power to facilitate pumping of fluid through narrow passages. Reduction of required power to cool an electronic component is a critical factor to reduce the operational cost of the system. Further, it is of paramount importance in space systems, as power is a precious commodity. To further illustrate this, the current martian rover, Curiosity, uses a “pumped fluid loop” to efficiently cool the on-board electronic components. If the pumping of fluid in a an electronics cooling system can be achieved by devising a technique to achieve self-propelled flow of liquid, the operational cost of the cooling system could potentially be reduced significantly. Such a self-propelled liquid cooling system also offers other advantages such as reduction in system weight by the removal of prime movers such as pumps.

The study reported in this dissertation, conducted in collaboration with Oregon State University, describes an innovative concept wherein a heat sink with microscopic asymmetric surface features in silicon is developed to create a self-propelled flow of a dielectric liquid, dissipating heat effectively while operating in the high heat transfer nucleate boiling regime. Nucleate boiling is sustained by the presence of re-entrant cavities, which are very effective vapor trapping sites. Under terrestrial conditions (1g), in such a heat sink, heat from the microprocessor (heater) causes nucleation of vapor bubbles (boiling) from the fabricated microscopic cavities located only on the shallow slopes of the silicon saw-tooth structures as shown in Fig. 1.3. The bubbles grow and depart from the sloped asymmetric surface of the ratchets at an angle normal to the shallow slope of the ratchets with significantly high velocities. This asymmetric bubble growth imparts an angular momentum to the fluid thus effecting liquid motion in the adjacent liquid.

Under microgravity, due to lack of buoyancy, bubbles generated tend to reside on the surface and grow to several times larger than under terrestrial conditions. In a plain flat surface, this would cause temperature to rise under the bubble leading to the failure of electronic device being cooled. However, using the micro-structured surface, the residing bubble which conforms to the shape of the structured surface is propelled due to pressure differences in the trapped thin liquid film underneath. This prevents any temperature rise and also leads to a self-propelled flow. This phenomenon is illustrated in Fig. 1.4

Primary objectives of the current study include:

- MEMS fabrication of the novel heat sink with an asymmetric saw-toothed surface with nucleation sites (re-entrant cavities) on only the long slope of the ratchets
- analysis of bubble growth and departure from such asymmetric silicon structures using high speed imaging environments
- analysis of effects of asymmetric bubble growth on net lateral liquid movement using experimental techniques such as hot wire anemometry and particle image velocimetry

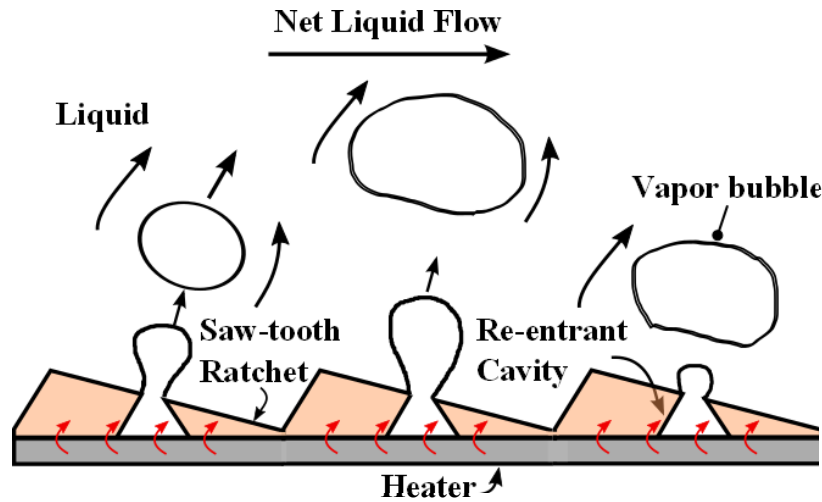


Figure 1.3: Schematic diagram of the concept under 1g showing the cross-section of the saw-toothed structure. Bubbles grow and depart from the re-entrant cavities at an angle that is normal to the surface. This is hypothesized to result in a net lateral velocity.

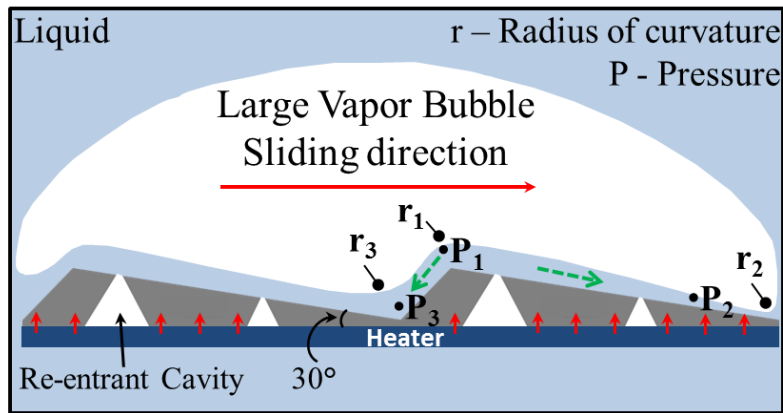


Figure 1.4: Schematic diagram of the concept under 0g showing the larger size of the bubble due to lack of buoyancy. Bubble slides from left to right due to pressure difference in the liquid film underneath, between the crest and trough, that arises due to differences in radii of curvature (r)

- experimentation aboard reduced gravity flight to analyze effect of microgravity on bubble dynamics and thereby its effects on net liquid movement

1.1 Thermally actuated pumping systems: Literature review

Thermally actuated pumping of a working fluid has been demonstrated in the past, in both single phase liquid and liquid-to-vapor phase change systems aided by different convective mechanisms. The current section reviews the applicability of both these types of systems for cooling of electronics.

1.1.1 Self-propulsion in single phase liquids

In the case of heating a liquid, a convective flow can be obtained by Marangoni convection and Rayleigh-Benard convection. Marangoni convection [1–5] is a surface tension driven flow while Rayleigh-Benard convection is driven by buoyancy.

As the liquid is heated, warmer liquid rises to the top and can move either to the left or right along the surface of the liquid, as illustrated in Fig. 1.5a. In this process, the liquid loses heat to the colder gas. This difference in temperature along the surface of the liquid causes a gradient in surface tension, since surface tension is inversely proportional to temperature in pure liquids. The colder liquid moves down due to difference in density. This causes the colder descending liquid to be surrounded by warmer liquid. The alternating pattern between colder liquid with high surface tension and warmer liquid with low surface tension, causes the deflection of liquid surface as shown in the Fig. 1.5b. This local convective flow due to surface tension gradients is known as the Marangoni effect [6].

A large number of studies have been conducted to analyze the aforementioned concept of Marangoni convection and to understand the effects of surface geometry [1–4], and the thickness of liquid layer [1, 3, 4] on the obtained convective transport. The surface geometry, especially, plays a very significant role since having a asymmetric heated surface geometry aids in setting up temperature gradients in the fluid which in turn aids Marangoni convection.

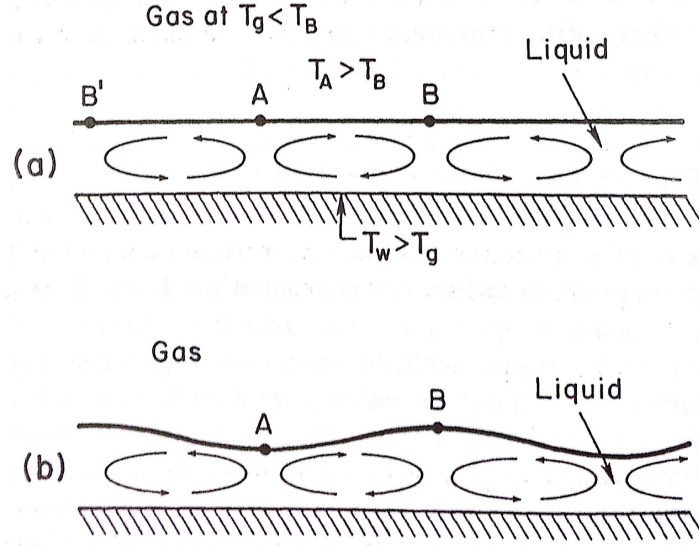


Figure 1.5: (a) Image illustrates the local convective flow at the liquid surface and the resulting convective cells (b) The surface tension gradients due to alternating difference in temperatures of warmer and cold liquids cause deflection of the free surface. Image was acquired from Carey [6].

This was demonstrated by Jo [1] where an asymmetric periodic saw tooth pattern was used for the heated surface and it was observed that the ratchets created asymmetric surface tension forces which induced a pumping effect in a thin layer of silicone oil over the ratchets. The effect of ratchet surface on the temperature gradients as observed by Jo [1] is shown in Fig. 1.6. Velocity measurements in oil using die-tracking demonstrated a maximum velocity of 0.86 mm/min at an optimum film thickness of 1 mm.

Stroock et al. [3] analyzed the effect of liquid thickness and temperature gradient across the liquid on the Marangoni-Benard convective flow over similar saw-tooth profiled ratchets. It was reported that the direction of flow was dependent on the film thickness and the temperature gradient. The maximum flow rate of oil observed was ≈ 2 mm/min at a temperature gradient of 130°C across the oil layer. The observed flow pattern over the asymmetric structures is shown in Fig. 1.7. In a thin film of oil over symmetrical triangular grooves, it was observed by Alexeev et al. [2] that surface tension gradients induce a flow

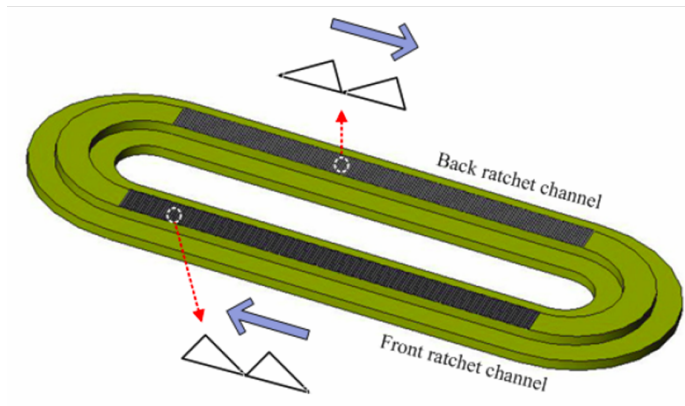
at the free surface of the film towards the trough of the groove and the flow is directed downwards at the trough as seen in Fig. 1.8, thus setting up symmetrical vortices over the period of a groove. In addition to Marangoni convection, surface geometry also affects the heat transfer from the surface. In experiments conducted with 0.5mm of silicone oil film heated on parallel symmetrical grooves, it was observed that the heat transfer rate was 30% more in the case of sinusoidal surface shape compared to a trapezoidal surface.

From the aforementioned studies, it can be inferred that Marangoni convection leads to a very low flow rate and operates in the natural convection regime which may not be applicable for high heat flux applications. The next section will continue the review of phase-change propulsion systems.

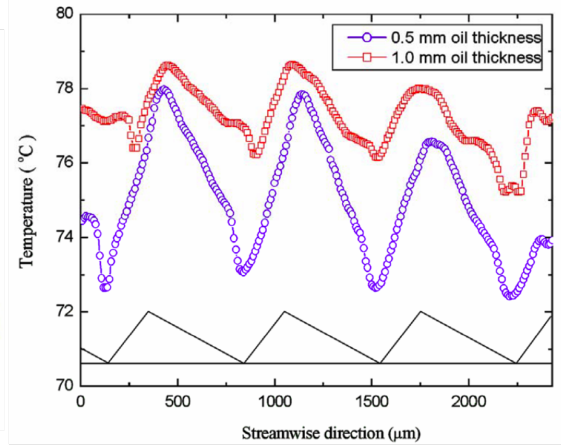
1.1.2 Self-propelled flow in phase change systems

A number of studies have been conducted in the recent past to develop self-propelled flow systems utilizing liquid-vapor phase change and asymmetry in heated surface structure or surface wetting characteristics. A self-propelled flow obtained during the nucleate boiling regime holds significant potential to be used as a high heat transfer, pump-less, phase change cooling system which is one of the objectives of the current study.

In phase change systems, bubble dynamics play a significant role in the promotion of the pumping effect. During phase change of liquid on a plain surface, vapor bubble ebullition cycle consisting of nucleation, growth and departure of the vapor bubble has been shown to induce a pumping effect by driving the superheated liquid away from the surface and bringing colder liquid to the surface [6]. The kinetic energy of the liquid due to spherical bubble growth on a plane heated wall has been studied in the past by Witze et al. [7], and



(a)



(b)

Figure 1.6: (a) Oval flow loop with saw-toothed heated ratchet sections used by Jo [1] (b) Asymmetric temperature gradients induced by the shape of the ratchet profile, which leads to surface tension gradients leading to liquid movement. The direction of liquid movement is marked in (a)

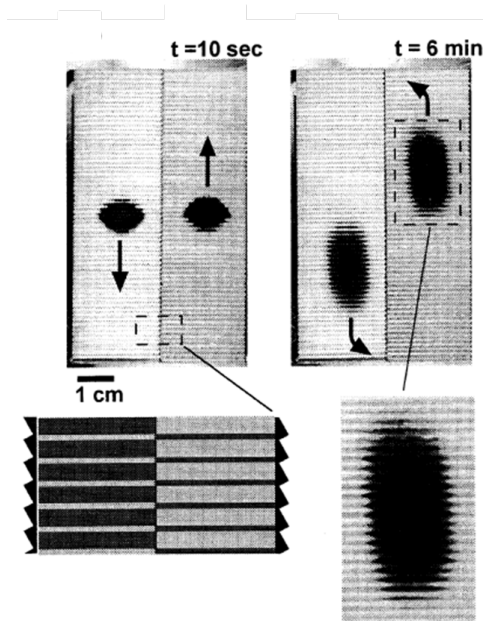


Figure 1.7: Flow pattern in oil observed by Stroock et al. [3] over asymmetric mini-ratchets at velocities up to 2mm/min.

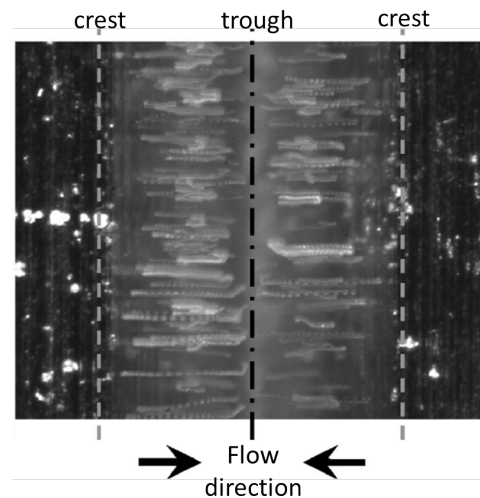


Figure 1.8: Surface tension induced flow towards the trough of a symmetrical triangular groove which is marked by the movement of glass particles. Alexeev et al. [2] reported that this results in liquid flow towards the wall at the trough and away from the wall at the crest, thus setting up a vortex flow.

the liquid kinetic energy was expressed as,

$$K.E. = 9.35\rho_l \left(\frac{dR}{dt}\right)^2 R^3 \tag{1.1}$$

where, $K.E.$ = kinetic energy of liquid

$\frac{dR}{dt}$ = bubble growth rate

From this equation it is also evident that if the bubble dynamics could be altered to cause bubble growth at an angle inclined to the vertical, then the velocity of the resulting liquid motion has a horizontal component which contributes towards the net lateral horizontal velocity.

Linke et al. [8] demonstrated that liquid R-134a droplets over a surface with periodic saw-tooth structures, similar to the structure used in the current study, were propelled at velocities as high as 5 cm/s in the film boiling regime at a significantly high temperature. The propulsion of the droplet was attributed to pressure differences under the droplet in the thin layer of vapor as observed in Fig. 1.9. Pressure differences arise due to difference in radii of curvature of the liquid-vapor interface at the trough and crest of the saw-teeth. This is also known as the Leidenfrost phenomenon and the droplets are called Leidenfrost droplets.

Theoretical models developed by Yuan and Prosperetti [9] have shown that phase change in fluids could be utilized for producing a pumping effect. It was shown that repetitive growth and collapse of a vapor bubble nucleating at heaters located in a small liquid-filled tube, that connects two reservoirs, can lead to a net lateral liquid flow as long as the bubble is not generated from the mid-point of the tube. The net flow was attributed to unequal liquid columns on both sides of the bubble. Net pumping velocities of ≈ 500 cm/s were reported when the bubble is at the ends of the tubes and the velocity approached zero as the bubble move towards the center of the tube. Such systems in the past have led to the development of

bubble based micropumps based on pumping due to surface asymmetry which are attractive for microfluidic biological applications.

Bubble-based micropumps have also been developed by using asymmetry in structure and surface wetting characteristics. In experiments conducted by Meng and Kim [10], gas bubbles were generated in an asymmetric microchannel structure as shown in Fig. 1.10(i)a. The directional growth of gas bubbles due to asymmetry and bubble displacement using a hydrophobic-hydrophilic junction resulted in a net liquid flow. Liquid flow rates of up to 65 nL/s was reported. A similar bubble based micro-pump involving phase change was demonstrated by Jun and Kim [11]. A net pressure differential was obtained as a result of surface tension imbalance arising from asymmetric heating in a microchannel. A bubble produced by a heater as shown in Fig. 1.10(ii)a can be translated to the right by switching on the heater to its right, while switching the previous (upstream) heater off. This sequential powering up of the heaters, causes a pressure gradient due to gradients in vapor pressure of the bubble and surface tension. This causes the bubble occupying the entire cross-section to move towards the location of the heated area, thereby sweeping the liquid along. Liquid velocities of up to 160 $\mu\text{m/s}$ were reported using isopropanol as the fluid in microchannels of hydraulic diameter 3.4 μm and a length 726 μm .

All the aforementioned bubble based micropumps involving single phase flow of liquid and multi-phase flow of gas-liquid can find applications in electronics cooling applications as a way to pump fluid over the hot surface. As described above, activation of liquid motion at the micropump may require an additional mechanism. Also, the discussed mechanisms were not designed for effective heat transfer from the hot surface. The current study aims at developing a self-propelled flow mechanism, in which the heat transfer from a hot surface, such as a microprocessor, when immersed in a dielectric liquid leads to nucleate boiling which in turn propels the liquid. The current study aims at constructing a heat sink, as illustrated in Fig. 1.3, with periodic, asymmetric, saw-tooth structures on a silicon surface with a profile that is similar to the surface used by Linke et al. [8]. Nucleate boiling is promoted

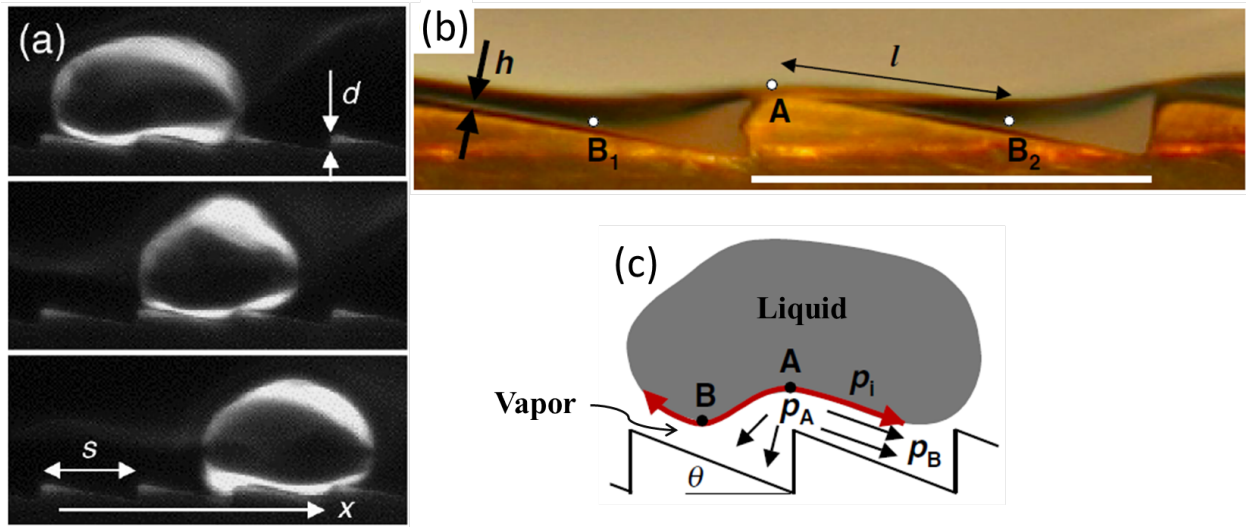


Figure 1.9: (a) Leidenfrost droplet motion over a saw-toothed surface demonstrated by Linke et al. [8] (b) Droplet propelled by pressure gradients in the thin liquid layer induced by the differences in radii of curvature of liquid-vapor interface (c) The direction of liquid movement due to the pressure gradient is shown. R-134a droplet velocities of up to 5 cm/s were reported

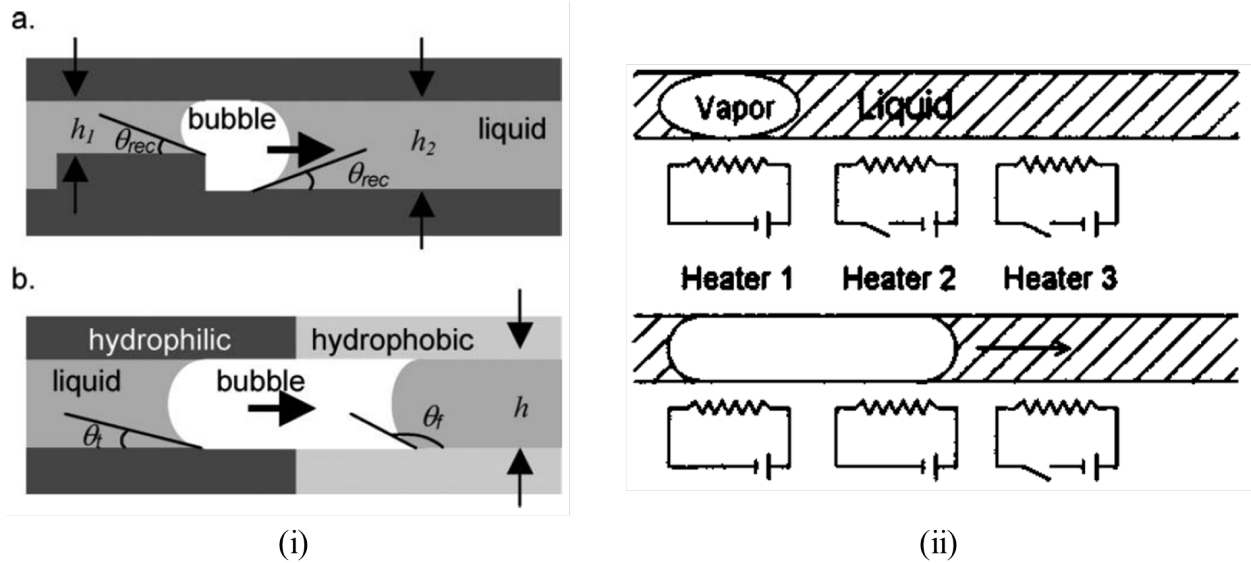


Figure 1.10: Bubble based micropumps that rely on asymmetry in surface structure, surface wetting characteristics and heater locations. (i) Meng and Kim [10] demonstrated preferential gas bubble motion due to surface asymmetry in the form of a neck in the microchannel structure as seen in (a). The gas bubble translation was promoted due to a hydrophilic-hydrophobic junction causing bubble translation to the right as seen in (b). Liquid flow rates of up to 65 nL/s were reported. (ii) Jun and Kim [11] demonstrated bubble motion due to surface tension gradients induced by sequential powering of the heaters. Liquid (isopropanol) velocities of up to 160 $\mu\text{m/s}$ were observed.

by fabricating re-entrant cavities only on the shallow slope of the saw-tooth structure to promote asymmetric bubble growth which leads to a net lateral flow of liquid.

1.1.3 Fabrication of re-entrant cavities and sloped surfaces: Background

The surface structure of the designed silicon heat sink to be used in the current study is unique and hence literature corresponding to its fabrication methods are not very widely available. Hence the fabrication methods that were devised for obtaining the sloped surfaces and re-entrant cavities that open up on the sloped surfaces, required extensive calibration.

In the past, fabrication of re-entrant cavities in silicon that are very similar to the profiles developed in the current study, and other bulb shaped re-entrant cavities, have been demonstrated in studies conducted by Goyal et al. [12] Baldwin et al. [13] and Nimkar et al. [14]. The aforementioned studies investigated bubble dynamics involved in nucleation from re-entrant cavities on plain surfaces, associated heat transfer enhancement and optimum spacing between the cavities for phase-change immersion cooling of electronics. An image of the re-entrant cavity used in [14] and a bulb shaped cavity used in [13] are shown in Fig. 1.11.

The pyramidal re-entrant cavities used in [12, 14] were fabricated by transferring the patterns of the cavity base that are printed on a glass mask to a silicon wafer coated with photoresist using standard photolithographic procedure. The developed wafer is then dipped in a solution of potassium hydroxide that etches the exposed silicon along the grain angle of silicon, which is 54.7° , to result in a pyramidal structure that opens a mouth on the other side of the silicon wafer.

In immersion cooling applications with dielectric liquids such as FC72, due to the low contact angle and highly wetting nature of the fluid, the naturally existing cavities or imperfections on a plain surface are flooded and hence vapor nucleation is delayed, thereby causing significant overshoot in wall temperature. One of the ways to mitigate overshoot as shown by Nimkar et al. [14] is to use re-entrant cavities of the shape shown in Fig. 1.11a,

that trap vapor more efficiently due to the presence of four corners. Re-entrant cavities also lead to significant reduction in onset of nucleate boiling as demonstrated by Baldwin et al. [13]. The mouth diameter of the cavities also significantly affect the bubble dynamics such as bubble growth rate, bubble departure diameter and departure frequency.

Numerous other shapes and forms of cavities have been investigated by researchers in an effort to enhance boiling characteristics and thereby the performance of the phase-change cooled heat sink. Kandlikar et al. [15] studied the effect of cavities, that are 100 μm punch marks as shown in Fig. 1.12a on flow instabilities during flow boiling in microchannels. Koşar et al. [16] investigated the performance of circular inter-connected re-entrant cavities as shown in Fig. 1.12. It was concluded that such re-entrant cavities decrease the heat flux required to initiate boiling and mitigate flow instabilities in microchannels.

Fabrication of sloped surfaces in silicon, similar to the saw-tooth structures in the current study, has been performed in the past primarily for diffractive optical elements such as deep phase Fresnel lens [18]. Such sloped surfaces in silicon are developed by gray-scale lithography and deep reactive ion etching (DRIE) which was first demonstrated by Whitley et al. [19]. Gray scale lithography is mainly used to develop structures in silicon that have a gradient in height. To achieve such structures in silicon, gray scale lithography is followed by DRIE which is a very common process to etch deep anisotropic structures such as channels or trenches in silicon. To better understand gray-scale lithography, the DRIE process and the factors affecting the etching process have to be understood. The DRIE process has four main steps as illustrated in Fig. 1.13[20, 21]. The pattern to be etched is transferred on to a photoresist layer on silicon. The photoresist is then developed to form a photomask and expose the silicon layer to be etched Fig. 1.13a. The DRIE process is carried out in an STS ICP etcher, where silicon is etched in two steps - etching and passivation. In the etching step, silicon is etched using SF_6 gas, as shown in Fig. 1.13b, and in the passivation step, a Teflon like film is deposited along the side walls and floor of the channel (Fig. 1.13c). In the subsequent etching cycle, the polymer film only on the floor of the channel is removed by

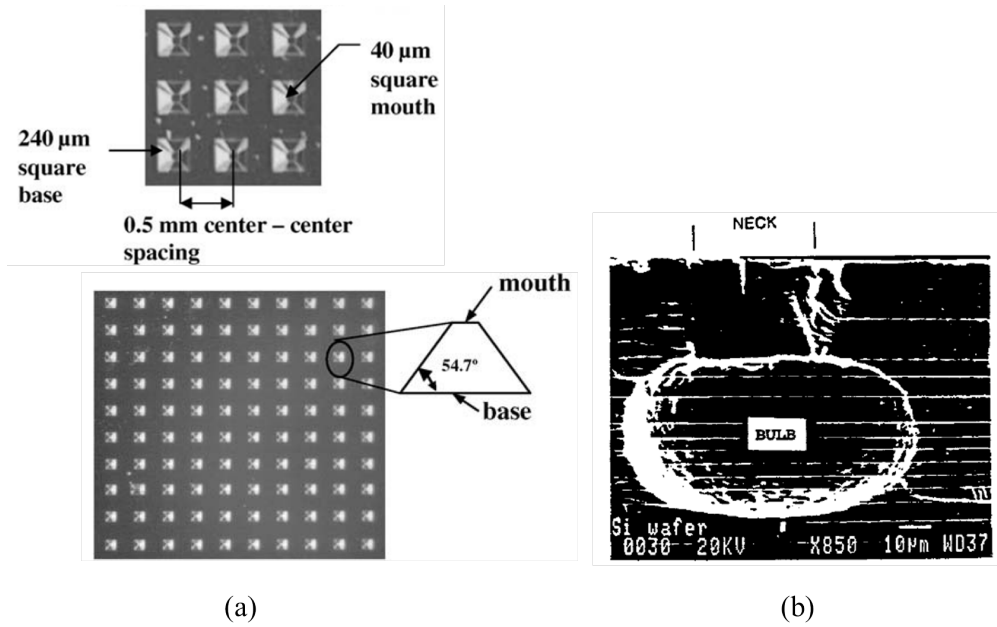


Figure 1.11: (a) Pyramidal re-entrant cavities used in immersion cooled surfaces studied by Nimkar et al. [14]. Such re-entrant cavities are formed by anisotropic potassium hydroxide etch (b) Bulb shaped re-entrant cavity used in immersion cooled heat sinks by Baldwin et al. [13] and Bhavnani et al. [17]

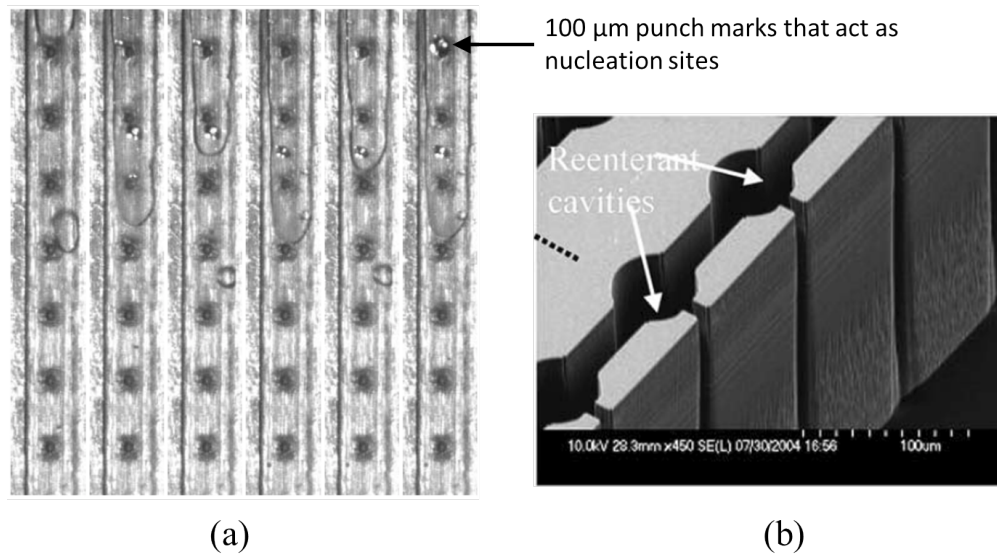


Figure 1.12: (a) Artificial cavities for nucleation formed by punch marks that were used in microchannel heat sinks by Kandlikar et al. [15] (b) Inter-connected re-entrant cavities to form slots that were used in silicon microchannel heat sinks by Koşar et al. [16]

SF_6 ion impingement, thereby protecting the walls of the channel from being etched in the subsequent cycles. This process is repeated until the required depth is achieved. It has to be noted that in the etching cycle, the plasma inside the etching chamber consists of a mixture of gases, usually SF_6 and O_2 . The increased concentration of SF_6 in the plasma makes the etch more isotropic, thereby lending a slight concave shape to the surface. Increased concentration of O_2 in the plasma leads to an increase in anisotropy but also increases the rate at which the photoresist is etched [21]. The ratio of silicon to photoresist rate is called etch selectivity.

A typical photolithography process involves transferring a pattern in a mask to the photoresist deposited on a silicon layer, as discussed above. The patterns form either the transparent or the opaque region of the mask. Ultra-violet light passes through the transparent regions of the mask to expose the photoresist layer on the mask, which is later developed to remove the exposed regions of the photoresist, to expose the silicon. In comparison, a gray-scale mask consists of a pattern that ranges from being opaque to transparent as shown in Fig. 1.14a. When ultra-violet light is passed through such a mask, the photoresist deposited on silicon is exposed to varying depths (Fig. 1.14b). This leads to a gradient in height in photoresist. The next step is DRIE (Fig. 1.14c) which transfers the slope in photoresist to a slope in silicon, although the angle of slope achieved in silicon is a function of etch selectivity. Hence, the DRIE process parameters such as the flow rate of gases, and duration of etching and passivation cycles have to be modified significantly to achieve the required angle. This step requires extensive calibration, as it involves optimization of a number of parameters. This step of tailoring the etch selectivity by manipulating the DRIE parameters has been investigated by Waits et al. [22, 23].

Although the steps of gray-scale lithography for optical elements, DRIE for forming channels, and wet etching for the formation of re-entrant cavities have been performed in the past separately for individual applications, the combination of three to form a large array of periodic delicate saw-tooth pattern to form a heat sink has never been attempted.

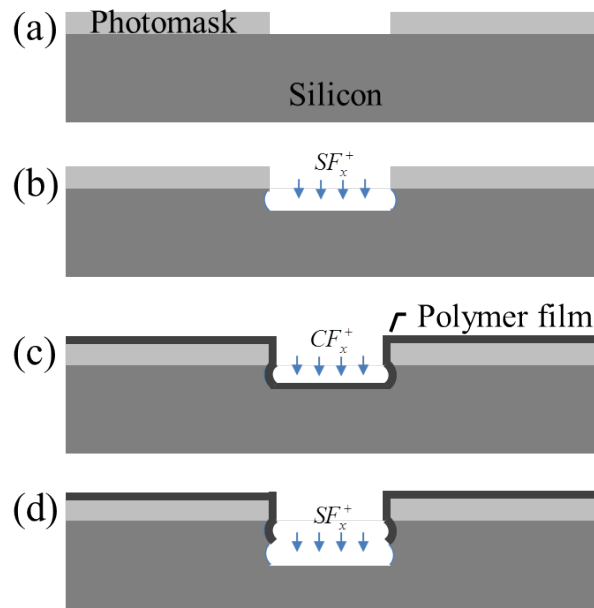


Figure 1.13: Steps involved in deep reactive ion etching (DRIE) (a) Formation of a photomask using photolithography (b) Etching of silicon using a plasma containing SF_6 (c) Passivation cycle involving the deposition of a polymer material which protects the side walls from being etched in the subsequent etching cycles (d) Etching cycle is repeated.

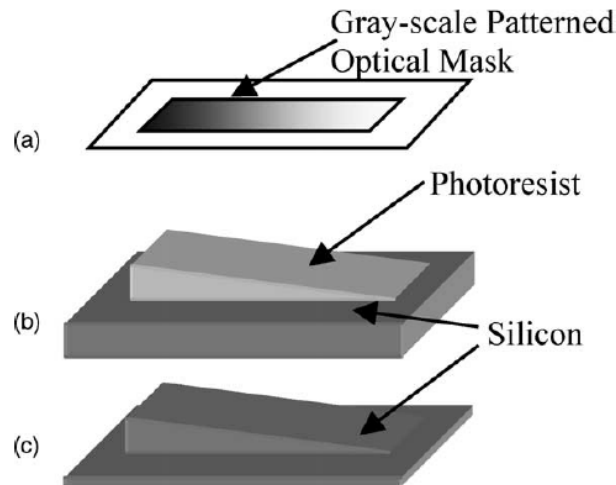


Figure 1.14: Steps involved in gray-scale lithography as illustrated in Waits et al. [23] (a) Design of gray-scale mask (b) Exposure and development of photoresist to obtain a gradient height in photoresist (c) DRIE to obtain a gradient height (slope) in silicon.

1.1.4 Bubble dynamics in pool boiling on plain and enhanced surfaces

Studies of bubble dynamics involved in liquid-vapor phase change and their interactions with the heated surface and the liquid is critical for understanding the underlying mechanism responsible for the enhanced heat transfer associated with boiling or phase change. Knowledge of bubble dynamics provides significant advantages in the design of phase-change heat exchangers and engineered surfaces. Bubble dynamics, in general, over the past decades were investigated for common fluids such as water and/or refrigerants such as R-113, R-134a and surfaces made of common metals. However, with the rising demands of high heat dissipation in modern high power electronics, phase-change cooling is well placed as an attractive cooling technique involving a range of surfaces such as silicon with micro-scale features and carbon nanotubes, and dielectric fluids such as FC-72 which promote direct contact cooling at low surface temperatures. These new combinations of surface structures, surface scales, and liquids alter the bubble dynamics significantly necessitating further study.

Investigations on this front have led to significant developments in phase change heat transfer for microelectronics such as flow boiling in microchannels, direct contact liquid immersion cooling and enhancements to engineered micro-surfaces. In the recent past, bubble dynamics have also been manipulated for the development of bubble based micro-pumps which are attractive for applications in electronics cooling since the latent heat required for the bubble production is acquired from the microelectronics leading to pump-less, power-free pumping with high heat dissipation.

It has been discussed earlier that the structure of heat sink used in the current study alters the bubble dynamics significantly to aid in asymmetric bubble growth and departure. This was also illustrated in the schematic diagram shown in Fig. 1.3. To analyze the effects of structural asymmetry and asymmetry in bubble growth on the net lateral liquid motion, it is important to characterize the bubble dynamics for the surface considered in this study and the experimental conditions tested. Analysis of bubble dynamics, which is one of the primary objectives of the study, includes the study of bubble growth rate, bubble departure

frequency and bubble departure diameter as a function of heat flux, subcooling, and type of fluid. Such information would also aid in the development of a model for the liquid velocity due to asymmetric bubble growth. Apart from contributing to the model developed, the analysis contributes to the scarce data available for bubble growth from re-entrant cavities and highly wetting fluids such as FC-72.

Analytical bubble growth models developed in the past can broadly be classified into two types - bubble growth in uniform and non-uniform temperature fields. In the former, a vapor bubble grows in a uniformly superheated pool of liquid where the bubble growth is symmetrical, as illustrated in fig. 1.15. In models using the uniform superheat theory, bubble growth is mainly attributed to the pressure difference between vapor inside the bubble (P_v) and the surrounding liquid (P_∞), which in-turn is related to $T_v - T_\infty$ using the Clausius Clapeyron equation. On the other hand, a non-uniform temperature field results from the presence of a heated surface at a temperature T_w which is greater than T_{sat} , leading to bubble nucleation and growth as the bubble stays attached to the surface. Compared to the uniform superheat theory, bubble growth on a heated surface is often not spherical and growth is not symmetrical. Bubble growth from a naturally occurring or a structured cavity on a heated surface, as illustrated in Fig. 1.16, can be classified into two types - inertia controlled and heat transfer controlled bubble growth [6]. After the departure of a bubble, colder ambient liquid is drawn on to the surface, during when heat transfer from the surface to the liquid is by transient conduction and this period is known as waiting period which lasts until the boundary layer thickness grows enough to sustain nucleation. During the initial stages of bubble growth, the growth rate is quite high as the radius of curvature increases suddenly, due to the presence of a highly superheated liquid layer adjacent to the vapor interface. This rapid bubble growth is only limited by the inertia of the liquid and is hence known as inertia controlled growth. As the bubble grows radially, a very small thin film of liquid underneath the bubble, known as the evaporation microlayer exists which evaporates at the vapor interface. With further growth, the superheated liquid film surrounding the bubble,

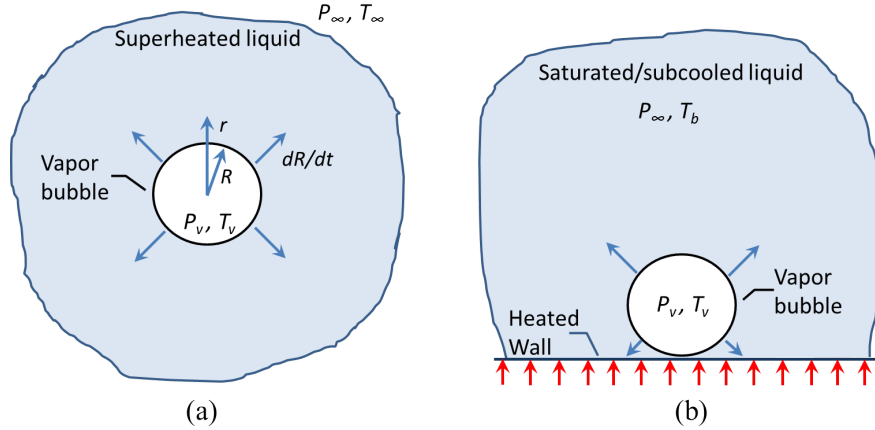


Figure 1.15: Types of bubble growth models (a) Uniform superheat theory, involving spherical vapor growth in a uniformly superheated liquid (b) Bubble growth in non-uniform temperature field; temperature highest at the wall[25].

known as the relaxation microlayer, depletes during which the bubble growth rate reduces. This regime of bubble growth is known as heat transfer controlled bubble growth. This process is illustrated in Fig. 1.16.

Models developed for the case of uniform temperature field can be divided into inertia controlled growth (Rayleigh [24]) and heat transfer controlled growth (Mikic et al. [25], Plesset and Zwick [26], Scriven [27]). These models were later extended for the case of bubble growth in a non-uniform temperature field like those of Zuber [28], Cole and Shulman [29], Van Stralen [30] and Mikic and Rohsenow [31]. However, the results in this study will show the inadequacy of these models to predict bubble growth for structured surfaces and highly wetting fluids such as FC-72.

Models for experimental conditions that are similar to those in the current study are mostly empirical in nature and often present asymptotic growth relationships as a function of time (Lee et al. [32], and Ramaswamy et al. [33]). Such models are, however, simplistic in nature and do not adequately explain the effects of liquid, and surface such as roughness or re-entrant cavities. The study presented here is an effort to contribute to the fundamental understanding of the bubble dynamics such as growth rate, departure frequency and diameter experimentally using high speed imaging for the unique surface structure with re-entrant

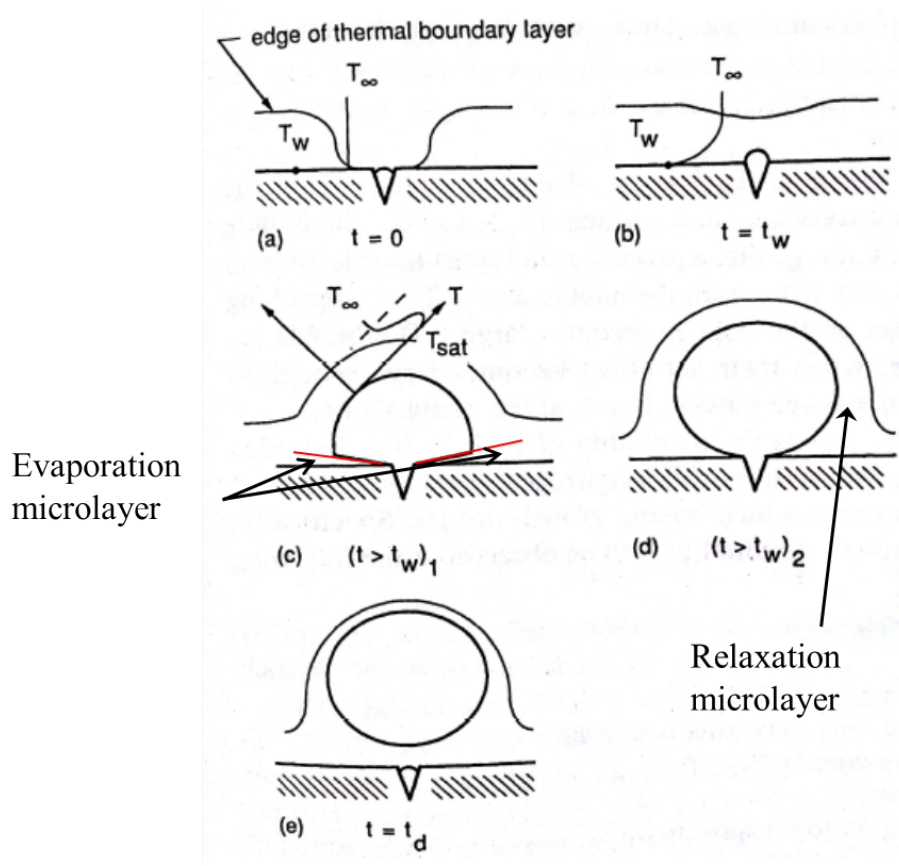


Figure 1.16: Regimes of bubble growth illustrated as shown in Carey [6] (a) Ambient cooler liquid is brought in to contact with the heater surface (b) Growth of boundary layer (c) Bubble nucleation and inertia controlled regime (d) Relaxation microlayer thickness decreases (d) Bubble departure.

cavities that was tested with FC-72. Some of the studies that are similar to the conditions of the current study, in the aspect of pool boiling on silicon surfaces using FC-72 include (Hutter et al. [34], Nimkar et al. [14], Ramaswamy et al [33], Moghaddam and Kiger [35], and Demiray and Kim [36]). Of the aforementioned studies, [14, 17, 33, 34] conducted pool boiling studies on silicon surfaces with structured cavities. No studies have been conducted for the nucleation of FC-72 on sloped surfaces with re-entrant cavities.

Growth rate of FC-72 was analyzed by Hutter et al. [34] on silicon surfaces with cylindrical cavities. The observed bubble growth and bubble shape is shown in Fig. 1.17. It was observed that the growth rates vary with time on the order of $\approx t^{-1/2}$ as noticed in Fig. 1.18, which is similar to the trends reported by Ramaswamy et al. [33] who conducted pool boiling experiments using FC-72 on structured surfaces with square cavities.

Nimkar et al. [14] and Bhavnani et al. [17] used pyramidal re-entrant cavities and bulb shaped re-entrant cavities, respectively, during pool boiling with FC-72. Effects of heat flux, cavity spacing, bubble departure frequency were studied. It was observed that the pyramidal re-entrant cavities completely avoided nucleation hysteresis compared to the bulb-shaped cavities. Also, bubble departure diameter and frequency were found to increase with wall superheat.

The data thus collected on bubble dynamics at 1g will be corroborated with data from microgravity experiments conducted using the same set up.

1.1.5 Bubble dynamics under reduced gravity

It was earlier stated that one of the objectives of the study would be to develop and test a pump less flow loop utilizing surface asymmetry and re-entrant cavities for space electronics applications. This requires a better understanding of vapor bubble dynamics under reduced gravity and hence its effect on pumping. Due to the complexity of such experiments, literature on micro gravity experiments and the related bubble dynamics is very limited.

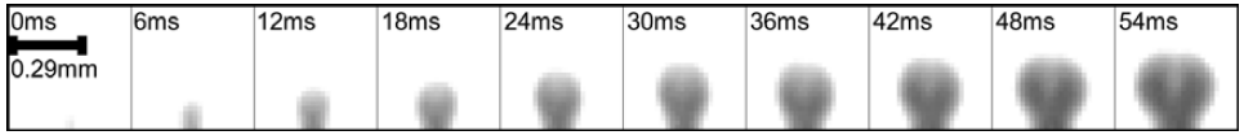


Figure 1.17: Bubble growth process from a cylindrical cavity on a silicon surface using FC-72 - Hutter et al. [34]

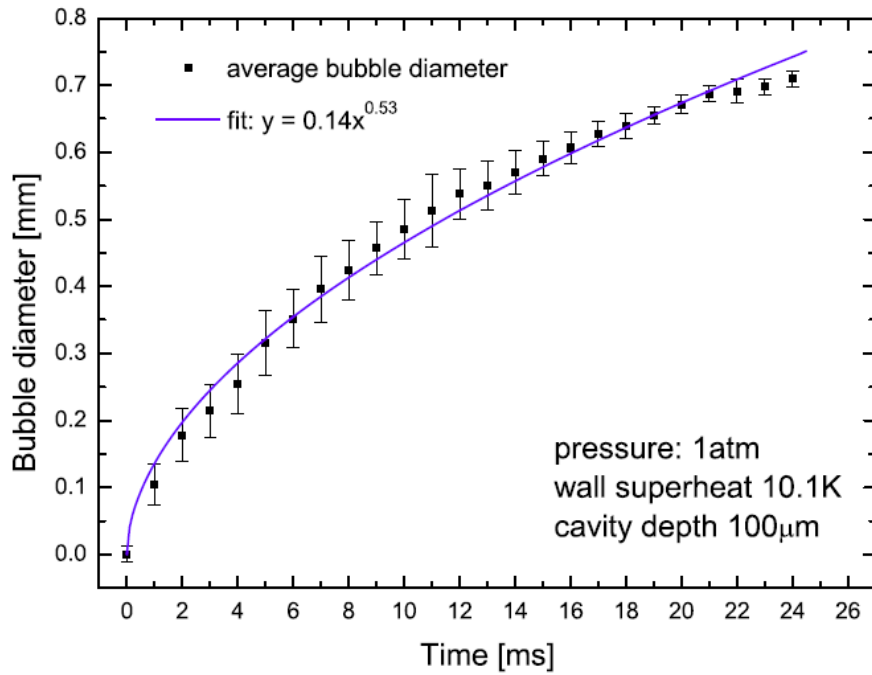


Figure 1.18: Bubble growth rate from a cylindrical cavity on a silicon surface using FC-72 - Hutter et al. [34]. The asymptotic growth relationship is marked as the equation of fit in the figure.

Microgravity testing methods

Microgravity, or reduced gravity, conditions can be produced in a number of ways by compensating for the earth's gravity. Some of the common methods to produce "weightlessness" or microgravity include a free fall in different trajectories, a freely drifting spacecraft or space station, and ballistic rockets. A free fall could be conducted in drop towers and drop shafts where the free falling object on guide rails experiences microgravity due to the absence of forces that oppose gravity [37]. The relationship between free fall height and time can be expressed as,

$$t = \sqrt{\frac{2H}{g}} \quad (1.2)$$

where,

t = time of free fall

H = free fall height

Key drop tower and drop shaft facilities in United States include NASA Glenn Research Center in Cleveland, Ohio, which has a drop tower of 24 m and a draft shaft of 132 m providing a microgravity duration of 2.2 and 5.2 seconds respectively. Marshall Space Flight Center in Huntsville, AL, can produce 4.6 s of microgravity with a drop tower of 106 m. The drawback of testing in a drop tower or drop shaft is the low duration of microgravity and the quality. The low duration significantly affects analysis of processes with longer time scales such as bubble growth in microgravity, which is considerably slower compared to that under earth gravity. Also, in a drop tower or a drop shaft the highest quality of reduced gravity is achieved during the initial period of fall, extending less than 2 seconds, after which the free falling object experiences a residual gravity due to the drag forces of surrounding gas. However, residual gravity can be reduced using evacuated conditions. The short duration of microgravity is also a drawback since any natural convection that started before the drop will not be eliminated completely within the short period of microgravity.

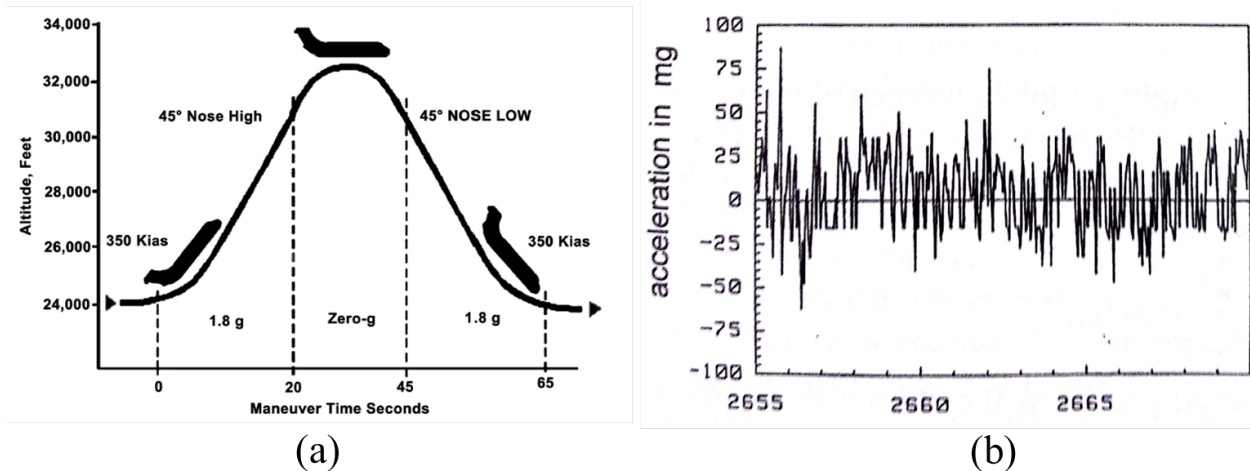


Figure 1.19: (a) Parabolic trajectory of a C-9B flight and the achieved reduced gravity periods (b) G-jitters in a parabolic flight due to disturbances such as air turbulence - Straub [37].

A similar method to produce microgravity involves free fall along parabolic trajectories that are flown by special aircraft such as KC-135, DC-9, C-9B, and recently Boeing 727-200F, by NASA from the Johnson Space Center in Houston (Fig. 1.19a). Advantages of such a method include longer durations of microgravity, up to 20 seconds, and the volume of experiments that can be tested. Also, different gravity levels can be achieved by altering the trajectory of the flight to simulate lunar and martian gravities. However, the quality of microgravity could be affected by air turbulence and flight maneuvers, producing gravity fluctuations on the order of $10^{-2}g$ as shown in Fig. 1.19b, known as g-jitters. However, such g-jitter could be dampened by free floating the experiment inside the flight.

Parabolic trajectories to produce reduced gravity are also achieved in ballistic missiles known as “sounding rockets” which are categorized as sub-orbital flights. The sounding rockets are powered by a solid propellant rocket motor to achieve the trajectory and the rockets reach altitudes of up to ≈ 165 km where the air density is very low, thereby reducing the air drag to produce a high quality ($\leq 10^{-6}g$), long duration (≈ 200 seconds) microgravity regime [38]. The payloads are retrieved using a parachute for re-use and data retrieval. Some

of the commonly used facilities include the sounding rockets under the German TEXUS program and NASA’s Terrier-Orion sounding rockets.

The best method for microgravity testing is aboard the International Space Station (ISS) which provides unlimited duration of high quality microgravity. The ISS facility used to conduct boiling experiments is known as Microheater Array Boiling Experiment (MABE) located in a module known as the Microgravity Science Glovebox (MSG) [39].

Bubble dynamics and heat transfer under microgravity

In boiling at terrestrial gravity, bubble departure from the heated surface is primarily a balance between surface tension which causes the bubbles to remain attached to the surface, and, drag and buoyancy forces which cause the bubbles to detach from the surface. But under reduced gravity, the forces due to buoyancy are negligible and hence the bubble tends to remain at the surface for longer periods resulting in larger bubble departure diameters as has been widely reported in previous studies [40–43]. An image of the large bubble diameters observed by during pool boiling of FC-72 under microgravity is shown in Fig. 1.20. The dependence of departure diameter on gravity can be expressed as,

$$\frac{D_{d,\mu g}}{D_{d,1g}} = \left(\frac{a}{g}\right)^{-1/2} \quad (1.3)$$

where,

D_d = bubble departure diameter

g = earth gravity

a = tested gravity

Because of the bubble size being as large as the heater as seen in Fig. 1.20, the heat transfer is significantly reduced and many studies have reported reduction in heat transfer compared to terrestrial gravity using a variety of fluids such as FC-72 [38, 41] and R-113 [40]. Heat transfer from a 2.7 mm x 2.7 mm array of heaters to FC-72, studied in [38] shows

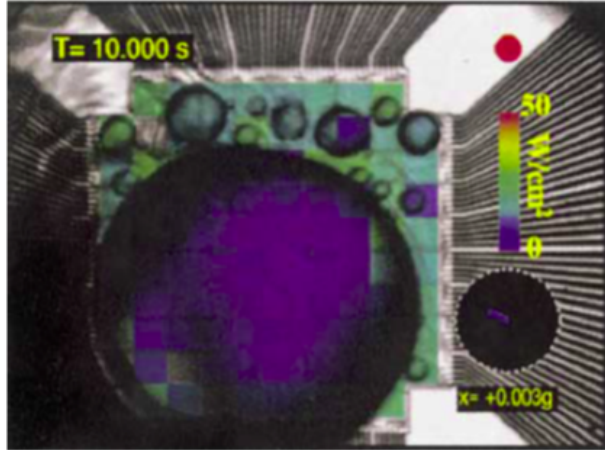


Figure 1.20: Large bubble of diameter ≈ 2.5 mm in pool boiling of FC-72 under reduced gravity at a wall superheat of 30°C - Kim and Benton[38].

that at high wall temperatures heat transfer at microgravity is significantly affected (Fig. 1.21a). It was also demonstrated by Henry and Kim [41] that heat transfer in microgravity is a function of heater size and liquid subcooling. In a large heater, the bubbles are distributed and the presence of a large number of smaller satellite bubbles lead to a higher heat transfer compared to that with smaller heater sizes (Fig. 1.21b). Also, high liquid subcooling resulted in a higher heat transfer compared to lower subcooling. Bubbles of larger sizes, observed under microgravity, also cause dry-out of the surface under the bubble which leads to critical heat flux (CHF). CHF is the maximum heat flux condition beyond which heat transfer decreases and wall temperature increases significantly (Fig. 1.21a).

Pool boiling experiments on flat heater surface using R-113 was performed in space shuttle flights by Lee and Merte Jr. [43]. Effects of heat flux and liquid subcooling were studied. While observations of larger bubble diameters similar to a number of other studies were reported at all tested conditions, an interesting observation of bubble migration was reported. It was observed that a number of small bubbles coalesced to form a very large bubble which departed from the surface and hovered close to the surface. Bubble departure was mainly attributed to the momentum and coalescence of smaller bubbles. Also, the migration of smaller bubbles towards the larger bubble at velocities of 2.5 cm/s noticed at

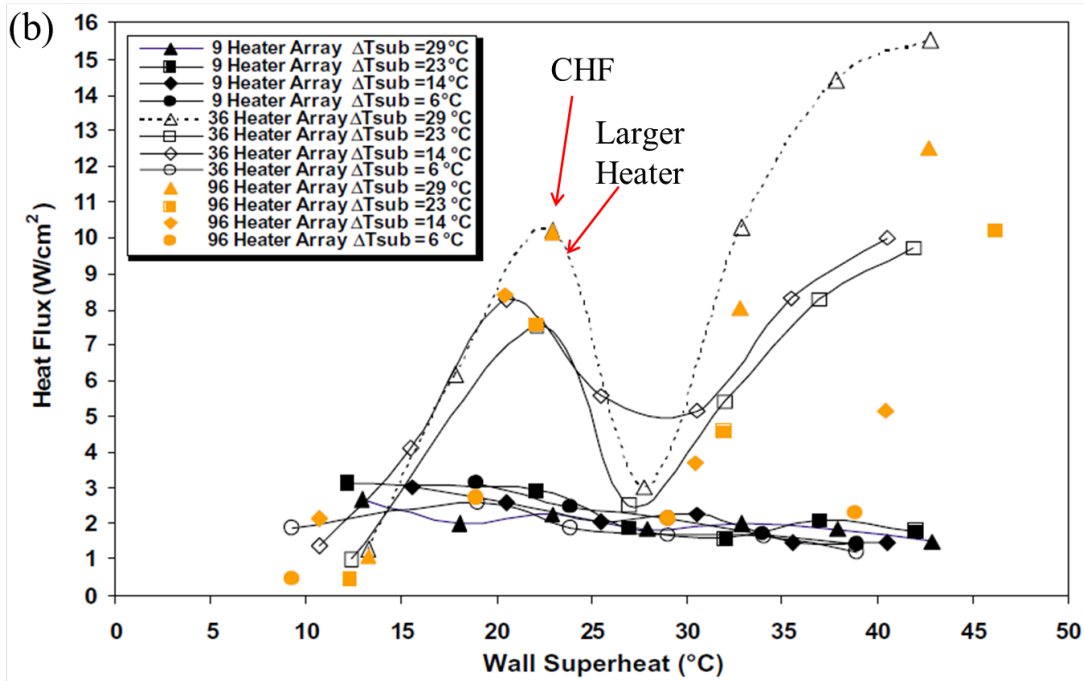
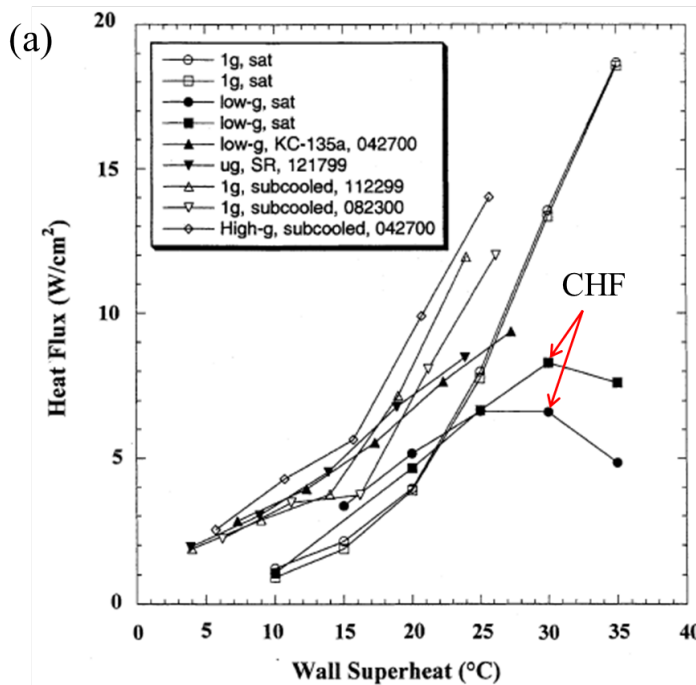


Figure 1.21: (a) Lower heat transfer observed under microgravity in pool boiling of FC-72 at higher wall superheat. Critical heat flux (CHF) also reduced compared to earth gravity - Kim and Benton[38] (b) Heat transfer increases with increasing heater sizes and liquid subcooling - Henry and Kim [41]

high subcooling led to a 40% increase in heat transfer compared to similar conditions at earth gravity. An image of the large hovering bubble and adjacent smaller bubbles are shown in Fig. 1.22



Figure 1.22: Large hovering bubble in R-113; smaller adjacent bubbles near the larger bubble were noticed to migrate towards the larger bubble at high subcooling - Lee and Merte Jr. [43].

Similar migration of vapor bubbles on plain heated surfaces has also been reported previously under reduced gravity attributed to g-jitters [42]. Sliding velocities of up to 2.25 cm/s were reported in pool boiling of distilled water. Marangoni and thermocapillary convection [38, 44–46] have also been shown to cause bubble migration due to boiling in a subcooled pool of liquid.

From the aforementioned studies it could be observed that the bubble dynamics in pool boiling are considerably altered under microgravity. Also, literature for such microgravity studies is extremely limited owing to the experimental constraints involved in a microgravity experiment, such as duration of microgravity, number of experiments, and the complicated experimental setup required for safety. Data is often limited to pool boiling on flat surfaces and wires in fluids such as water, R-113 and, FC-72. However, no studies have been conducted for surface profiles like the one used in current study, and hence no information is available on the effects of surface asymmetry and re-entrant cavities on bubble dynamics. Hence, the current study to analyze the effect of surface asymmetry at reduced gravity

on bubble dynamics and liquid pumping will be a novel attempt and will provide valuable information about bubble dynamics.

Chapter 2

Fabrication of Silicon Test Devices

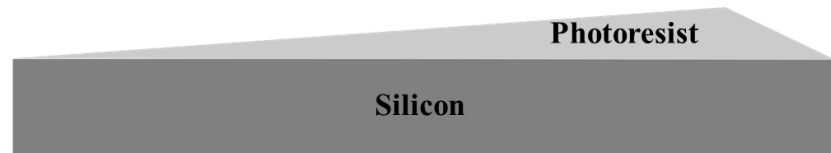
The silicon heat sinks used in this study consist of saw-tooth cross-sectioned, asymmetric surfaces and re-entrant cavities that are located only along the long slope of the surface. The heat sinks fabricated in this study are of two types and were designed to be used in two different sets of experiments. One set of experiments, termed as large array experiments, were designed for global measurements of liquid velocity, bubble dynamics and heat transfer. The test devices used in large array experiments consisted of 80 ratchets in silicon. The other set of experiments were designed to study local bubble dynamics and resulting effects on the adjacent liquid using a small array of silicon ratchets, termed as small array experiments. The small array test device consisted of only eight ratchets of smaller footprint compared to the large array experiments. The small array test devices were fabricated for use at Oregon State University, a partner institution on this research project. While the overall objective of the study, which is to obtain net lateral liquid flow using structural asymmetry, is the same in both sets of experiments, there are differences in the scale of the experimental setup, methods of experimentation, and techniques used. Because of these differences, the test devices used were designed and fabricated to cater to specific requirements of the techniques used and experiments conducted. Some of the important characteristics of the test device required for the different experiments are outlined below:

- Fabricate saw-tooth cross-sectioned ratchets on silicon to obtain a nominal profile of $30^\circ - 60^\circ - 90^\circ$.
- The surface of the resulting ratchets required a smooth finish as the presence of any surface imperfections will act as nucleation sites.

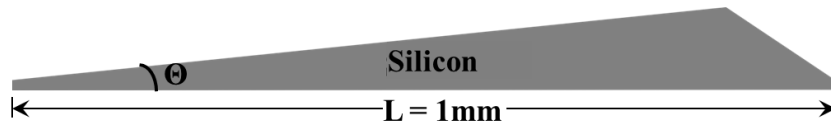
- Etch re-entrant cavities from the back side of the ratchets to open up trapezoidal mouth on the sloped face of the saw-teeth. The presence of these features only on the shallow slope is to cause an asymmetry in vapor bubble nucleation thereby leading to an asymmetry in momentum imparted to the liquid.
- Design and fabricate aluminum serpentine heaters on separate silicon wafers. The traces were designed to prevent electromigration while providing adequate power to induce vapor nucleation. Electromigration is the severance of current carrying metal paths due to excessive current density in a metal of given cross-section [47, 48].
- The heaters for the small array experiments were also designed for infrared imaging of cavities from the back side of test devices, requiring optimum spacing between the aluminum heater traces and anti-reflective coating on the heater to prevent reflection from the aluminum traces.
- Dice the silicon wafer consisting of saw-tooth ratchets into large and small array of ratchets for the two different sets of experiments.
- Bond the silicon wafer consisting of ratchet array to the heater wafer with minimal thermal interface resistance. Due to the difference in the footprint area of the large and small array test devices different bonding schemes were used.

Because of the unique cross-section of the test structures utilized, literature corresponding to the fabrication processes was limited and fabrication steps involved elaborate calibration and trials to precisely obtain the required structure.

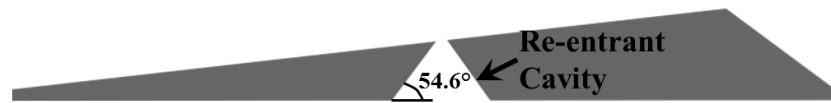
Broadly, the fabrication of the heat sink consists of four steps. Gray-scale photolithography to obtain the saw-tooth ratchets in silicon, etching re-entrant cavities on the shallow slope of the saw-tooth ratchets, fabrication of serpentine aluminum heater on silicon, and finally dicing and bonding the two silicon layers using techniques such as fusion and gold eutectic bonding. These basic fabrication steps are represented in Fig. 2.1.



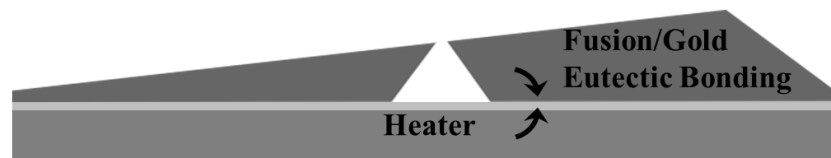
(a) Gray-scale photolithography to deposit a photoresist layer with a gradient in height



(b) Deep Reactive Ion Etching (DRIE) to obtain the asymmetric saw-tooth cross-sectioned ratchet



(c) Anisotropic wet etching to fabricate re-entrant cavities from the back side to open trapezoidal mouth on the long slope of ratchet



(d) Bonding of heater to the saw-tooth ratchet array using fusion bonding for the large array test devices and gold eutectic bonding for the small array test devices

Figure 2.1: Illustration of steps involved in fabrication of the silicon test devices to be used in the large and small array experiments

2.1 Fabrication of silicon ratchet array

The saw-tooth structures were fabricated on a 100 mm diameter and 0.5 mm thick double side polished <100>silicon wafer. Gray-scale photolithography process involves deposition of photoresist with a gradient in height. The height gradient in photoresist is obtained by allowing UV light to pass through a gray-scale optical mask consisting of patterns ranging from being completely transparent to opaque. This causes light penetrating to increasing depths in photoresist, which when developed results in a gradient in height [18, 22, 23]. The photoresist used in the current study is SPR 220-7.

This asymmetric photoresist structure is transformed into a silicon structure of required dimensions using DRIE, as illustrated in Fig. 2.2. The angle of surface etched in silicon is dependent upon the etch selectivity (ratio of silicon to photoresist etch rate) of the photoresist used, the duration of the etching and passivation cycles, and the ratio of gas flow rates in the plasma during DRIE. Extensive calibration was conducted to analyze the effects of flow rate of the constituent gases in the plasma during the DRIE etching cycle and cycle duration, on the etched angle of the silicon structure and the surface quality.

Prior to DRIE, the wafer with the photoresist structure was subjected to an oxygen plasma, known as the plasma de-scum process, to remove a thin layer of photoresist so as to expose a few micrometers of silicon at the trough. Without this step, etching would begin unevenly across the wafer leading to a poor saw-tooth profile. All the DRIE processes were performed using an STS ICP etcher. As discussed earlier, the DRIE process consists of an etching cycle, during which silicon is etched using SF_6 flow, and a passivation cycle which involves deposition of a Teflon layer (C_4F_8) along the side walls. The first wafer was etched using a standard Bosch process with the flow rate of SF_6 set at 130 SCCM and O_2 at 13 SCCM in the etching cycle, and 85 SCCM of C_4F_8 in the passivation cycle. The time duration used for etching and passivation cycles were 13s and 7s respectively. This resulted in a very high etch selectivity of ≈ 100 which in turn resulted in a very high angle of the saw-tooth and a rough surface. Hence to reduce the selectivity i.e., increase the photoresist

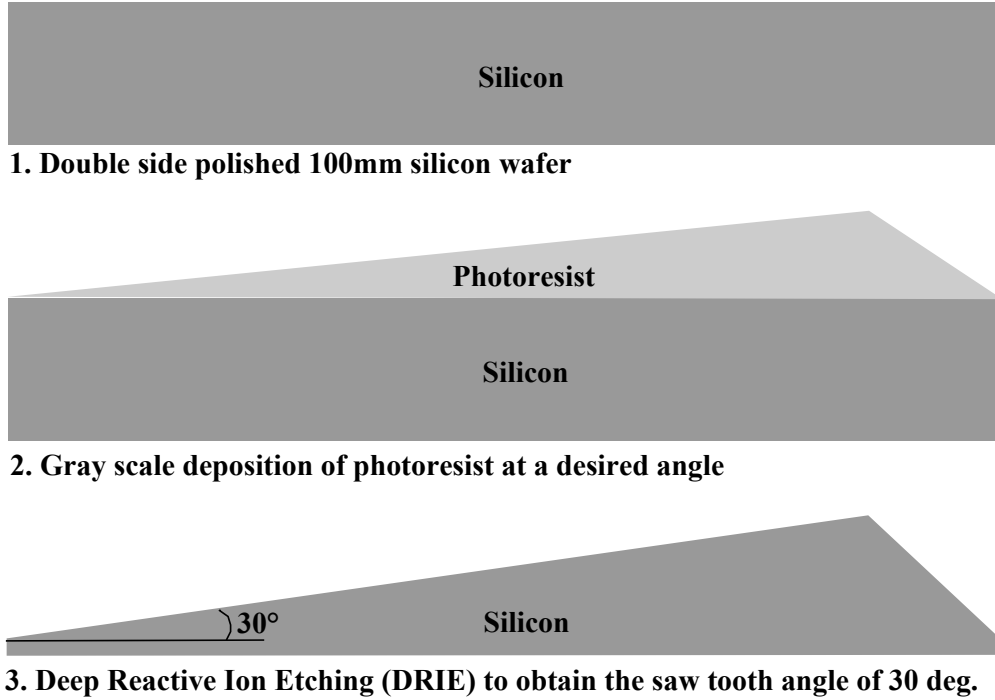


Figure 2.2: Steps involved in the fabrication of silicon saw-tooth ratchets

removal rate, the oxygen flow rate was increased sequentially in the subsequent cycles as oxygen has been shown to etch the photoresist faster [20, 23]. Reduction of the duration of passivation cycles also has the effect of increasing the photoresist etch rate and hence in all subsequent recipes the duration of passivation cycle was reduced to 3s.

The recipes followed for DRIE in the subsequent trials have been tabulated in Table 2.1. In recipe A, the flow rate of O_2 was increased drastically which decreased the selectivity resulting in an angle of 19° . However, short passivation cycles resulted in poor surface quality due to the formation of black oxide or silicon grass as shown in the SEM image in Fig. 2.4. These nanostructures in silicon or grass are generally formed when the polymer material is not completely etched due to short etching cycles or low concentration of etching species (F radicals) in the plasma [20]. This scenario of low concentration of etching species arises when O_2 flow rate is increased in the plasma. It has also been reported that high concentration of oxygen forms micromasks which results in grass like structures due to the directional etching [21]. Hence, to prevent the silicon grass formation, the concentration of

the etching species can be increased by increasing SF_6 flow rate. But increasing SF_6 also leads to deterioration of anisotropy [21]. Hence, in all the subsequent recipes B, C and D short periodic etching lasting not more than 10 seconds using SF_6 in the absence of O_2 and C_4F_8 was introduced in between sets of etching/passivation cycles.

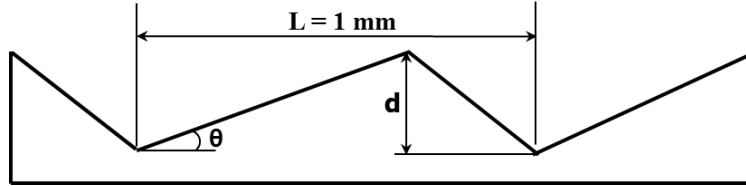


Figure 2.3: Illustration of DRIE parameters discussed in Table 2.1

Table 2.1: DRIE etch parameters and resulting saw-tooth angle

Recipe	Flow Rate in the Etching Cycle O_2/SF_6 (SCCM)	Duration of Etching/ Passivation Cycles (s)	Angle (θ)	Depth d (μm)
A	80/100	13/3	19	235
B	65/100	13/3	24	305
C	50/100	13/3	32.15	440
D	53/100	13/3	30.5	415

Since the objective is to achieve an angle of 30° for the saw-tooth, it was required to slow down the photoresist etching rate and hence in recipe B, O_2 flow rate was decreased to 65 SCCM keeping the other parameters constant along with periodic 10 second SF_6 etching. This procedure resulted in a saw tooth angle of 24° without the silicon grass. In recipe C, by further decreasing the O_2 flow rate to 50 SCCM an angle of 32.5° was achieved and finally with 53 SCCM of O_2 , noted as recipe D, an angle of 30.5° was achieved without any grass formation. An image of a cross-section of the ratchet array with a nominal saw-tooth angle of 24° and without any silicon grass is shown in Fig. 2.5.

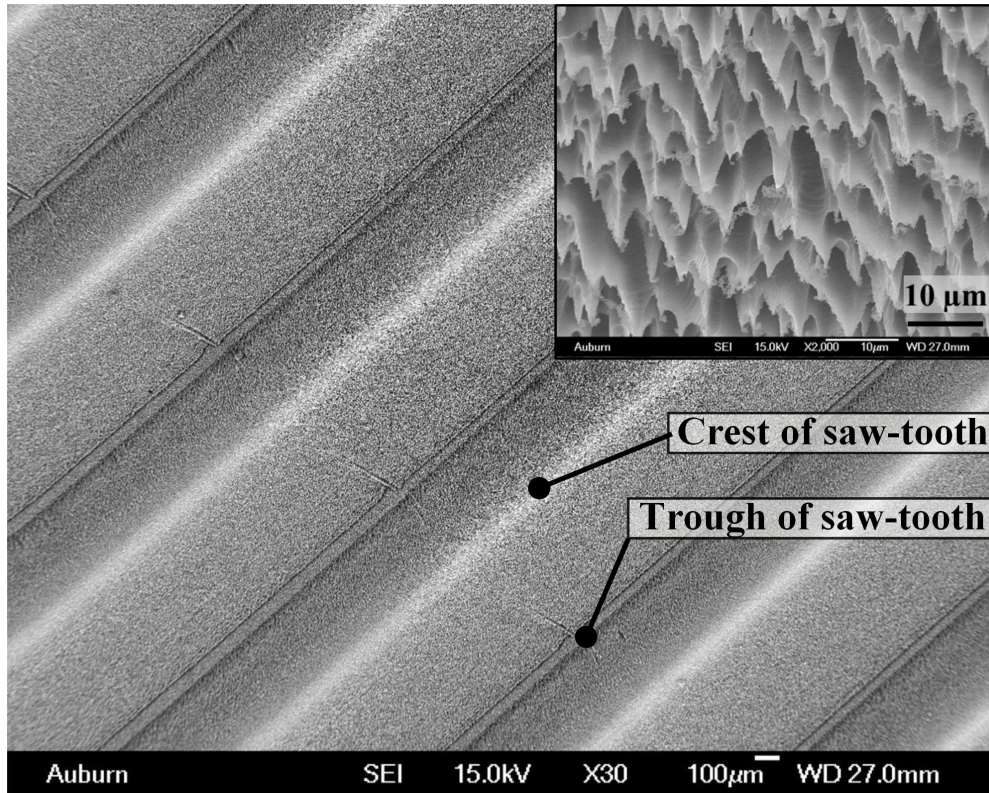


Figure 2.4: SEM image of the ratchets with an angle 19° . The inset shows an SEM image of silicon nano-structures, known as “silicon grass”, formed during the DRIE process with Recipe A.

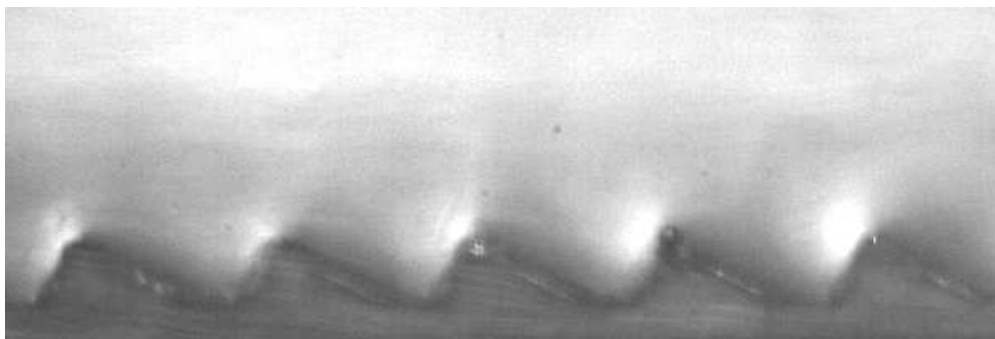


Figure 2.5: Cross-section of a ratchet array with a nominal saw-tooth angle of 24°

2.2 Fabrication of re-entrant cavities

The next step in the process was to etch the re-entrant cavities from the back side of the saw-tooth structure using potassium hydroxide (KOH), known as anisotropic wet etching process. The fabrication steps involved in etching the re-entrant cavities are illustrated in Fig. 2.6. Before the etching process, a 2000 Å silicon nitride layer was deposited using low pressure chemical vapor deposition (LPCVD), which acts as a barrier layer preventing the KOH from etching silicon. To prevent any damage to the delicate ratchets during the process of etching cavities and subsequent handling of the wafer, a 500 μm thick, 100 mm diameter Pyrex wafer was stuck on top of the ratchets. The Pyrex wafer was coated with photoresist AZ 5214 after treatment with hexamethyldisilazane (HMDS) vapor for 5 minutes which improves adhesion of photoresist to the surface. The Pyrex wafer with the photoresist is stuck to the ratchet side of silicon wafer and baked on a hot plate at 100°C. The back side of the saw teeth was then coated with photoresist AZ 5214 after treatment with HMDS. This is followed by patterning of the photoresist using an optical mask to define an array of squares of side 0.655 mm and 0.246 mm for each pair of cavities - large and small respectively as shown in Fig. 2.7. Each saw tooth had eight such pairs spaced equidistantly along the transverse length of the saw tooth. The pattern of cavities on the optical mask held on the back side of the saw teeth was aligned with the saw teeth on the other side. This ensured that the cavities were etched only on the shallow slope. The alignment process was performed using a mask aligner consisting of two microscopes - one on the side of ratchets and other on the side of cavities, and the position of mask was adjusted until the cavity pattern was aligned to the ratchets. The photoresist was then developed to expose the nitride layer as shown in Fig. 2.6(iii). This exposed silicon nitride is etched to transfer the pattern to silicon. The wafers were then dipped into a solution consisting of 30% KOH in DI water with 20% isopropyl alcohol. The temperature of the solution was maintained at 80°C during the etching process. The beaker containing the mixture is covered by a reflux condenser that was mounted on top to prevent evaporation of the solution thereby maintaining the

integrity of mixture. The etching process occurs along the grain angle of silicon, which is 54.6° . The anisotropic etching process was periodically monitored by measuring the depth of etch under the microscope until the cavities breached the other side of the wafer on the long slope of the saw teeth to form a trapezoidal mouth Fig. 2.6(vi). Once the cavities were formed, the photoresist was stripped by cleaning with acetone, isopropyl alcohol and DI water. The remaining silicon nitride was removed using a phosphoric acid etch at 154°C . After the completion of all the steps, the Pyrex wafer was removed by dipping the wafer in acetone until the Pyrex wafer parted from the silicon wafer.

It has to be noted that test devices with a saw-tooth angle of 24° has only one cavity along the shallow slope of the ratchet compared to the two cavities along the long slope in other test devices. An SEM image with cavity mouth measurements for a 24° test device is shown in Fig. 2.8. This can be attributed to misalignment of the mask used to pattern the cavities on the back side of saw teeth. During DRIE, due to non-uniformity in etching, the saw tooth angle across the wafer varies between the outer periphery and the center of the wafer. This also leads to a variation in cavity mouth sizes. So even a slight misalignment could cause huge shifts in the cavity mouth diameter.

2.3 Fabrication of heater

An aluminum serpentine heater was used in the study to supply heat for the pool boiling experiments. Two different heater designs were used for the study - one for the large array test device and another for the small array test device. The two different heater designs are shown in Fig. 2.9. The steps involved in the fabrication of heater are shown in Fig. 2.10. All the heaters were fabricated on a 100 mm diameter and 0.5 mm thick double side polished $\langle 100 \rangle$ silicon wafer. The wafer was oxidized in a furnace to deposit 5000\AA of silicon oxide. This is followed by evaporating a $2\ \mu\text{m}$ thick layer of aluminum on to the SiO_2 surface using e-beam evaporation process. Photoresist AZ 5214 was deposited on the aluminum layer for photolithography. The heater design was then transferred to the photoresist from an optical

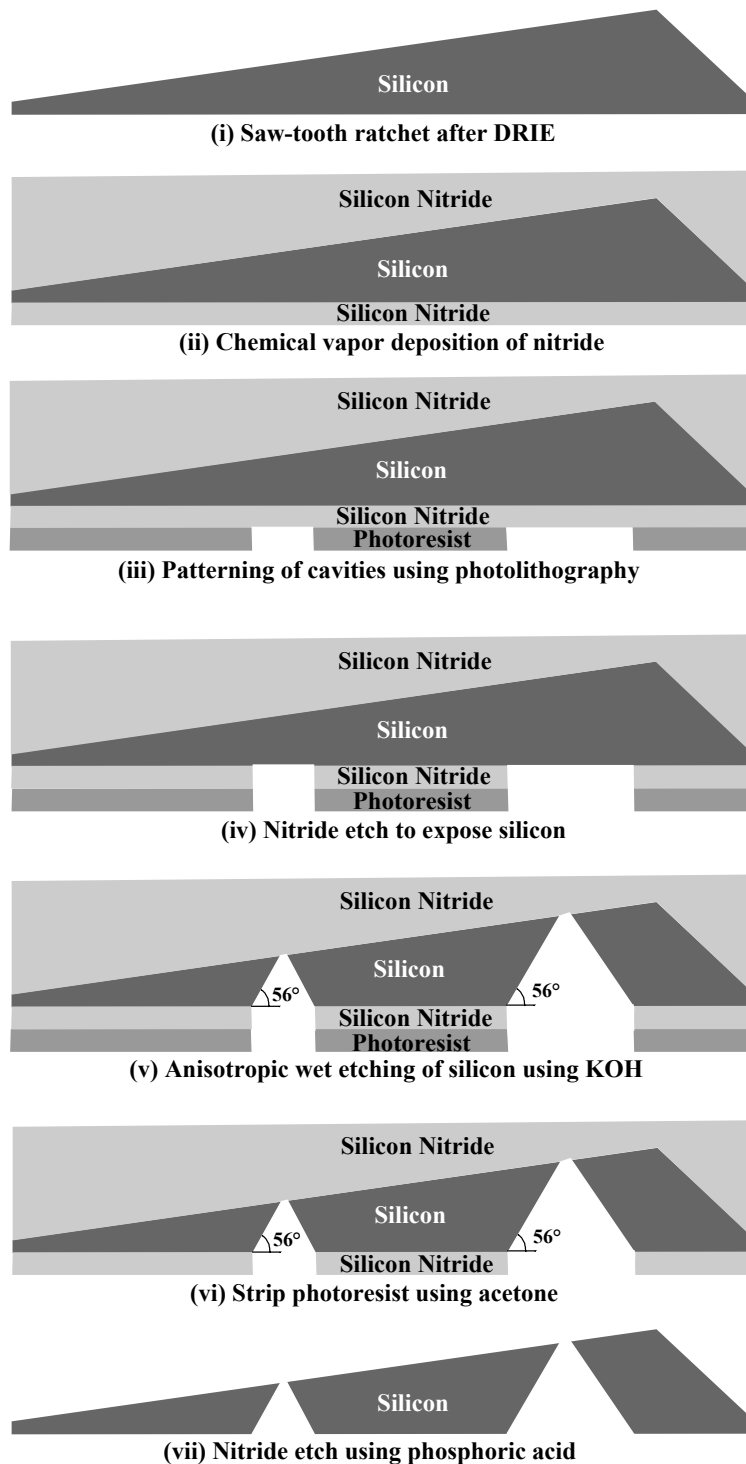
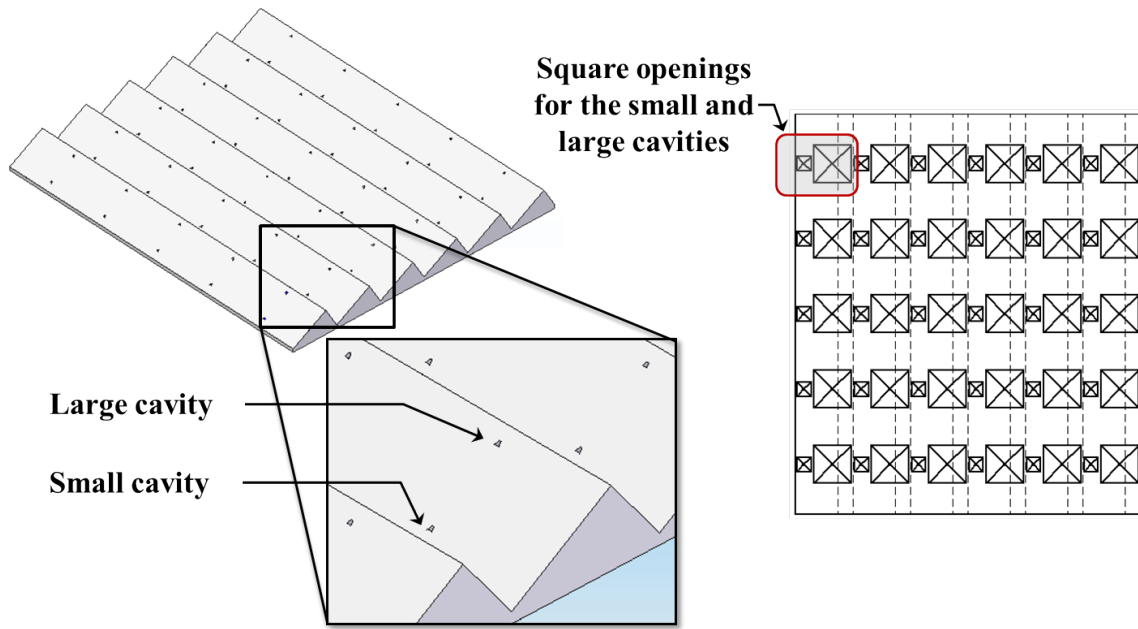


Figure 2.6: Illustration of fabrication steps involved in etching re-entrant cavities from the back side of saw-teeth to form trapezoidal cavity mouths only on the shallow slope



(a) Isometric view showing small and large cavities on the shallow slope of saw-tooth ratchets

(b) Back side of the ratchets showing the footprint of small and large cavities

Figure 2.7: Isometric and back side view illustrations of small and large array cavities on the shallow slope of saw-toothed surface

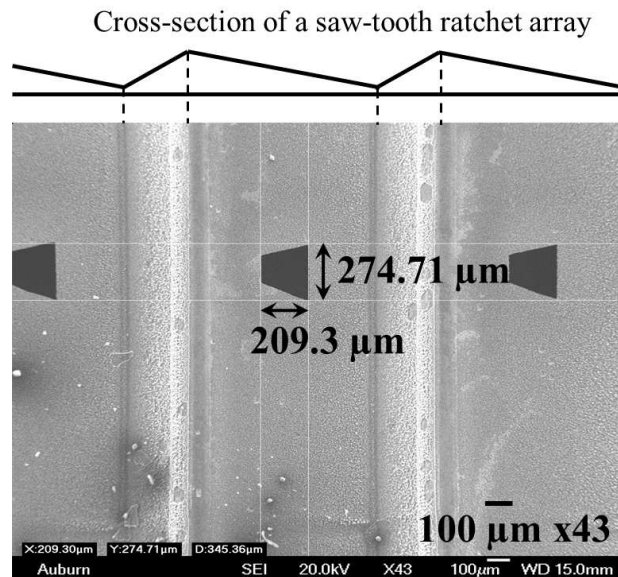
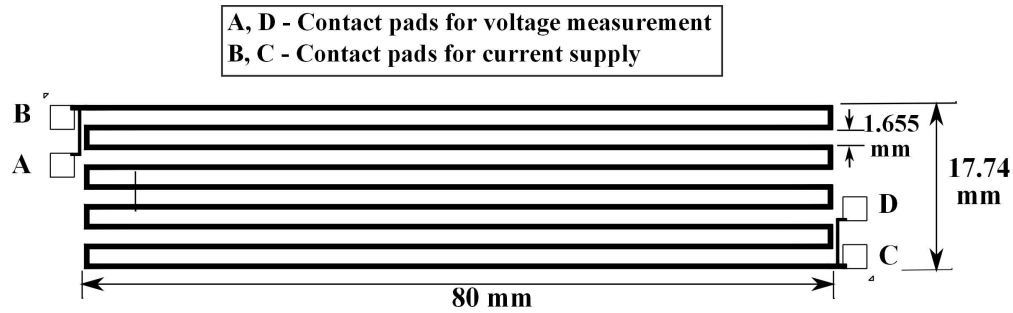


Figure 2.8: SEM image showing the top view of saw teeth and cavity mouth measurements in the test device with a saw-tooth angle of 24°

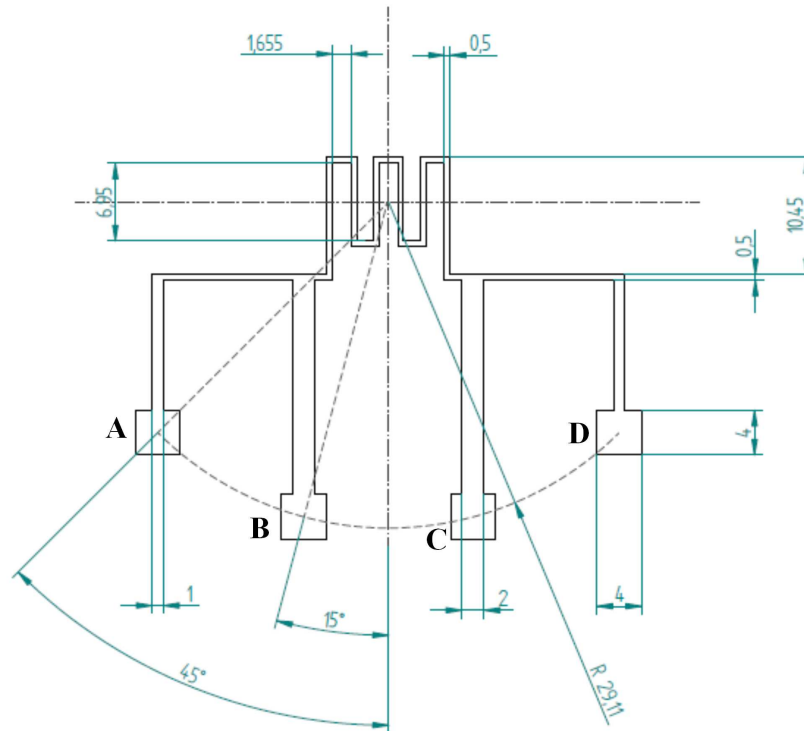
mask using a mask aligner. This is followed by the development of photoresist to expose the aluminum layer as per the heater design. The heater was formed by etching the exposed aluminum in a solution of phosphoric acid and acetic acid etchant (PAE) for 60 minutes. The heater was then diced to the size of the footprint of large array test section.

The fabrication of heater for small array test section involved additional steps. A thermal isolation trench was etched using DRIE along the perimeter of the heater to promote one dimensional heat transfer across the heater wafer to the silicon ratchets. This process is conducted along with the process to reduce the diameter of the heater wafer to three inches to fit in the test setup for the small array experiments. The wafer diameter was reduced by etching a ring of diameter equal to three inches through the silicon using DRIE. Prior to the etching of isolation trenches and the three inch ring, photoresist was coated on the side of heater and patterned using one mask for both the aforementioned steps. Since the trench was only designed to be $350\ \mu\text{m}$ deep, after etching to this depth the trench was covered with photoresist to prevent any further etching. However, etching along the three inch ring continued until the silicon wafer was completely etched through to reduce the wafer to a diameter of three inches. The photoresist was stripped from the wafer using acetone. Further, to facilitate IR temperature measurements the entire surface of the heater was coated with a $1.1\ \mu\text{m}$ thick layer of silicon nitride using plasma enhanced chemical vapor deposition (PECVD). This layer of silicon nitride serves to prevent the reflection of infrared radiation. Photoresist was spun on top of the silicon nitride layer and patterned using a mask in a mask aligner to expose the nitride layer over the electrical contacts. This was followed by etching the nitride layer from the electrical contact pads of the heater to enable power supply as silicon nitride acts as an insulator. The additional steps required in the heater for small array experiments are illustrated in Fig. 2.11.

Images of fabricated aluminum serpentine heaters on silicon for the large and small array test devices are shown in Fig. 2.12.



(a) Sketch of aluminum serpentine heater used in the large array test devices



(b) Sketch of aluminum serpentine heater used in the small array test devices

Figure 2.9: Sketch of aluminum serpentine heaters used in large and small array experiments that were fabricated on silicon. The width and thickness of heater traces are $500 \mu m$ and $2 \mu m$ respectively. The electrical contact pad configuration is labeled in the figure. The arrangement of electrical contact pads for the small array heater is based on the arrangement of electrical contacts in the wafer fixture.

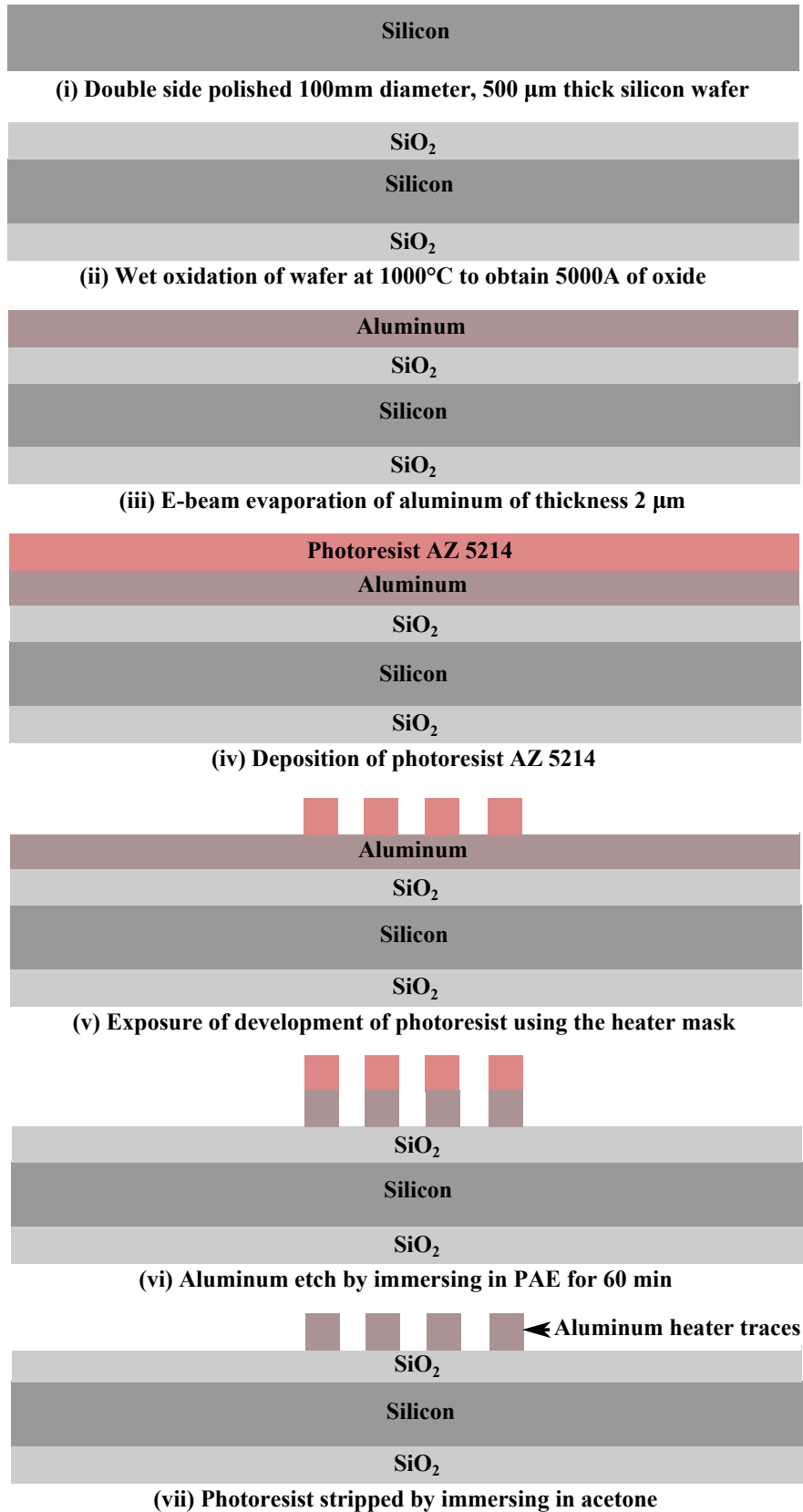
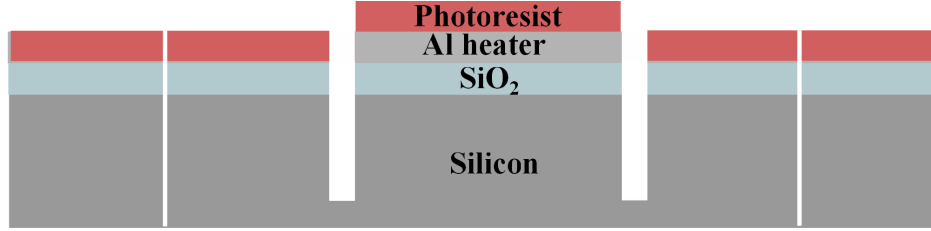
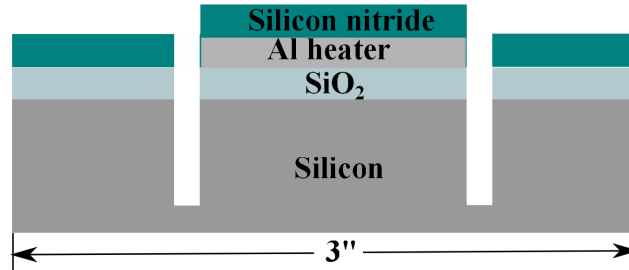


Figure 2.10: Fabrication of aluminum serpentine heaters used in large and small array test devices.



(i) DRIE to etch isolation trenches and reduce to a 3 inch wafer



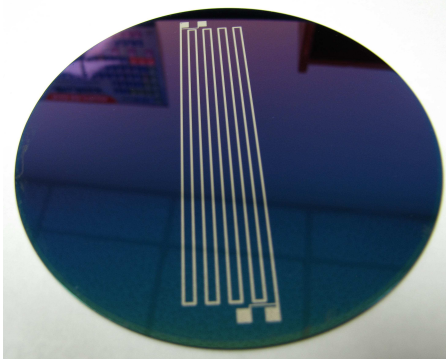
(ii) PECVD of silicon nitride to make heaters anti-reflective

Figure 2.11: Fabrication of isolation trenches on the back side of heater footprint and reduction of wafer diameter to 3 inches. Silicon nitride was coated to eliminate reflection of radiation during infrared measurements made during the small array experiments at OSU.

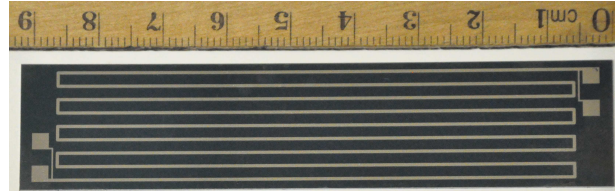
2.4 Bonding of saw-tooth ratchet wafer to the heater wafer

Bonding of the silicon wafer containing the saw-tooth ratchet array to the heater wafer was performed differently for the large array and small array test structures.

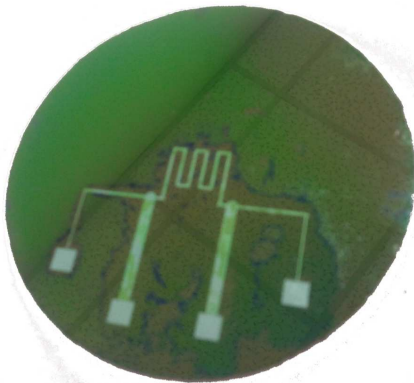
Large array test structures were bonded to the heater wafer using fusion bonding where the bonding between two ultra-flat extremely clean surfaces is due to bonding bridge replacements and bonds between OH groups [49]. Surfaces to be fusion bonded are required to be extremely clean, particle free, flat, smooth and hydrophilic. The surfaces to be bonded were rendered hydrophilic using an RCA-1 clean which is used to remove organic residues from the silicon wafer. The recipe for RCA-1 clean is 5 parts of DI water, 1 part hydrogen peroxide (H_2O_2), and 1 part ammonium hydroxide (NH_4OH). The solution was heated up to $70^\circ C$ when it starts boiling. The surfaces were immersed in to the solution for not more than 5 minutes. This was followed by rinsing the surfaces with DI water and thoroughly drying it. The surfaces to be bonded were immediately brought into contact with each other



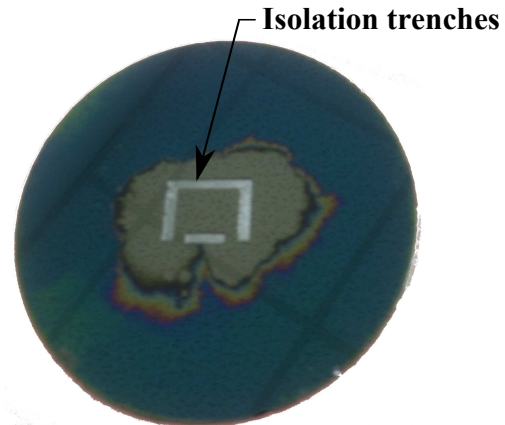
(a) Fabricated aluminum serpentine heater on a silicon wafer for large array test devices



(b) Diced aluminum serpentine heater



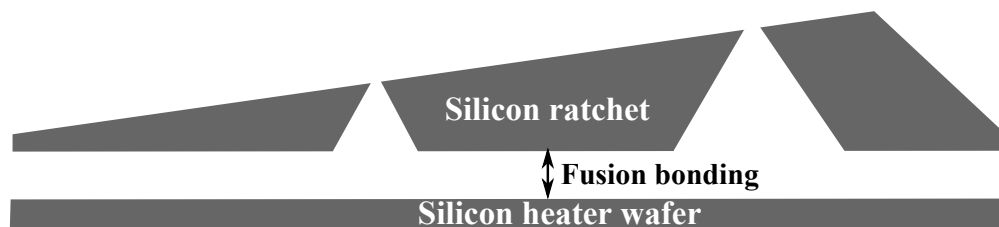
(c) Fabricated aluminum serpentine heater on a 3" silicon wafer for small array test devices



(d) Back side of the small array heater showing the isolation trenches (350 μm deep) along the perimeter of the heater footprint

Figure 2.12: Images of fabricated aluminum serpentine heaters used in large and small array experiments. The diameter of heater wafer for the large and small array test experiments are 4 inches and 3 inches respectively.

mechanically at room temperature. Under the right conditions, the two surfaces would bond together instantly, although weakly. This was followed by placing the weakly bonded surfaces in an oxidization furnace under pressure at 1100°C for 2 hours. The resulting bonds have a very high fracture strength of up to 20 MPa [49]. Because of the high temperature, any aluminum on the surface would soften or melt away. Hence, for the large array test devices, the aforementioned heater fabrication process was carried out after the bonding process. The fusion bonding process required multiple trials at different oven temperatures and durations before achieving one successfully bonded test device. By conducting initial calibration tests for fusion bonding at two different temperatures of 450°C and 1100°C, it was learned that the voids were significantly reduced at higher temperature. The fusion bonding process of large array silicon saw-tooth ratchet array with the heater is schematically represented in Fig. 2.13



Flat, ultra clean, hydrophilic surfaces mechanically brought into contact at room temperature. Bond strength increased by heating at 1100°C in a furnace for 2 hours

Figure 2.13: Illustration of fusion bonding process used to bond the large array of silicon saw-teeth to the heater wafer.

The bonding of the small array test devices by fusion bonding process could not be carried out due to the very small area available for bonding. For the small array test devices, bonding of the saw-teeth to the heater was achieved using gold eutectic bonding. Gold eutectic bonding is a low temperature process which involves the use of a solder made of gold-tin alloy which when held between the surfaces to be bonded and heated to the eutectic temperature of the solder, the materials fuse to provide a high strength bond. In this process, both the bonding surfaces were prepared by evaporating 1000Å titanium followed by 2700Å

of nickel and finally 1500Å of gold. Titanium improves the adhesion of gold to silicon [49] and nickel serves as a diffusion barrier between gold and silicon [50]. The deposition of layers of Ti-Ni-Au on the back of heater wafer was performed after coating photoresist and patterning the back side to only expose the silicon spanning the footprint of the heater. After the deposition of Ti-Ni-Au a lift-off process is performed by immersing the heater wafer in acetone. This causes the thin layer of photoresist under the layers of Ti-Ni-Au to dissolve, thereby causing the lift-off of Ti-Ni-Au from the surface except for the area where the layers are directly in contact with silicon, thus leaving layers of Ti-Ni-Au to span only the footprint of the heater. The bonding process was carried out using an FC150 automated die bonding machine where an upper arm holds the die and the substrate (heater) rests on a stage. A 1 mil thick alloy of 80% Au 20% Sn was used as a solder in the bonding process. The solder with a eutectic temperature of 280°C was advantageous since this temperature is well below the melting point of aluminum used in the heater. The bonding process was carried out at a temperature of 300°C by applying a weight of 200g for a period of 100 s. This process is illustrated in Fig. 2.14. The bonded test structures were inspected for voids using x-ray imaging. Presence of voids at the interface would appear dark in an x-ray image. From the x-ray images shown in Fig. 2.15 it can be noticed that the bonding was void free. The dark square regions in the x-ray image are the re-entrant cavities. It can also be noticed that some of the cavities appear lighter as the solder melted into the cavities.

In summary, two types of large array test sections were fabricated - one with a saw tooth angle of 24° and the other with an angle of 31°. The 24° test section has one cavity along the long slope between the crest and trough of each saw tooth, and 31° test section has two cavities. The small array test sections that were fabricated, similar to the large array test section, differed in saw tooth angle and number of cavities on the long slope of the saw tooth. Additionally, small array test sections also differed in the number of rows of cavities along the transverse length of saw-tooth. In only one type of small array test sections, the

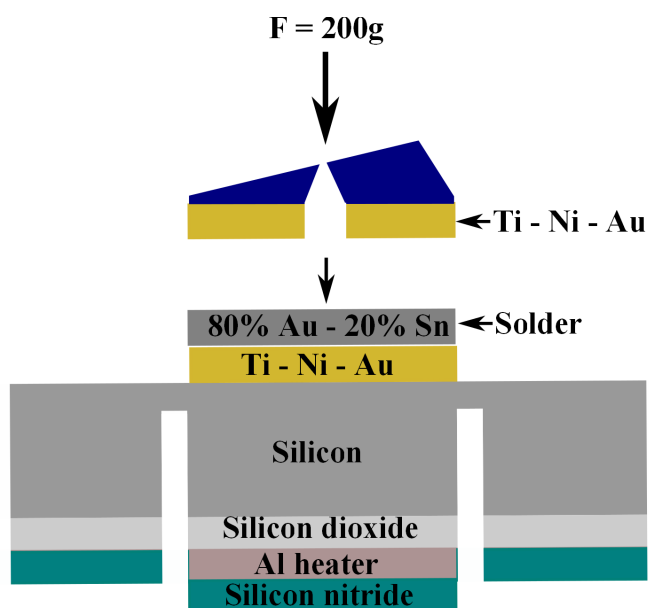
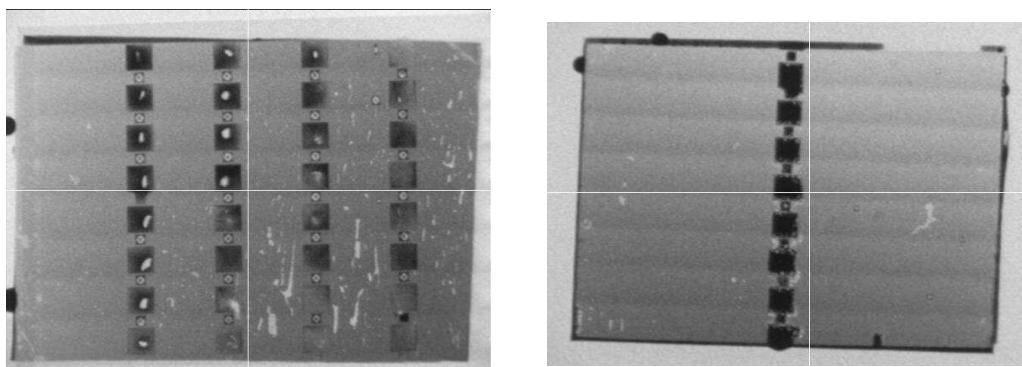


Figure 2.14: Illustration of gold eutectic bonding process used for bonding the small array saw-tooth ratchets to the 3 inch heater wafer



(a) X-ray image of bonded 24° small array silicon saw-tooth test section with 3" heater wafer. Voids appear dark in the image. The dark square spots in the image are the re-entrant cavities. No voids in the bond were noticed. Some cavities appear lighter since the solder melts and flows into the cavities partly.

(b) X-ray image of bonded 31.5° small array silicon saw-tooth test section with 3" heater wafer. No voids in the bond were noticed. A few smaller cavities appear to be filled partly by the solder

Figure 2.15: X-ray image showing the bond quality of gold eutectic bonding process

number of rows of cavities were reduced from four to one to reduce the nucleation activity. Characteristics of all the test devices built are summarized in Table 2.2

Table 2.2: Characteristics of different types of test sections fabricated

Test section parameters	Large array test section		Small array test section		
	A	B	A	B	C
Number of saw teeth	80	80	7	7	7
Saw tooth angle	24	31	24	31	31
Number of cavities along the long slope of the saw tooth	1	2	1	2	2
Number of rows of cavities along the transverse length of saw tooth	8	8	4	4	1
Foot-print area (mm x mm)	80 x 20.32	80 x 20.32	8 x 11.75	8 x 11.75	8 x 11.75

Chapter 3

Terrestrial Experiments

3.1 Experimental Setup

The silicon test device used for the large array, terrestrial, pool boiling experiments shown in Fig. 3.1a, is made of two layers - the asymmetric saw-toothed heat sink, and a serpentine aluminum heater. The heat sink has an asymmetric saw tooth cross-section with a $24^\circ - 90^\circ - 66^\circ$ profile and 1 mm pitch. The heat sink constitutes 80 such saw-teeth spanning a foot print of 80 mm x 20.5 mm. The asymmetric cross-section of the saw teeth was obtained using a combination of novel gray-scale photolithography and Deep Reactive Ion Etching (DRIE). The long, shallow slope of each saw tooth is structured with re-entrant cavities, or vapor trapping sites, that aid in triggering bubble nucleation. The pyramidal re-entrant cavities, fabricated using a wet etching procedure, have a trapezoidal mouth of size ranging between 200 – 250 μm . An SEM image of the cavities is shown in Fig. 3.1b. Each saw tooth has 8 cavities spaced equally along the ratchet on the long slope and in total the heat sink consists of 640 cavities acting as nucleation sites. Heat was provided using an aluminum serpentine heater shown in Fig. 3.1c. The voltage leads on the heater also aid in surface temperature measurements. The fabrication details of the asymmetric structure with re-entrant cavities and heater were discussed in the previous chapter.

The bonded test section is soldered on to a printed circuit board for electrical connections and under-filled for structural integrity. The board also serves as the base of a transparent polycarbonate open channel which is 130.8 mm long, 25.4 mm wide and 7 mm deep, and mounted right on top of the test device as illustrated in Fig. 3.1d. The channel serves to confine the volume of fluid for realization of net liquid flow. The test board was suspended from the lid into a pool of FC-72 (C_6F_{14}), a highly dielectric highly wetting fluid, contained in

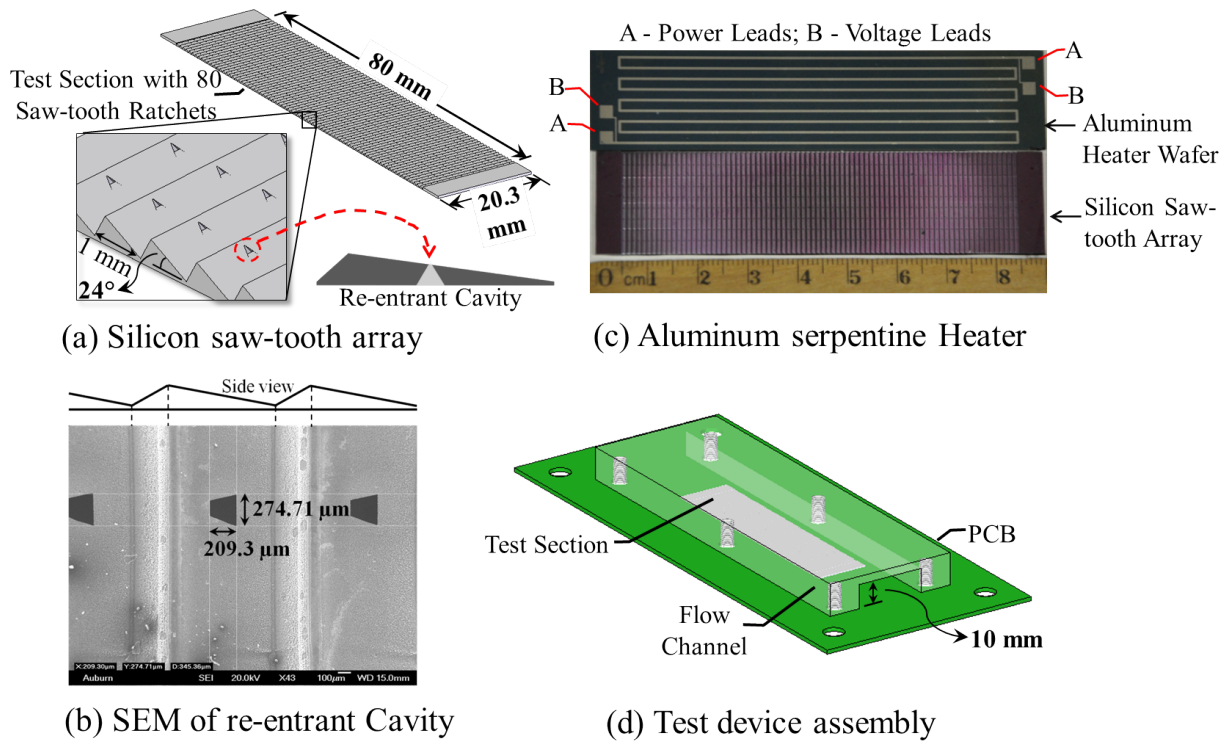


Figure 3.1: Silicon test device

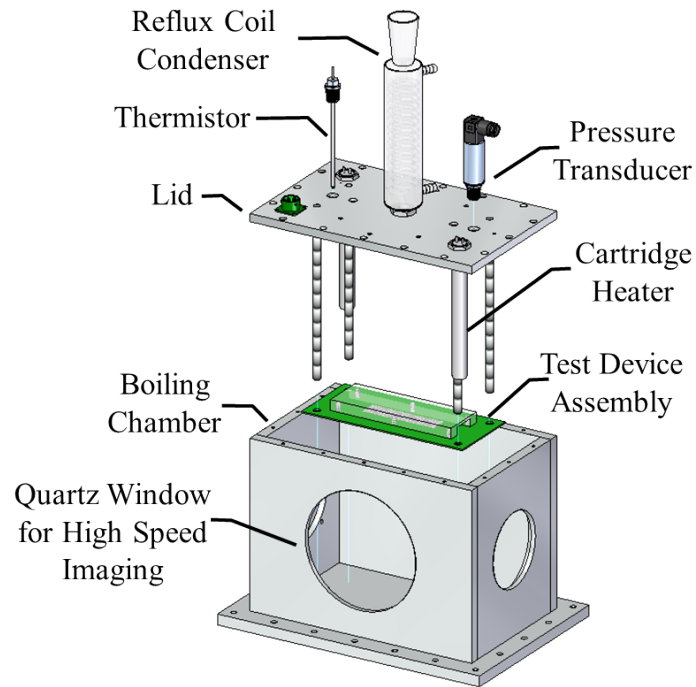


Figure 3.2: Boiling chamber assembly

an aluminum boiling chamber (Fig. 3.2) of dimensions 33 cm x 23 cm x 22 cm (L x W x H). Properties of FC-72 are summarized in Appendix A. A thermistor and a pressure transducer were used to measure liquid temperature and absolute pressure respectively. A reflux coil condenser open to the atmosphere helped maintain atmospheric pressure inside the boiling chamber and condense the vapor. Prior to experiments, FC-72 was thoroughly degassed by boiling using the submerged cartridge heaters in the boiling chamber. The cartridge heaters were controlled using a PID controller to obtain the required pool temperature along with chilled water circulation through copper cooling coils immersed in the pool. Note that an earlier embodiment of the fluid chamber, in the form of a closed loop was built, but had to be replaced in light of issues associated with vapor management in the small volume. Details of that flow loop are in Appendix B.

The boiling chamber was also equipped with quartz windows for high speed imaging. A Phantom V310 high speed camera was fitted with K2SC long working distance microscope lens for capturing bubble images. Also, to obtain different levels of magnification close up objectives CF-1, CF-2 and CF-3 were fitted to the lens. Images were captured at 3200 fps with a resolution of 1280 x 800. A 250 W halogen lamp was used as a light source.

The test section heater was powered by an AMREL 220V programmable DC power supply. Data including the supplied current, voltage measurements from the test section heater, thermistor and pressure transducer was recorded using NI data acquisition system and LabView. The four slot NI data acquisition system chassis consisted of three data acquisition modules - NI 9201 for voltage measurements from the pressure transducer, NI 9219 (universal input module) for anemometry, heater voltage, and thermocouple measurements, and NI 9227 for measurements of current supplied to the test section heater by the DC power supply.

3.2 Results and Discussion

Pool boiling experiments were conducted using FC-72 at atmospheric pressure. Experimental parameters tested include a heat flux range of 0 - 4.5 W/cm^2 and pool subcooling ranging from 0°C to 20°C. After degassing the fluid, the pool temperature was increased using the cartridge heaters until the required subcooling was achieved. The applied heat flux was increased and once steady state was achieved data were acquired and high speed images of bubbles were recorded. This procedure was repeated for a cycle comprising increasing heat flux followed by decreasing heat flux. It is to be noted that the low heat flux range is mainly due to constraints in heater design and not limited by critical heat flux. The results from the large array experiments discussed in this section include bubble dynamics such as bubble growth, bubble departure frequency and diameter, heat dissipation characteristics of the surface, and liquid velocity measurements.

3.2.1 Bubble Dynamics using High Speed Photography

Bubble dynamics were studied using the high speed images of bubble growth recorded during the experiments. The captured high speed images were processed and analyzed using NI Vision Assistant software to estimate bubble characteristics.

Fig. 3.3 shows bubble departure from the re-entrant cavities on the shallow slope of the saw-teeth at a heat flux of 2.2 W/cm^2 . It was observed that the bubbles grew and departed at an angle normal to the slope of the ratchets. The angle of departure could be noted by observing the angled line of departed bubbles in the saturated pool at the left end of saw-tooth array. To further illustrate the bubble dynamics at the saw-toothed surface, Fig. 3.4 shows a close-up image of bubble growth and departure from re-entrant cavities on the shallow slope of the saw-teeth. As discussed earlier, it can be observed that the bubble growth is normal to the slope of the saw-teeth and the bubbles depart in a direction normal to the sloped surface at high velocities. This asymmetric growth with respect to the vertical axis, was consistent across the entire surface and at all tested conditions. The growth of



Figure 3.3: Image showing bubble departure from re-entrant cavities at an angle normal to the sloped surface of saw-teeth during saturated pool boiling at a heat flux of $q'' = 2.20 \text{ W/cm}^2$.

the bubble continues until the buoyancy force overcomes the surface tension force to cause bubble departure. The departed bubble, as noticed in Fig. 3.4 transits in the pool at an angle that is approximately normal to the sloped surface. In the sections to follow, it will be demonstrated that such asymmetric growth of bubbles has the potential to impart a net lateral motion of liquid in the immediate vicinity using a semi-empirical momentum transfer model.

3.2.2 Bubble growth - Experiments

Fig. 3.5 shows one complete cycle of bubble ebullition cycle, consisting of bubble nucleation, growth and departure from a re-entrant cavity at 2.0 W/cm^2 and saturated pool conditions. The vapor bubble nucleating from the cavity is initially hemispherical in shape. The hemispherical bubble grows rapidly, entirely in a direction normal to the shallow slope of the saw-toothed surface and not laterally. In a naturally occurring nucleation site on a planar surface, bubble growth would be concentrated in both lateral and vertical directions. This

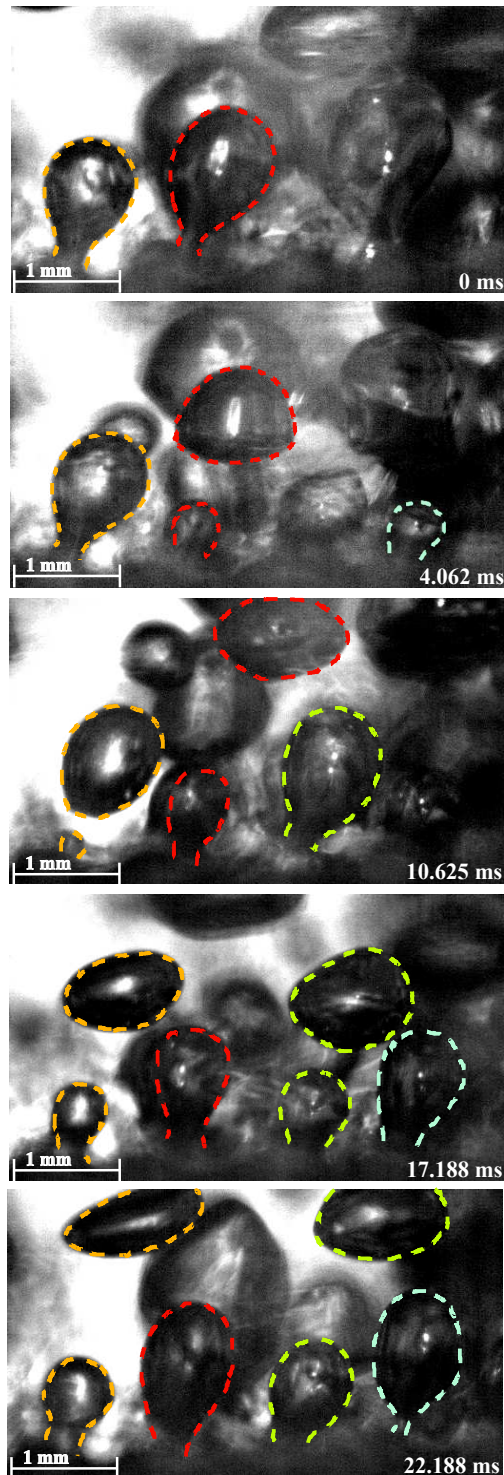


Figure 3.4: Bubble growth and departure from re-entrant cavities at $q'' = 2.0W/cm^2$ and saturated pool conditions. Bubbles nucleating from neighbouring cavities are marked with a different color. Relative time stamps are marked at the bottom right of each image.

initial rapid bubble growth is inertia controlled where the driving potential for bubble growth is the temperature difference between the thin superheated liquid layer (relaxation microlayer) surrounding the bubble, and the vapor. During this initial rapid growth of the bubble normally into the pool, the bubble remains pinned to the cavity as the bubble foot-print remains constant while the dome becomes more spherical. With increasing time, the dome grows larger in size, although at a considerably slower rate as the microlayer depletes. The growth continues until the buoyancy force is large enough to overcome the surface tension force that holds the bubble. As the bubble begins to depart, the neck of the bubble narrows as it breaks and leads to bubble departure normal to the surface. It was also observed that the waiting time, the period between bubble departure and nucleation of the next vapor bubble, is less than $312.5 \mu\text{s}$ which is the time interval between two successive image frames. An interesting observation from these bubble images was the shape of the bubble as it is attached to the surface. Vapor bubbles in highly wetting fluids such as FC-72 are generally observed to be more spherical and possess a very low contact angle due to the low surface tension of the liquid. However, in all the bubble images captured in this study the bubbles are consistently “light-bulb” shaped and the contact angles appear to be very high between $\approx 60^\circ - 90^\circ$. Similar bubble shapes (Fig. 1.17) were reported by Hutter et al. [34] during pool boiling of FC-72 on a plain silicon surface with cylindrical cavities. This high contact angle also suggests that the evaporation microlayer, which often exists as a thin liquid layer underneath a bubble, as shown in Fig. 1.16, is less significant or nearly absent. It is the evaporation of this microlayer which has been shown in the past to contribute significantly to the rapid bubble growth in the inertia controlled regime and high heat transfer rates involved in nucleate boiling [30, 51]. However, Demiray and Kim [36] studied the nucleate boiling heat transfer under a single FC-72 bubble and observed that the microlayer contribution is not significant compared to transient conduction and microconvection contributions, which also supports the earlier observation about the evaporation microlayer in this study. Similar conclusions were also drawn in [35] in pool boiling of FC-72.

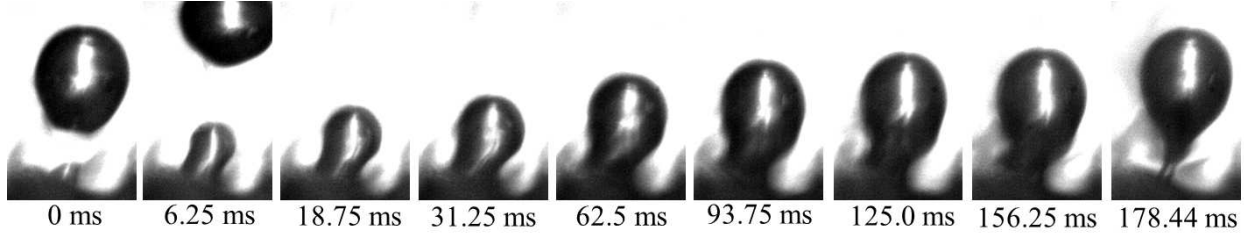


Figure 3.5: Ebullition cycle of a bubble at $q'' = 1.6 \text{ W/cm}^2$ and 21°C subcooling

In the current study, bubble diameter was estimated from the captured images utilizing standard image processing techniques using NI Vision Assistant software. The main steps involved in processing a single captured frame is shown in Fig. 3.6. The raw image is first enhanced using a Look Up Table (LUT) with a power ($1/x$) function to increase the contrast. This is followed by a filtering technique using a convolution theorem to highlight the details such as bubble edges. Next, image thresholding is performed to binarize the image using a threshold value of image intensity. In this process, the pixels with an intensity above the threshold are identified (these appear white in the image). This aids in eliminating the noise emanating from light reflection such as at the center of the bubble. An image mask is applied to remove the saw-tooth from the images. A clear image of the saw-tooth without nucleation is selected to be used as a mask. This step is followed by other filtering techniques such as removing smaller particles and regions near the border. The hole in the bubble due to image thresholding is filled and the final image in the process is used to calculate projected bubble area and perimeter among other parameters. Using the projected area of the bubble from the final step of image processing shown in the figure, bubble diameter of the non-spherical bubble is calculated as the equivalent diameter of a projected circular disk with the same area as that of the bubble. This estimate of diameter for non-spherical entities is also known as the Waddel disk diameter which can be expressed as

$$D = 2\sqrt{\frac{A}{\pi}} \quad (3.1)$$

This process is repeated for hundreds of frames involved in a single bubble growth cycle and multiple bubbles at different experimental conditions.

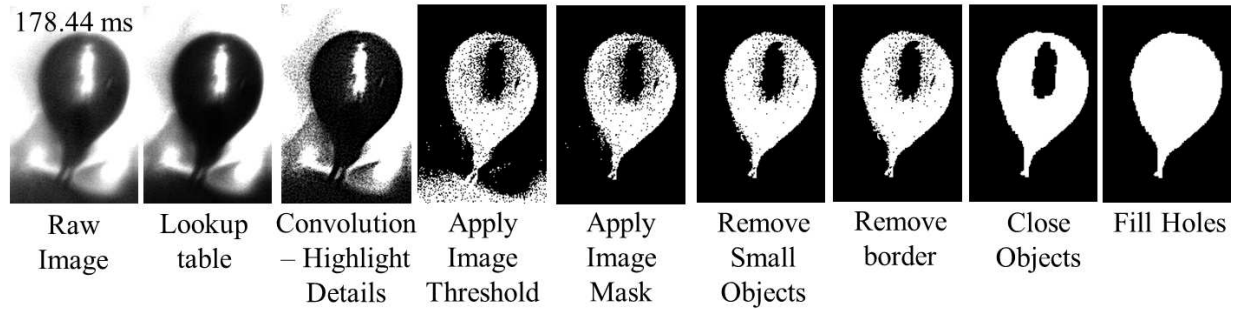


Figure 3.6: Image processing steps of a single bubble frame at 178.44 ms in Fig. 3.5

The bubble diameter estimated using this process during a single growth cycle is shown in Fig. 3.7 as a function of time. As described earlier, it could be noted that the growth of bubble involves a rapid initial inertia controlled growth phase right after nucleation followed by a slower heat transfer controlled growth phase leading to departure. This observation agrees with the results reported in studies by Ramaswamy et al. [33] and Hutter et al. [34] for FC-72, and Lee et al. [32] for R-11 and R-113. Using a linear curve fit for the inertia controlled growth and a power law fit for heat transfer controlled growth for the single bubble shown in Figures 3.5, the asymptotic bubble growth rate relationship between bubble diameter and time can be obtained. For the inertia controlled growth, the bubble diameter was observed to scale linearly with time expressed as [24, 25],

$$D = At \tag{3.2}$$

where

$$A = 2 \left(\frac{\pi h_{lv} \rho_v \Delta T}{7 \rho_l T_{sat}} \right)^{1/2}$$

This linear relationship is similar to the experimental growth rate reported in a number of other studies in the literature for the inertia controlled regime . In the heat transfer controlled regime, the asymptotic relationship is of the form, $D \approx \beta t^m$ where, β and m

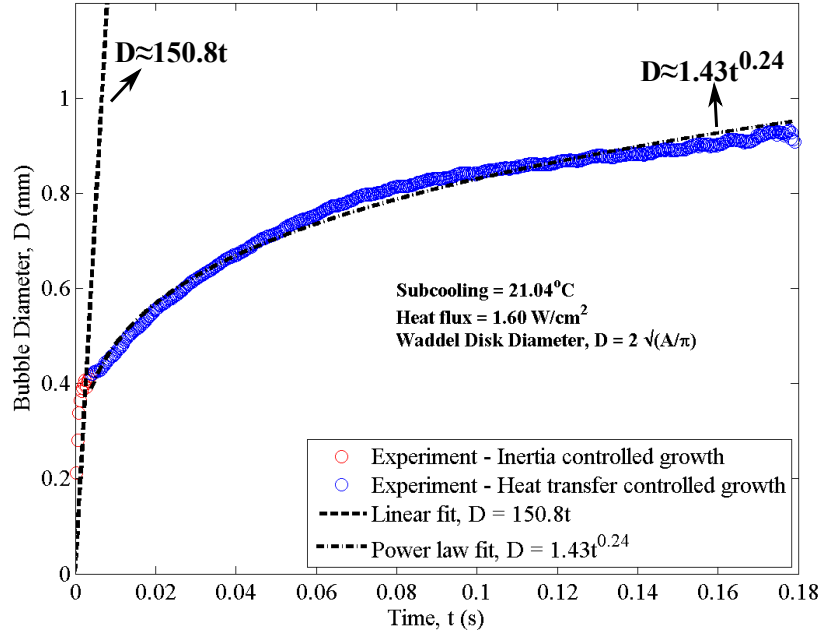


Figure 3.7: Estimated bubble growth for images shown in Fig. 3.5 at $q''=1.6 \text{ W/cm}^2$ and 21°C subcooling

are curve fitting parameters. The parameter β is also termed as a growth constant [27, 29] for the heat transfer controlled regime which is given as a function of wall superheat and fluid properties. The bubble growth expression and growth constant as reported in Cole and Shulman [29] is,

$$D = 4\beta\sqrt{at} \quad (3.3)$$

where,

$$\beta = \frac{\phi_c}{\sqrt{\pi}} Ja$$

ϕ_c = experimentally determined constant

$$Ja = \text{Jacob number} = \frac{(T_w - T_{sat})C_{p,l}\rho_l}{\rho_v h_{lv}}$$

In the above equation, the value of ϕ_c was experimentally determined to be $1, \pi/2, \sqrt{3}$ by Fritz and Ende [52], Forster and Zuber [53], and Plesset and Zwick [26] for bubble growth in a uniformly superheated liquid.

The value of m for the experimental conditions shown in Fig. 3.7 is 0.24 which is much lower than the $t^{1/2}$ relationship reported by a large number of studies in the literature for water [25, 29, 54] and for FC-72 [33]. In a recent study conducted with FC-72 and structured cavities in silicon, Hutter et al. [34] reported values of 0.37 and 0.53 for m , and in studies with saturated R-11 and R-113 Lee et al. [32] observed m to be between $\approx 1/5$ and $1/3$. The lower value of m reported in the current study could be due to the lower liquid equilibrium superheat, ≈ 0.1 K for the conditions shown in Fig. 3.7, experienced due to larger cavities. In comparison, an equilibrium superheat of 0.92 K was reported by Hutter et al. [34]. The equilibrium liquid superheat is the temperature rise of the liquid above the saturation temperature ($T_{le} - T_{sat}$) which is a requirement for vapor nucleation to be sustained. It is defined as,

$$T_{le} - T_{sat} = \frac{2\sigma T_{sat}}{\rho_v h_{lv} r_c} \quad (3.4)$$

where,

$$r_c = \text{cavity mouth radius}$$

Fig. 3.8 shows the effect of heat flux at a liquid subcooling of $\approx 21^\circ\text{C}$. As the heat flux increases, the wall superheat increases which vaporizes the liquid near the bubble interface at a faster rate and hence the bubble growth rate increases with heat flux. Also as the wall superheat increases, surface tension of pure fluids which holds the bubble on the heated surface decreases. Additionally, since the bubble grows at a faster rate, at a given time the bubble size is larger at a higher heat flux thereby leading to increased buoyancy force which is responsible for bubble detachment. This increasing magnitude of buoyancy forces and the decreasing magnitude of surface tension forces, lead to faster bubble detachment, or smaller overall growth periods as heat flux increases which is evident in Fig. 3.8. These observations corresponding to the influence of heat flux, and hence wall temperature, on growth rate accord well with studies conducted especially with FC-72 such as Hutter et al.

[34] and Ramaswamy et al. [33]. The increase in rate of bubble growth with increasing heat flux was also noticed in the inertia controlled regime which is supported by the increasing value of A in the linear relationship, $D = At$. The experimental values of A for different heat flux values are summarized in Table 3.1. From Fig. 3.8, it could also be noticed that, at a constant subcooling of 21°C, the transition from inertia to heat controlled regime occurs within a narrow range of bubble diameter, ≈ 0.45 to 0.55 , and observed to be unaffected by heat flux.

Similarly, when the liquid subcooling is decreased (increasing pool temperature), the wall superheat increases leading to faster bubble growth rates as seen in Fig.3.9 for a nominal heat flux of 1.0 W/cm^2 . But unlike Fig. 3.8, with decreasing subcooling the inertia controlled regime was sustained for higher bubble diameters which could be attributed to the increasing thermal boundary layer thickness with decreasing subcooling.

The effect of independent parameters - heat flux and subcooling, on the curve fitting parameters β and m in the asymptotic relationship for heat transfer controlled regime can be studied from Figures 3.8 and 3.9, which are summarized in Table 3.1. In Table 3.1, the units for 'A' and 'B' are mm/s and mm/s^m , if the diameter is expressed in mm and time in s . The value of m ranges between 0.13 and 0.27 without being affected much by heat flux or subcooling, and it is also similar to the range reported by Lee et al. [32]. The value of β was found to increase with increasing heat flux and decreasing subcooling and hence β , increases with increasing wall superheat which agrees well with the observation by Scriven [27] for bubble growth in a uniformly superheated liquid (Equation 3.3). Similarly, in the experiments conducted by Cole and Shulman [29] with R-113, it was observed that the growth constant increased with increasing wall superheat. The values of ϕ_c used in Equation 3.3 using the uniform superheat theory significantly over estimated the growth constant. Cole and Shulman [29] reported better predictions of growth constant by using a modified Jacob number with the wall superheat approximated as $0.5(T_w - T_{sat})$, which is valid since

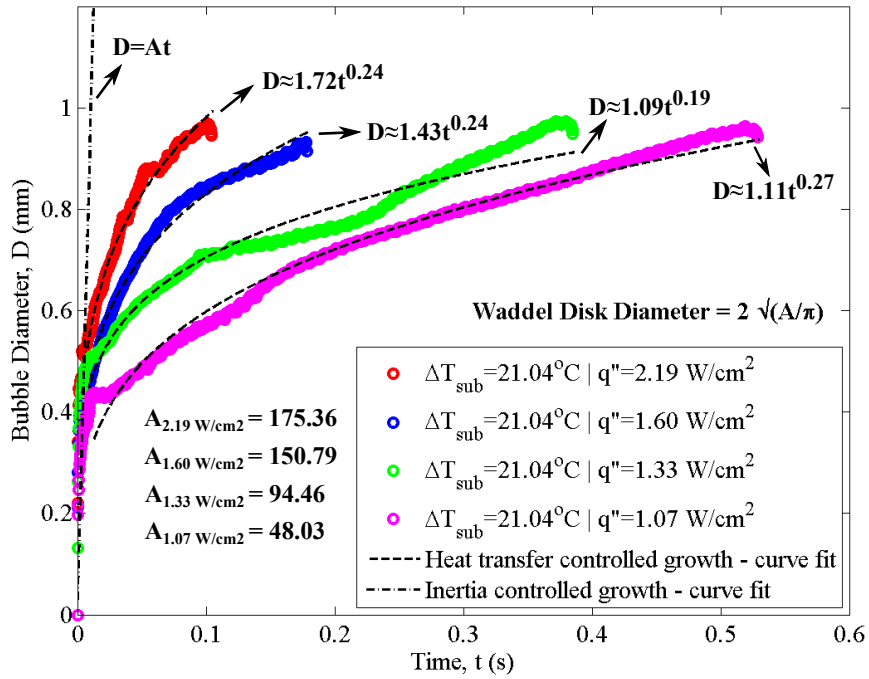


Figure 3.8: Effect of heat flux on bubble growth at a liquid subcooling of 21°C

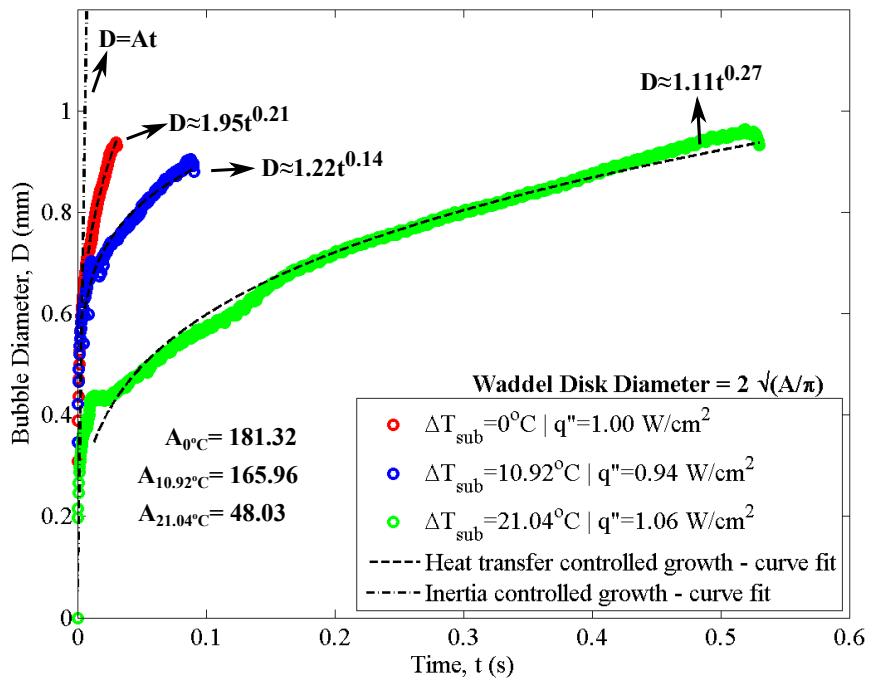


Figure 3.9: Effect of subcooling on bubble growth at a nominal heat flux of 1.0 W/cm²

the liquid superheat away from the heated wall approaches zero. Cole and Shulman [29] reported a modified equation for growth constant (β) as,

$$\beta \cong \frac{5}{4} Ja^{\frac{3}{4}} \quad (3.5)$$

In comparison, the experimental values of growth constant from the current study are plotted in Fig. 3.10 as a function of wall superheat. It can be observed that the modified equation (Eq. 3.5) for bubble growth near heated surfaces reported by Cole and Shulman [29] still over-estimates the growth constant. The equation for growth constant obtained using curve fitting the experimental data from the current study can be expressed as,

$$\beta \cong 0.034Ja \quad (3.6)$$

Table 3.1: Summary of curve fitting parameters from Fig. 3.8 and Fig. 3.9

Experimental conditions		Bubble growth regime			Fig. #
		Inertia controlled $D = At$ (mm)	Heat transfer controlled $D = \beta t^m$ (mm)		
ΔT_{sub} (°C)	q'' (W/cm ²)	A (mm/s)	β (mm/s ^{m})	m	
21.04	2.19	175.36	1.72	0.24	Fig. 3.8
21.04	1.6	150.79	1.43	0.24	Fig. 3.8
21.04	1.33	94.46	1.09	0.19	Fig. 3.8
21.04	1.06	48.03	1.11	0.27	Fig. 3.8, 3.9
10.92	0.94	165.96	1.22	0.14	Fig. 3.9
0	1	181.32	1.95	0.21	Fig. 3.9

Figures 3.11 and 3.12 also represent the effect of heat flux and subcooling on growth rate but with overall asymptotic relationships for growth rate obtained by a power law curve fit for both the inertia and heat transfer controlled regimes combined. The growth relationships are only slightly different from Figures 3.8 and 3.9 in the heat transfer controlled regime. In comparison with Hutter et al. [34], who conducted a similar analysis for bubble growth rate

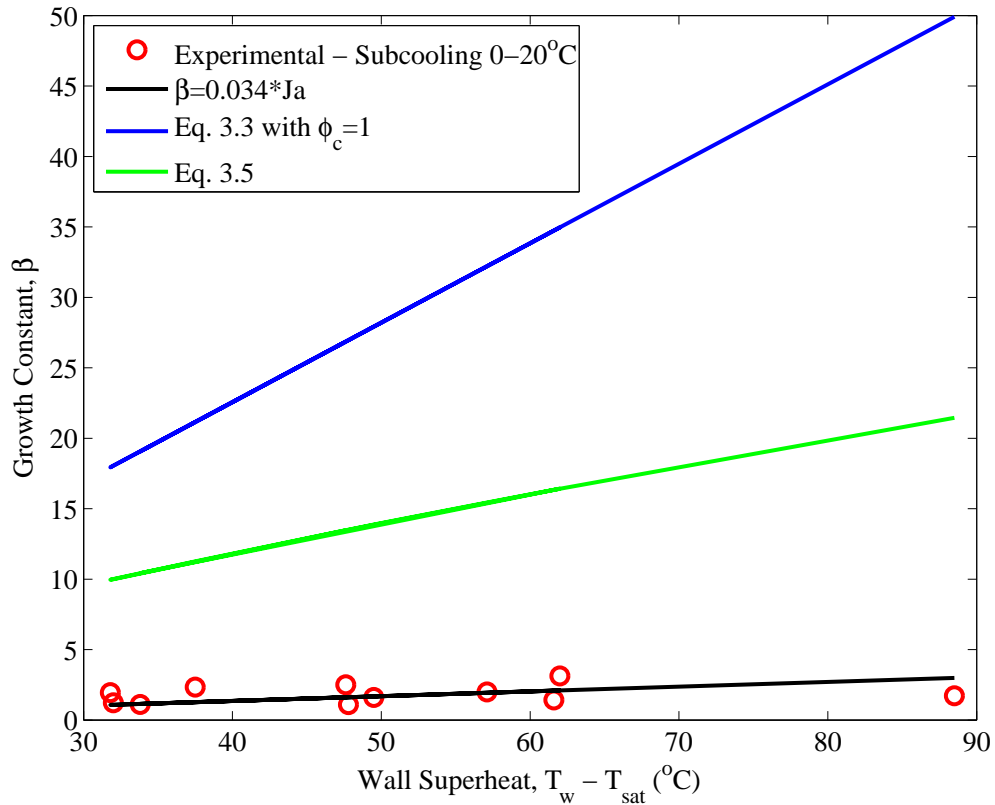


Figure 3.10: Growth constant from experiments at a liquid subcooling of 0-20 $^{\circ}\text{C}$. The figure shows a linear curve fit used to approximately express the growth constant. The equations 3.3 and 3.5 used for comparison from the studies Fritz and Ende [52] and Cole and Shulman [29] respectively, were calculated for saturated pool conditions.

in FC-72, observed the values of m to be in the range of 0.37 - 0.53 which is slightly higher than those reported in this study.

3.2.3 Bubble departure frequency and diameter

As discussed earlier, bubble departure from a nucleation site is a balance between the surface tension and buoyancy forces, in the absence of forces due to liquid flow. As surface temperature increases, surface tension decreases and hence buoyancy forces tend to cause the bubbles to depart from the nucleation site earlier than at lower surface temperatures or wall heat flux, thereby leading to increased bubble departure frequencies or truncated bubble growth period. The average bubble departure frequency was estimated by calculating the average time period between a bubble's nucleation and departure. As shown in Fig. 3.13, bubble departure frequency is a function of both subcooling and heat flux. As heat flux increases the bubble departure frequency also increases, although with a few anomalies. Similarly, the bubble departure frequency increases with decreasing subcooling and the highest frequency of ≈ 60 Hz was observed under saturated pool conditions and high heat flux. The frequencies observed under saturated conditions agree well with other pool boiling experiments conducted with FC-72 [14, 34]. However, in those studies, the bubble departure diameter was not observed to be affected by subcooling or heat flux as seen in Figures 3.11, 3.12 which was unexpected. In other pool boiling studies conducted with FC-72 [14, 17, 33, 34], the bubble departure diameter was observed to increase with heat flux, or wall superheat. In [17], the bubble departure diameter increased between 0.26 mm to 0.38 mm over a heat flux range of 0 - 40 W/cm². However, in the current study the range of heat flux tested was very low, and this could be a reason for the absence of any trend in the variation of bubble departure diameter.

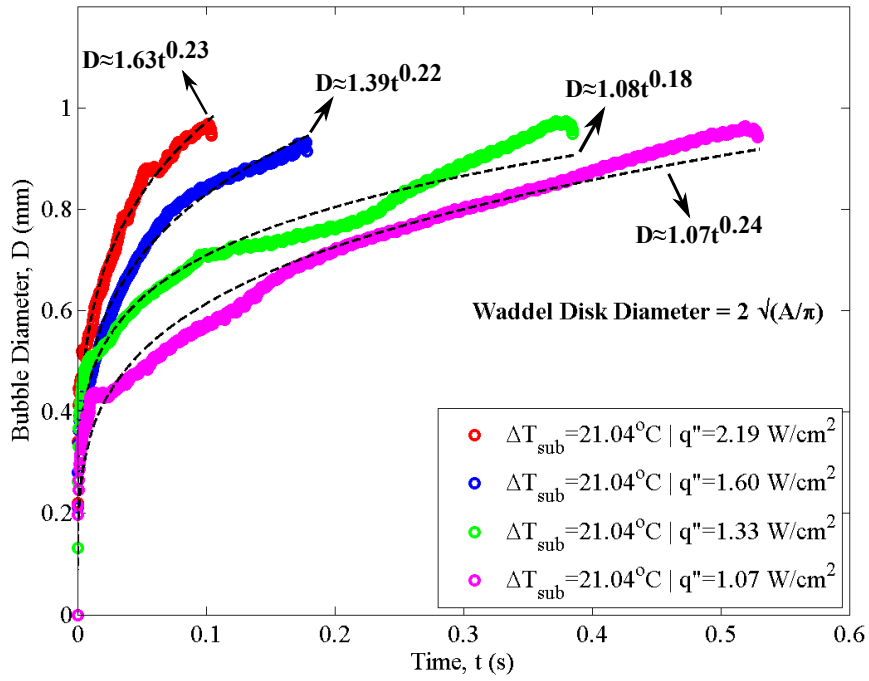


Figure 3.11: Effect of heat flux on bubble growth at a liquid subcooling of 20°C

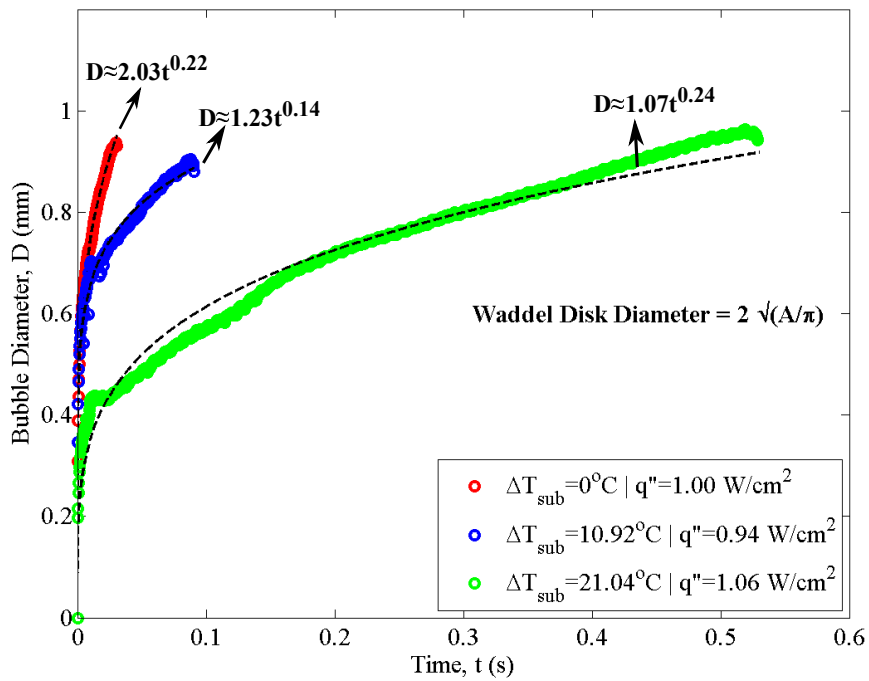


Figure 3.12: Effect of subcooling on bubble growth at a nominal heat flux of 1.0 W/cm²

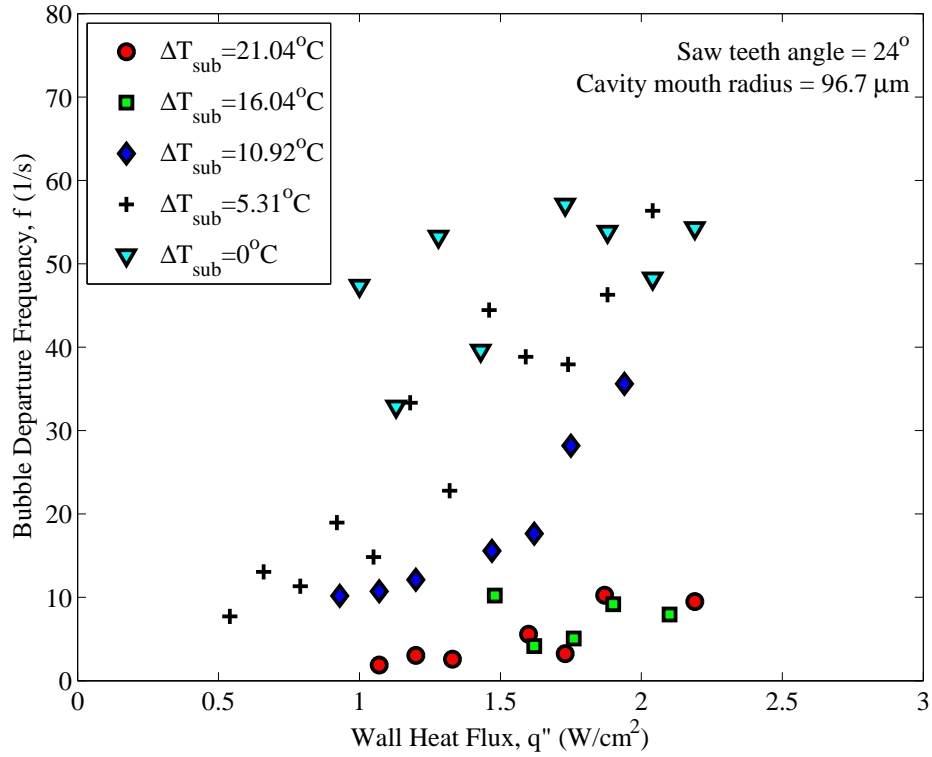


Figure 3.13: Effect of subcooling and heat flux on bubble departure frequency

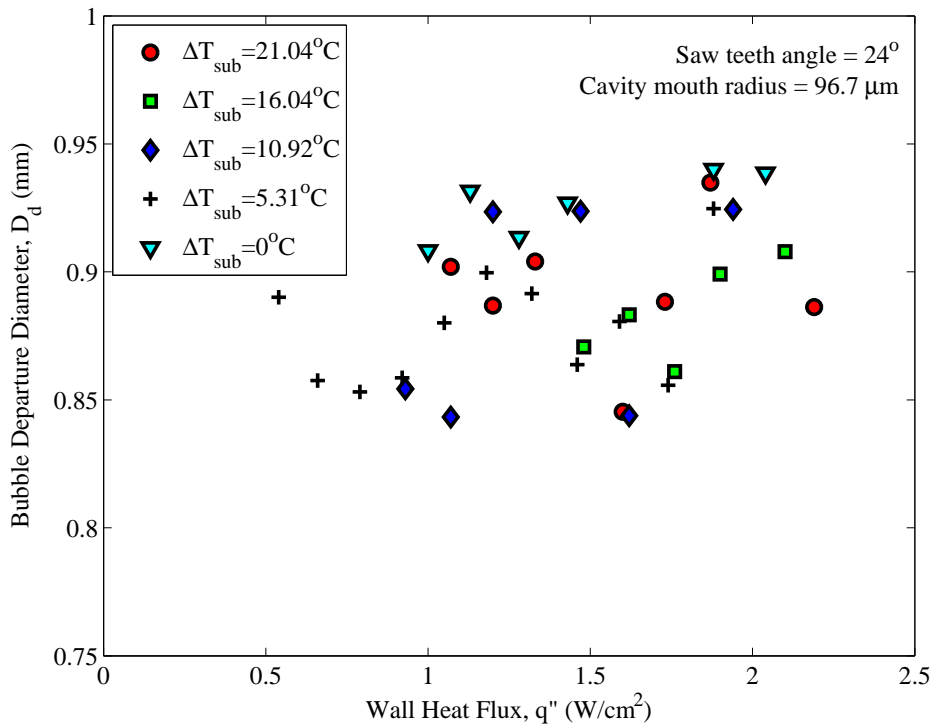


Figure 3.14: Effect of subcooling and heat flux on bubble departure diameter

3.2.4 Bubble growth - Comparison of experimental data with models

The experimental results presented in this study show that the bubble growth rates are dependent on the regime of growth. Models developed in the past to predict bubble growth rates, in general, are also regime specific and universal analytical solutions are only available for very specific experimental conditions. As discussed earlier models for bubble growth can be classified into two types - one developed for the growth of a spherical symmetric bubble in a uniformly superheated pool and the other for bubble growth near heated walls where the temperature field is non-uniform. Models for inertia controlled regime are very limited [24, 30] and most of the models developed apply mainly for the heat transfer controlled bubble growth. Models developed for the heat transfer control regime are often empirical in nature [27–29] and depend on the power law relationship of bubble growth with time ($D \approx t^{1/2}$). However, no analytical models are available for experimental conditions similar to those in the current study such as bubble growth in highly wetting fluids on surfaces with structured cavities. Bubble growth for such conditions is often expressed as an asymptotic relationship of bubble diameter as a function of time. Analytical models and empirical relationships discussed in the literature that are used for comparison with the current study are summarized in Table 3.2

Table 3.2: Summary of available models and experimental data for bubble growth during inertia controlled (IC) and heat transfer controlled (HTC) regimes.

Model	Conditions	Bubble growth correlation
Rayleigh [24]	Uniform super- heat theory	$D = At$ where $A = 2 \left(\frac{\pi h_{lv} \rho_v \Delta T}{7 \rho_l T_{sat}} \right)^{1/2}$

(3.7)

Model	Conditions	Bubble growth correlation
Mikic and Rohsenow [31]	Non-uniform temperature field	$D = \frac{4Ja\sqrt{3\alpha_l t}}{\sqrt{\pi}} \left\{ 1 - \frac{T_w - T_\infty}{T_w - T_{sat}} \left[\left(1 + \frac{t_w}{t} \right)^{1/2} - \left(\frac{t_w}{t} \right)^{1/2} \right] \right\}$

where

$$t_w = \frac{1}{4\alpha_l} \left\{ \frac{r_c}{\operatorname{erfc}^{-1} \left[\frac{T_{sat} - T_\infty}{T_w - T_\infty} + \frac{2\sigma T_{sat}(v_v - v_l)}{(T_w - T_\infty)h_{lv}r_c} \right]} \right\}^2$$

r_c = cavity mouth radius

(3.8)

Van Stralen [30]	Bubble growth due to evaporation and relaxation microlayer near heated surfaces. Applicable for both IC and HTC.	$D = \frac{D_1(t) D_2(t)}{D_1(t) + D_2(t)}$ $D_1(t) = 1.633 \sqrt{\frac{\rho_v h_{lv} (T_w - T_{sat}) \exp \left[- (t/t_d)^{1/2} \right]}{\rho_l T_{sat}}} t$ $D_2(t) = 3.9088 \left\{ b^* \exp \left[- \left(\frac{t}{t_d} \right)^{1/2} \right] + \frac{T_\infty - T_{sat}}{T_w - T_{sat}} \right\}$ $Ja\sqrt{\alpha_l t} + 0.746 \operatorname{Pr}_l^{-1/6}$ $\left\{ \exp \left[- \left(\frac{t}{t_d} \right)^{1/2} \right] + \frac{T_\infty - T_{sat}}{T_w - T_{sat}} \right\} Ja\sqrt{\alpha_l t}$ $b^* = 0.6964 \frac{D_2(t)}{Ja\sqrt{\alpha_l t}} - 0.1908 \operatorname{Pr}_l^{-1/6}$
------------------	--	---

(3.9)

Cole and Shulman [29]	Non-uniform temperature field	$D = 5Ja^{3/4}\sqrt{\alpha t}$
-----------------------	-------------------------------	--------------------------------

(3.10)

Model	Conditions	Bubble growth correlation
Zuber [28]	Non-uniform temperature field	$D = \phi_c \frac{4}{\pi} Ja \sqrt{\pi \alpha t} \left[1 - \frac{q_w \sqrt{\pi \alpha t}}{2k(T_w - T_{sat})} \right]$ (3.11)
Lee et al. [32]	Non-uniform temperature field - R11 and R113	$R^+(t^+) = 2\alpha t^{+1/5} \tanh(t^{+1/5}) + R_0^+$ <p>where</p> $R^+ = R/R_c, t^+ = t/t_c$ $R_c = \frac{\sqrt{27}}{2} Ja \alpha \sqrt{\frac{\rho_l R_d}{\sigma}}$ $t_c = \frac{9}{4} Ja \alpha \frac{\rho_l R_d}{\sigma}$ <p>$\alpha, \beta =$ fitting parameters</p> <p>$R_0^+ =$ dimesionless critical radius</p>
	Experiments with R11 and R113	$D \propto t$ (IC) $D \propto t^{1/2}$ (HTC)
Ramaswamy et al. [33]	Experiments with FC-72 on structured surfaces	$D \propto t$ (IC) $D \propto t^{1/2}$ (HTC)
Hutter et al. [34]	Experiments with FC-72 on silicon with cylindrical cavities	$D \propto t^{1/2}$

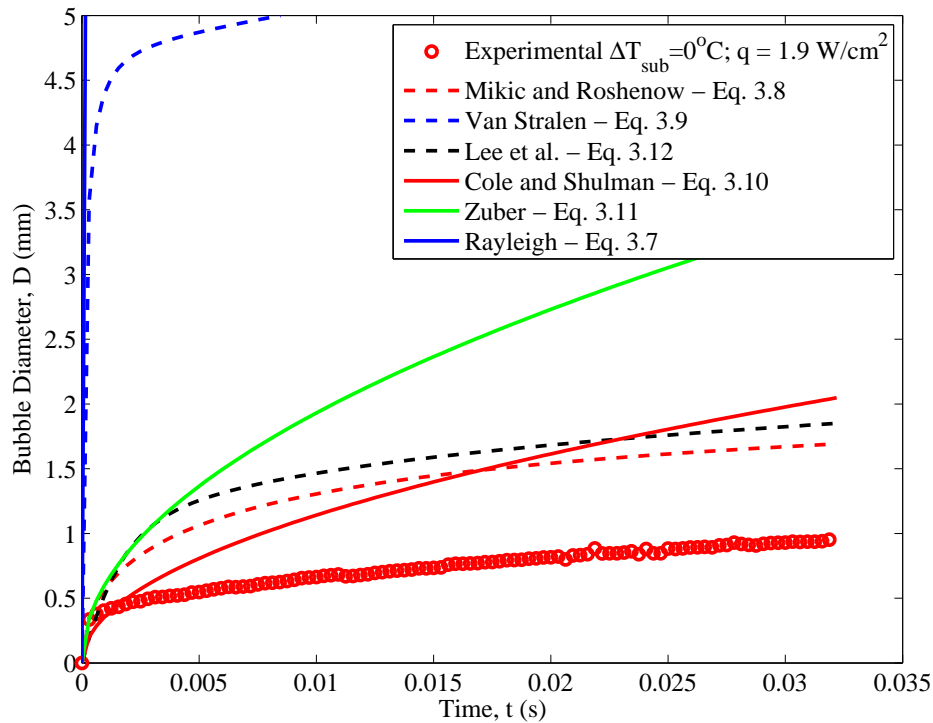


Figure 3.15: Comparison with existing models for bubble growth

From Fig. 3.15, it can be observed that all the tested models deviate significantly from the experimental results shown for saturated conditions. Rayleigh’s equation (Equation 3.7) captures the high growth rate involved in the inertia controlled growth regime adequately. All the other equations for the heat transfer controlled growth, although they represent the shape of the bubble growth rate, deviate significantly from the experimental data. The model developed for refrigerant R-113 by Lee et al. [32] showed significant deviations although the asymptotic growth relationships represented in that study were similar to those reported in the current study. These results suggest that all the available models perform poorly for the experimental conditions tested in the current study. This re-emphasizes the need for further studies and models to analytically explain the effects of structured surfaces and low surface tension fluids.

3.2.5 Heat Dissipation

Heat transfer characteristics of the surface can be analyzed by plotting wall superheat ($T_w - T_{sat}$) against wall heat flux (q_w), which is known as the boiling curve. Wall temperature was calculated from the test section heater resistance measurements using a linear relationship that was previously obtained by calibration. Calibration of heater resistance was performed in a convection oven using an NIST calibrated thermistor as a standard, by varying the oven temperature from 25°C to 85°C. Heater calibration data are presented in Appendix C. Saturation temperature was calculated at the measured pressure inside the tank using a pressure transducer.

Heat flux was calculated as,

$$q'' = \frac{q - q_{loss}}{A_{st}} \quad (W/cm^2) \quad (3.13)$$

where,

$$q = V \times I \quad (W)$$

$$A_{st} = \text{Surface area of saw-toothed surface, } cm^2$$

$$V = \text{Applied voltage, } V$$

$$I = \text{Applied current, } A$$

Heat loss (q_{loss}) was quantified by attaching a thermocouple to the back of the test device. Heat loss, which is heat transfer from the back side of the test device, was estimated by assuming 1D steady conduction across the device. It has to be noted that such an estimate of heat loss is only a conservative measure as it does not account for any spreading associated within the PCB.

Fig. 3.16 shows the boiling curve at different liquid subcooling values. At a constant subcooling, as heat flux increases, heat transfer from the surface is by natural convection defined by Newton's law of cooling. As wall superheat increases high enough to trigger vapor nucleation from the cavities, the heat transfer increases sharply, marked by the change in

slope of the curve, without causing a significant increase in wall temperature. This can be attributed to the effects of microconvection due to mixing induced by bubble growth and departure, transient conduction due to the constant disruption of the boundary layer and also due to the microlayer evaporation which is less significant in the current study owing mainly due to the shape of the bubble [6, 36]. As heat flux increases further, more nucleation sites become active increasing the heat transfer further. It has to be noted that the highest heat flux applied to the device was only 4.5 W/cm^2 , which was not limited by critical heat flux but only due to limitations of the designed heater, as discussed earlier. Also, at the highest tested heat flux the wall temperature was 92°C and observations of bubble dynamics showed that the boiling regime was still not fully developed suggesting that the CHF was much higher than the highest heat flux tested. This could also be attributed to the re-entrant cavities which prevents bubble coalescence by controlling the location of nucleation sites. Another important characteristic of boiling curve for a highly wetting fluid such as FC-72 is the nucleation overshoot which is due to the flooding of cavities caused by the low contact angle of the the liquid. However, in the current study nucleation overshoot was not observed mainly because of the wide variation in cavity mouth radius. According to Hsu's analysis [6], cavities with larger mouth radius are activated first and as wall temperature increases cavities with smaller radius nucleate. This causes nucleation to happen in stages with increasing wall superheat and hence overshoot was not observed.

As subcooling increases, pool temperature decreases causing increase in heat transfer in the natural convection regime. Also, in the partially developed boiling regime heat transfer is higher as subcooling increases. These observations accord well with the results of number of other studies in the literature. As heat flux increases, it could also be observed that the boiling curves at different subcooling tend towards merging with each other, as fully developed nucleate boiling is independent of both liquid subcooling and mass flux and mainly controlled by bubble ebullition cycle.

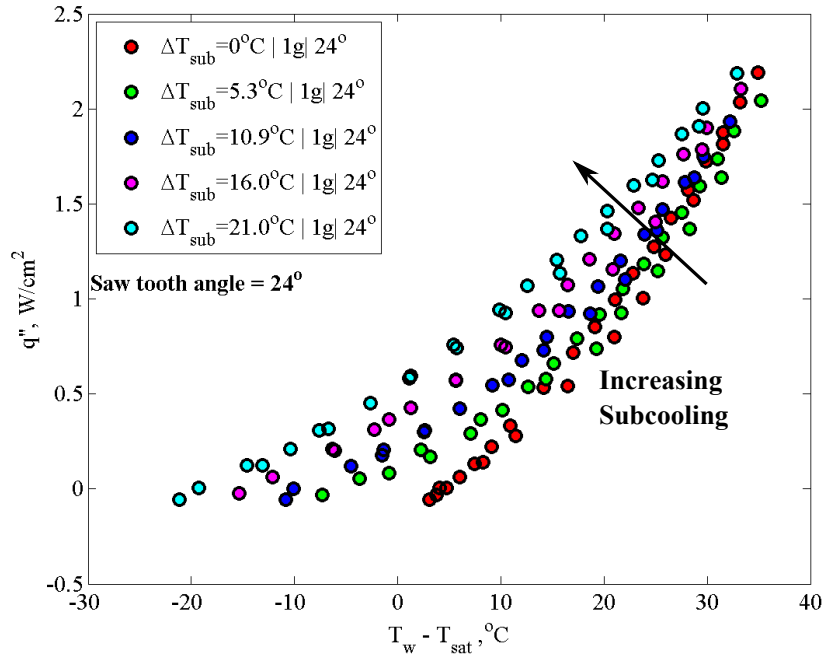


Figure 3.16: Effect of subcooling on pool boiling curve for the test device with a saw-tooth angle of 24°

3.2.6 Lateral Liquid Velocity Measurements Using Hot Wire Anemometer: Parametric Effects

In the previous sections it has been demonstrated that asymmetry in the location of re-entrant cavities and asymmetry in surface structure can be used to cause bubble growth and departure at an angle normal to the slope of the surface. Using a semi-empirical model it was shown that such asymmetric bubble growth has the potential to impart an angular momentum to the surrounding liquid, thereby causing a net lateral flow. It was shown that in water, the asymmetric growth of bubbles can lead to liquid velocities up to 20 mm/s and in FC-72 the velocities are much lower at ≈ 1 -2 mm/s due to higher liquid inertia associated with FC-72.

In this section, experimental results of liquid velocity measurements over the saw-toothed surface using hot wire anemometry are reported. Hot wire anemometry involves a micro-wire or film made of platinum or tungsten that is electrically heated to a constant

temperature. The heat convected from the probe due to liquid flow causes a change in current which in turn causes a change in voltage at the anemometer output. The measured voltage output is directly proportional to the liquid velocity (V).

In the current study, a TSI Model 1750 constant temperature anemometer was used for the liquid velocity measurements. The anemometer setup includes a power supply, a probe, probe support and an angle adapter. An image of the anemometer along with the power supply is shown in Fig. 3.17a and b. Current supply to the probe and voltage measurements are made using a Wheatstone bridge circuit shown in Fig. 3.17c which is built in to the anemometer. The probe used in the experiments is a TSI Model 1210-20 straight probe with a platinum film. The probe was held inside the polycarbonate flow channel as shown in Fig. 3.18 using a Model 1152 angle adapter which aids in positioning the probe inside the flow channel horizontally. The angle adapter is connected to a probe support which is connected to the anemometer power supply connection pins. One of the pins in the anemometer is connected to a control resistor which is used to set the operating temperature of the probe. The resistance of the control resistor is calculated based on the prescribed operating resistance for the probe and the cable resistance. The operating temperature of the probe 1210-20 is 67°C and the operating resistance is 48 Ohms. Based on these specifications the control resistor used has a resistance of 34 Ohms. The selection of control resistor is explained in the manual [55]. The bridge output from the anemometer ranging between 0-5V is connected to the data acquisition system. The assembly of the probe setup is shown in Fig. 3.18. The probe is positioned 4mm over the saw-toothed surface and midway along the length of the test device facing the direction of liquid flow. The hot film of the probe is enclosed in an aluminum sleeve with a slit at the top. The aluminum sleeve serves to prevent the contact of the vertical convection currents from the surface with the probe, so that the probe measures only the horizontal component of velocity.

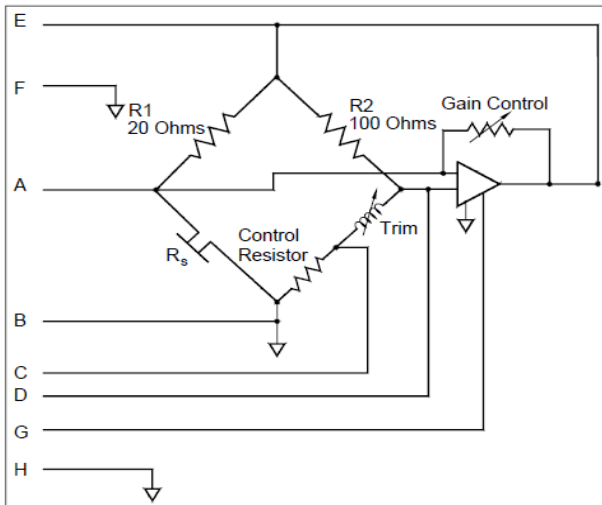
The heat transfer from the probe (hot wire/film) maintained at a constant temperature, apart from liquid velocity, is also strongly a function of liquid temperature and liquid



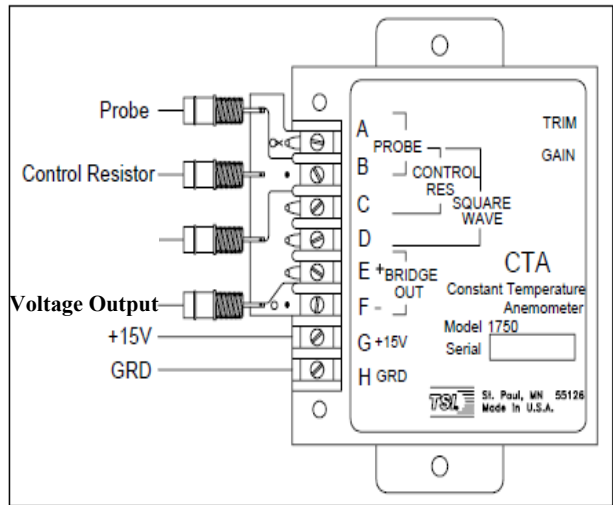
(a) TSI Constant Temperature Anemometer (Model 1750)



(a) Power supply used with the anemometer (Model 1751)



(c) Wheatstone bridge circuit used for voltage measurement



(d) Block diagram of the anemometer showing the pin connections

Figure 3.17: (a) and (b) TSI constant temperature anemometer and power supply used for liquid velocity measurements. Electrical circuit and connections are shown in (c) and (d) [55]

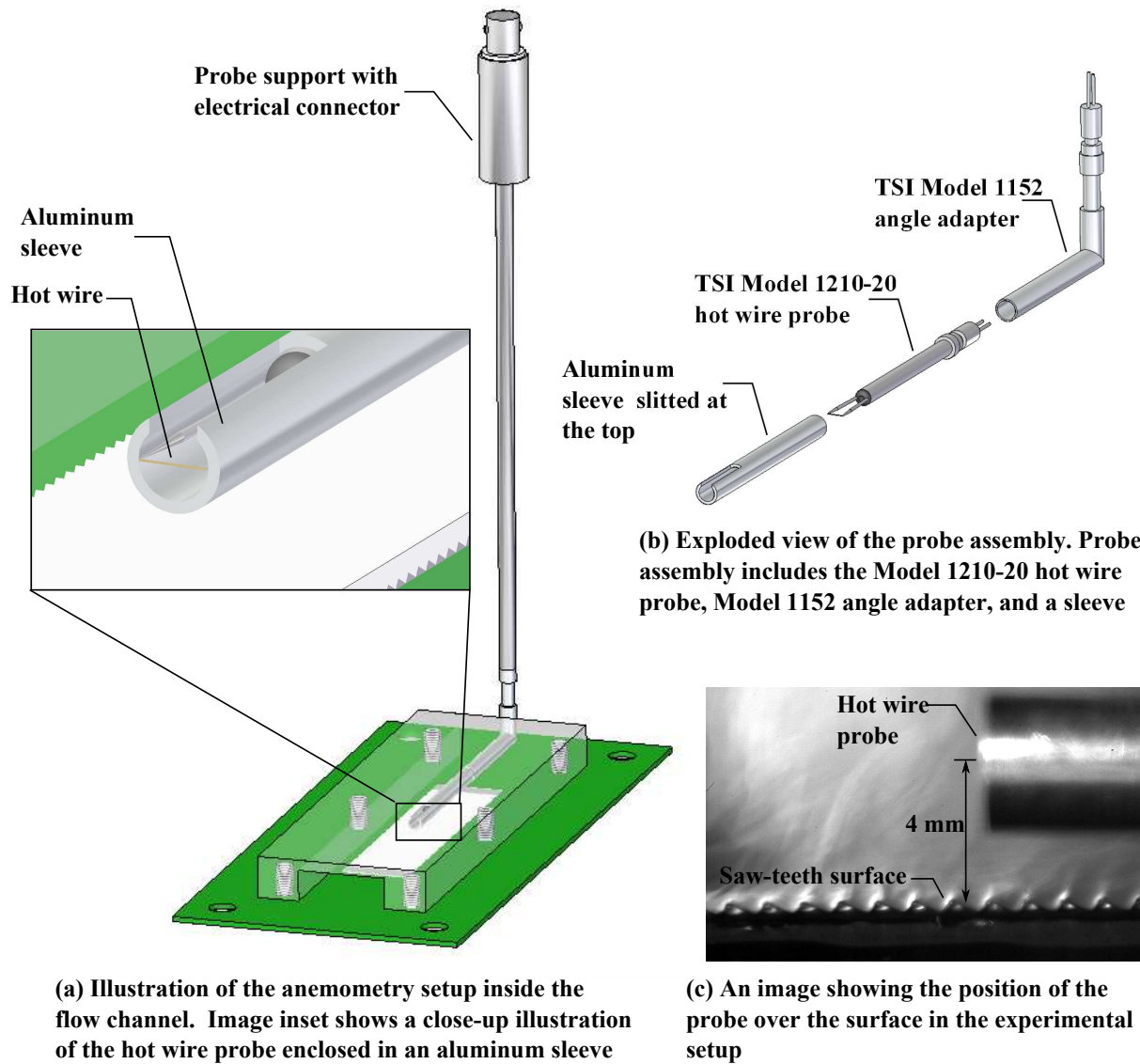


Figure 3.18: Illustration of the probe set up over the test device with a saw-teeth angle of 24°

properties. Hence for a constant liquid and operating temperature of the probe, the voltage output of the anemometer is primarily a function of liquid velocity and liquid temperature. To estimate the velocity of the liquid from the bridge output of the anemometer, the probe was calibrated in FC-72. A metered magnetic drive gear pump was used to pump the liquid upwards through a vertical tube in which the probe was placed. The calibrated velocity ranges from 1 - 50 mm/s at room temperature. By plotting output voltage against velocity, a fifth order polynomial expressing velocity as a function of output voltage was obtained by curve fitting. Calibration data for the hot wire probe are presented in Appendix C. The data from the anemometer was also corrected for actual temperature of liquid in the experiment by using the expression,

$$E_{cor}^2 = E_{meas}^2 \times CF$$

$$CF = \frac{T_s - T_{e,cal}}{T_s - T_e} \quad (3.14)$$

where,

$$E_{cor} = \text{corrected output of the anemometer, } V$$

$$E_{meas} = \text{measured output of the anemometer, } V$$

$$CF = \text{correction factor}$$

$$T_s = \text{film operating temperature, } ^\circ C$$

$$T_e = \text{liquid temperature during the experiment, } ^\circ C$$

$$T_{e,cal} = \text{liquid temperature during calibration, } ^\circ C$$

Experiments were conducted at a pool subcooling range of 0-20 °C and a heat flux range of 0 - 4.5 W/cm^2 . For a constant liquid subcooling, power to the test device was increased periodically and the bridge output from the anemometer was measured after steady state conditions were achieved. This step was repeated while decreasing the applied heat flux and for experiments at other liquid subcooling values.

Figure 3.19 shows the raw and temperature corrected bridge output of the anemometer. The output of the anemometer showed a lot of fluctuations due to two reasons. One, was

due to operation at the lower limit of hot wire anemometer's output. The lower limit of velocity measurement using a hot wire anemometer is ≈ 10 mm/s for liquid flows. Secondly, the fluctuations are also caused by contact between departing vapor bubbles and the probe. The voltage measurements shown in Fig. 3.19 represent the peak amplitude of the recorded data. Using the temperature corrected voltage, liquid velocity can be measured using the calibration equation which is represented in Fig. 3.20. It can be noticed that at high subcooling, the measured velocity increases with heat flux thus indicating the pumping potential although at low velocities. However, at low subcooling the velocity was observed to be independent of heat flux and the measured velocities were very low. This net horizontal velocity component increased slightly at higher subcooling but increased consistently with heat flux.

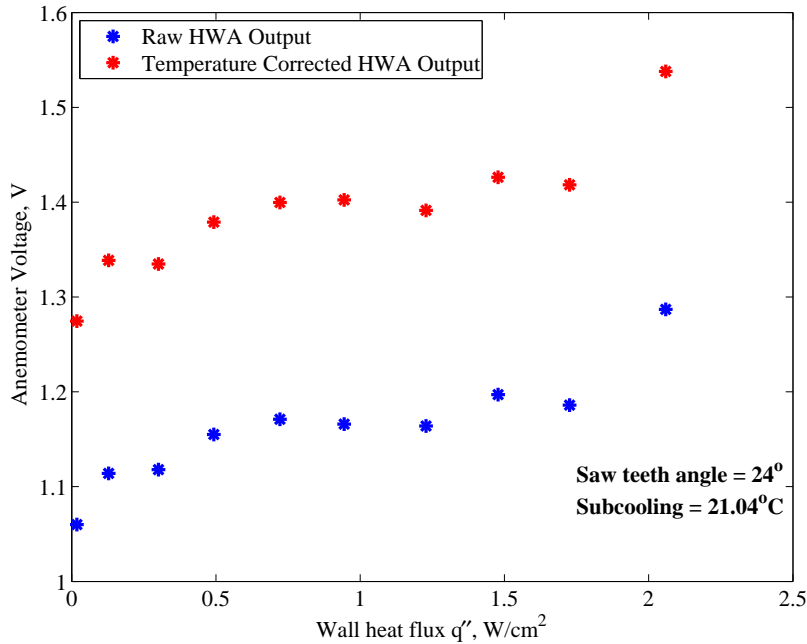


Figure 3.19: Raw and temperature corrected voltage measurements using hot wire anemometer over the test device with a saw-tooth angle of 24°

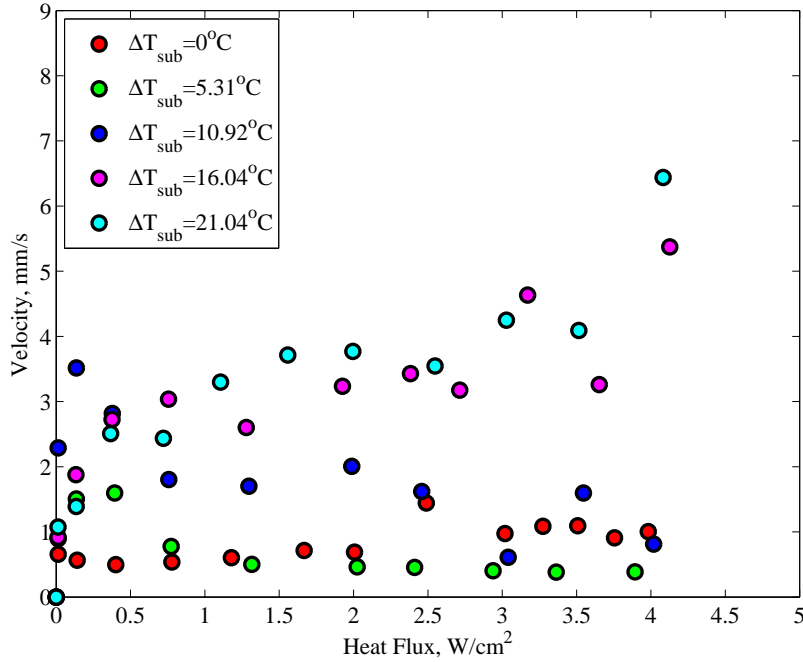


Figure 3.20: Temperature corrected liquid velocity measurements using hot wire anemometer over the test device with a saw-tooth angle of 24°

3.3 Summary

Pool boiling experiments were conducted on asymmetric silicon heat sinks using FC-72. The independent parameters controlled in the experiment include heat flux and liquid subcooling. In the experiments that were discussed in this section, the parameters measured include bubble diameter, bubble departure frequency, wall surface temperature and liquid velocity. High speed imaging was used to capture bubble images and image processing techniques were used to estimate the characteristics of vapor bubble such as shape, diameter, and departure frequency as a function of time, heat flux and inlet subcooling. Based on the observed bubble characteristics, bubble growth was characterized as inertia and heat transfer controlled and asymptotic relationships for bubble growth were presented as a function of time, for both inertia and heat transfer controlled regimes. Based on the wall temperature measurements and heat flux, pool boiling curves were presented which illustrated the heat dissipation characteristics of the surface. Net lateral liquid velocity due to asymmetric bubble

growth, measured using hot wire anemometry, showed potential pumping velocities of up to 6 mm/s. To further corroborate the results from hot wire anemometry, PIV experiments were conducted with FC-72 which are described in Appendix E. Due to light reflection from bubbles and non-availability of fluorescent particles with densities similar to that of FC-72, results from PIV experiments were inconclusive about lateral velocity of liquid.

Chapter 4

Microgravity Experiments

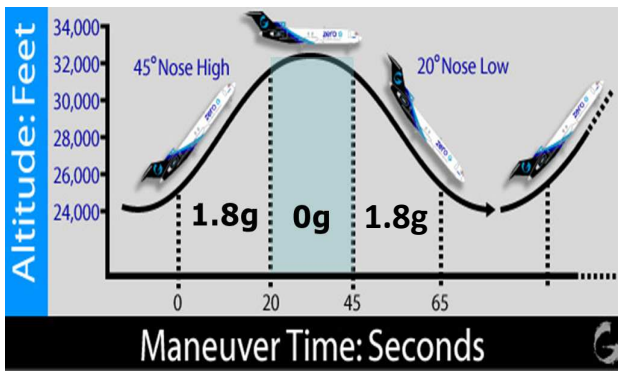
In pool boiling experiments conducted at 1g, it was observed that bubble growth and departure were normal to the sloped surface of the saw teeth. The buoyancy force acting on the asymmetrically growing and departing bubble, thereby, has a horizontal and a vertical component. The vertical component of buoyancy at 1g acting on an asymmetrically growing bubble is less than the buoyancy force acting on a vertically growing bubble on a plain surface. In the previous sections, it was observed that this led to significant change in bubble dynamics. To further understand the role of buoyancy, it is important to study the bubble dynamics and the resulting lateral motion in the absence of buoyancy which is only possible under microgravity. Hence, microgravity experiments were conducted to study bubble dynamics during phase change on an asymmetric surface in the absence of buoyancy and its effect on lateral velocity of liquid. The experiments were conducted aboard a Boeing 727 aircraft (Zero-g Inc.) (Fig. 4.1) carrying out parabolic maneuvers to achieve reduced gravity. The maneuvers were carried out on two separate days. Each day consisted of 40 consecutive parabolas with each parabola consisting of a 1.8g pull up, 0g and a 1.8g pull out with periods of 60 seconds for hyper-gravity ($\approx 1.8g$) and up to 17 seconds for microgravity (μg) as shown in Fig. 4.1b. Fig. 4.1c shows the recorded accelerometer readings during a single parabolic maneuver consisting of 1.8g, μg , and 1.8g. The flight operations initiated and terminated at Ellington field, Johnson Space Center in Houston, Texas.

4.1 Experimental Setup

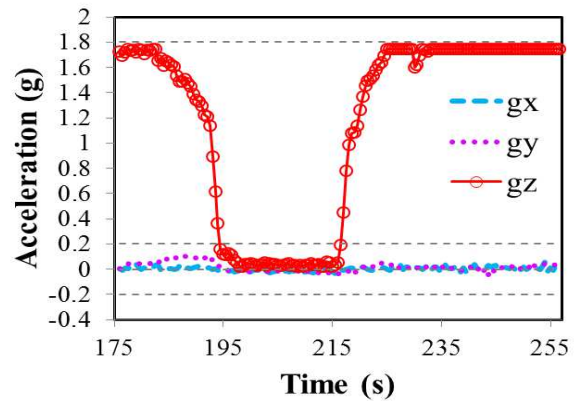
Fig. 4.2 shows the experimental setup used in the study. The silicon test device used for the pool boiling experiments, shown in Fig. 4.2a, is made of two layers - the asymmetric



(a) A NASA Zero-g flight on a 1.8g pull up maneuver



(b) Parabolic maneuver of the aircraft and period of gravity regimes



(c) Accelerometer data of the gravity profile

Figure 4.1: Zero gravity flight used for parabolic maneuvers - (a) A NASA Zer0-g flight on it upward ascent. Boeing 727 was used for the flight experiments (b)-(c) Gravity profile and recorded accelerometer readings of the achieved parabolic maneuvers

saw-toothed heat sink, and a serpentine heater layer. The heat sink has an asymmetric saw tooth cross-section with a $31^\circ - 90^\circ - 59^\circ$ profile and 1 mm pitch (hereafter referred to as the 31° test section). The heat sink used for large array experiments with FC-72, shown in Fig.4.2a consists of 80 such saw-teeth spanning a foot print of 80 mm x 20.3 mm. Each saw tooth has a long slope that is structured with re-entrant cavities. The cavities have a trapezoidal mouth of size ranging between 50 – 100 μm . Each saw tooth has 8 pairs of cavities spaced equally along the transverse length of ratchet on the long slope, with each pair consisting of a large and small cavity (marked as (a) and (b) in Fig.4.2a) spaced between the crest and the trough. In total, the heat sink consists of 1280 cavities acting as nucleation sites. Heat was provided using an aluminum serpentine heater fabricated on silicon. The voltage leads on the heater also aid in surface temperature measurements. The test device is mounted on a printed circuit board for electrical connections. The board also serves as the base of a transparent polycarbonate open channel which is 130.8 mm long, 25.4 mm wide and 7 mm deep, and mounted right on top of the test device as shown in Fig. 4.2b. The channel serves to confine the volume of fluid for realization of net liquid flow. The test board was suspended from the lid into a pool of FC-72 contained in an aluminum boiling chamber (Fig. 4.2c) of dimensions 33 cm x 23 cm x 22 cm (L x W x H). A thermistor and a pressure transducer were used to measure liquid temperature and pressure respectively. Prior to flight experiments, the fluid was charged into the system and degassed thoroughly at the ground station. Once the fluid was charged, the bellows on top of the boiling chamber were compressed and the valve on top of it was closed with pressure inside the chamber remaining at atmospheric conditions. During the flight experiments, the boiling chamber was completely sealed and any increase in pressure due to the boiling process was compensated by the expansion of rubber bellows, thereby maintaining ground atmospheric pressure within the boiling chamber. A similar experimental apparatus was used by Oregon State University research group for small array experiments with deionized water as working

fluid. The test section used for small array experiments with water is similar in cross-section consisting of only 8 saw-teeth ratchets with a footprint of 8 mm x 11.3 mm.

During the experiment, data from sensors were recorded using NI Compact DAQ, and a Phantom high speed camera fitted with an Infinity K2SC microscope lens and a CF2 close-up objective was used to record bubble images. The electrical equipment in the setup were grouped in to 110 V and 220 V equipment and power was drawn from separate sources on the flight. Emergency cut-off was setup for disconnecting both the 110 V and 220 V equipments from the power source. The other significant difference between terrestrial and microgravity gravity experimental setup was that the entire boiling chamber compartment was covered by polycarbonate sheets to form a double containment to prevent the liquid from entering the aircraft cabin in the event of a leak. The assembled view of the experimental setup is shown in Fig. 4.3. Experimentation aboard the flight also required adherence to strict mechanical design guidelines which required a factor of safety of 4 while withstanding forces up to 9g at every joint and all the load bearing members of the experimental setup. Details of the experimental design and structural analysis were furnished in a report, Test Equipment Data Package (TEDP), that was submitted to NASA. The submitted version of TEDP is presented in Appendix F.

4.2 Results and Discussion

The data reported in this section were collected from experiments on large and small arrays of saw-teeth ratchets with highly subcooled FC-72 and 10°C subcooled deionized water respectively (subcooling, ΔT_{sub} , is the difference between saturation and pool temperature, $T_{sat} - T_{pool}$) at μg ($\approx 10^{-2}$ g). The following sections carry discussion of bubble dynamics such as bubble diameter, bubble sliding motion, heat dissipation and a model for the estimation of bubble sliding velocity.

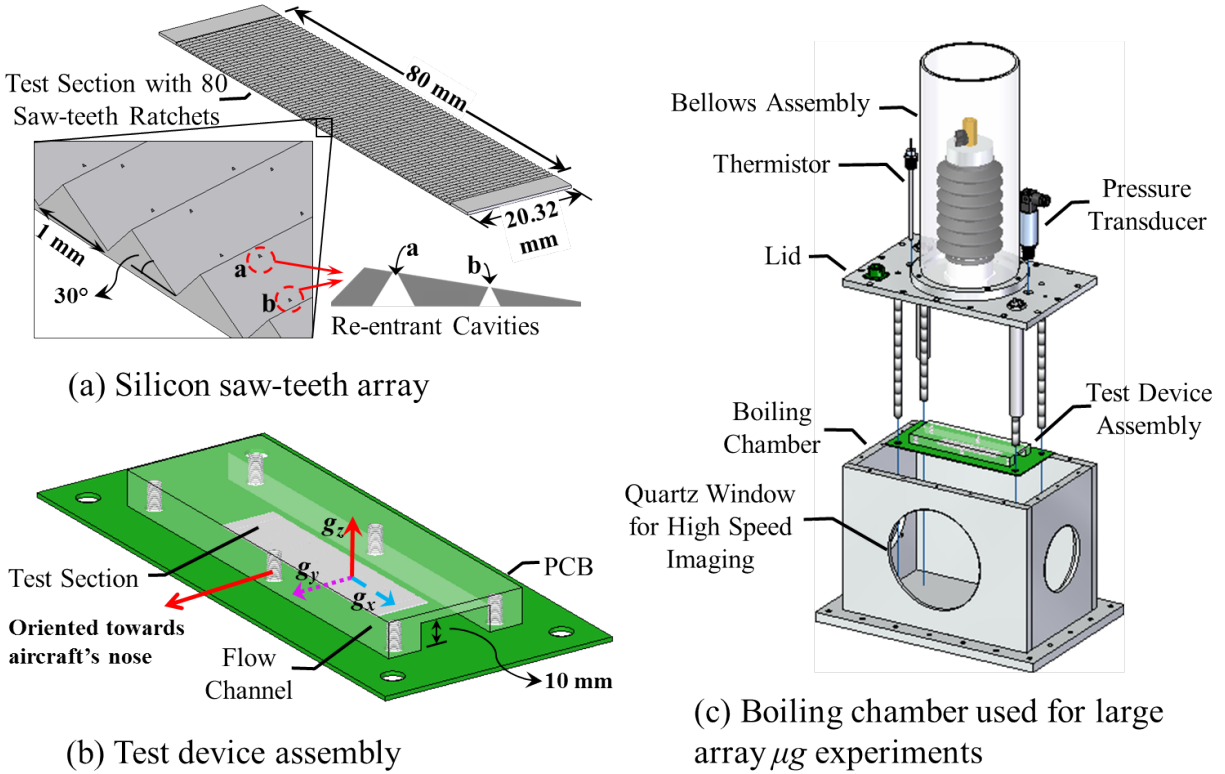


Figure 4.2: Experimental setup for reduced gravity experiments - (a) 31° test device with two re-entrant cavities per saw-tooth (b) Assembled test device with the polycarbonate flow channel. Co-ordinate system shows the orientation of the test device with respect to the aircraft. (c) Boiling chamber used for the reduced gravity experiment. Bellows assembly with double containment is used to maintain a constant chamber pressure.

4.2.1 Bubble Dynamics

At reduced gravity, due to lack of buoyancy it was observed that the bubbles reside on the heater surface and grow to several diameters larger than those in $1g$, as previously reported by a number of studies discussed in the literature. In experiments with water, because of the small size of the heat sink the entire surface of the test device was covered by a single large vapor bubble of diameter as large as 8.5 mm. It was observed that the single large bubble was pinned to the edges of the test section and the bubble interface appeared undulated at all tested heat flux values. Smaller vapor bubbles nucleating from the cavities under the footprint of the large bubble, at an angle normal to the shallow slope of the surface, were observed as shown in the image inset shown in Fig. 4.4a. This phenomenon is only

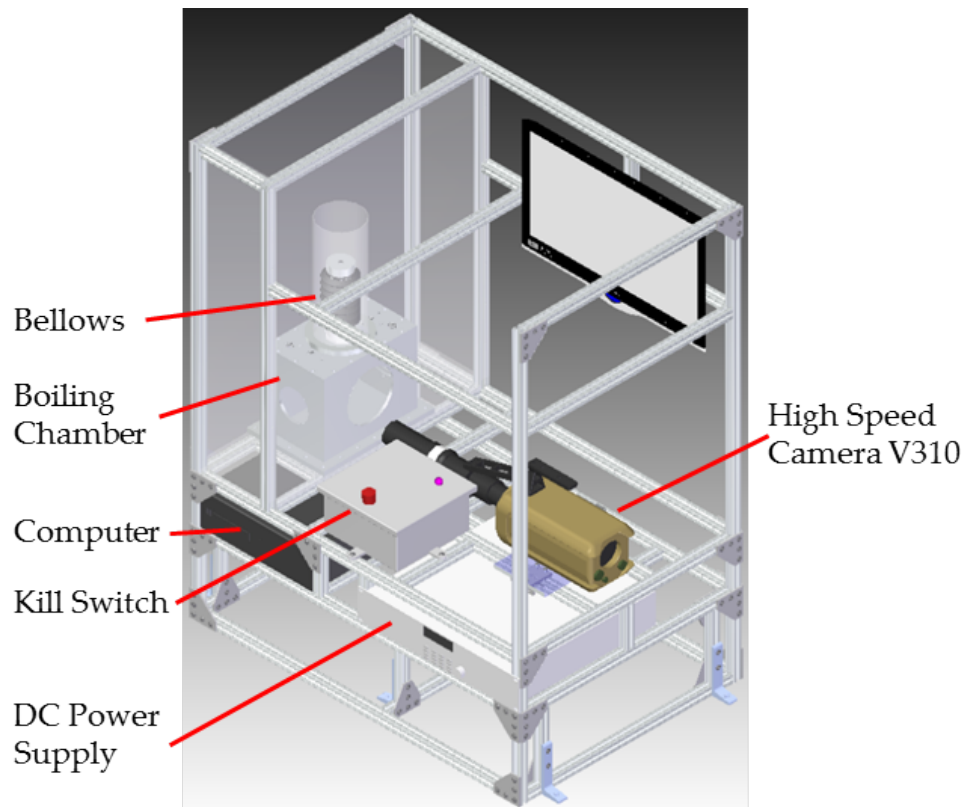
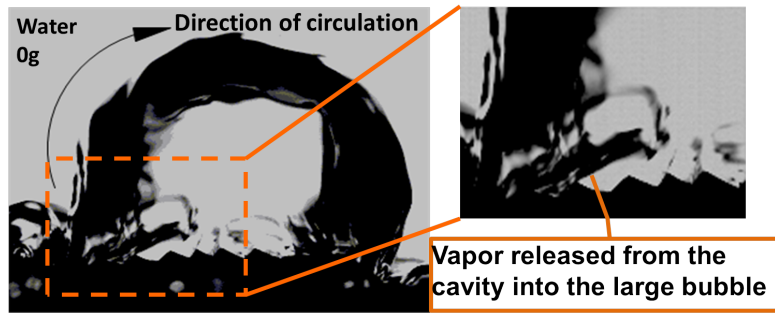


Figure 4.3: Assembled view of the experimental structure used for microgravity experiments. Details of the individual components in the structure and the related structural analysis are provided in Appendix F.

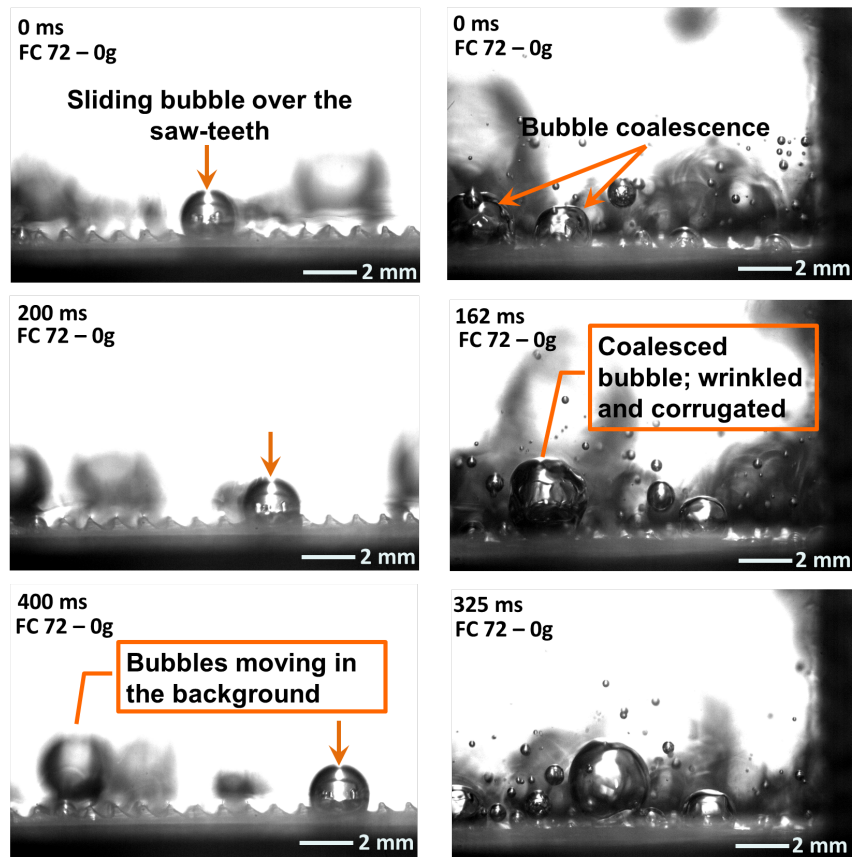
possible by the presence of a thin liquid film between the larger bubble and the surface; the presence of this thin liquid film is supported by the low measured surface temperature of 113°C, which is well below the Leidenfrost temperature. Straub [37] discusses a similar phenomenon with circulating vapor inside a bubble which was attributed to the shear forces induced by thermocapillary convection at the interface.

In the case of large array experiments with FC-72, the bubbles were $\cong 6$ times larger compared to 1g. Interestingly, in the large array experiments, the bubbles departed the nucleation site laterally and continued to slide at high velocities across the saw teeth and along the length of test device as shown in Fig. 4.4b and 4.4c. At a low heat flux of 0.5 W/cm², the interface of sliding bubbles appeared smooth and hemispherical as observed in the time sequence of images shown in Fig. 4.4b, and no departure from the surface was observed. As the heat flux was increased the bubble interface exhibited an unstable behavior as the surface appeared wrinkled, corrugated and more spherical. The corrugated sliding bubbles lifted-off and hovered over the surface which could be attributed to the momentum associated with bubble coalescence. This was also reported in studies with R-113 by Lee and Merte Jr. [43]. Fig. 4.4c at time 325 ms shows a corrugated bubble hovering over the surface at a heat flux of 1.4 W/cm². Lee and Merte Jr.[43] observed similar corrugated rough bubble surface which was to Rayleigh-Taylor instabilities. The smaller bubbles that appear in Fig. 4.4c resulted from bubble departure during the preceding 1.8g regime that remain suspended in the pool during the next microgravity regime.

At 1.8g (Fig. 4.5) with FC-72, due to increased buoyancy forces, the bubble departure diameters ($D_{d,1.8g}$) were very small compared to microgravity or 1g, $D_{d,1.8g} < D_{d,1g} < D_{d,\mu g}$ ($D_{d,1.8g}/D_{d,1g} = 0.24$). Also at 1.8g, bubble growth and departure was asymmetric and at an angle normal to the shallow slope similar to the observations under 1g (Figures 3.3 and 3.4).



(a) Water, μg , at 11.1 W/cm^2



(b) FC-72, μg , at 0.5 W/cm^2 (c) FC-72, μg , at 1.4 W/cm^2

Figure 4.4: Bubble dynamics in water and FC-72 under μg (a) Vapor bubble 10 times larger than at 1g was observed at microgravity. Image inset shows vapor nucleation from re-entrant cavities, under the foot print of the larger bubble, illustrating the presence of a liquid film. (b) Sliding motion of vapor bubbles at a velocity of $\approx 10 \text{ mm/s}$, across the saw-teeth (left to right in images) at $q'' = 0.5 \text{ W/cm}^2$. Sliding motion was observed at all tested conditions. (c) Sliding motion of vapor bubbles (left to right in the images) at $q'' = 1.4 \text{ W/cm}^2$.

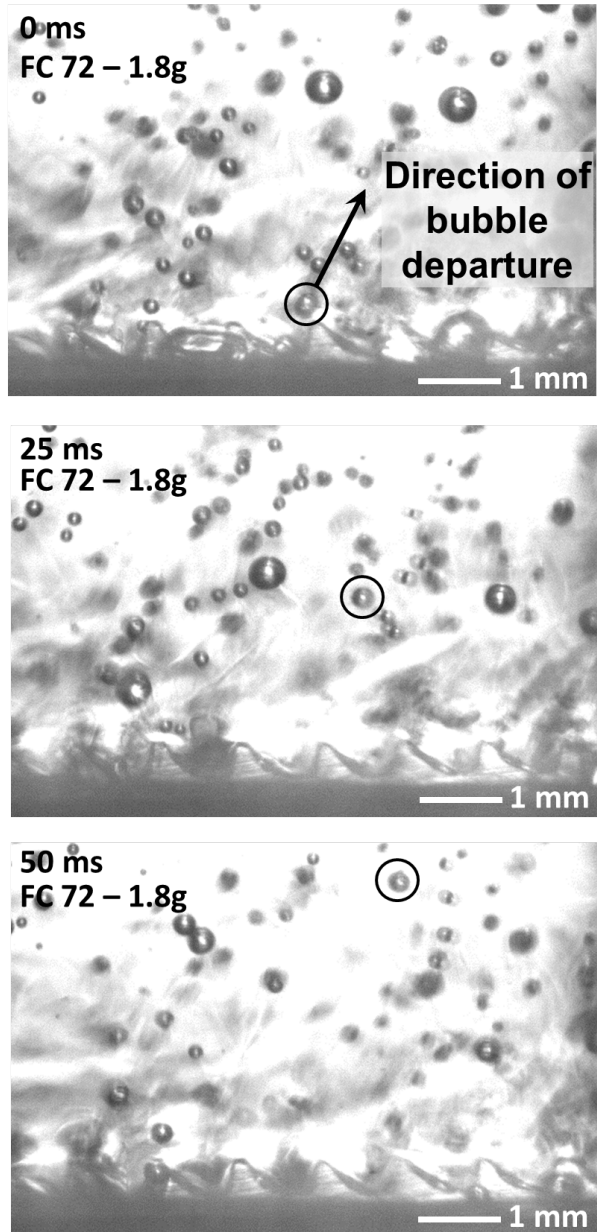


Figure 4.5: Bubble dynamics in FC-72 under 1.8g. Bubble departure diameters are very small compared to those at 1g ($\approx 0.25 D_{1g}$). Bubbles were observed to grow and depart at an angle normal to the shallow slope of the saw-teeth, a phenomenon that was previously demonstrated under 1g.

For saturated liquids in parabolic flights, empirical relationships for bubble departure diameter of the form shown in Equation 4.1 were reported by Qiu et al. [42] and Straub [37].

$$\frac{D_{d,\mu g}}{D_{d,1g}} = \left(\frac{g_z}{g_e} \right)^{-m} \quad (4.1)$$

where, $m = 0.5$ for saturated water and a plain silicon heater [42] and for heater geometries such as wires and cylinders the exponent was evaluated to be $0.3 < m < 0.39$ [37]. Equation 4.1 is used with the data from the microgravity experiments conducted in this study with both FC-72 and water and it can be observed from Fig. 4.6 that the bubble diameter ratio ($\frac{D_{d,\mu g}}{D_{d,1g}}$) is predicted to within 40% for 10°C subcooled water and highly subcooled FC-72 tests under μg conducted on the small array and large array test sections respectively.

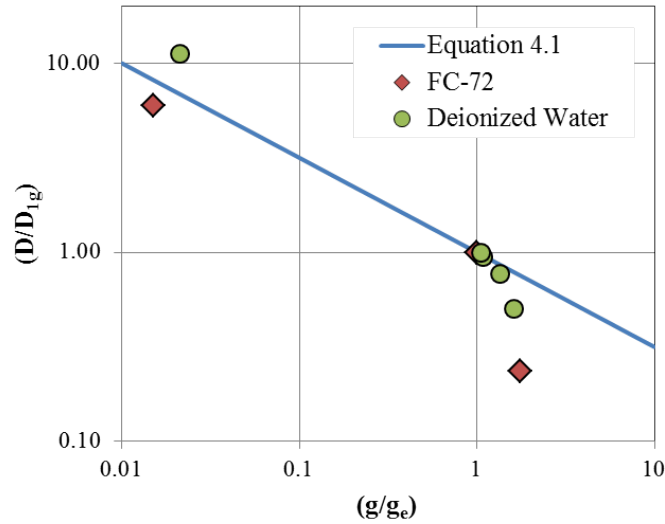


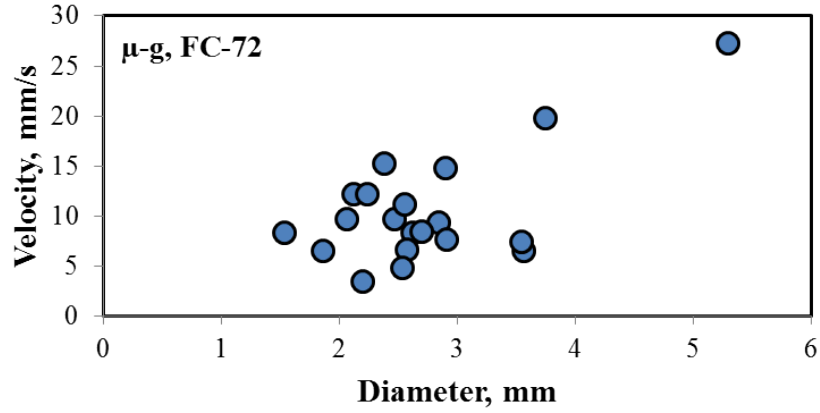
Figure 4.6: Comparison of experimental data with departure diameter estimated using Equation 4.1 for water and FC-72 under μg

The average bubble sliding velocities are represented as a function of bubble diameter in Fig. 4.7a. The phenomenon of sliding bubbles over the saw-toothed surface was consistent at all tested conditions. There was no correlation between bubble velocity and bubble diameter/heat flux as shown in Fig. 4.7a. However, the highest bubble velocity observed was 27.4 mm/s which corresponds to the largest observed bubble diameter of 5.3 mm at a

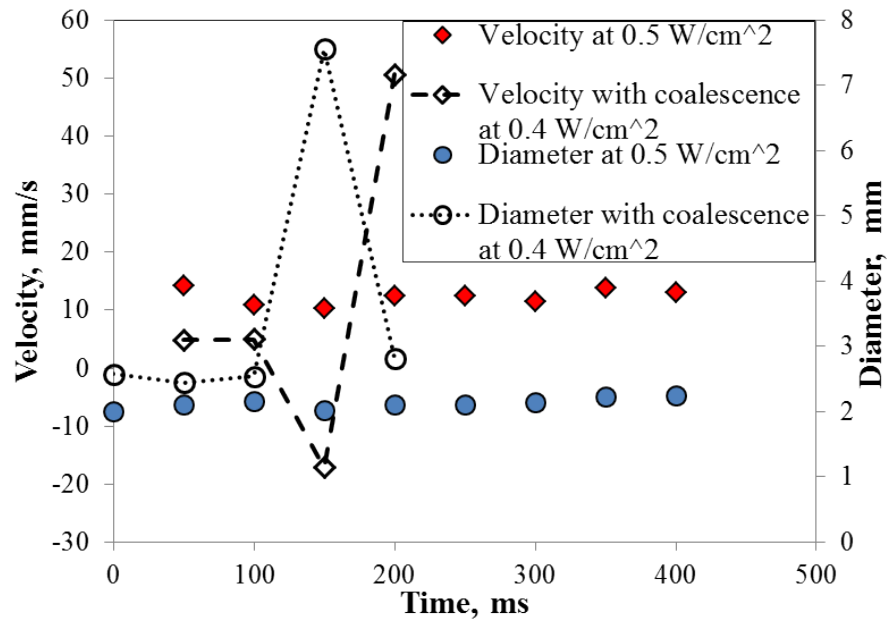
heat flux of 0.45 W/cm^2 . The lack of a correlation is mainly due to coalescence of sliding bubbles with other stationary bubbles growing on the surface and with bubbles moving at a lower velocity. Bubble coalescence leads to abrupt local changes in velocity and diameter of sliding bubbles compared to bubbles without coalescence as shown in Fig. 4.7b.

The observed lateral motion of bubbles under μg is hypothesized to be due to two phenomena. The first, at the nucleation sites, is due to the momentum imparted to the larger bubbles by the smaller bubbles growing at an angle, very similar to the observations in Fig. 4.4a for the case of water. Secondly, as the bubbles moved away from the nucleation site, pressure differences in the liquid film under the vapor bubble, similar to the Leidenfrost droplets reported by Linke et al. [8], propel the bubble as seen in fig. 4.4b and 4.4c. Pressure differences in the liquid layer could arise due to differences in radii of curvature of the liquid-vapor interface under the bubble, as the bubble conforms to the shape of the saw teeth. Owing to the difficulty in resolving the shape and size of the bubble interface at the saw teeth, it was not possible to calculate the pressure difference forces with certainty. However, Fig. 4.7b also shows that in the absence of bubble coalescence bubble diameter and sliding velocities were constant with time. The lack of bubble deceleration suggests that the bubble, after departure from the nucleation site, may be propelled along the surface due to forces arising from pressure differences. The bubble diameter remained constant owing to the condensation at the top of the bubble due to contact with cooler liquid, while vapor is added to the bubble due to contact with the heater surface at the bottom.

Lateral motion of bubbles under reduced gravity conditions, as discussed in the literature, has been attributed to g-jitters and in some cases Marangoni convection due to subcooled liquid conditions. Qiu et al. [42] in experiments with distilled saturated water noticed that a single bubble slid and lifted off at similar magnitude of velocity to those reported in the current study. The sliding motion on a plain silicon surface was attributed to the horizontal component of acceleration. By comparison, in the current study, the bubble motion observed was consistently unidirectional (left to right in the images shown in Figures



(a) Average sliding velocity of bubbles



(b) Effect of bubble coalescence on sliding velocity

Figure 4.7: Sliding velocity of bubbles in FC-72 under μg . Uncertainty in bubble velocity is $\pm 0.5\%$.

4.4b and c) across the saw teeth , and not random as it would be in the case of g-jitter induced bubble motion. Also, from the accelerometer data recorded during the experiment (Fig. 4.1c), it was observed that the horizontal component of acceleration (g_x) along the length of test device ranged between $-0.01 \leq g_x \leq 0.01$ indicating that any motion induced due to this variation would be along both directions of length of the test device. However, Marangoni convection could have still played a role due to the highly subcooled fluid conditions in the large array experiments. Due to short periods of μg conditions and other experimental constraints, the captured images do not show the entirety of a bubble's growth, departure, movement and lift-off across the saw teeth as the time scales involved in the entire process are much larger. Further explanation is provided in the following sections.

4.2.2 Bubble Transit Hypothesis

The lateral motion of bubbles observed under microgravity is schematically represented in Fig. 4.8 based on the observations from high speed images. The vapor bubble was observed to have different radii of curvatures between the crest and trough of the saw teeth and appeared to be suspended on a thin layer of liquid of thickness H . The forces contributing towards such lateral motion of bubbles could be attributed to:

1. Pressure differences in the liquid layer between the vapor bubble and the saw toothed surface due to the difference in radius of curvature of the vapor-liquid interface
2. Marangoni convection resulting from a gradient in surface tension around the bubble due to a temperature gradient in the liquid pool
3. Force due to vapor production from the cavities that imparts a momentum to the vapor bubble over it
4. Since the vapor bubble moves through the liquid, forces due to Stokes drag retard the motion of the bubble

In the next section each of these forces will be analyzed to find the magnitude of the driving potential.

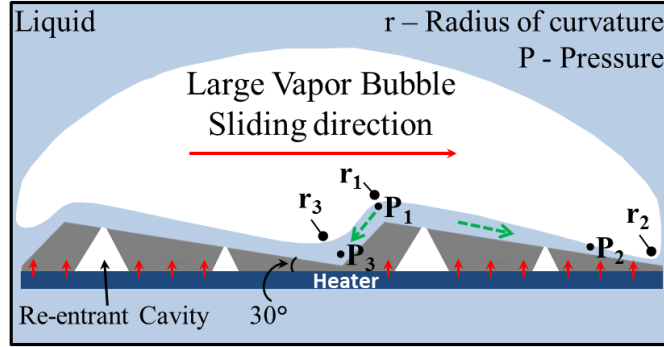


Figure 4.8: Schematic diagram of bubble motion over a saw-tooth in FC-72 under μg (not to scale). The arrows marked between the saw tooth and the vapor bubble indicate the direction of forces acting on the bubble due to pressure differences.

Force due to pressure difference in the liquid

From Fig. 4.8, the radius of curvature at point 1, r_1 is concave which leads to $r_1 < 0$. This in turn leads to pressure in the liquid locally at point 1, $P_{1,l}$, to be greater than the pressure in the vapor $P_{1,v}$ which can be expressed using the Young-Laplace equation [6] as shown in Equation 4.2. Similarly, at point 2 $r_2 > 0$ and $P_{2,v} > P_{2,l}$. The pressure inside the vapor bubble is assumed to be same throughout ($P_{1,v} = P_{2,v}$) Equations 4.2 and 4.3 can be combined to obtain an expression for pressure drop along the saw-tooth (Equation 4.4)

$$P_{1,l} - P_{1,v} = \frac{2\sigma}{r_1} \quad (4.2)$$

$$P_{2,v} - P_{2,l} = \frac{2\sigma}{r_2} \quad (4.3)$$

$$P_{1,l} - P_{2,l} = 2\sigma \left(\frac{1}{r_1} + \frac{1}{r_2} \right) \quad (4.4)$$

The shear force acting on the bubble due to the pressure gradient in the liquid film can be calculated by approximating the flow to be a fully developed plane Couette-Poiseuille flow

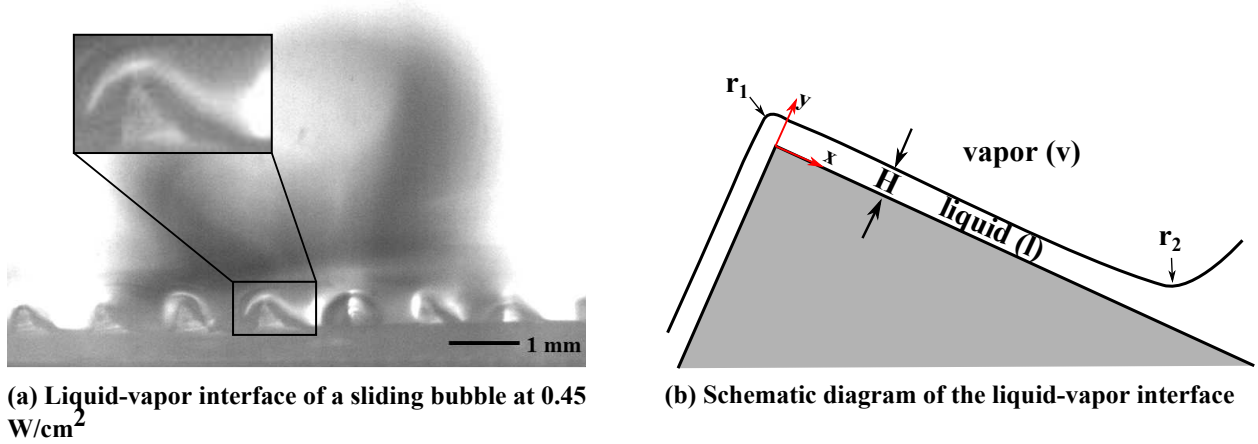


Figure 4.9: Liquid-vapor interface of a sliding vapor bubble in FC-72 under μg with no slip. Assuming the bubble to be initially moving at a constant velocity V , for a flow of liquid between parallel plates (bubble and surface of saw tooth) at zero gravity under a constant pressure gradient $(\frac{\partial P}{\partial x})$, the momentum equation can be expressed as

$$u(x) = \frac{1}{2\mu} \frac{\partial P}{\partial x} y^2 + c_1 y + c_2 \quad (4.5)$$

Boundary conditions for the flow represented in Fig. 4.9 are:

$$u_x = 0 \text{ at } y = 0 \text{ (no slip)}$$

$$u_x = V \text{ at } y = H \text{ (no slip)}$$

where H is the thickness of the liquid film between the vapor bubble and surface of saw tooth, as shown in Fig. 4.9.

By using the boundary conditions in Equation 4.5

$$c_2 = 0$$

$$c_1 = \frac{V}{H} - \frac{1}{\mu} \frac{\partial P}{\partial x} \frac{H}{2}$$

Using the constants c_1 and c_2 , the equation for velocity profile is

$$u(x) = \frac{V}{H}y - \frac{1}{2\mu} \frac{\partial P}{\partial x} (Hy - y^2) \quad (4.6)$$

Shear stress exerted by the liquid film on the bubble wall at $y = H$ is given by

$$\tau_w = -\tau_{yx}|_{y=H} = -\mu \left. \frac{du}{dy} \right|_{y=H} = -\frac{H}{2} \frac{\partial P}{\partial x} - \frac{\mu V}{H} \quad (4.7)$$

The total shear force acting on the bubble is then

$$\begin{aligned} \frac{F}{W} &= - \int_0^L \tau_w dx = \left[\frac{\mu V}{H} + \frac{H}{2} \frac{\partial p}{\partial x} \right] L \text{ (force per unit width)} \\ F_{\Delta P} &= \left[\frac{\mu V}{H} + \frac{H}{2} \frac{\partial p}{\partial x} \right] LW \end{aligned} \quad (4.8)$$

where L is the length of the liquid film that exists between the surface of saw tooth and vapor bubble.

The horizontal component of this force acting on the liquid along the shallow slope of the saw tooth is,

$$F_{\Delta P} = \left[\frac{\mu V}{H} + \frac{H}{2} \frac{\partial P}{\partial x} \right] LW \cos \theta \quad (4.9)$$

where, $\theta = \text{angle of saw tooth} = 31^\circ$

Equation 4.8 represents the force due to pressure drop over the long slope of a single saw tooth. The same form of the equation also applies for the short steep slope of the saw tooth, which is a force opposing the sliding motion of bubble in the direction marked. For a bubble moving at a velocity V with a foot print A_b spanning over m number of long slopes and n number of short slopes of the saw-teeth, the total force due to pressure difference is

expressed by

$$F_{\Delta P, tot} = \left\{ m \left[\left(\frac{\mu V}{H} + \frac{H}{2} \frac{\partial P}{\partial x} \right) LW \cos \theta \right]_{\text{long slope}} - n \left[\left(\frac{\mu V}{H} + \frac{H}{2} \frac{\partial P}{\partial x} \right) LW \sin \theta \right]_{\text{short slope}} \right\} \quad (4.10)$$

Force due to Marangoni convection

Marangoni forces arise due to presence of a surface tension gradient caused by a gradient in temperature. In the case of a heated wall in a pool of liquid, if the wall temperature T_w is larger than the pool temperature, a temperature distribution exists in the liquid close to the wall with temperatures ranging between T_w close to the wall and T_{pool} far away from the surface. A pure liquid, unlike a binary mixture, exhibits a negative surface tension gradient with respect to temperature, meaning, the surface tension decreases with increasing temperature. This surface tension gradient gives rise to a flow from high surface tension (cold liquid) to low surface tension (warmer liquid). When the temperature gradients in the liquid exist vertically and if the bubble is attached to a sloped wall, Marangoni convection will lead to a net force acting on the bubble which could result in its displacement.

The force due to Marangoni convection, F_M , for an hemispherical bubble is,

$$F_M = 2\pi R^2 \left(-\frac{d\sigma}{dT} \right) \left(\frac{dT}{dy} \right) \quad (4.11)$$

where

$\frac{d\sigma}{dT}$ = surface tension gradient between top and base of the bubble, N/mK

$\frac{dT}{dy}$ = temperature gradient between top and base of the bubble, K/m

R = radius of bubble, m

For a sliding bubble shown in Fig. 4.9a, Marangoni force acts vertically downwards and does not lead to a net lateral force. However, during the initial stages of bubble growth the Marangoni force may play a vital role in displacing the bubble from the nucleation site

laterally. Since, the model is developed for a sliding bubble the Marangoni force will be neglected.

Force due to vapor nucleation from cavities

In the case of a large vapor bubble hovering over a bubble growing over a cavity, the growth and departure of the bubble from the nucleation site exerts a force on the bubble hovering close to the surface. This force calculated by using momentum balance was given by Lee and Merte[43]

$$F_v = \pi \sum_{i=1}^{n_t} \bar{f}_i \left(\frac{\sigma_i \rho_{v,i}}{3} \right)^{1/2} D_i^{5/2} \quad (4.12)$$

where

$$\bar{f}_i = \text{mean bubble departure frequency, } s^{-1}$$

$$D_i = \text{bubble departure diameter, } m$$

$$\sigma_i = \text{surface tension, } N/m$$

Due to lack of information about bubble growth and departure from the nucleation site, the force due to nucleation from cavities using Equation 4.12 cannot be determined. Also, since the bubble growth rates are significantly lower in microgravity compared to earth gravity, the momentum transferred to the surrounding liquid is not expected to be a significant factor.

Viscous drag on the vapor bubble

The drag force experienced by the bubble as it moves against the inertia of liquid is given by the Stokes drag [56],

$$F_d = 4\pi\mu RV \quad (4.13)$$

where R is the radius of bubble.

The overall force balance using Newton's second law is

$$F_{\Delta P, tot} - F_d = 0 \quad (4.14)$$

By substituting Equations 4.10 and 4.13 in Equation 4.14, an expression for velocity of bubble is given by

$$V = \left\{ m \left[\left(\frac{\mu V}{H} + \frac{H}{2} \frac{\partial P}{\partial x} \right) LW \cos \theta \right]_{\text{long slope}} - n \left[\left(\frac{\mu V}{H} + \frac{H}{2} \frac{\partial P}{\partial x} \right) LW \sin \theta \right]_{\text{short slope}} \right\} \frac{1}{4\pi\mu R} \quad (4.15)$$

where

m = number of long shallow slopes under the bubble

n = number of short steep slopes under the bubble

$W \approx$ Diameter of bubble, m

H = thickness of liquid film under the bubble, m

L = length of liquid film under the bubble, m

μ = dynamic viscosity of liquid, Nsm^{-2}

$\frac{\partial P}{\partial x}$ = Pressure drop per unit length across the liquid film, N/m^3

R = radius of bubble, m

In the derivation of Equation 4.15, the thickness of liquid film under the bubble is assumed to be a constant and to be same over both the short and long slope of the saw teeth. For simplicity and to check the adequacy of the model, it could also be assumed that the parameters of liquid film and the radius of curvatures of bubble (r_1, r_2, r_3) repeat across every saw tooth over which the bubble interface resides.

As an example, for the sliding bubble shown in Fig. 4.9a, which was experimentally observed to be moving at 27 mm/s, the parameters such as the radii of curvature and thickness of film could be estimated by image processing.

The vapor bubble properties estimated are:

$$r_1 = 0.26 \text{ mm}; r_2 = 0.35 \text{ mm}; D = 5.3 \text{ mm}$$

It is assumed that the radii of curvature of the liquid-vapor interface over every saw tooth is repeated. This also leads to the conclusion that $r_2 = r_3$.

The estimated values for the liquid film parameters are shown below:

$$L_{longslope} = 0.85 \text{ mm}; L_{shortslope} = 0.53 \text{ mm}$$

The thickness of the film is assumed to be a constant over both the short and long slope of the saw tooth. The parameter L is the length of the film that is trapped between the vapor bubble and the the saw tooth, and it is assumed that the vapor bubble occupies the entire slopes of the saw tooth.

The fluid properties are estimated at the saturation temperature of the fluid. By using all the aforementioned parameters in Equation 4.15, and varying the thickness of the liquid film between the vapor bubble and saw tooth, H , from 1-25 μm , the velocity of the bubble can be calculated as a function of H . The effect of H on the velocity of bubble is illustrated in Fig. 4.10. The other liquid and bubble parameters which were held constant are represented in the figure. It can be observed that the experimentally observed velocity of 27.4 mm can be obtained from the model for $H \approx 17 \text{ mm}$. By observing the bubble images, it can be inferred that the values of H plotted in the Fig. 4.10 are plausible. This agreement between the model and the experiments proves that pressure differences in the liquid film is a potential driving force for the sliding motion of bubbles under microgravity. In a similar study conducted by Linke et al. [8], for R-134a droplet velocities of $\approx 5 \text{ cm/s}$, the value of vapor film thickness was $\approx 10 \text{ mm}$. In the current analysis, the values of r_1 , r_2 , and r_3 were estimated from images. However, those values were varied to analyze their effect on bubble velocity and it was observed that small changes in the radii of curvature did not affect the velocity much. Similarly, the values for the length of liquid film, L , were also varied and the bubble velocities were not affected significantly. Sample calculations are provided for bubble velocity are provided in Appendix G.

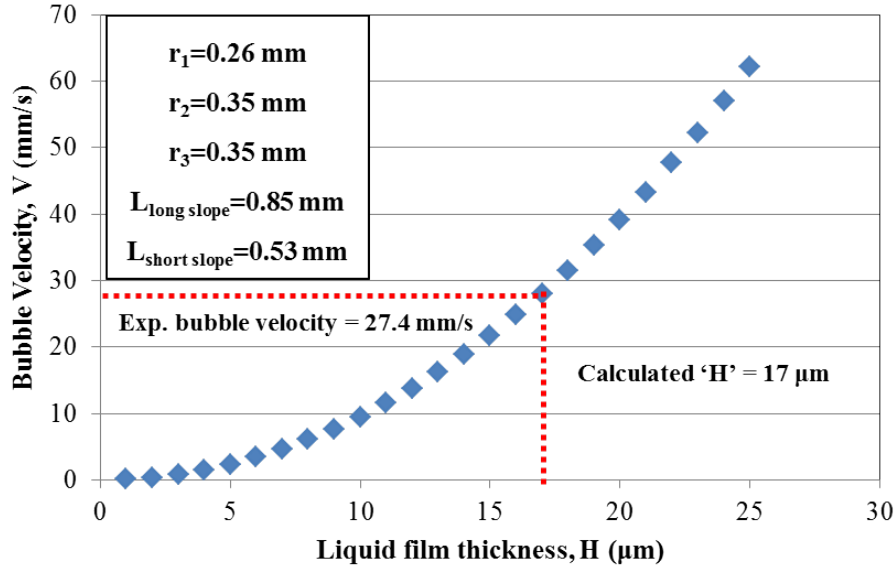


Figure 4.10: Estimated bubble sliding velocities for liquid film thickness varying from 0-25 μm . The experimental bubble velocity of 27.4 mm/s is predicted closely for a H value of 17 mm. From bubble images, a value of H .

4.2.3 Heat Dissipation

The boiling curve shown in Fig.4.11 represents the heat transfer from the large array experiments with FC-72 at reduced gravity. Wall superheat defined as $(T_w - T_{sat})$, represents the difference between the saw teeth surface temperature and liquid saturation temperature. It was observed that heat dissipation rates over 2 W/cm^2 were achieved at a wall superheat as low as 0°C without reaching critical heat flux (CHF) or dry-out under the bubble. Henry and Kim [41] who conducted similar pool boiling experiments with FC-72 under reduced gravity conditions with a silicon heater of size $2.7 \text{ mm} \times 2.7 \text{ mm}$ reported similar heat dissipation rates although at much higher wall temperatures of $\approx 15^\circ\text{C}$. By comparison with the current study, the higher heat transfer at lower heater temperatures could be partly attributed to sliding bubbles leading to net lateral liquid velocity in the channel which also prevents CHF due to dry-out under a stagnant vapor bubble.

In comparison with experiments under $1g$ performed with the 24° test device, it was observed that heat dissipation was higher under μg in the nucleate boiling regime. This

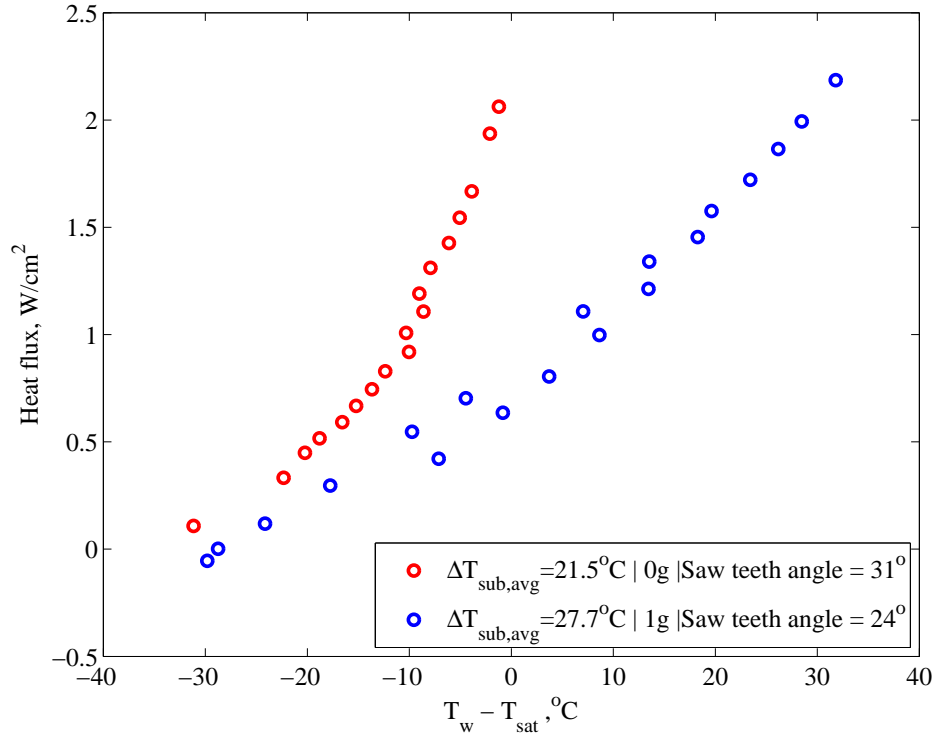


Figure 4.11: Boiling curves for large array experiments with FC-72 under μg and $1g$. $\Delta T_{sub} = T_{sat} - T_{pool}$. Both experiments were performed with a highly subcooled pool and pool temperature was not controlled. Uncertainties in q'' and $(T_w - T_{sat})$ are $\pm 1\%$ and $\pm 0.3\%$ respectively.

enhancement in the nucleate boiling regime is partly due to the drop in chamber pressure during the flight experiment which led to a drop in saturation temperature to 50.5°C . This drop in pressure caused early nucleation which could be observed as a shift in slope in Fig. 4.11. Also, the 31° test device, which was used in the microgravity experiments has 2 cavities per saw-tooth whereas the 24° test device has only one per saw-tooth. However, the enhancement may also be attributed to the the sweeping motion of sliding bubbles which can enhanced heat transfer. In pool boiling experiments conducted with R-113, Lee and Merte Jr. [43] reported heat transfer enhancement of up to 40% under microgravity compared to $1g$, and the enhancement was attributed to vapor bubble migration along the surface.

Chapter 5

Conclusions and Recommendations

A novel concept of using surface asymmetry to develop self-propelled flow of liquid has been studied for electronics thermal management applications. The driving potential for the flow is the heat dissipated from the hot surface by nucleate boiling. Surface asymmetry arises from two sources - one, a saw tooth profile, and two, re-entrant cavities that are located only on the shallow slope of the saw tooth. Such a heat sink was designed to achieve bubble nucleation only from the shallow face of the saw teeth. The asymmetric surface with re-entrant cavities was fabricated using gray-scale lithography, DRIE, anisotropic etching and other photolithographic processes. The control of etch selectivity and the surface quality was achieved by varying the gas flow rates in DRIE.

Pool boiling experiments with FC-72 were conducted on a heat sink with asymmetric silicon ratchets and pyramidal re-entrant cavities. Integrated aluminum serpentine heaters deposited in silicon, were used to supply heat to the heat sink. Experiments were conducted over a subcooling range of 0°C - 20°C and heat flux ranging from 0 - 4 W/cm^2 under both terrestrial gravity (1g) and reduced gravity (μg). The following conclusions can be drawn from the experiments conducted:

5.1 Bubble dynamics: Terrestrial experiments

- In FC-72, under terrestrial gravity, the designed surface profile and asymmetry in location of re-entrant cavities caused vapor bubbles to nucleate, grow and depart at an angle normal to the shallow slope of the saw teeth, at all tested conditions.
- Using image processing techniques, the high speed images were processed to obtain bubble growth data which is unique to the surface being tested. The bubble shape,

interestingly, resembled a “light-bulb” and was not circular as would be expected for a low surface tension fluid. This also suggests that the evaporation microlayer may play a less significant role than it would in water, as reported by Demiray and Kim [36].

- Bubble growth rate was observed to be both inertia and heat transfer controlled. The inertia controlled regime witnessed a linear rapid growth rate of the form $D \approx t$. In the heat transfer controlled regime, growth was observed to increase at the rate of $\approx t^{1/4}$ which is less than the $t^{1/2}$ relationship reported in a number of studies.
- Bubble growth was studied as a function of heat flux and subcooling and it was observed that the growth rate increased with increasing heat flux and reducing liquid subcooling. For the inertia controlled regime, in the growth rate relationship expressed as $D = At$, A was noticed to increase with increasing heat flux between ≈ 48 and 175. Similarly, A increased between $\approx 48 - 181$ with reducing subcooling. In the heat transfer controlled regime where the growth rate is expressed as $D = \beta t^m$, while m was $\approx 0.20-0.25$, β (growth constant) was observed to increase with increasing heat flux and reducing subcooling. This suggests that the growth constant increases linearly with increasing wall superheat which was also observed by Cole and Shulman [29].
- Bubble departure frequency increased with increasing heat flux (or wall temperature) and reducing subcooling as reported by number of other studies. However, subcooling or heat flux did not significantly affect the bubble departure diameter which was attributed to the low range of tested heat flux.
- Available analytical models for bubble growth performed poorly for the experimental conditions of the current study emphasizing the need for further studies.
- Heat dissipation of up to 2.5 W/cm^2 was obtained from the surface while keeping the surface temperatures less than 90°C . Heat transfer increased with increasing subcooling.

5.2 Net lateral liquid velocity under terrestrial gravity

- Using the bubble growth model developed earlier by Kapsenberg et al. [57] in a complementary study at Oregon State University, it was demonstrated that asymmetric bubble growth can lead to a net lateral liquid velocity of up to 5 mm/s in FC-72 and 18 mm/s in water.
- Hot wire anemometry was used to measure liquid velocity over the surface. While no velocity was detected at saturated conditions, liquid velocity of up to 5 mm/s was noticed at subcooled conditions. However, the output from the hot wire probe fluctuated a lot owing to contact with the vapor bubbles and operation at the lower limit of the anemometer.

5.3 Bubble dynamics: Microgravity

Pool boiling experiments with FC-72 on silicon saw teeth were conducted aboard NASA's reduced gravity flight to investigate the effects of surface asymmetry, re-entrant cavities on bubble dynamics and lateral liquid velocity under microgravity. The following conclusions can be drawn from the reduced gravity experiments aboard the parabolic flights:

- In FC-72, bubbles were six times larger under μg than under 1g. Under 1.8g bubbles were very small ($\approx 1/4 D_{1g}$).
- Under μg , bubbles were observed to slide across the saw teeth at velocities as high as 27 mm/s. Bubbles were driven across the saw teeth by forces such as pressure drop in the thin liquid under the bubble, similar to the sliding motion of liquid droplet over a saw-toothed surface observed by Linke et al. [8]. Pressure differences arise due to differences in the radii of curvature of liquid-vapor interface at the crest and trough of the saw teeth.

- In the absence of asymmetry (i.e. a plain heater surface), the vapor bubble would be stationary as observed in a number of studies discussed in the literature, which would lead to heat transfer deterioration owing to a premature dry-out under the bubble. The ability to move the bubble passively, as demonstrated, leads to a self-propelled flow resulting in heat transfer enhancement rather than deterioration, which underscores the potential of the study to cool high heat flux microelectronics under reduced gravity conditions.
- A model was proposed to study the effect of pressure differences in the liquid film on vapor bubble propulsion. It was inferred that pressure difference in the liquid film is a potential force to cause bubble propulsion. Other forces include Marangoni convection which could not be tested due to the very limited number of microgravity parabolas available.

5.4 Recommendations

- Based on the observations from the experiments, asymmetric bubble growth from sloped surfaces has the potential to effect lateral motion of liquid in the bubble's immediate vicinity. Also, microgravity testing proved the importance of inducing a thin liquid film between the saw-toothed surface and the vapor bubble. Both of these could be achieved by constructing a closed loop microchannel test device with saw-toothed heated side walls, which while keeping the liquid volume low, will also promote the existence of a thin liquid film along the walls. This would also result in heat transfer enhancement due the annular flow regime that would prevail in such a scenario. This configuration, however, will be very sensitive to gravity and hence may be a very effective thermal management solution for space electronics.
- To further study the role of forces due to Marangoni convection in bubble propulsion, it may be very useful to conduct experiments with saturated pool conditions which would

eliminate temperature gradients in the pool, and thereby surface tension gradients. Also, high speed imaging to further study the liquid-vapor interface may help improve the model. It also has to be made sure that the exposure time for the high speed images is high enough to capture both the bubble nucleation and its transit across the surface.

- The current study was mainly focused on heat dissipation from the electronic component to the liquid using an asymmetric heat sink, that was fabricated to achieve self-propelled flow of liquid. While heat transfer from the surface to the liquid is important, it is also necessary for the heat to be rejected to another sink, so that the liquid could be continuously used in a closed loop. A complimentary process to the one discussed in the current study is condensation heat transfer, which is often used in waste heat recovery systems. A surface similar to the one constructed in the current study, coupled with asymmetry in surface tension induced by hydrophilic-hydrophobic junctions, could effectively be used in self-propelled transport of the condensate.

Bibliography

- [1] M. C. Jo, Thermally actuated pumping of a single-phase fluid using surface asymmetry, Master's thesis, Oregon State University, OR, 2008.
- [2] A. Alexeev, T. Gambaryan-Roisman, P. Stephan, Marangoni convection and heat transfer in thin liquid films on heated walls with topography: experiments and numerical study, *Physics of Fluids* 17 (2005) 062106.
- [3] A. D. Stroock, R. F. Ismagilov, H. A. Stone, G. M. Whitesides, Fluidic ratchet based on marangoni-bénard convection, *Langmuir* 19 (2003) 4358–4362.
- [4] R. F. Ismagilov, D. Rosmarin, D. H. Gracias, A. D. Stroock, G. M. Whitesides, Competition of intrinsic and topographically imposed patterns in Bénard–Marangoni convection, *Applied Physics Letters* 79 (2001) 439–441.
- [5] S. J. VanHook, M. F. Schatz, W. D. McCormick, J. Swift, H. L. Swinney, Long-wavelength instability in surface-tension-driven Bénard convection, *Physical review letters* 75 (1995) 4397.
- [6] V. Carey, Liquid-vapor phase-change phenomena: an introduction to the thermophysics of vaporization and condensation processes in heat transfer equipment, Taylor & Francis London, 1992.
- [7] C. Witze, V. Schrock, P. Chambre, Flow about a growing sphere in contact with a plane surface, *International Journal of Heat and Mass Transfer* 11 (1968) 1637–1652.
- [8] H. Linke, B. Alemán, L. Melling, M. Taormina, M. Francis, C. Dow-Hygelund, V. Narayanan, R. Taylor, A. Stout, Self-propelled leidenfrost droplets, *Physical review letters* 96 (2006) 154502.

- [9] H. Yuan, A. Prosperetti, The pumping effect of growing and collapsing bubbles in a tube, *Journal of Micromechanics and Microengineering* 9 (1999) 402.
- [10] D. Meng, C.-J. Kim, Micropumping of liquid by directional growth and selective venting of gas bubbles, *Lab Chip* 8 (2008) 958–968.
- [11] T. K. Jun, C.-J. Kim, Valveless pumping using traversing vapor bubbles in microchannels, *Journal of Applied Physics* 83 (1998) 5658–5664.
- [12] A. Goyal, R. C. Jaeger, S. H. Bhavnani, C. D. Ellis, N. K. Phadke, M. Azimi-Rashti, J. S. Goodling, Formation of silicon reentrant cavity heat sinks using anisotropic etching and direct wafer bonding, *Electron Device Letters, IEEE* 14 (1993) 29–32.
- [13] C. Baldwin, S. Bhavnani, R. Jaeger, Toward optimizing enhanced surfaces for passive immersion cooled heat sinks, *Components and Packaging Technologies, IEEE Transactions on* 23 (2000) 70–79.
- [14] N. Nimkar, S. Bhavnani, R. Jaeger, Benchmark heat transfer data for microstructured surfaces for immersion-cooled microelectronics, *Components and Packaging Technologies, IEEE Transactions on* 29 (2006) 89–97.
- [15] S. G. Kandlikar, D. A. Willistein, J. Borrelli, Experimental evaluation of pressure drop elements and fabricated nucleation sites for stabilizing flow boiling in minichannels and microchannels, *Sat* 8 (2005) 1–1.
- [16] A. Koşar, C.-J. Kuo, Y. Peles, Boiling heat transfer in rectangular microchannels with reentrant cavities, *International Journal of Heat and Mass Transfer* 48 (2005) 4867–4886.
- [17] S. H. Bhavnani, G. Fournelle, R. C. Jaeger, Immersion-cooled heat sinks for electronics: insight from high-speed photography, *Components and Packaging Technologies, IEEE Transactions on* 24 (2001) 166–176.

- [18] B. Morgan, C. M. Waits, J. Krizmanic, R. Ghodssi, Development of a deep silicon phase fresnel lens using gray-scale lithography and deep reactive ion etching, *Microelectromechanical Systems, Journal of* 13 (2004) 113–120.
- [19] M. Whitley, R. Clark, J. Shaw, D. Brown, P. Erbach, G. Dorek, Deep grayscale etching of silicon, 2002.
- [20] K.-S. Chen, A. A. Ayón, X. Zhang, S. M. Spearing, Effect of process parameters on the surface morphology and mechanical performance of silicon structures after deep reactive ion etching (drie), *Microelectromechanical Systems, Journal of* 11 (2002) 264–275.
- [21] H. Jansen, M. de Boer, R. Legtenberg, M. Elwenspoek, The black silicon method: a universal method for determining the parameter setting of a fluorine-based reactive ion etcher in deep silicon trench etching with profile control, *Journal of Micromechanics and Microengineering* 5 (1995) 115.
- [22] C. M. Waits, A. Modafe, R. Ghodssi, Investigation of gray-scale technology for large area 3d silicon mems structures, *Journal of Micromechanics and Microengineering* 13 (2003) 170.
- [23] C. Waits, B. Morgan, M. Kastantin, R. Ghodssi, Microfabrication of 3d silicon mems structures using gray-scale lithography and deep reactive ion etching, *Sensors and Actuators A: Physical* 119 (2005) 245–253.
- [24] L. Rayleigh, On the pressure developed in a liquid during the collapse of a spherical cavity, *The London, Edinburgh, and Dublin Philosophical Magazine and Journal of Science* 34 (1917) 94–98.
- [25] B. Mikic, W. Rohsenow, P. Griffith, On bubble growth rates, *International Journal of Heat and Mass Transfer* 13 (1970) 657–666.

- [26] M. Plesset, S. A. Zwick, The growth of vapor bubbles in superheated liquids, *Journal of Applied Physics* 25 (1954) 493–500.
- [27] L. Scriven, On the dynamics of phase growth, *Chemical Engineering Science* 10 (1959) 1–13.
- [28] N. Zuber, The dynamics of vapor bubbles in nonuniform temperature fields, *International Journal of Heat and Mass Transfer* 2 (1961) 83–98.
- [29] R. Cole, H. L. Shulman, Bubble growth rates at high jakob numbers, *International Journal of Heat and Mass Transfer* 9 (1966) 1377–1390.
- [30] S. Van Stralen, M. Sohal, R. Cole, W. Sluyter, Bubble growth rates in pure and binary systems: combined effect of relaxation and evaporation microlayers, *International Journal of Heat and Mass Transfer* 18 (1975) 453–467.
- [31] B. Mikic, W. Rohsenow, Bubble growth rates in non-uniform temperature field, *Progress in Heat and Mass Transfer* 2 (1969) 283–293.
- [32] H. C. Lee, B. D. Oh, S. W. Bae, M. H. Kim, Single bubble growth in saturated pool boiling on a constant wall temperature surface, *International journal of multiphase flow* 29 (2003) 1857–1874.
- [33] C. Ramaswamy, Y. Joshi, W. Nakayama, W. Johnson, High-speed visualization of boiling from an enhanced structure, *International journal of heat and mass transfer* 45 (2002) 4761–4771.
- [34] C. Hutter, D. Kenning, K. Sefiane, T. Karayiannis, H. Lin, G. Cummins, A. Walton, Experimental pool boiling investigations of fc-72 on silicon with artificial cavities and integrated temperature microsensors, *Experimental Thermal and Fluid Science* 34 (2010) 422–433.

- [35] S. Moghaddam, K. Kiger, Physical mechanisms of heat transfer during single bubble nucleate boiling of fc-72 under saturation conditions-i. experimental investigation, *International Journal of Heat and Mass Transfer* 52 (2009) 1284–1294.
- [36] F. Demiray, J. Kim, Microscale heat transfer measurements during pool boiling of fc-72: effect of subcooling, *International journal of heat and mass transfer* 47 (2004) 3257–3268.
- [37] J. Straub, Boiling heat transfer and bubble dynamics in microgravity, *Advances in heat transfer* 35 (2001) 57–172.
- [38] J. Kim, J. Benton, Highly subcooled pool boiling heat transfer at various gravity levels, *International journal of heat and fluid flow* 23 (2002) 497–508.
- [39] R. Raj, J. Kim, J. McQuillen, Pool boiling heat transfer on the international space station: Experimental results and model verification, *Journal of Heat Transfer* 134 (2012) 101504.
- [40] M. Zell, J. Straub, A. Weinzierl, Nucleate pool boiling in subcooled liquid under microgravity results of texus experimental investigations, in: *5th European Symp. on Material Science under Microgravity*, 1984, pp. 327–333.
- [41] C. Henry, J. Kim, A study of the effects of heater size, subcooling, and gravity level on pool boiling heat transfer, *International journal of heat and fluid flow* 25 (2004) 262–273.
- [42] D. Qiu, V. Dhir, D. Chao, M. Hasan, E. Neumann, G. Yee, A. Birchenough, Single-bubble dynamics during pool boiling under low gravity conditions, *Journal of thermophysics and heat transfer* 16 (2002) 336–345.
- [43] H. Lee, H. Merte Jr, Pool boiling mechanisms in microgravity, *Ann Arbor* 1001 (1999) 48109–2125.

- [44] R. Thompson, K. DeWitt, T. Labus, Marangoni bubble motion phenomenon in zero gravity, *Chemical Engineering Communications* 5 (1980) 299–314.
- [45] P. Hadland, R. Balasubramaniam, G. Wozniak, R. Subramanian, Thermocapillary migration of bubbles and drops at moderate to large marangoni number and moderate reynolds number in reduced gravity, *Experiments in fluids* 26 (1999) 240–248.
- [46] C. Henry, J. Kim, J. McQuillen, Dissolved gas effects on thermocapillary convection during boiling in reduced gravity environments, *Heat and mass transfer* 42 (2006) 919–928.
- [47] J. R. Black, Electromigration failure modes in aluminum metallization for semiconductor devices, *Proceedings of the IEEE* 57 (1969) 1587–1594.
- [48] J. R. Black, Electromigration a brief survey and some recent results, *Electron Devices, IEEE Transactions on* 16 (1969) 338–347.
- [49] R. Wolffenbuttel, K. Wise, Low-temperature silicon wafer-to-wafer bonding using gold at eutectic temperature, *Sensors and Actuators A: Physical* 43 (1994) 223–229.
- [50] S. Lani, A. Bosseboeuf, B. Belier, C. Clerc, C. Gousset, J. Aubert, Gold metallizations for eutectic bonding of silicon wafers, *Microsystem technologies* 12 (2006) 1021–1025.
- [51] M. Cooper, A. Lloyd, The microlayer in nucleate pool boiling, *International Journal of Heat and Mass Transfer* 12 (1969) 895–913.
- [52] W. Fritz, W. Ende, Über den verdampfungsvorgang nach kinematographischen aufnahmen an dampfblasen, *Phys. Z* 37 (1936) 391–401.
- [53] H. K. Forster, N. Zuber, Growth of a vapor bubble in a superheated liquid, *Journal of Applied Physics* 25 (1954) 474–478.
- [54] H. S. Lee, H. Merte Jr, Hemispherical vapor bubble growth in microgravity: experiments and model, *International journal of heat and mass transfer* 39 (1996) 2449–2461.

- [55] Model 1750 Constant Temperature Anemometer - User Manual, revision n ed., TSI, 2008.
- [56] T. Papanastasiou, G. Georgiou, A. N. Alexandrou, Viscous fluid flow, CRC Press, 2010.
- [57] F. Kapsenberg, N. Thiagarajan, V. Narayanan, S. Bhavnani, Lateral motion of bubbles from surfaces with mini ratchet topography modifications during pool boiling-experiments and preliminary model, in: Thermal and Thermomechanical Phenomena in Electronic Systems (ITherm), 2012 13th IEEE Intersociety Conference on, IEEE, 2012, pp. 165–175.
- [58] T. G. Beckwith, R. D. Marangoni, J. H. Lienhard, Mechanical measurements, Pearson Prentice Hall, 2007.
- [59] J. Westerweel, Fundamentals of digital particle image velocimetry, Measurement Science and Technology 8 (1997) 1379.

Appendices

Appendix A

Thermophysical Properties of FC-72 and Water

Thermophysical properties of the working fluid used in this study, FC-72, are listed in the table below, along with properties of water for comparison.

Table A.1: Thermophysical properties of FC-72 and saturated water at 1 atm

Properties	FC-72	Water
Saturation temperature, T_{sat} (°C)	56.6	100
Specific heat, C_p (J/kg-K)	1097.41	4190
Latent heat of vaporization, h_{fg} (J/kg)	84510.9	2257030
Liquid density, ρ_l (kg/m ³)	1619.73	957.85
Vapor density, ρ_v (kg/m ³)	13.396	0.598
Thermal conductivity, k (W/m-K)	0.05216	0.68
Dynamic viscosity, (Ns/m ²)	0.000454	0.000279
Prandtl number, Pr	9.555	1.76
Surface tension, σ (N/m)	0.008273	0.0589

From Table A.1, it can be noticed that FC-72 boils at 56.6 °C, which is one of the significant advantages compared to water as this property allows the temperatures of surface being cooled by phase change to be maintained at a level considerably lower than that with water. Also, FC-72 is heavier and more viscous than water. Especially, for the application of liquid pumping due to nucleate boiling, the velocities obtained in FC-72 will be lower owing to the higher liquid inertia. Lower surface tension of FC-72, compared to water, leads to very low contact angles and smaller vapor bubbles. The drawbacks of FC-72 include poor heat transfer properties such as lower thermal conductivity and latent heat of vaporization.

Appendix B

Preliminary Closed Loop Experiments Under Terrestrial Gravity Using FC-72

Prior to conducting experiments in a large chamber using an open loop channel, experiments were conducted to test the concept in a closed loop set up. The closed loop experimental set up has a “race-track” shaped flow channel as shown in Fig. B.1. The two part experimental setup was made of polycarbonate. The top plate served as a lid with ports for with ports for condenser and an accumulator. The bottom plate comprises the flow channel with ports for temperature and pressure measurements at both ends of the test device. The slot on the surface of the flow channel serves to hold the three layered test section. On the inlet side of the test section, a ceramic heater of capacity 1000W is fitted on to the surface of a copper block to preheat the liquid upstream of the test section, hence providing the required inlet subcooling. The exit of the test section is connected to an accumulator which serves to control the pressure at the exit. The degassing operation was accomplished by heating the fluid in the flow channel using both the pre-heater and the test section heater. The dissolved gases will be vented out through the Graham condenser fitted to the top plate.

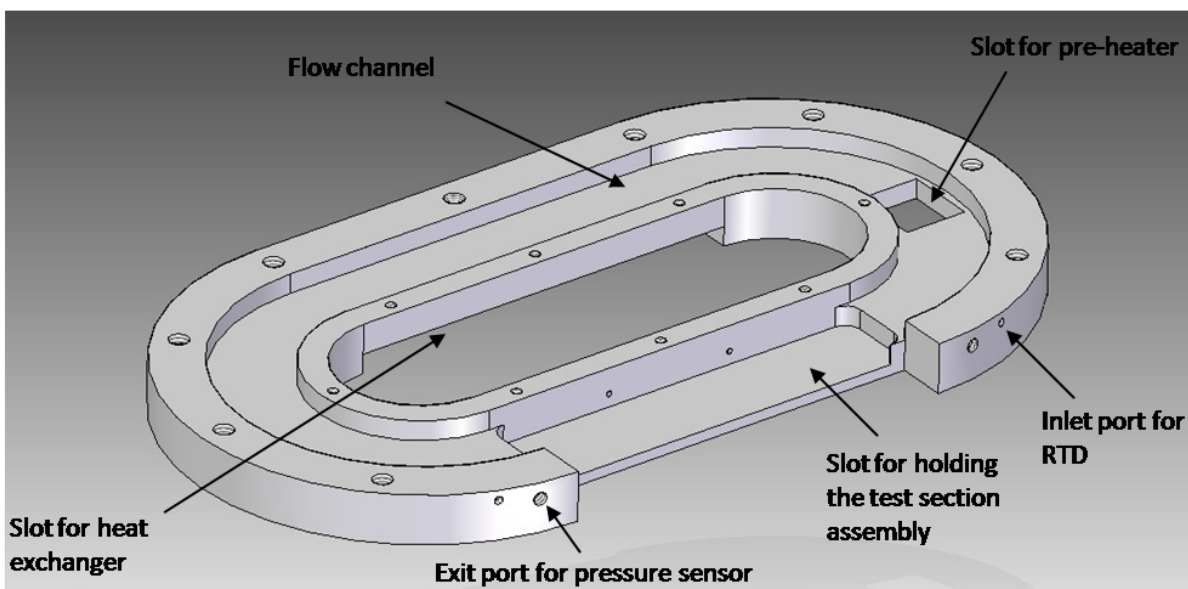


Figure B.1: Bottom plate used in the closed loop experiments with FC-72. The “race-track” is the flow channel in which flow is intended to occur in the clockwise direction.

The silicon test device is the same as the one use for open channel experiments. However, additional layers of a glass plate and a Teflon block of the same footprint as that of the test

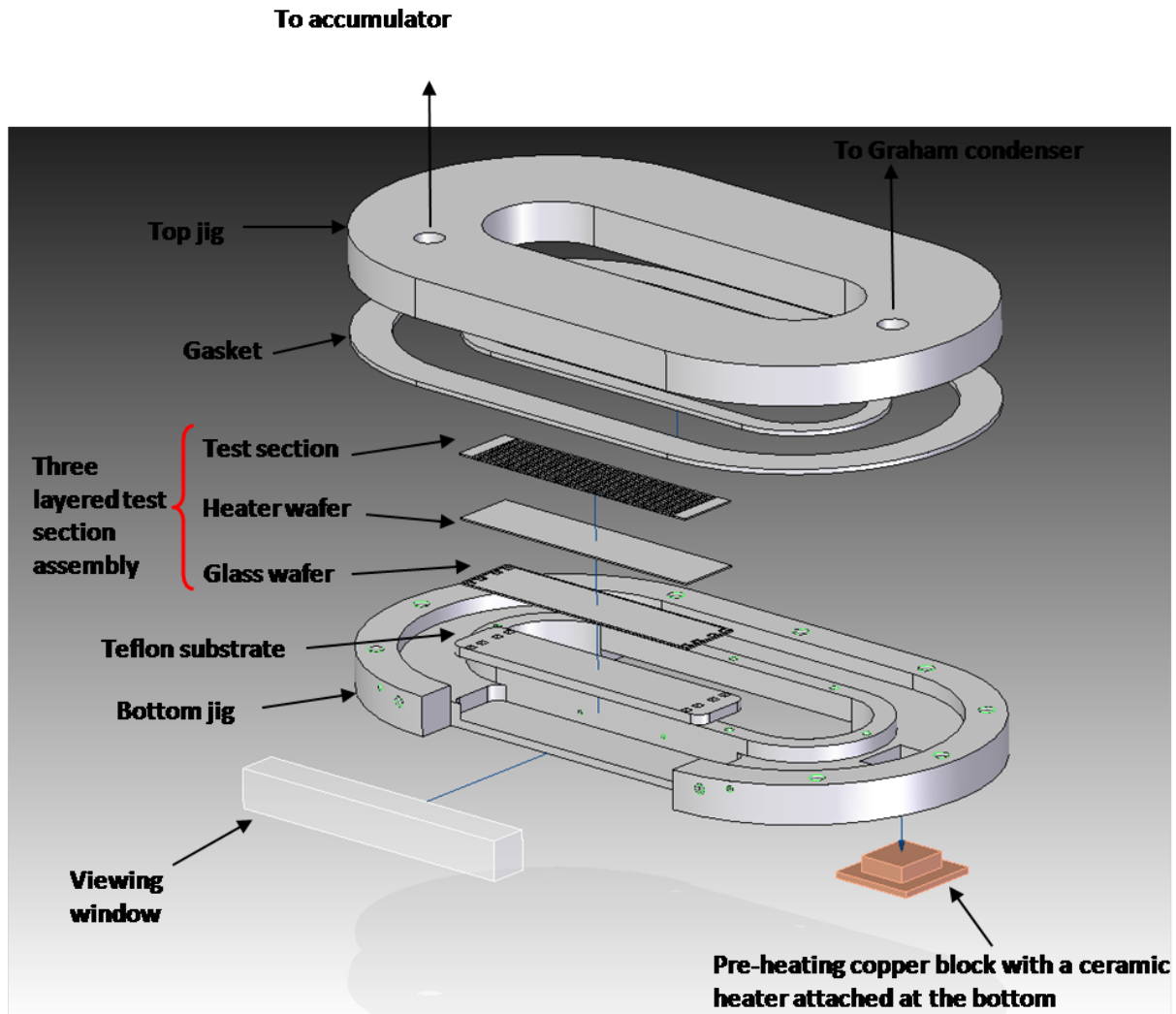


Figure B.2: Assembly of the closed loop experimental set up showing the polycarbonate flow loop and the assembly of the test device.

device were attached. The Teflon layer was added to increase the structural rigidity of the entire test device, and the glass layer acts as an insulator. The three layered test device was mounted on pogo pins that served as electrical contacts. The electrical contacts, in turn were connected to the power supply and NI DAQ. An assembled view of the experimental set up is shown in Fig. B.2. The flow loop is schematically represented in Fig. B.3

In the experiments conducted with the closed flow loop held at close to 0, an interesting phenomena was noticed which actually caused a net flow although in the direction opposite to the intended direction.

As the power supplied to the test section was increased, the vapor cloud over the test device increased as illustrated in Fig. B.4. As the growth increased, the liquid vapor interface on the left reached the condenser and stopped growing. But the interface on the right continued its growth to the right of the test device and reached the subcooled pool of liquid

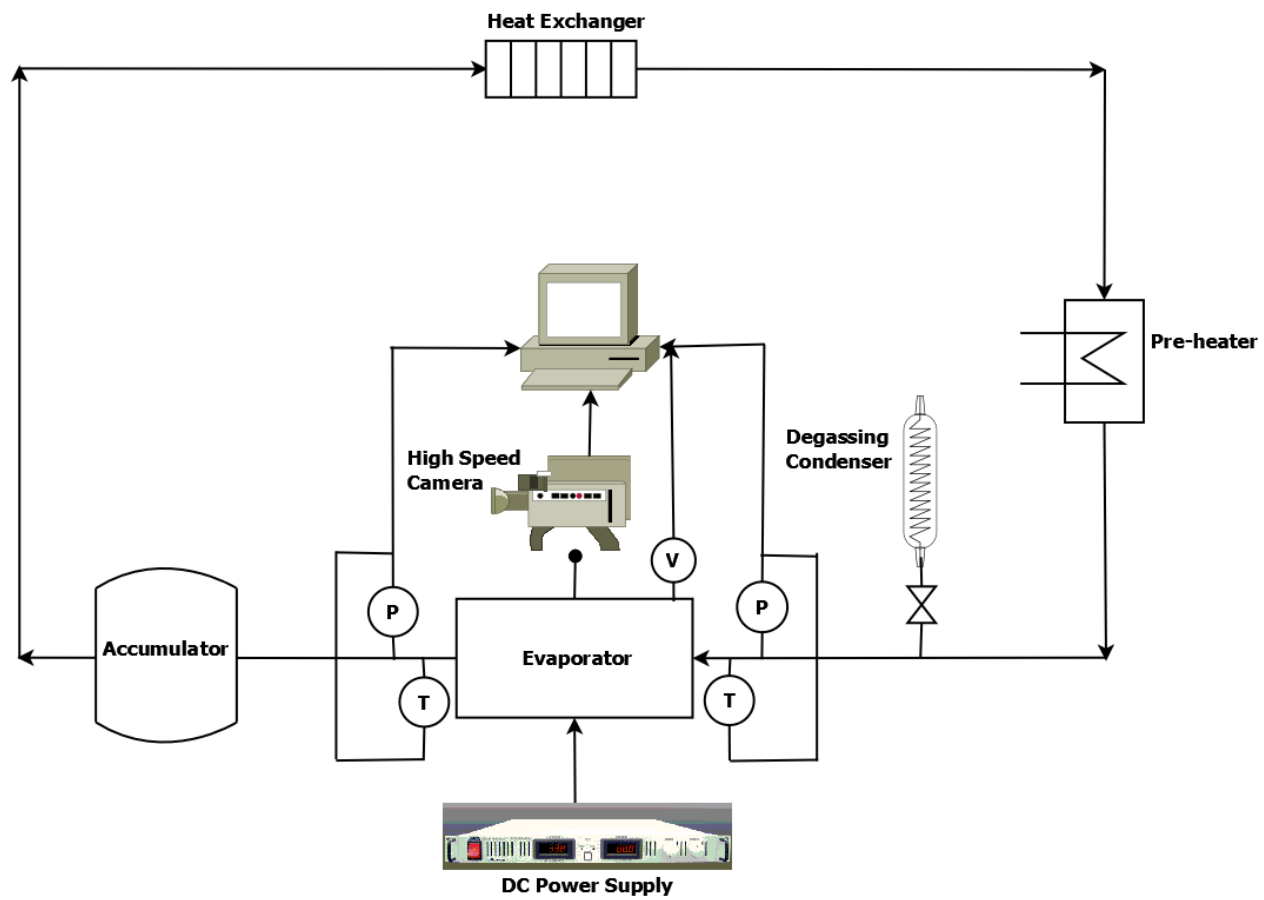


Figure B.3: Schematic representation of the closed flow loop used in the study.

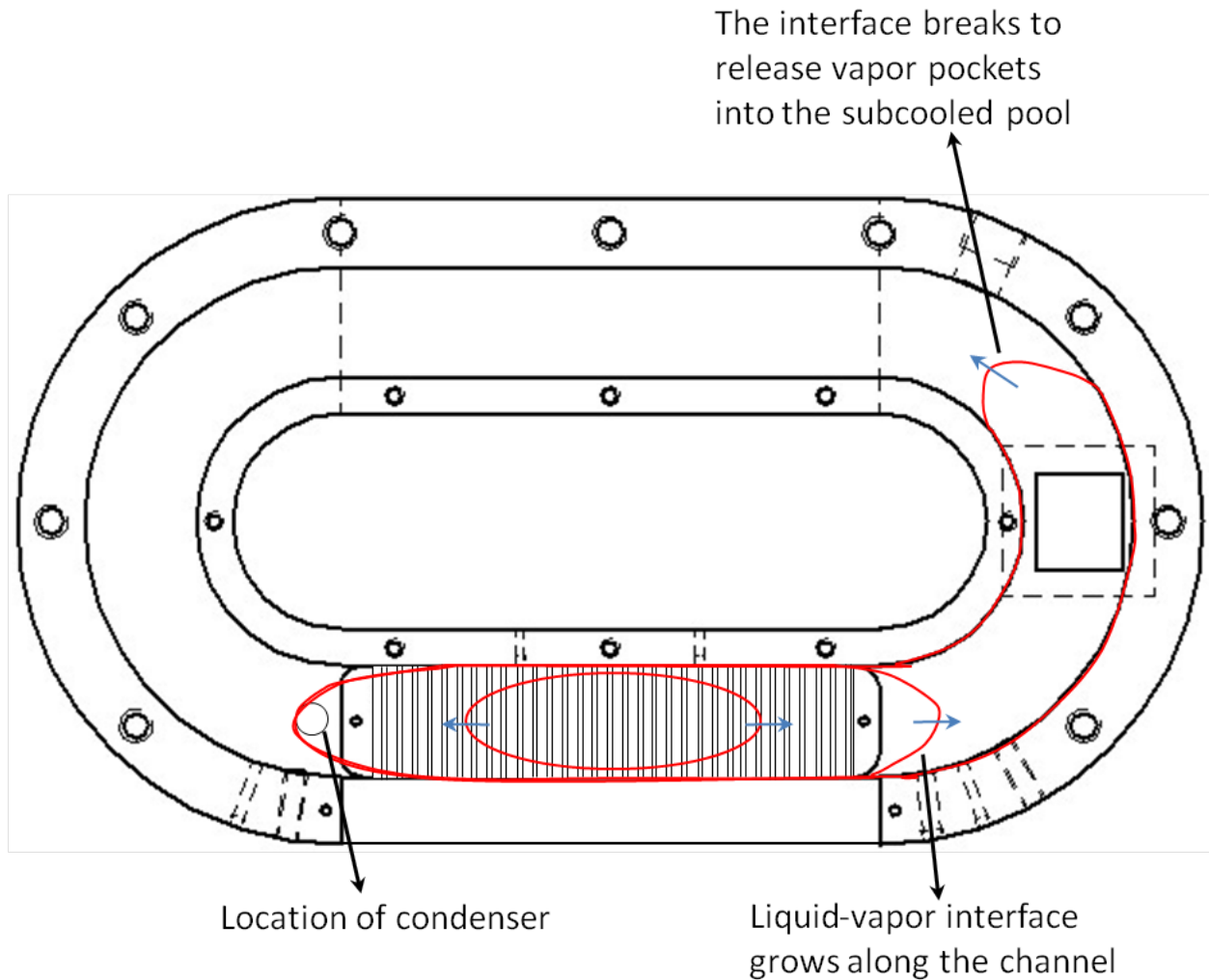


Figure B.4: Schematic representation of the net flow effected mainly by the condenser location.

on the other side of the flow track. This resulted in the condensation of vapor on the other side of race-track, where the liquid-vapor vapor blanket breaks in to smaller bubbles that circulate in an anti-clockwise direction. As the supplied power increased this mechanism increased in strength and frequency and resulted in a net flow as the vapor pockets reached the condenser by flowing in a counter clockwise direction.

However even as this mechanism existed, a portion of vapor over the test device also moved to the left into the condenser, but there is nothing to suggest that this was being caused by the bubbles departing at an angle. The flow was mainly dictated by the position of the condenser. By shifting the condenser to the other side of the condenser, flow in the opposite direction, clockwise, was achieved. However, as seen in all the previous experiments conducted in a chamber in an open channel, the bubbles departed at an angle normal to the saw-teeth.

Appendix C

Calibration of Sensors

This section discusses the calibration of sensors used in the experiments and the associated uncertainty in the measurements.

C.1 Calibration of thermistor and thermocouple

An Omega thermistor ON44007 was used in the experiments for pool temperature measurements and a K-type thermocouple was used for the measurement of heat loss from the back of the test section. Both sensors were calibrated using an NIST certified thermistor as a standard in an oven, where the temperature was periodically increased from room temperature to 80°C. The calibration plot from the experiment is shown in Fig. C.1.

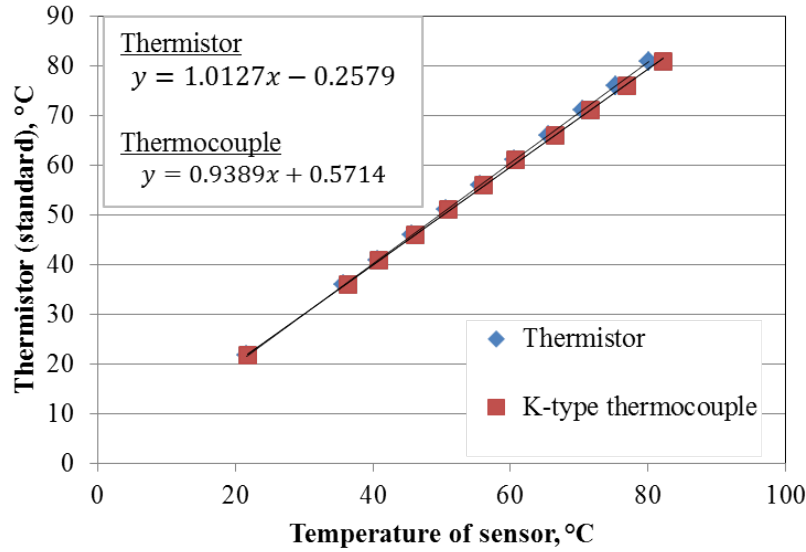


Figure C.1: Calibration of Omega ON44007 thermistor and a K-type thermocouple using a NIST certified thermistor as a standard

From Fig. C.1, the calibration equations for thermistor and K-type thermocouple are,

$$T_{std,thermistor} = 1.0127T_{thermistor} - 0.2579 \quad (C.1)$$

$$T_{std,thermistor} = 0.9389T_{thermocouple} + 0.5714 \quad (C.2)$$

Based on the calibration equations, the experimental uncertainty [58] can be expressed as,

$$U_a = \pm t_{\alpha/2, \nu} \frac{S_{y/x}}{S_{xx}} \quad (\text{C.3})$$

where,

$$\begin{aligned} \pm t_{\alpha/2, \nu} &= \text{student T-distribution} \\ S_{y/x} &= \text{data's vertical standard deviation about the fitted line} \\ S_{xx} &= \text{mean horizontal variation of data} \end{aligned}$$

The uncertainty values were estimated to be $\pm 2.12\%$ and $\pm 1.81\%$ in the thermistor and thermocouple, respectively.

C.2 Calibration of test section heater

As discussed in chapters 2 and 3, the aluminum serpentine heater also serves as a temperature sensor by using the resistance measurement from the heater. This is made possible since the resistance of the current carrying material is a function of temperature. Resistance can be estimated by measuring the voltage from the heater and the current supplied (50 mA) using an ammeter. The calibration was performed using an NIST certified thermistor as a standard, in an oven where the temperature was periodically increased from room temperature to 85°C in 5°C increments. The calibration plot from the experiment is shown in Fig. C.2.

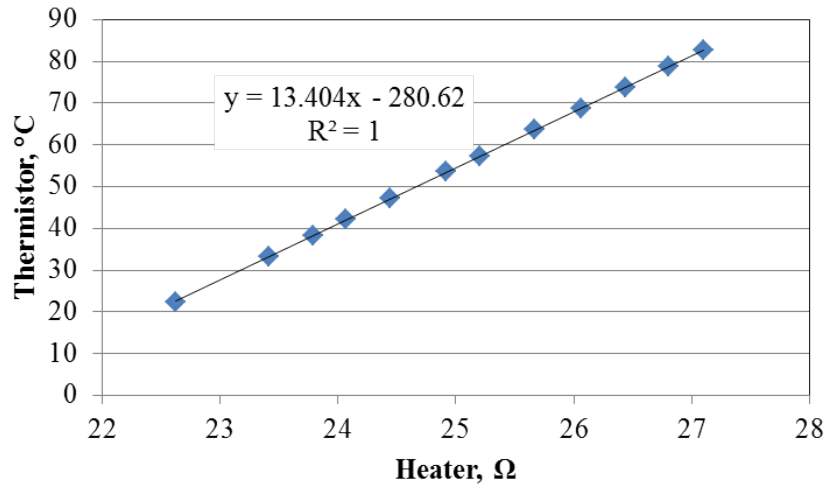


Figure C.2: Calibration of test section heater using a NIST certified thermistor as a standard

From Fig. C.2, the calibration equation for the heater is,

$$T = 13.404R_{heater} - 280.62 \quad (\text{C.4})$$

where,

$$T = \text{Temperature, } ^\circ\text{C}$$

$$R_{heater} = \text{Resistance of heater, } \Omega$$

Based on the calibration equations, and the procedure stated previously in the calibration of temperature sensors, the uncertainty in heater temperature measurement is estimated to be $\pm 6.4\%$ of measured temperature.

C.3 Calibration of hot wire anemometer

Hot wire anemometer was used in the experiments to estimate the net lateral liquid velocity of the surface. Hot wire anemometer involves the use of a probe which is maintained at a constant temperature. When the probe is immersed in a liquid, the heat transfer from the probe causes a change in the bridge output of the anemometer which is a measure of liquid velocity. While it is a relatively simple process to calibrate the probe for use in air, the calibration for use in a fluid such as FC-72 was extensive and required building a separate flow loop as shown in Fig. C.3.

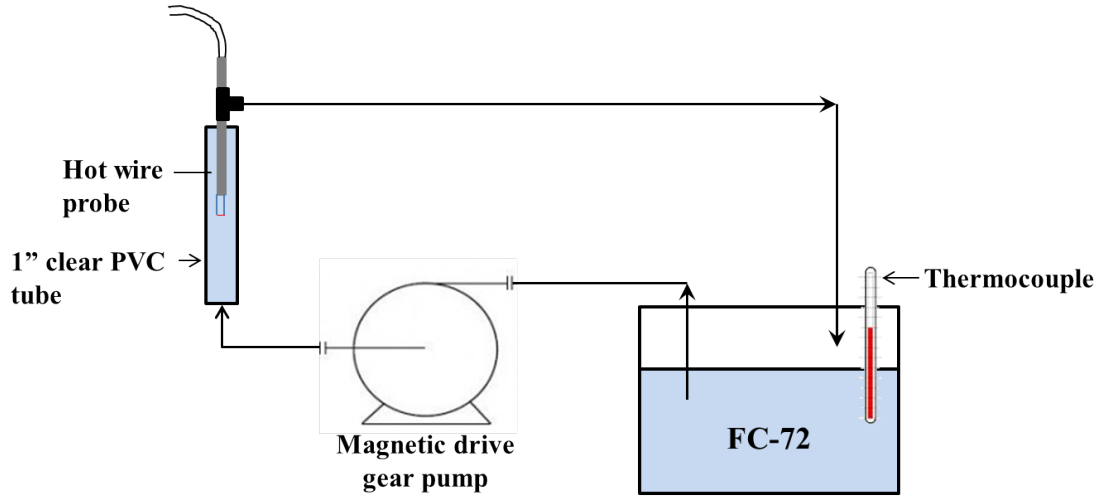


Figure C.3: Flow loop for the calibration of hot wire probe

The probe used in the experiment is TSI 1210-20 and the pump's meter is used as the known velocity of flow. Velocity was increased periodically from 1 mm/s to 130 mm/s and the output from hot wire anemometer was sent to the data acquisition system.

From Fig. C.4, the calibration equation for the hot wire anemometer probe is,

$$v = 0.1521V_{HWA}^4 - 1.0704V_{HWA}^3 + 2.8182V_{HWA}^2 - 3.2705V + 1.4083 \quad (\text{C.5})$$

where,

$$v = \text{velocity, } m/s$$

$$V_{HWA} = \text{voltage output of anemometer, } V$$

Based on the calibration equation, the estimated uncertainty is 0.2% of the measured velocity.

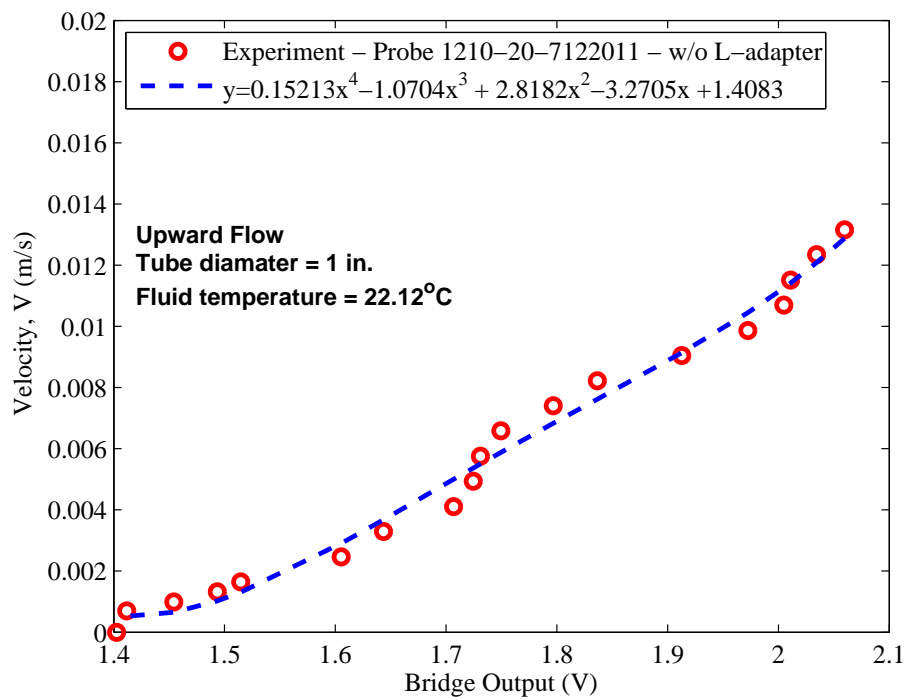


Figure C.4: Flow loop for the calibration of hot wire probe

Appendix D

Emperical Model for Lateral Liquid Velocity in Nucleate Boiling

From chapter 3, it is evident that the asymmetry in surface cross-section and location of re-entrant cavities results in bubble growth and departure to take place at an angle, approximately, normal to the shallow slope of the ratchet. It was earlier hypothesized, that such angled growth and departure leads to an angular momentum imparted to the adjacent liquid, which in turn leads to a net lateral liquid velocity. Based on the available data for bubble dynamics such as growth rate and bubble departure frequency, an expression for the net lateral liquid velocity was derived [57] by estimating the momentum imparted by the growth of the vapor bubble while being attached to the re-entrant cavity on the sloped surface as illustrated in Fig. 3.15a. The drag force due to bubble growth, F_g , can be estimated as,

$$-\vec{F}_g = \frac{d\vec{P}_l}{dt} = \frac{1}{8}\pi\rho_l C_D D^2 \left(\frac{dD}{dt}\right)^2 \quad (\text{D.1})$$

where,

$$\begin{aligned} \vec{F}_g &= \text{force due to bubble growth} \\ \vec{P}_l &= \text{momentum imparted to the liquid} \\ \frac{dD}{dt} &= \text{bubble growth rate} \\ C_D &= \text{co-efficient of drag} = \frac{24}{\text{Re}} \end{aligned}$$

For the model, the entire surface of the the heat sink is divided into equal number of regions, with each region representing an area around the mouth of a single re-entrant cavity as shown in Fig. 3.15b. The volume projected by this area will be treated as the control volume for the analysis.

By re-arranging Equation D.1, the momentum imparted by the bubble is estimated for a bubble growth cycle starting with nucleation at time, $t = 0$, to the time frame penultimate to bubble departure, $t = t_d$, as shown in Equation D.2 The bubble diameter, D , in Equation D.2 is the average diameter of bubble in successive time frames, and $\frac{dD}{dt}$ is the experimental bubble growth rate.

$$\left|\vec{P}_l\right| = \frac{1}{8}\pi\rho_l \sum_{i=t_0}^{i=t_d-1} C_D \left(\frac{D_i + D_{i+1}}{2}\right)^2 \left(\frac{D_i - D_{i+1}}{dt}\right)^2 dt \quad (\text{D.2})$$

where,

$$\begin{aligned} t_0 &= \text{time at bubble inception} \\ t_d &= \text{time at bubble departure} \\ D &= \text{average bubble diameter} = \frac{D_i + D_{i+1}}{2} \\ \frac{dD}{dt} &= \text{bubble growth rate} = \frac{D_i - D_{i+1}}{dt} \end{aligned}$$

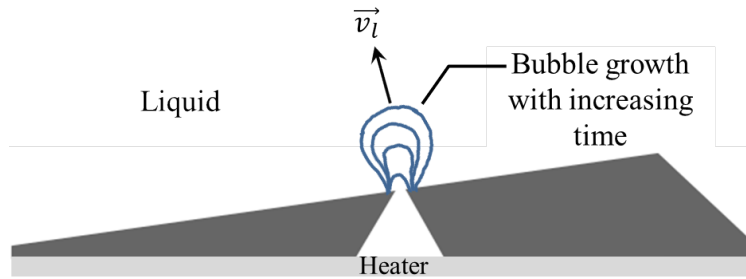


Figure D.1: Illustration of the angular momentum imparted by a growing bubble normal to the shallow slope, leading to a net lateral liquid velocity

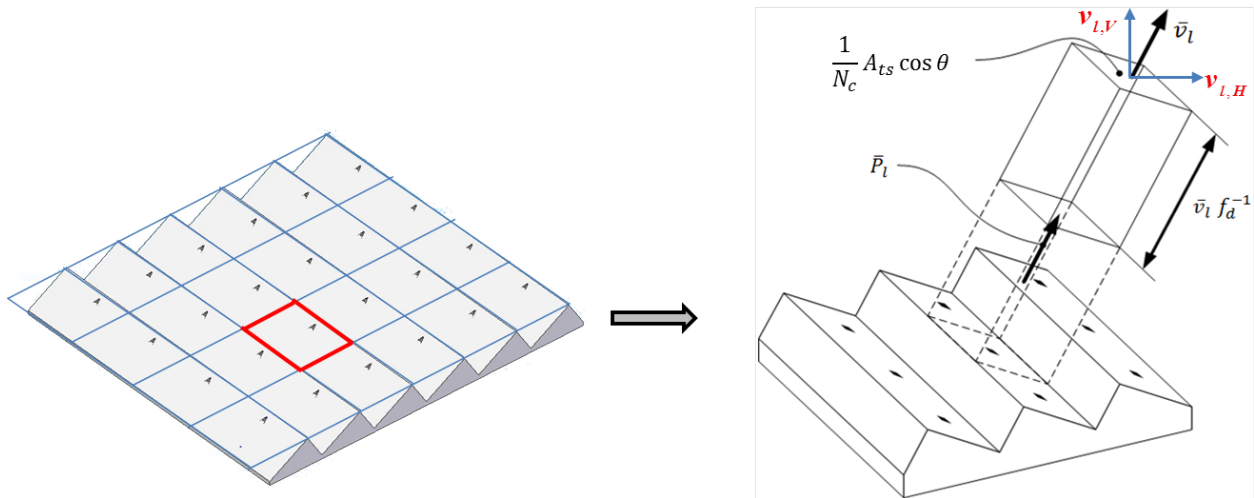


Figure D.2: Control volume defined for estimation of resulting net lateral liquid velocity due to bubble growth at an angle normal to the shallow slope of the ratchet

Momentum imparted to the liquid for the control volume shown in Fig. 3.15 can be expressed as,

$$\vec{P}_l = m_l \vec{v}_l = \left(\rho_l \frac{A_{ts}}{N_c} \cos \theta \vec{v}_l f_d^{-1} \right) \vec{v}_l \quad (\text{D.3})$$

where,

$$\begin{aligned} A_{ts} &= \text{area of footprint of the test section} \\ N_c &= \text{number of cavities} \\ \theta &= \text{angle of saw - tooth} \\ f_d &= \text{bubble departure frequency} \\ \vec{v}_l &= \text{net liquid velocity} \end{aligned}$$

Using Equations D.2 and D.3, the equation D.4 for net liquid velocity is expressed as,

$$\vec{v}_l = \sqrt{\frac{N_c \pi f_d}{8 A_{ts} \cos \theta} \sum_{i=t_0}^{i=t_d-1} C_D \left(\frac{D_i + D_{i+1}}{2} \right)^2 \left(\frac{D_i - D_{i+1}}{dt} \right)^2 dt} \quad (\text{D.4})$$

From the above equation, the net lateral or horizontal component of liquid velocity is

$$v_{l,H} = \vec{v}_l \cos(90 - \theta) \quad (\text{D.5})$$

Pool boiling experiments using water on a small array test device was conducted by the research group at Oregon State University [57]. Using the above equation, net horizontal lateral liquid velocities of 7 mm/s and 18 mm/s were estimated for low and high subcooling cases, respectively. These velocities were compared with experimental observation of bubbles during nucleate boiling from the asymmetric structure. It was observed that the bubble growth and departure from the re-entrant cavities were asymmetric in nature. As the bubbles departed in to the subcooled pool, the volume of bubbles reduced significantly. These small bubbles in the far-field, known as plume bubbles, were observed to be moving horizontally. It was hypothesized that the lateral motion of the far-field bubbles were effected by the asymmetric growth of bubbles on the surface. The experimentally observed velocities of the plume bubbles were between 30 and 70 mm/s. Since, the velocities predicted by the model were close to the experimentally observed plume bubble velocity, it was inferred that, asymmetric bubble growth is a primary force in effecting lateral motion of liquid in its vicinity.

Appendix E

Particle Image Velocimetry (PIV)

Particle image velocimetry (PIV) is an optical technique to measure fluid flow. In PIV, fluid is seeded with particles which are imaged at two instances of time. By estimating the displacement of the particles, the instantaneous velocity of the flow can be measured, provided the selected tracer particles track the flow adequately [59]. A schematic arrangement of a PIV system is shown in Fig. E.1, which illustrates the sheet of light formed by a laser used for illuminating the seeding particles. The image of the light reflected from the particles is recorded using a digital camera which is synchronized with the laser.

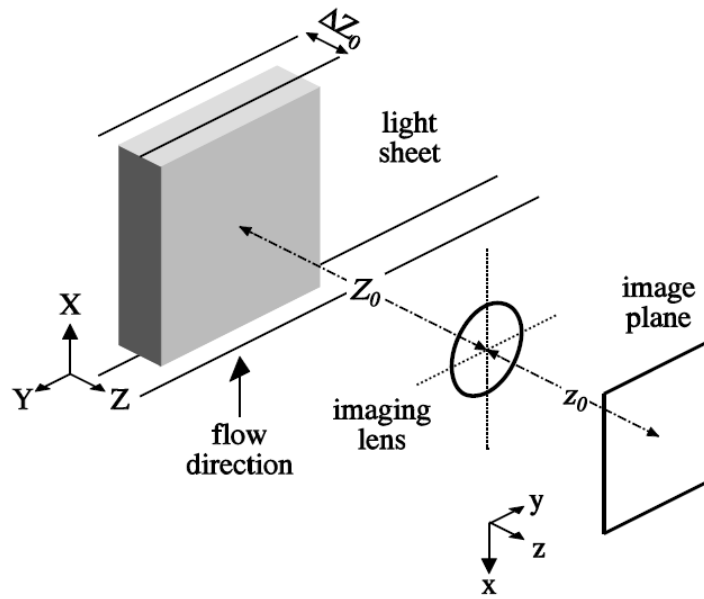


Figure E.1: Illustration of a PIV system showing the laser sheet that is used to illuminate the particles. The image of the particles is recorded at two time instances using a camera to measure velocity [59]

Since the measured fluid velocity using this technique is that of the particle velocity, it has to be determined that the particles follow the flow. Particles in a flow can be influenced by gravitational forces if the density of particles and density of the fluid are different. Difference in densities will cause the particles to settle or rise in a fluid. The settling velocity can be expressed as,

$$V_{\text{settling}} = \frac{2R^2 (\rho_p - \rho_f) g}{9\mu} \quad (\text{E.1})$$

where,

$$\begin{aligned} V_{\text{settling}} &= \text{settling velocity of tracer particles, } m/s \\ R &= \text{mean radius of tracer particles, } m \\ \rho_p &= \text{density of tracer particles, } kg/m^3 \\ \rho_f &= \text{density of fluid, } kg/m^3 \\ g &= \text{acceleration due to gravity, } m/s^2 \\ \mu &= \text{viscosity of fluid, } Ns/m^2 \end{aligned}$$

In chapter 3, liquid velocity measurements using hot wire anemometry showed that asymmetric bubble growth and departure can, potentially, induce net lateral velocities of liquid of up to 6 mm/s. In the current study, PIV is used to measure the flow field of liquid in the immediate vicinity of the bubbles growing and departing at an angle normal to the surface. Measured velocities will be used to corroborate the results from hot wire anemometry. The PIV system used in the current system consists of a dual ND:YAG 532 nm, 200 mJ, pulsed laser that is used to produce a laser sheet to illuminate the particles. The imaging system consists of a PowerView Plus (Model no. 63002) 11 megapixel camera with a pixel resolution of 4008 x 2672, pixel size of 7.4 μm x 7.4 μm , and a 12-bit output. Silver coated hollow glass particles with a mean diameter of 14 μm , and a specific gravity of 2.2, were used as tracer particles. The settling velocity of these particles in FC-72 calculated using Eq. E.1 is 5.4 $\mu\text{m/s}$.

The boiling chamber used is made up of 2 inch x 2 inch borosilicate glass as shown in Figures E.2 and E.3. The borosilicate glass tube containing FC-72 was covered by a polycarbonate lid at the top with ports for various sensors used. A thermistor was used for pool temperature measurements, and a cartridge heater was used for heating the fluid. A central port was used to connect a Graham condenser for condensing the FC-72 vapor. One of the ports was also used for introducing the tracer particles and another port was used for thermocouples that were used for heater temperature measurements. The heater used is cartridge type, 50 W, 3.17 mm diameter, and 31.7 mm in length. The heater was enclosed in a copper block of 7.9 mm square cross-section, and power to the heater was controlled using an AC variac. The copper block was equipped with three 1 mm holes for thermocouples that are spaced equidistantly, and the temperature measurements were used to calculate the applied heat flux. The copper heating block was covered by a 19.0 mm diameter Teflon block that serves in promoting one-dimensional heat transfer through the copper block, by insulating the sides. A small array silicon test device with a saw-tooth angle of 24° was fixed to the surface of the copper block using a colloidal silver paste.

Before the PIV experiment, the pre-processor, processor, and post processor settings were adjusted in the software, Insight 4G. In the pre-processor settings, image calibration was performed to convert pixel values to mm using the distance between the peaks of the saw teeth. Also, an image mask was applied to set the processing area to cover the region right over the test section. In the processor settings, the size of the interrogation window was set to be 128 pixels x 128 pixels. Post-processor settings were adjusted to display the velocity vector statistics. During the experiment, the laser was triggered from the software in a continuous mode to align the laser sheet with the test section. During the alignment process, the aperture of the camera was adjusted to remove any light saturation in the captured images. Once the camera was aligned, the laser was triggered in a single mode in

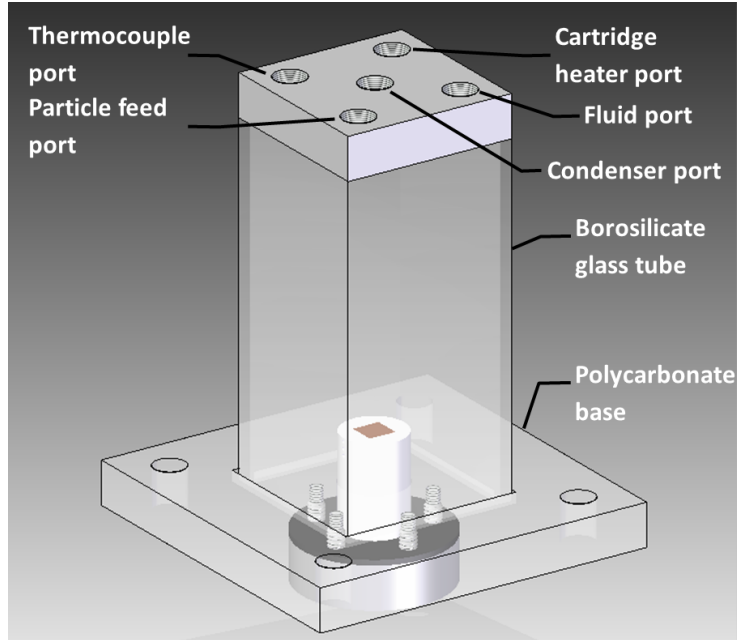


Figure E.2: Assembled view of the PIV chamber - basic parts include borosilicate glass chamber, and a top polycarbonate lid with ports for sensors

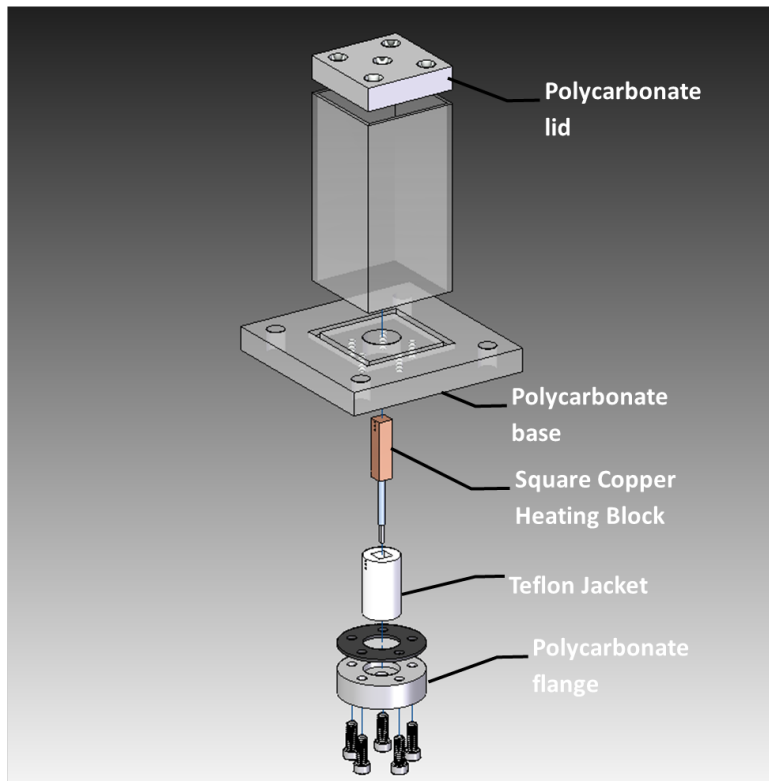


Figure E.3: Exploded view of the PIV chamber showing the assembly of the copper heating block, borosilicate glass chamber, and a top polycarbonate lid with ports for sensors

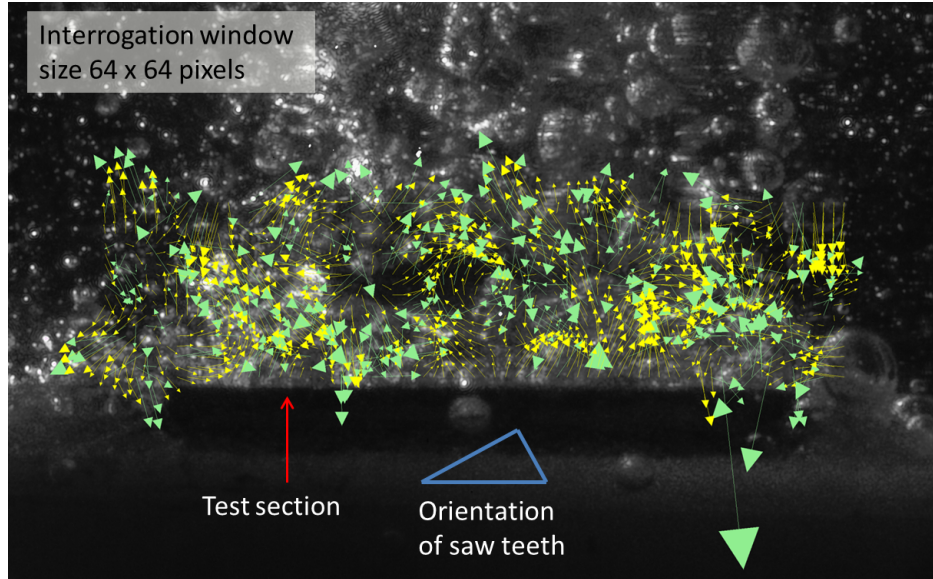


Figure E.4: Velocity vectors obtained from a PIV experiment that are overlaid on top of the captured image. In this image, the shallow long slopes of the saw teeth face towards the left side of the image, and any expected flow due to asymmetric bubble growth will be from right to left in the image. Vectors colored in green and yellow represent measured and interpolated velocities, respectively.

which the laser is pulsed twice between a set time interval (in this case $10,000 \mu\text{s}$) to obtain a set of two images. The captured images were processed to obtain the velocity vectors in the fluid. Fig. E.4 shows the obtained velocity vectors overlaid on top of the captured image, and Fig. E.5 shows the magnitude of velocity. The color chart indicates the velocity in m/s. In the images, saw teeth were oriented with the shallow long slope facing the left side of the image and the expected liquid flow direction is from right to left in the image.

From the figures, while liquid velocities of up to 17 mm/s were observed, the velocity vectors were scattered in different directions. Hence, no inference could be made about the effect of asymmetric bubble growth on the liquid flow around the bubble. The scatter in vectors can be caused due to multiple factors:

- Particles used in the study were reflective in nature. In two-phase processes, bubbles reflect the light significantly, and hence distinction between the light from the particles and bubbles is very difficult. To avoid this problem in PIV for two-phase flows, fluorescent particles with a 532 nm lens filter for the camera is often used. While such a system was tested in the current study, finding fluorescent particles of a specific gravity value that matches the specific gravity of FC-72 was difficult. Hence, PIV using fluorescent particles of specific gravity 1.2 did not yield good results.
- Although efforts were taken to eliminate bubbles from the edge of the test section, there were a few bubbles nucleating from locations other than re-entrant cavities on the saw-toothed surface which could alter the flow around the bubbles nucleating from cavities. To get an accurate measure of the flow field around the bubble, it is important to have

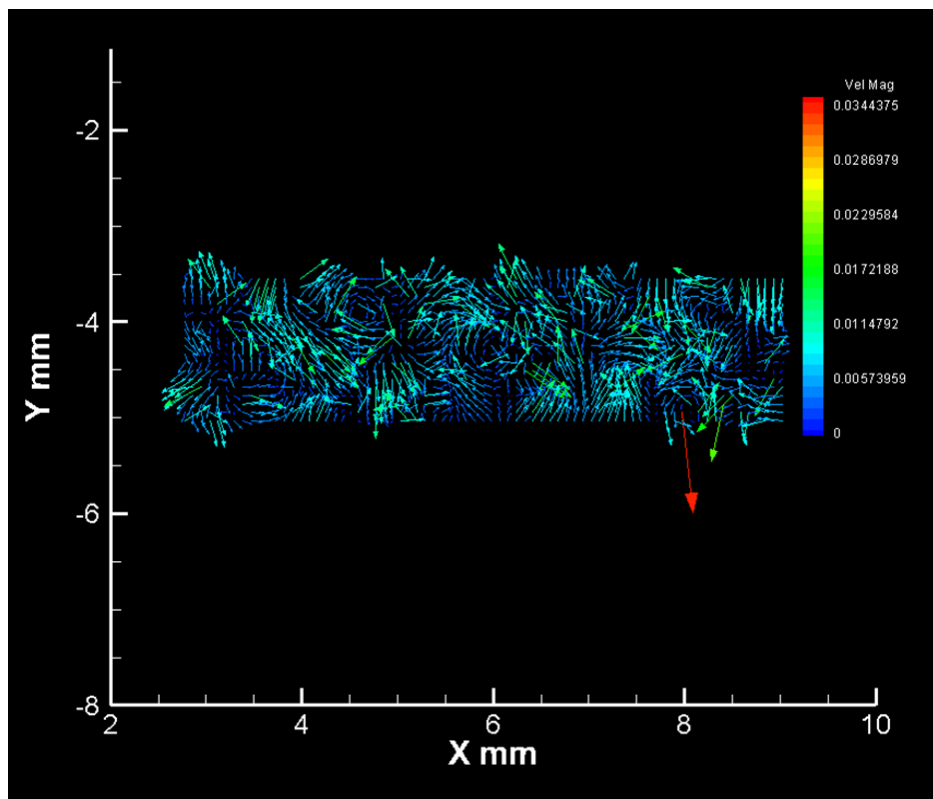


Figure E.5: Magnitude of velocity vectors obtained from the PIV experiment. Color chart indicates liquid velocities of up to 17 mm/s, although scattered in different directions

just one single nucleating bubble, which is a very difficult objective to accomplish during phase-change.

Appendix F

Microgravity Experiments: Test Equipment Data Package (TEDP)

Design of pool boiling experiments that were conducted aboard Zero-g flight required strict adherence to mechanical, electrical and fluid containment guidelines. Structurally, every joint and load bearing member of the structure required a factor of safety of at least 4 for load conditions of up to 9g. This required a thorough structural analysis of the structure using ANSYS and the factor of safety was calculated based on the stresses calculated at every joint and structural member. Some of the electrical design guidelines include the design of an emergency stop for every current drawing device on the set up and adherence to proper wiring and grounding procedures. Since the experiments involved the use of fluids, the experimental setup had to be double contained to prevent any fluid leak in to the aircraft cabin. Also, any drop in cabin pressure could cause the welded joints of aluminum boiling chamber to leak due to the increase in pressure differential. Hence, pressure testing of the boiling chamber was performed to withstand a pressure differential of up to 12 psi between the inside and outside of the boiling chamber.

Prior to experimentation aboard the aircraft at Johnson Space Center, a document consisting of all the design data, structural analysis, electrical design and experimental procedures, known as the Test Equipment Data Package (TEDP) was submitted for approval, which was tested against the actual set up for conformance to design specifications. This section includes the submitted version of TEDP to the Reduced Gravity Program at NASA Johnson Space Center.

Fluid Lateral Motion using Surface Microstructures-Channel Flow from a Large Array

Test Equipment Data Package

4/27/2012



DEPARTMENT OF MECHANICAL ENGINEERING
AUBURN UNIVERSITY

Sushil H. Bhavnani
Principal Investigator
Professor, Mechanical Eng.,
Auburn University, AL - 36849.
bhavnsh@auburn.edu

Naveenan Thiagarajan
Author
Doctoral Candidate
Mechanical Eng.,
Auburn University, AL - 36849
thiagna@auburn.edu

CHANGE PAGE

Revision	Description of changes	Date
TEDP-1.0	Initial release	02/27/12
TEDP-2.0	Updated release after review of initial release	03/13/12
TEDP-3.0	Updated release incorporating joint structural analysis, grounding method, and other minor changes	04/06/12
TEDP-4.0	Updated structural analysis for the LCD monitor	04/12/12
TEDP-5.0	Added structural analysis for DAQ, power strip and keyboard docking tray and updated overall weight. Flight manifest has been updated. Camera assembly to be stowed during take-off and landing. Weight of the equipment frame has been updated and structure analysis on the floor attachment has been modified to reflect this.	04/27/12

QUICK REFERENCE DATA SHEET

Principal Investigator: Prof. Sushil H. Bhavnani

Contact Information: bhavnsh@auburn.edu, (334) 844-3303

Experiment Title: Boiling Heat Transfer Mechanism During Thermally Actuated Pumping by Asymmetric Surface Structures

Work Breakdown Structure (WBS):

Flight Date(s): April 30th – May 4th, 2012

Overall Assembly Weight: 205.64 [lbs.] (187.64 lbs during take-off and landing)

Assembly Dimensions (L, W, H): 26.0, 40, 48 [in]

Equipment Orientation Requests: None

Proposed Floor Mounting Strategy (Bolts/Studs or Straps): Bolts (AN-6)

Gas Cylinder Requests (Type & Quantity): No

Overboard Vent Request (Yes or No): No

Power Requirement (Voltage and current required): 220VAC and 10A; 115 VAC and 20 A, see the electrical analysis section for power breakdown.

Free Float Experiment (Yes or No): No

Flyer Names for Each Proposed Flight Day: Prof. Sushil Bhavnani, Naveenan Thiagarajan, and Travis Wheeler on all flight days

Camera Pole and/or Video Support: No

TABLE OF CONTENTS

1.	FLIGHT MANIFEST.....	1
2.	EXPERIMENT BACKGROUND.....	1
3.	EXPERIMENT DESCRIPTION.....	3
4.	EQUIPMENT DESCRIPTION.....	4
5.	STRUCTURAL VERIFICATION.....	14
6.	ELECTRICAL ANALYSIS.....	32
7.	PRESSURE VESSEL/SYSTEM.....	35
8.	LASER CERTIFICATION.....	36
9.	PARABOLA DETAILS & CREW ASSISTANCE REQUIRED.....	36
10.	INSTITUTIONAL REVIEW BOARD.....	36
11.	HAZARD ANALYSIS.....	36
12.	TOOL REQUIREMENTS.....	37
13.	PHOTO REQUIREMENTS.....	37
14.	AIRCRAFT LOADING.....	37
15.	GROUND SUPPORT REQUIREMENTS.....	37
16.	HAZARDOUS MATERIALS.....	37
17.	MATERIAL SAFETY DATA SHEETS.....	38
18.	EQUIPMENT PROCEDURE DOCUMENTATION.....	43
19.	BIBLIOGRAPHY.....	44

1. FLIGHT MANIFEST

Flight One (Day 3): Sushil H. Bhavnani, Naveenan Thiagarajan, and Travis Wheeler

Flight Two (Day 4): Sushil H. Bhavnani, Naveenan Thiagarajan, and Travis Wheeler

2. EXPERIMENT BACKGROUND

Liquid-vapor phase change systems are now being considered as an attractive solution for the heat dissipation problems in modern computers and high power electronics. Several investigations in the last couple of decades have been aimed at providing a solution for the problem of rising demands of heat flux dissipation. Boiling as a mode of high heat flux dissipation can be realized in two different ways, namely, pool boiling which involves heat rejection to a stagnant pool of boiling liquid as in the case of liquid immersion cooling techniques, and flow boiling which involves heat rejection to a liquid flowing in a closed loop such as in a microchannel which has a very high heat dissipation capabilities. However, microchannels are associated with high pumping requirements owing to the high pressure drops associated with flow in narrow passages. This challenge only grows in cases of high power electronics and even more in thermal management of electronics in space since power availability is very limited.

So the challenge remains to be the development of a heat dissipation module utilizing the high heat transfer rates involved in boiling without the pumping requirements involved in a flow boiling system. Such a challenge can be confronted only by the design of a self propelled fluid flow system i.e. a pump-less flow loop, where liquid flow will be thermally induced by vapor bubbles departing from an asymmetric surface.

Studies in the past have shown that liquid flow can be thermally induced by the repeated growth and collapse of a bubble asymmetrically in a tube [1]. Bubble micro-pumps have also been demonstrated where the pumping effect was due to asymmetry in surface tension forces created by the shape of the flow channel [2]. Experiments conducted by Linke et al. [3] demonstrated that in a two-phase film boiling regime, droplet motion as shown in Figure 1 was observed due to the asymmetry of the surface like the one used proposed in this study. However, the droplet motion occurred at Liedenfrost temperatures and the net motion was attributed to the pressure differences in the vapor layer between the droplet and the surface.

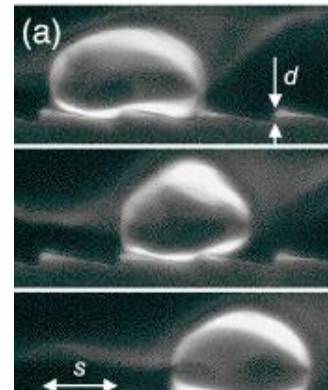


Figure 1: Liedenfrost droplet movement due to surface asymmetry demonstrated by Linke et al. [1]

Hence, from the aforementioned studies it can be understood that surface asymmetry along with controlled ebullition cycle can be effectively used to alter the bubble dynamics to obtain a net pumping effect, so as to develop a pump less flow boiling thermal management device for electronics. The current study derives its inspiration from the work of Linke et al. [3] and pool boiling enhancement using artificial re-entrant cavities [4]. It is hypothesized that surface asymmetry along with controlled nucleation can be effectively used to alter the bubble dynamics to obtain a net pumping effect, so as to develop a pump less flow boiling thermal management device for electronics. Figure 2 shows a schematic of the proposed thermally-actuated, phase-change pumping concept. In the proposed study, surface asymmetry is obtained by use of an array of miniature saw-tooth ratchets and the bubble ebullition cycle is controlled by the use of re-entrant cavities fabricated on one of the sloped walls of the ratchets.

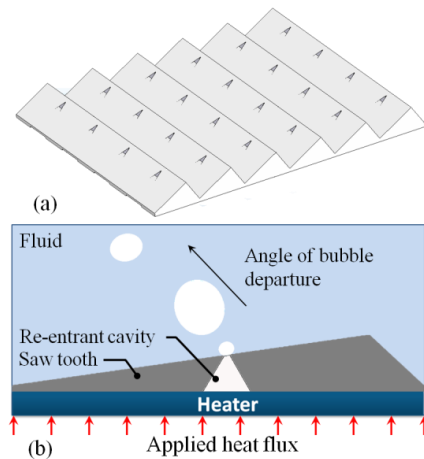


Figure 2: (a) Heat sink structure (b) Schematic representation of the concept

As a first step in the development of such a technique, pool boiling experiments were conducted at 1g with de-ionized water using the test device shown in Figure 2. The surface asymmetry resulted in net force imbalance acting on the vapor bubbles departing from the re-entrant cavities, thereby resulting in bubbles departing at an angle to the vertical with instantaneous velocities in excess of 600 mm/s near the surface [5]. This movement of bubbles demonstrates the significant potential of such a heat sink to be used for thermally actuated pumping of liquids contained in a narrow channel as illustrated in Figure 3 (a) and (b).

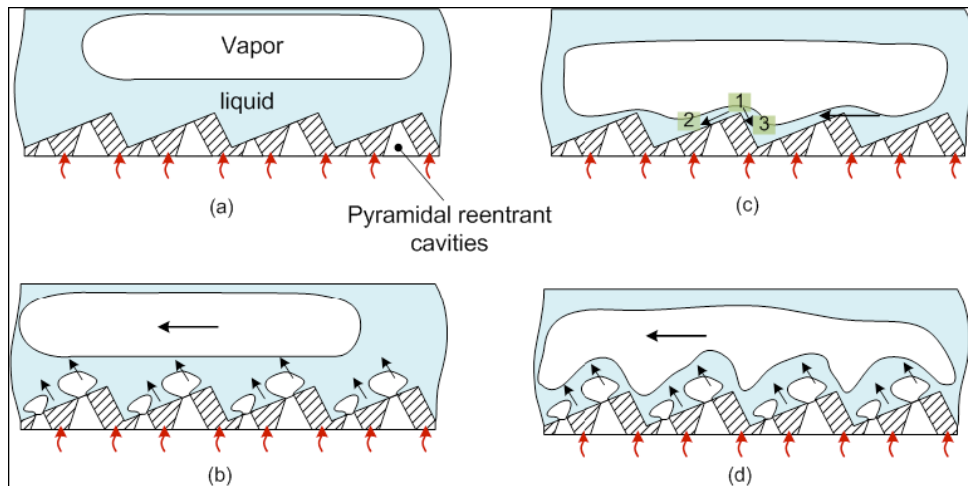


Figure 3: Schematic of the induced flow in (a-b) terrestrial gravity and (c-d) microgravity

One of the primary objectives of the microgravity experiments is to develop and test the effects of surface asymmetry and re-entrant cavities on boiling mechanisms under reduced gravity and analyze the potential of the developed micro phase change heat sinks for space electronics applications. This however requires a better understanding of vapor bubble dynamics under reduced gravity, but due to the complexity of such experiments, literature corresponding to micro gravity experiments and the related bubble dynamics is very limited.

In flow boiling at terrestrial gravity, bubble departure diameter is primarily a function of surface tension (causes the bubbles to remain attached to the surface), drag and buoyancy forces (causes the bubbles to detach from the surface). But at reduced gravity, the forces due to buoyancy are negated and hence the bubble tends to remain at the surface for longer periods and also results in larger bubble departure diameters. This phenomenon was observed by Zhang et al. [6] and Celata [7] in their microgravity experiments performed on FC72. Under such conditions, the vapor slug does not stratify and hence conforms to the shape of the ratchet as illustrated in figure# c and d. The pressure at location 1 is greater than the pressure at 2 or 3, thus resulting in a favorable pressure gradient. Due to asymmetry, and due to the inertial force of the liquid when the cavities are nucleating, the liquid below the slug will cause the vapor slug to move from location 1 to 2. This is similar to the flow of the Leidenfrost droplet observed by the aforementioned study conducted by Linke et al. [3]

3. EXPERIMENT DESCRIPTION

Objective:

The primary objective of the experiment is to study the effects of microgravity on thermally actuated pumping effects in pool boiling on micro-asymmetric structures. High speed imaging will be used to study the bubble dynamics and the recorded temperature and heat flux data will be used to quantify the heat transfer characteristics.

Description:

The asymmetric silicon surface used for boiling will be suspended into a rectangular aluminum sealed boiling chamber containing 13.31 lb of FC72 (boiling point - 56.6°C). The required heat input for boiling the fluid will be supplied using a 220VDC power supply with a maximum required current of 10A. All the boiling experiments will be conducted at 1 atm which will be maintained in-flight using bellows. Thermistors and pressure transducers measure the temperature and pressure inside the chamber. The measured data from the sensors will be recorded using NI Compact DAQ. A Phantom high speed camera will be used to record images of departing bubbles under microgravity. All acquired data will be logged into a computer and the data will be monitored on the mounted LCD display. All the components will be mounted onto a frame built using Aluminum t-slot extrusions.

4. EQUIPMENT DESCRIPTION

Table 1 shows the physical dimensions and weight of all the components and assemblies used in the experiment.

Table 1: Physical properties of experimental equipment

Equipment	Physical Dimensions (H, W, D) [in]	Weight [lbs.]
Equipment Frame	48.0 x 26.0 x 38.625	44.53
Power Supply	3.94 x 17 x 16.94	29.37
Data Acquisition System (DAQ)	2.3 x 6.28 x 3.5	2.26
Boiling Chamber (incl. weight of fluid, and other accessories)	8.75x 13 x 9	34.50
Bellows Assembly	6 Diameter x 18 Height	6
Outer Containment	33 x 24 x 9	18.50
High Speed Camera	5.5 x 12.25 x 5	12
Microscope lens	9.436	3.5
Lights		1.32
Emergency kill switch	4.75 x 11.5 x 11.5	9.92
CPU	13.25 x 4 x 14.94	7.32
Monitor	12.7 x 20.5 x 1.8	7.1
Power strip	12.5 x 2.5 x 1.5	1.45
Keyboard tray	2 x 13.3 x 21.8	2.76
	Total	205.64
	Total (without camera assembly)*	187.64

*Represents the actual weight during take-off and landing as the camera assembly will be stowed

Equipment Frame

The support structure for the experiment was assembled using Aluminum t-slot extrusions. All the electrical and electronic equipments required for the experiment will be mounted onto this support structure shown in Figure . The vectors marked in the figure represent the forces acting at the center of mass of the frame. The physical dimensions of the structure are 26 x 38.625 x 48 in (L x W x H). The space required around the structure for operations during the experiment has been marked in Figure 5. The structure will be mounted on to the aircraft floor using six AN-6 bolts using the floor attachment hardware as shown in Figure 6. The floor attachment hardware will be attached to the structure at six points configured in a 20 x 20 in. fashion. The structure is also equipped with steel handles along the length on both the sides which will be used to load and unload the structure. The various components attached to the equipment frame include the boiling chamber with the

outer fluid containment box, a power supply, data acquisition system, camera, computer and a monitor for data visualization.

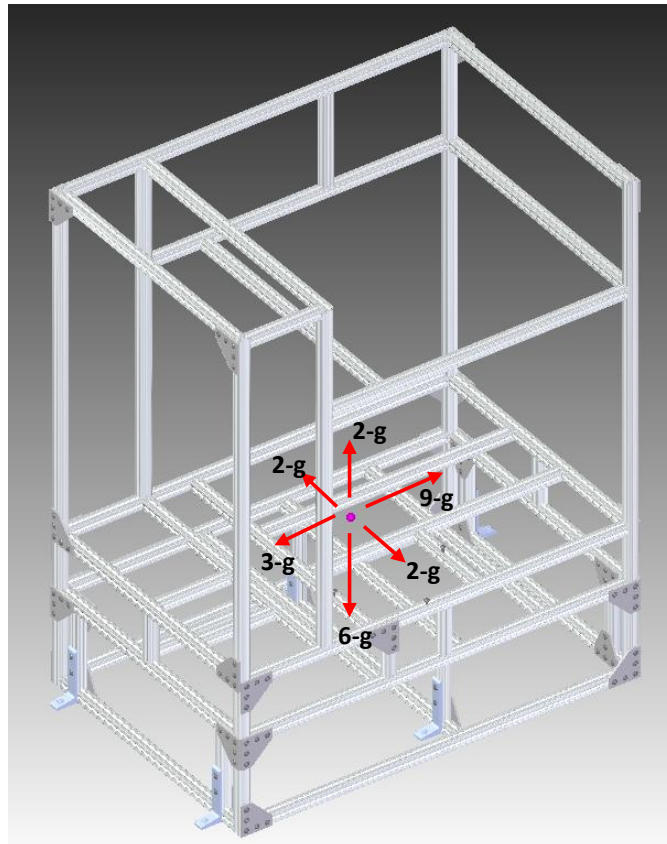


Figure 4: Equipment frame and the forces acting. 9g represents the forward force in the direction of the aircraft.

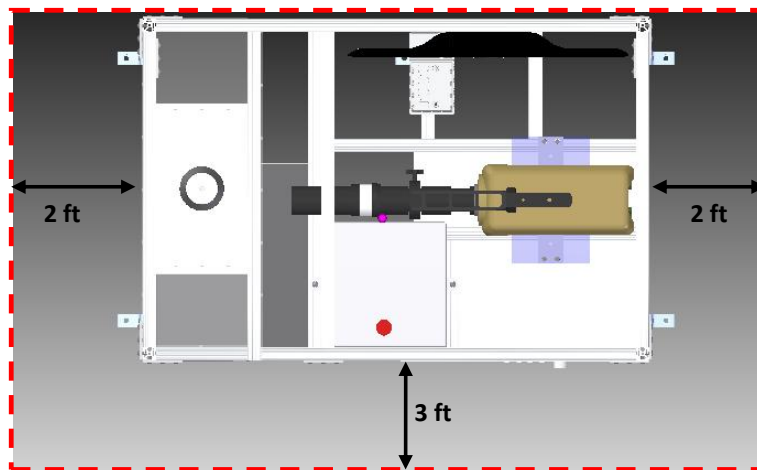


Figure 5: Image showing top view of the experimental structure with minimum space required around the setup

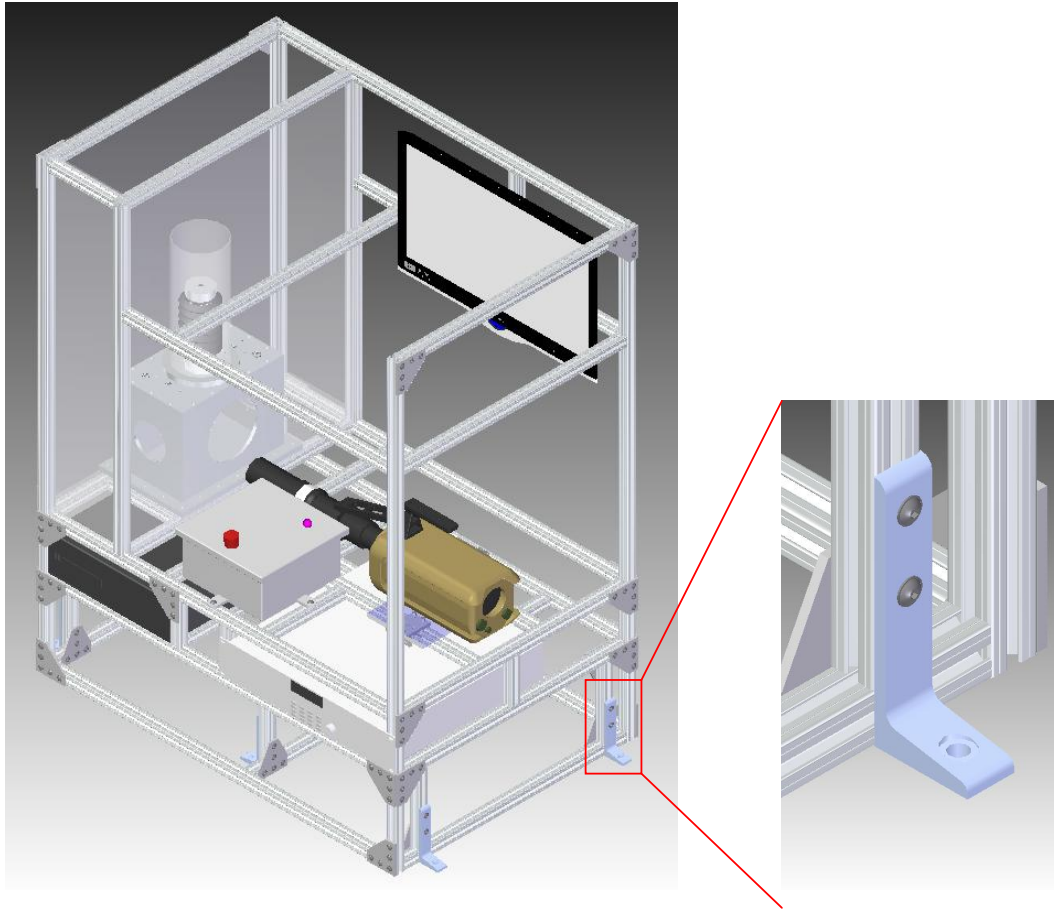


Figure 6: Isometric view of the equipment frame. Inset shows the floor mounting attachment for the AN-6 bolt.

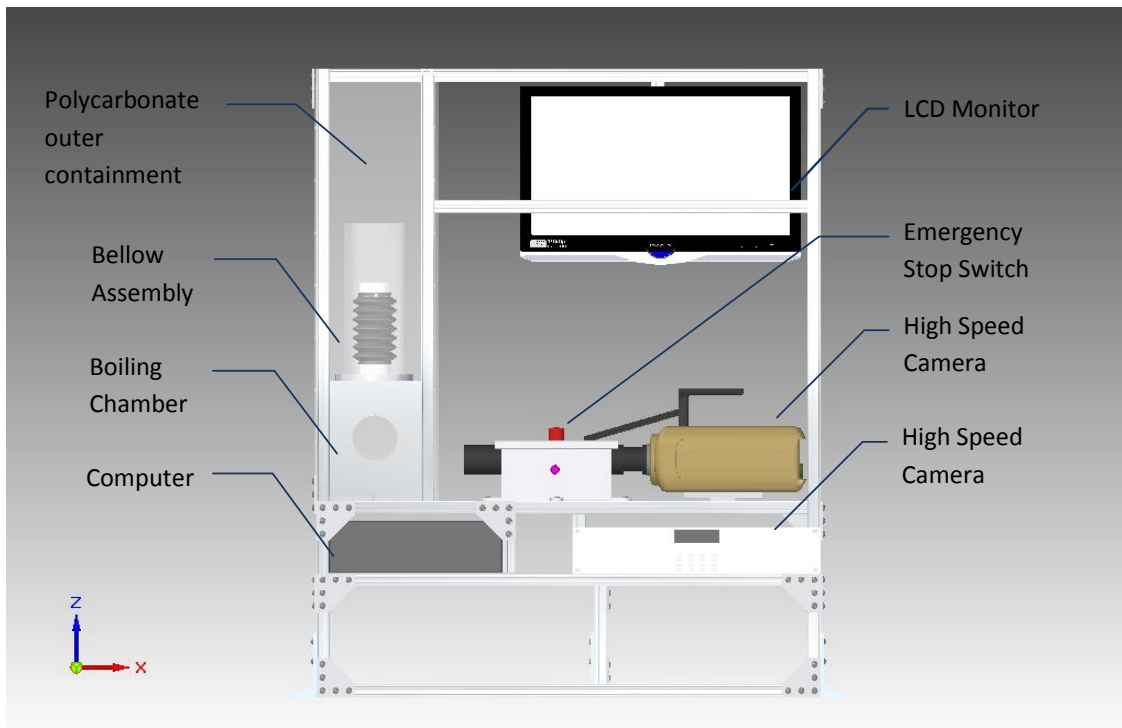


Figure 7: Front view of the equipment frame

Boiling Chamber

The boiling chamber shown in Figure 8 consists of a rectangular aluminum tank of dimensions 13in x 9in x 8.75in (L x W x H). The side walls of the tank, each 0.5 in. thick, and the bottom plate are welded together. The top lid is mounted on the tank using socket screws and sealed with an EPDM rubber gasket in between. The silicon test section consists of two layers of silicon – the top layer constituting the asymmetric ratchet structure and the bottom layer consists of a serpentine aluminum heater. An AMREL SPS series power supply is used to power up the test section heater. The silicon test section mounted on a PCB is suspended from the lid using threaded rods into a pool of FC 72. The liquid is heated to the required pool temperature by two cartridge heaters (Omega model# EMH-060-120V) located on opposite ends of the tank to avoid temperature gradients. Temperature of the pool is measured using two pipe plug thermistors (Omega model# ON-970-44006) probes that are suspended in the liquid. The cartridge heaters with ½ NPT thread and the thermistors with 1/8 NPT thread are mounted on to the lid. To facilitate high speed imaging of the boiling process, the front wall of the tank is fitted with a 6” diameter quartz window to facilitate high speed imaging. Lights for imaging will be through two 4” diameter quartz windows located on the other two sides of the tank. All quartz windows are 0.25” thick and will be mounted on the shoulders on the side walls using polyurethane and also

held against the walls by a 0.25" polycarbonate ring that is fastened on the wall using eight ¼-20 socket screws as shown in Figure 9.

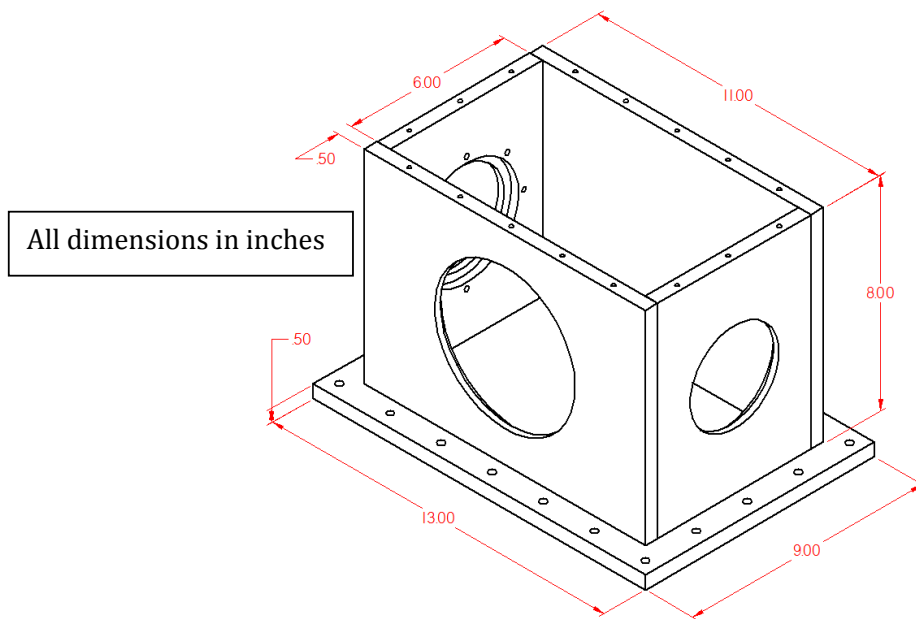


Figure 8: Boiling chamber shown without the lid

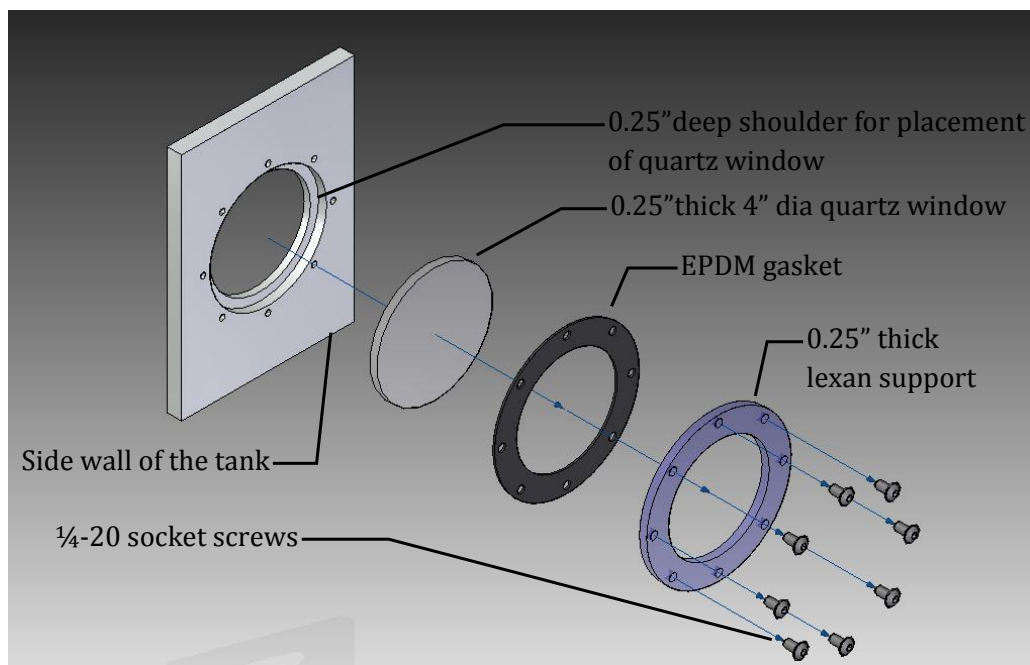


Figure 9: Exploded view of the quartz window assembly

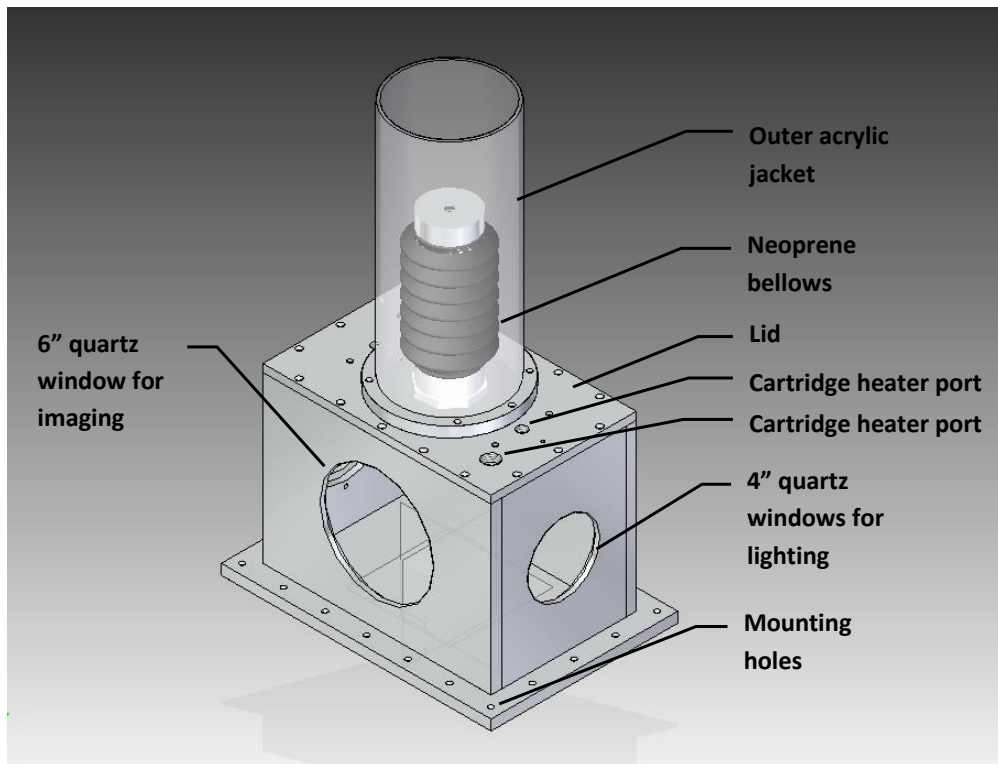


Figure 10: Boiling chamber assembly

During the experiment, as the fluid is heated, increase in fluid volume will cause the bellows to expand thereby maintaining a constant pressure. The outer acrylic vessel is held on to the top lid of the boiling chamber using an aluminum flange.

An assembly of the boiling chamber is shown in Figure 10. The whole assembly will be enclosed by 1/8" thick polycarbonate sheets sealed on to the frame using an EPDM rubber gasket around the boiling chamber as shown in Figure 9. To further prevent leaks in the outer containment, the corners of all the polycarbonate sheets are sealed with a polyurethane adhesive.

Pressure Transducers

The experiment uses a miniature absolute pressure sensors with an amplified output in the range of 0 – 4V corresponding to a pressure range of 0.3 psi to 100 psi. The sensor utilizes silicon, micro-machined, stress concentration enhanced structure that provides a linear output. The sensor is temperature compensated and has a calibrated zero and span. The sensors require an excitation voltage of 5VDC for operation. Electrical connections and the physical dimensions of the sensor are shown in Figure 11.

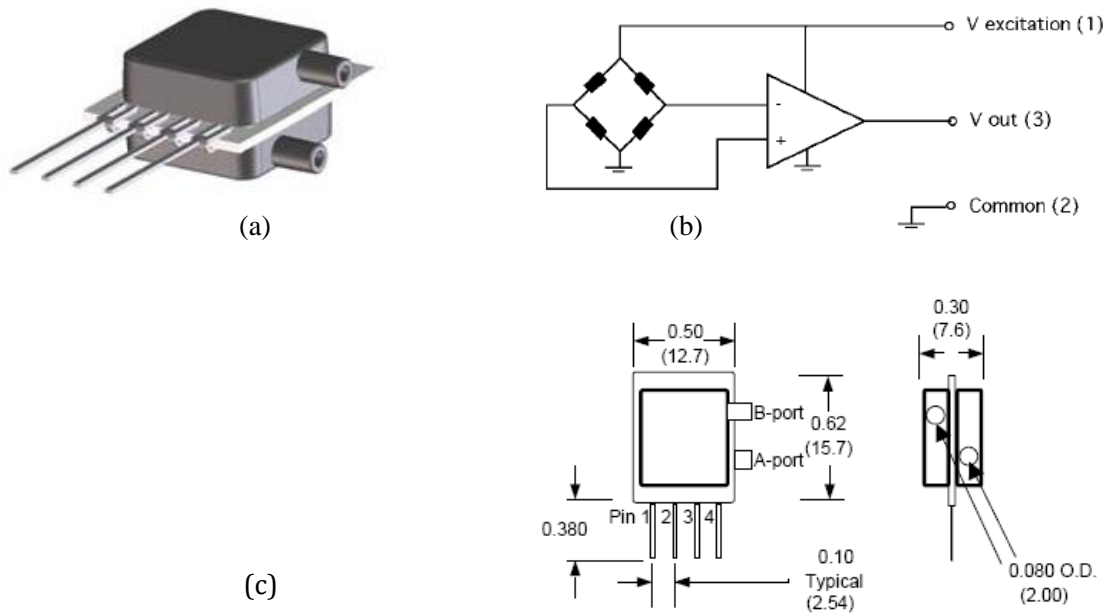
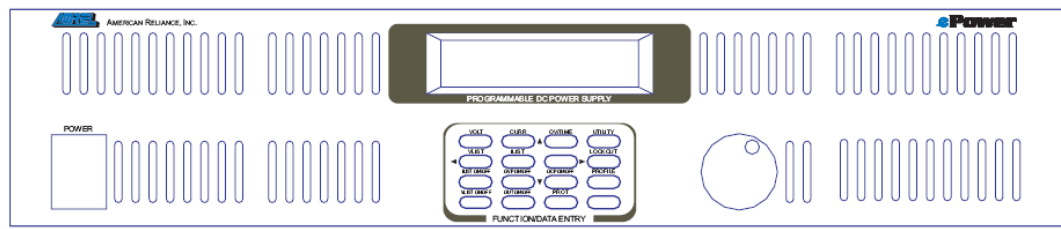


Figure 11: (a) Absolute pressure sensor (b) Pin-out diagram (c) Physical dimensions

Power Supply

The experiment uses a programmable DC power supply to power the test section heater. The power supply used is an AMREL e-POWER SPS series 300V, 3 KW, single phase unit (Model # SPS300-10-K0E1). During the in-flight experiment, the power supply which is facilitated by RS232 interface will be remotely controlled using LABVIEW. The physical dimensions of the power supply are show in Figure 12.



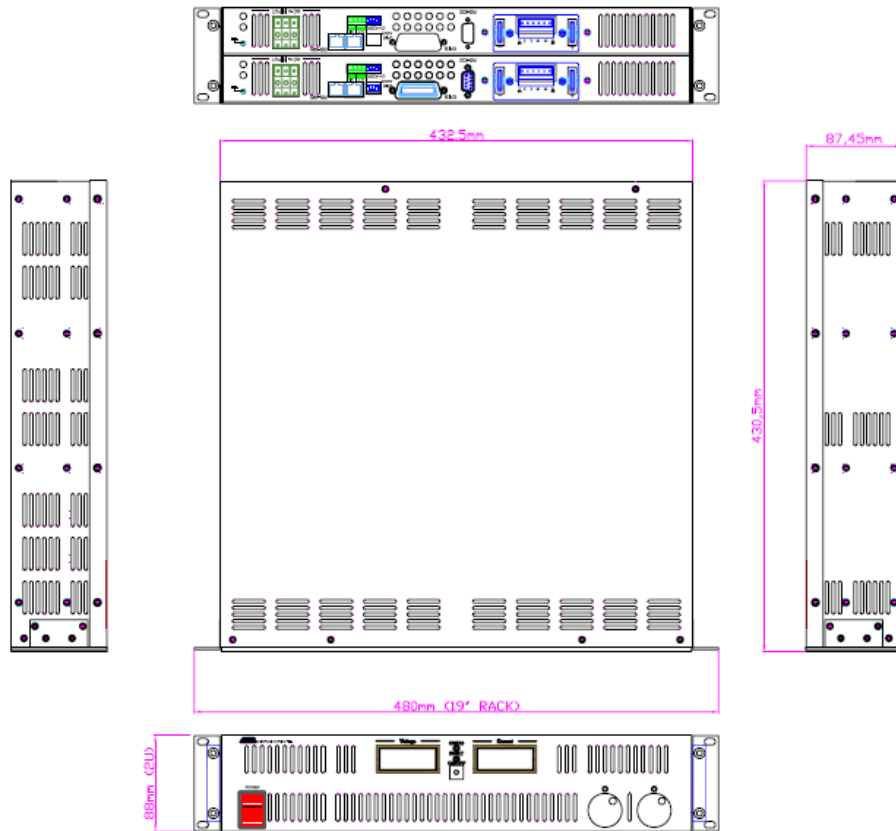


Figure 12: Physical dimensions of the power supply

POWER SUPPLY SPECIFICATIONS:

Maximum Voltage (VMAX): 300 V
 Maximum Current (IMAX): 10 A

Programming Accuracy:

Voltage: $0.05\% \cdot V_{MAX} + 0.1\%$ of FS
Current: $0.01\% \cdot I_{MAX} + 0.1\%$ of FS
Over-voltage: 0.2% of Vout + 0.3% of FS

Measurement Accuracy:

Voltage: 0.1% of RDG + 0.1% of FS
 Current: 0.1% of RDG + 0.2% of FS

Load Regulation:

Voltage: $0.01\% \cdot V_{MAX} + 2 \text{ mV}$

Current: $0.01\% \cdot I_{MAX} + 2 \text{ mA}$

Line Regulation:

Voltage: $0.001\% \cdot V_{MAX} + 2 \text{ mV}$

Current: $0.001\% \cdot I_{MAX} + 2 \text{ mA}$

Transient Response Time: 3ms

Programming/Measurement Resolution: 14-bit

OVP Programmable Range: 5% - 110% of V_{MAX}

Drift7 (8 Hours):

CV Mode: $0.5\% \cdot V_{MAX}$

CC Mode: $0.5\% \cdot I_{MAX}$

Temp. Coefficient:

CV Mode: $0.02\% \cdot V_{MAX} / ^\circ\text{C}$

CC Mode: $0.03\% \cdot I_{MAX} / ^\circ\text{C}$

ac Input: 1 Φ 240Vac 50/60Hz

dc Output Isolation:

$\leq 400\text{Vdc}$: $\pm 600\text{Vdc}$

$\leq 600\text{Vdc}$: $\pm 1000\text{Vdc}$

$\geq 800\text{Vdc}$: $\pm 1500\text{Vdc}$

Data acquisition system (DAQ)

The data acquisition chassis as shown in Figure 13 consists of embedded modules – NI 9219 and NI 9202 that acquire signals from the various sensors in the experiment. The data acquired include voltage from heater, temperature, pressure and accelerometer signals which are monitored and recorded using a desktop computer.

Computer

A HP Compaq CPU with a quad core processor and 16 GB RAM will be used for monitoring, controlling and recording data from the experiment. The dimension and weight of the mini-tower have been tabulated in Table 1. All data logging and experimental controls will be handled using a wireless keyboard.



Figure 13: NI Compact DAQ chassis

High Speed Camera

A Phantom V310 high speed camera will be used to capture high speed videos of the boiling process. Images will be recorded at a frame rate of 3250 fps with a resolution of 1280 x 800. A K2SC Infinity microscope lens with a CF3 objective will be used along with the camera. Both the camera and the lens are supported on a sliding plate attached to the frame on two linear motion bearings which can be locked using brakes as illustrated in Figure 15. The camera and the lens will be stowed during take-off and landing.

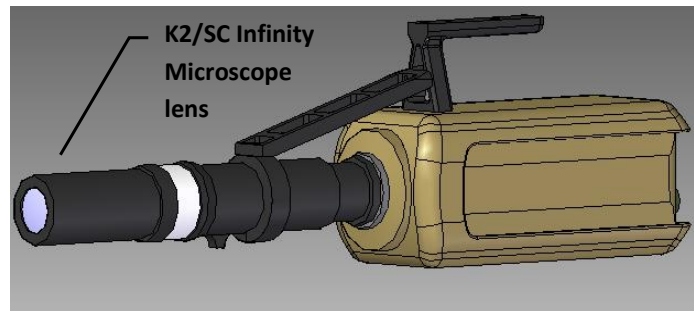


Figure 14: Phantom V310 high speed camera

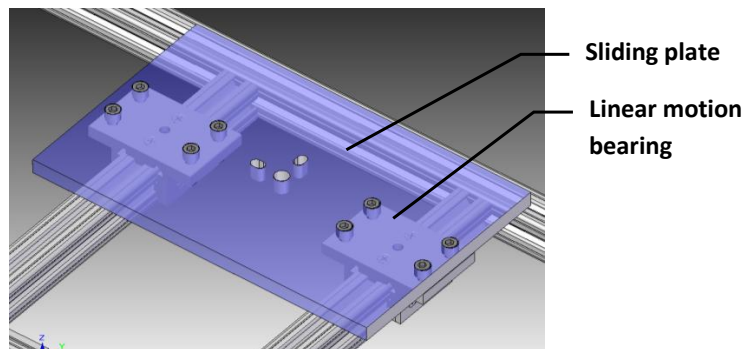


Figure 15: Camera plate mounted on two linear motion bearings

5. STRUCTURAL VERIFICATION

The equipment frame has been designed to withstand the g-load specifications during take-off and landing. The various loads acting on the assembly during takeoff/ landing has been represented in Figure .

Stress analysis was performed on every component and assembly placed on the t-slot extrusions and the factor of safety was determined. Factor of safety (FS) can be expressed as,

$$FS = \frac{\text{Maximum Allowable Stress}}{\text{Actual Stress}} - 1$$

where the maximum allowable stress is the material's yield strength.

The T-slot extrusions used in the frame is made up of Aluminum alloy 6105-T5 and its properties are tabulated in Table 2.

Table 2: Properties of T-slot extrusion material

Material	Aluminum alloy 6105-T5
Modulus of Elasticity, E	10,200,000 psi
Moment of Inertia, I	0.0442 in ⁴
Yield Strength (Max. Allowable Stress)	35000 psi

Using the properties, the allowable stress was calculated for the extrusions on which the components were placed.

Analysis of loads on components:

Analysis of stress due to the components placed on the equipment frame at 6g and 9g forces was simulated using Ansys. For the ease of analysis, the cross section of the aluminum extrusion used in the equipment frame was simplified by removing edges of least importance on the face of the extrusion. For the 6g downward acting force, loads were modeled as pressure distributed on the contact area with the extrusion. For the 9g forward acting force, the forces due to the individual components were located at the center of mass of the individual components placed on the frame. The results of the analysis shown in Figures 16 - 20 illustrate the deformation in the members and the Von Mises equivalent stress. To analyze the structural integrity of the brackets at the joints, the forces acting at the joints were manually compared with the maximum load specifications provided by the manufacturer to obtain a measure of factor of safety for the joints.

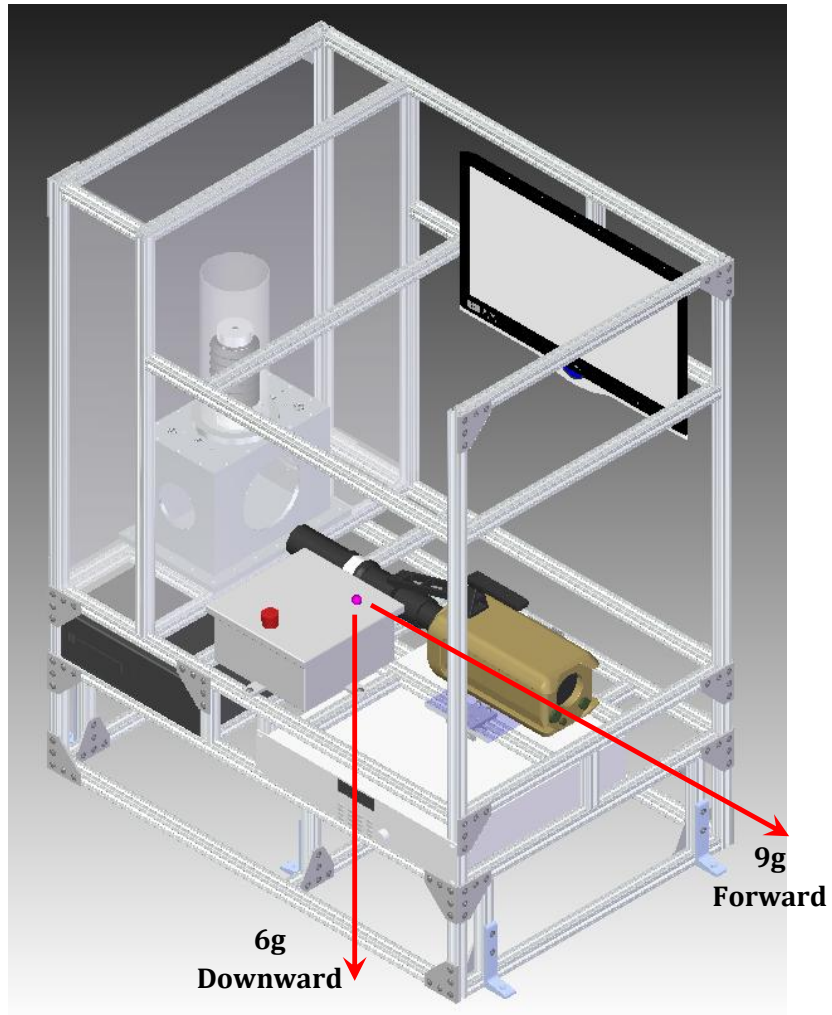


Figure 16: Image showing the location of the components for comparison with results of stress analysis

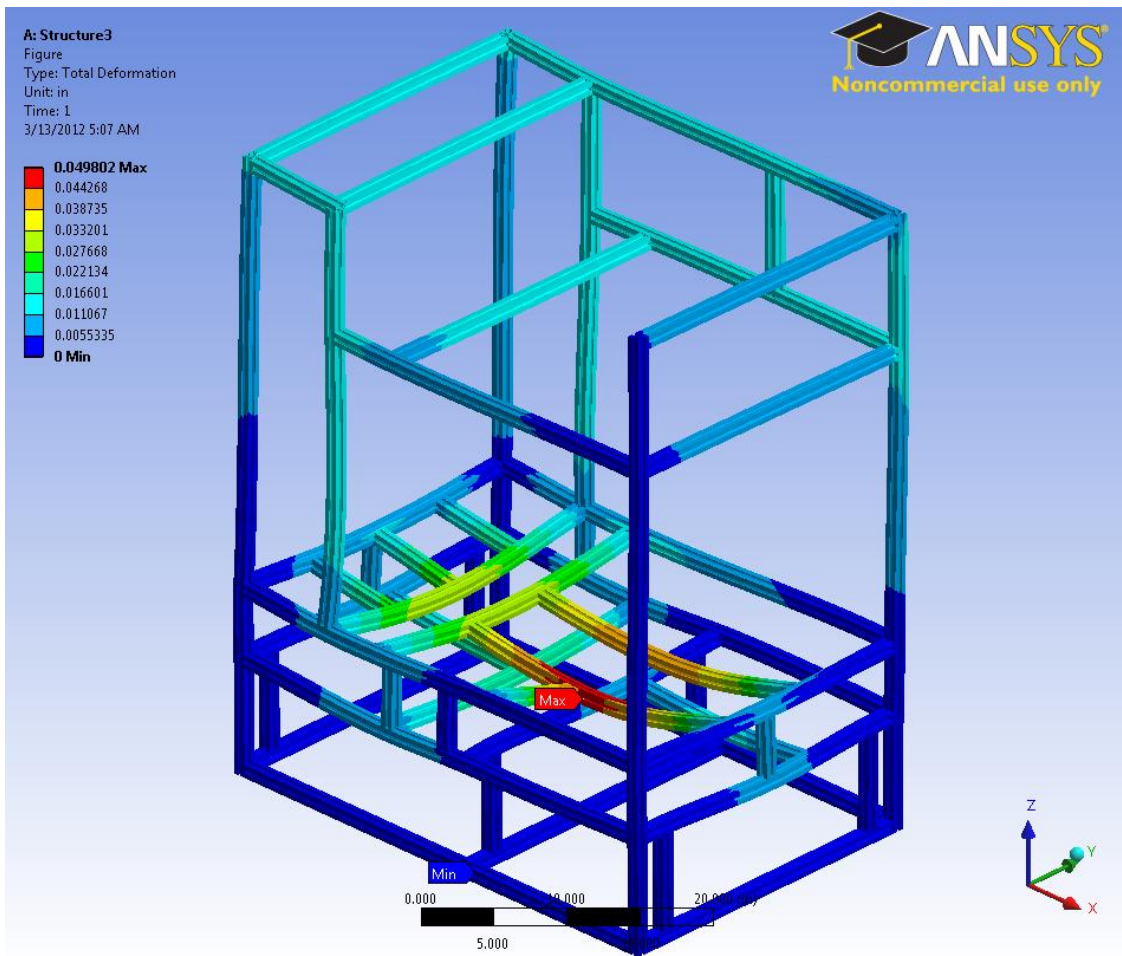


Figure 17: Total deformation due a 6g force acting downwards

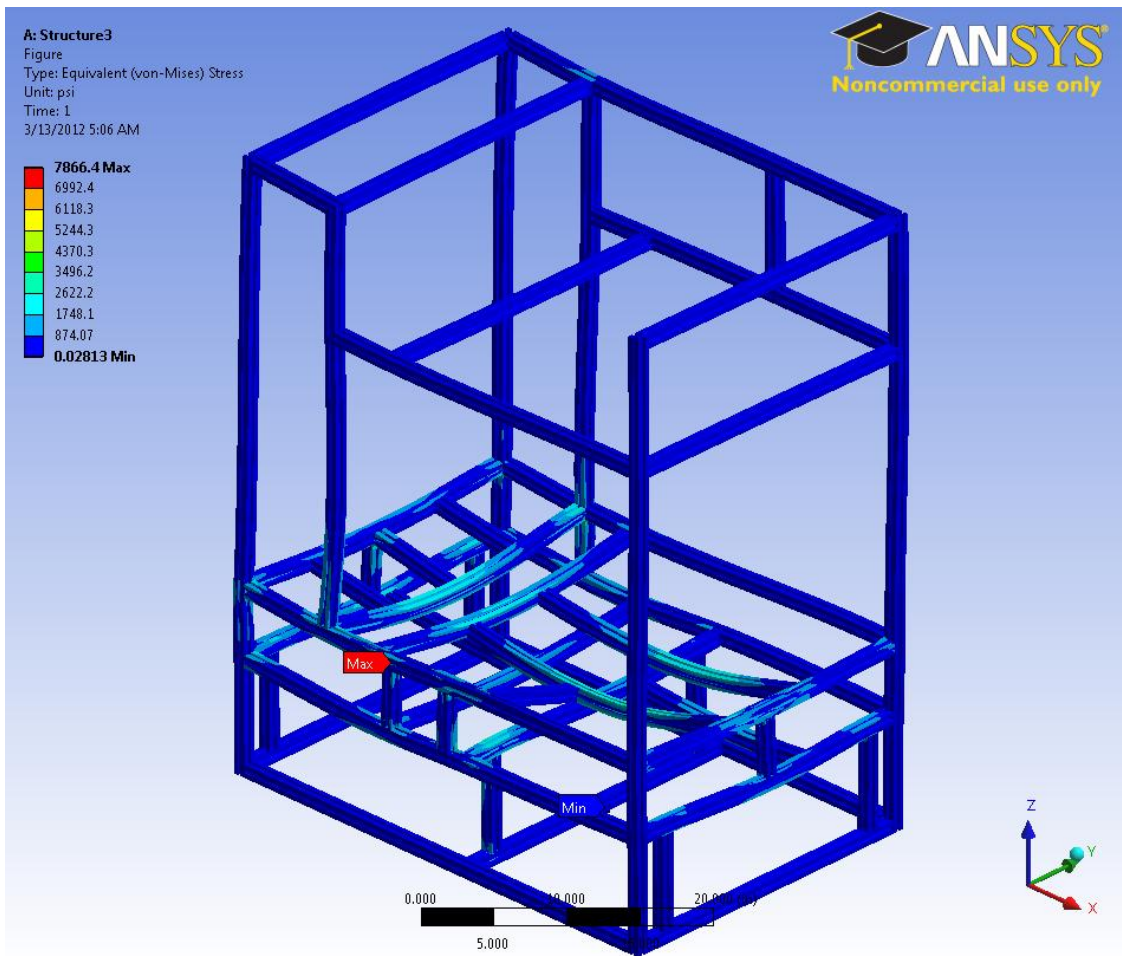


Figure 18: Von-Mises equivalent stress due to 6g downward force

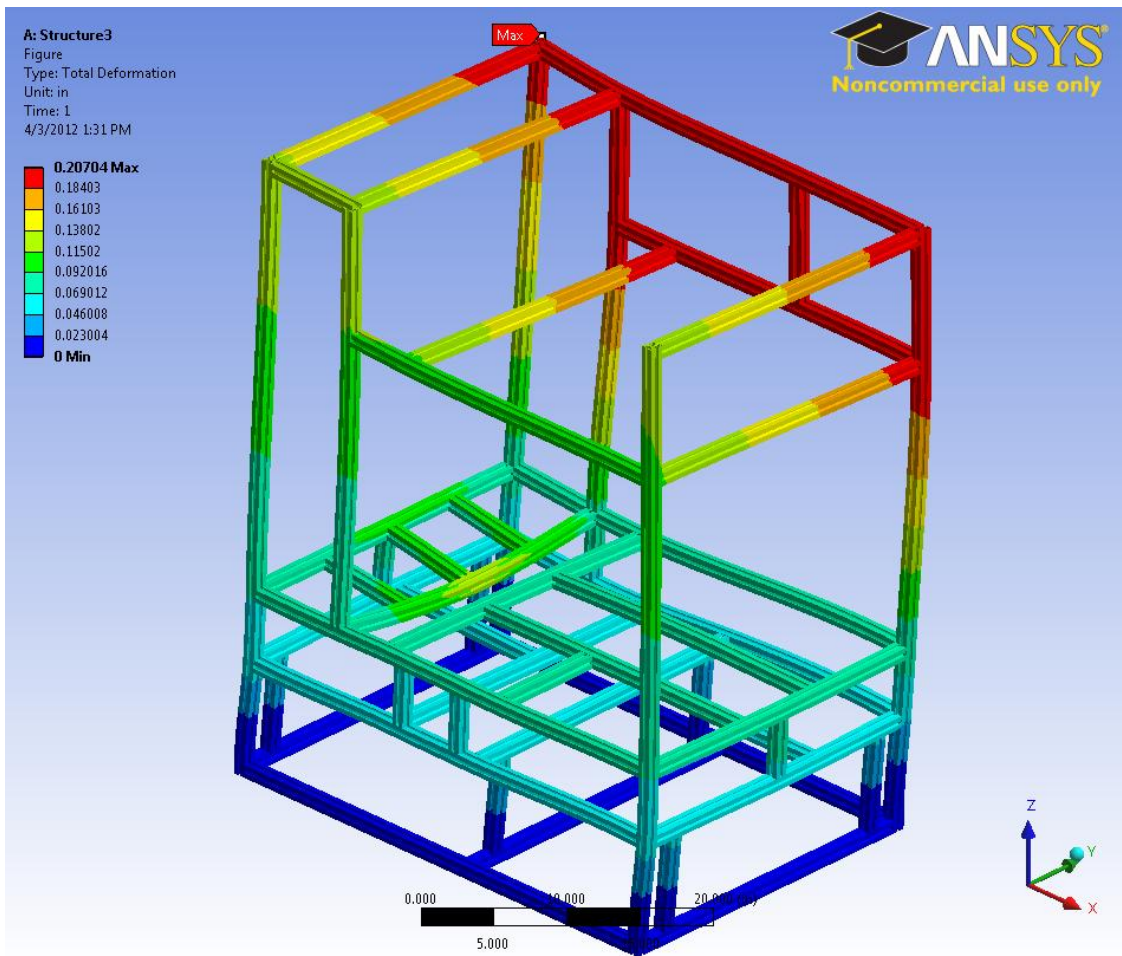


Figure 19: Total deformation due a 9g force acting forward

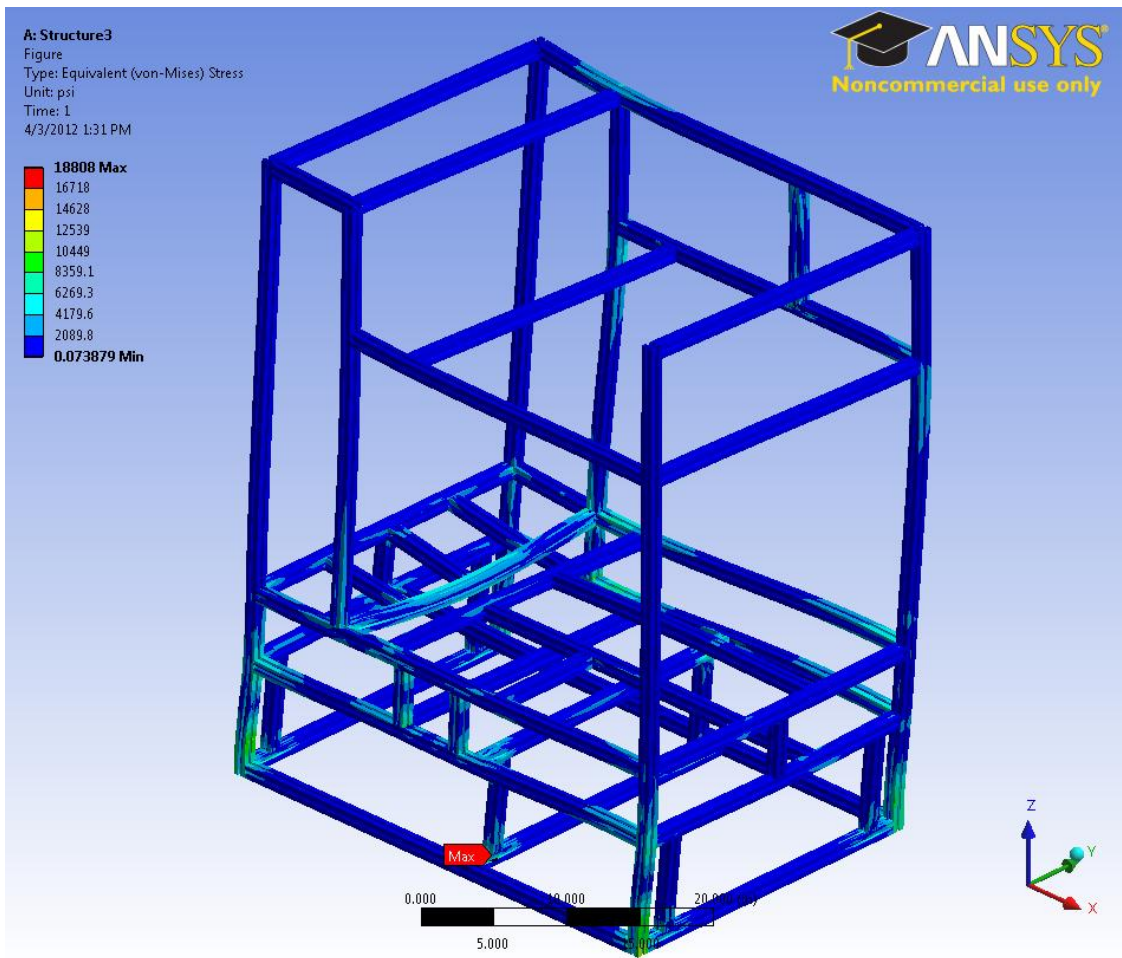


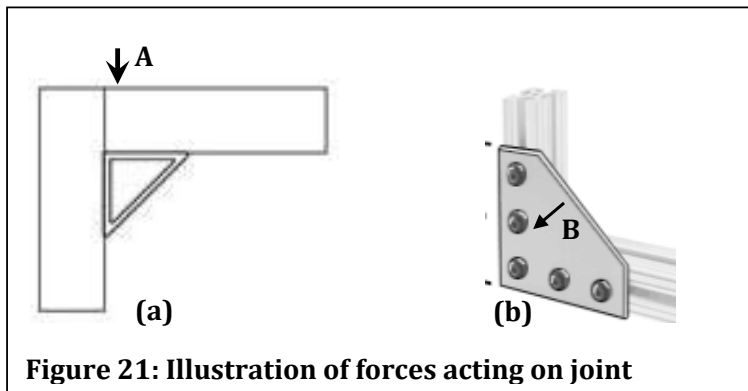
Figure 20: Equivalent (Von-Mises) stress due to forward acting 9g force

Analysis of Joints:

The frame made up of several aluminum extrusions are joined together using different types of joints. The various joints used in the experiment and its maximum allowable loads are tabulated in Table 3. The factor of safety for each joint is evaluated as shown below:


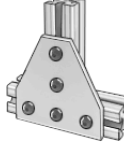



$$\text{Joint factor of safety, FS} = \frac{\text{Max. allowable load}}{\text{Actual load}} - 1$$

The maximum allowable load for each of the joints under a direct force (A), as shown in the Figure 21a, is provided by the manufacturer (8020).



For other loading conditions such as a normal force acting on the face of the bracket (shown in 21 b), it was assumed that the maximum allowable load is comparable to the direct force scenario. At each of the joints marked in Figure 22, the forces acting in three directions were compared manually to the allowable loads of the bracket.

Table 3: Types and specifications of brackets used at the joints

Joint Type	A	B	C	D	E
					
Max. allowable load under direct force (A) (lbs)	175	175	325	325	325

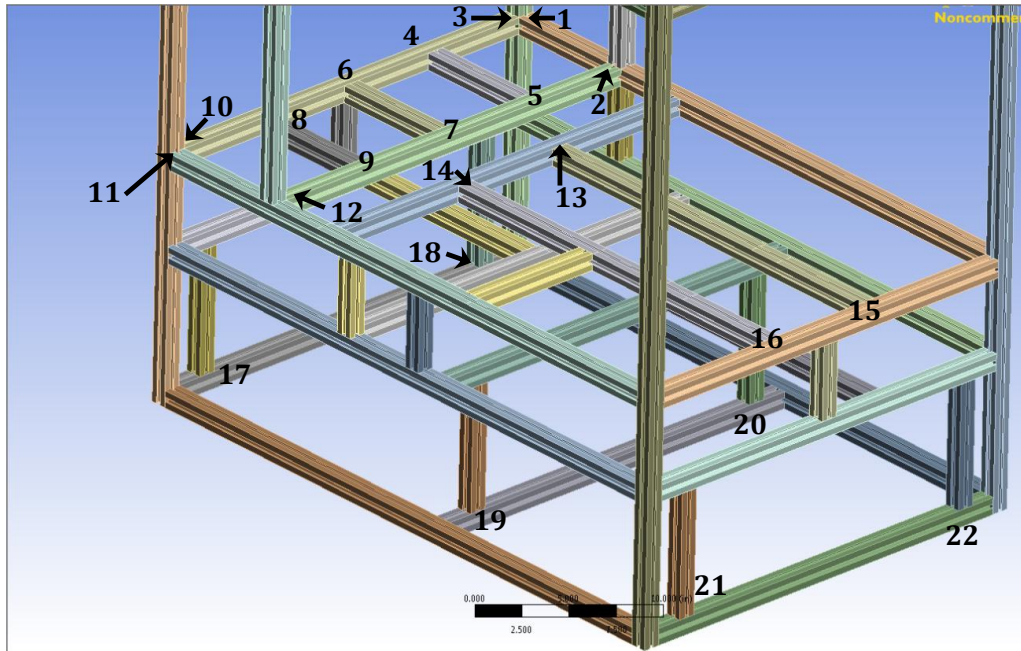


Figure 22: Illustration of joints whose factors of safety were analyzed

Table 4: Factor of safety for the joints marked in Figure #

Joint No.	Joint Type	6g			9g		
		FS _x	FS _y	FS _z	FS _x	FS _y	FS _z
1	A & D	20.29	54.56	12.92	9.42	7.12	7.90
2	D & D	294.45	64999.00	8.63	4.29	18.66	3.46
3	A & E	65.76	11.59	9.60	4.69	1427.57	5.05
4	B	42.97	32.46	10.64	88.29	1.59	11.92
5	B	42.97	32.46	11.57	3.43	1.59	11.69
6	B	10.41	65.54	4.36	9.57	43.19	10.89
7	B	10.41	65.54	46.68	6.09	43.19	11.09
8	B	55.27	19.02	10.02	22.71	1.39	13.07
9	B	55.27	19.02	12.39	2.62	1.39	12.80
10	A & E	90.91	13.37	9.78	4.85	33.67	4.26
11	A & D	7.00	184.19	7.74	3.16	8.31	27.84

12	D & D	51.97	105.21	10.80	3.78	14.01	4.01
13	B	21874	109.06	5.70	3.56	9.34	20.58
14	B	17.96	64.79	11.49	5.24	80.78	13.60
15	B	17.98	64.79	3.78	4.69	80.78	13.60
16	B	349.00	471.97	3.38	3.14	8.19	8.68
17	B & C	891.86	67.40	4.74	12.33	32.99	4.36
18	B & C	441.48	44.58	5.11	15.40	74.41	3.73
19	B & C	260.78	128.53	1.54	7.69	13.21	2.85
20	B & C	134.50	205.61	7.86	6.68	14.79	16.22
21	B & C	358.71	53.29	9.90	11.68	67.78	1281.05
22	B & C	461.96	80.17	5.84	13.33	90.74	8.32

From the above analysis, for the joints with a factor of safety less than 4.0 additional brackets of type C will be added.

Analysis of components:

In this section stress analysis on the frame members and the fasteners holding the components placed on the frame was performed at various load conditions. The factor of safety results are summarized in Table 5.

Table 5: Summary of results from stress analysis

Component/Assembly	G-Load	Load effect	Weight (lbf)	Factor of Safety (FS)
Boiling Chamber	9g forward	Shearing of screws	408.87	322.57
	6g downward	Bending of extrusion	272.58	15.75
Camera	9g forward	Shearing of screws	153	96.06
	6g downward	Bending	102	7.00
Power supply	9g forward	Shearing of screws	265.5	41.96
	6g downward	Bending of extrusion	176.22	13.73

	2g lateral	Tension in screws	58.74	257.84
Kill switch assembly	9g forward	Shearing of screws	89.28	664.32
	6g downward	Bending	59.52	28.48
CPU	6g downward	Bending of extrusion	43.92	10.78
	9g forward	Bending of extrusion	65.88	249.48
	2g lateral	Tension in screws	14.64	6035.21
Monitor	9g forward	Shearing of screws	63.9	82.85

Boiling Chamber:

The aluminum tank used for the boiling experiments is supported on the frame using the bottom polycarbonate sheet used for the secondary containment (26in x 9in). The tank is also fastened on to five t-slot extrusions using twenty ¼-20 socket screws through the polycarbonate sheet as shown in the Figure 23. The load acting on the extrusions includes the weight of the tank, fluid contained in the tank, the sensors and the bellow assembly.



Figure 23: Location of boiling chamber. Red shaded area shows contact area with the extrusion.

The stress and deformation due to 6g forces due to the assembly has been illustrated in Figures 17 and 18. The 6g forced causes a deformation of 0.03 inches in the extrusion

member leading to a bending stress of 2089.1 psi in the extrusion. Safety factor during bending due to 6g downward force can be evaluated as follows:

$$\text{Factor of safety, FS} = \frac{\text{Yield strength}}{\text{Actual stress}} - 1 = \frac{35000}{2089.1} - 1 = 15.75$$

Shear force due to 9g forward force (significantly larger than shear due to 2g lateral force):

Weight of boiling chamber, $W = 45.43$ lbs (including fluid, polycarbonate plate and bellows)

Force due to 9g force on each bolt, $F = (45.43 \times 9)/20 = 20.44$ lbs

Bolt diameter = 0.25 in; Bolt cross-sectional area = 0.049 in²

Bolt ultimate shear strength = 135,000 psi

Shear stress on each bolt, $\tau = \text{Force on each bolt} / \text{Bolt area} = 417.21$ psi

$$\text{Factor of safety, FS} = \frac{\text{Ultimate shear strength}}{\text{Shear stress}} - 1 = 322.57$$

Power Supply:

The power supply is supported on horizontal t-slot extrusion members and fastened to two vertical extrusions using four 8-32 screws as shown in Figure 24. The 6g downward force causes bending stress in the extrusion while the 9g forward force acts to shear the four 8-32 screws supporting the power supply. Forces acting in the lateral direction at 2g will cause tensile forces on the fasteners.

For the downward force of 6g acting on the extrusions,

The bending stress due to the load,
 $\sigma = 2376.2$ psi (from ANSYS analysis)

The maximum yield strength of the extrusion is 35000 psi.

$$\text{Factor of safety, FS} = (35000 / 2376.2) - 1 = 13.73$$

Shear stress due to 9g forward force:

Force due to 9g force on each bolt, $F = (29.37 \times 9)/4 = 66.08$ lbs

Bolt diameter = 0.164 in

Shear stress on each bolt, $\tau = \text{Force on each bolt} / \text{Bolt area} = 3146.67$ psi

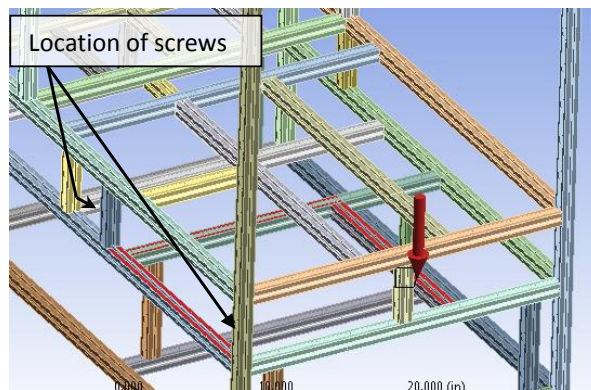


Figure 24: Red shaded area shows the location of power supply and its contact area with the extrusion

$$\text{Factor of safety, FS} = \frac{\text{Ultimate tensile strength}}{\text{Axial stress}} - 1 = 41.90$$

Axial tensile stress due to 2g lateral force:

The power supply is held on to the vertical frame using four 8-32 alloy steel fasteners on the front face of the power supply. The lateral axial force of 2g induces a tensile stress in the fasteners. Weight of the power supply, $W = 29.37$ lbs

$$\text{Force due to 2g force on each bolt, } F = (29.37 \times 2)/4 = 14.69 \text{ lbs}$$

Bolt diameter = 0.164 in

Bolt ultimate tensile strength = 180,000 psi

Axial stress on each bolt, $\sigma = \text{Force on each bolt} / \text{Bolt area} = 695.42$ psi

$$\text{Factor of safety, FS} = \frac{\text{Ultimate tensile strength}}{\text{Axial stress}} - 1 = 257.84$$

CPU assembly:

The CPU is supported on three t-slot extrusion members as shown in Figure 25. Downward force of 6g induces bending stress in the extrusion members. The CPU is restrained against the 2g lateral force by two L-joining plates with five 1/4-20 bolts each. In the forward direction, the 9g forces induce a bending stress in the two t-slot extrusions restraining the movement of CPU in that direction.

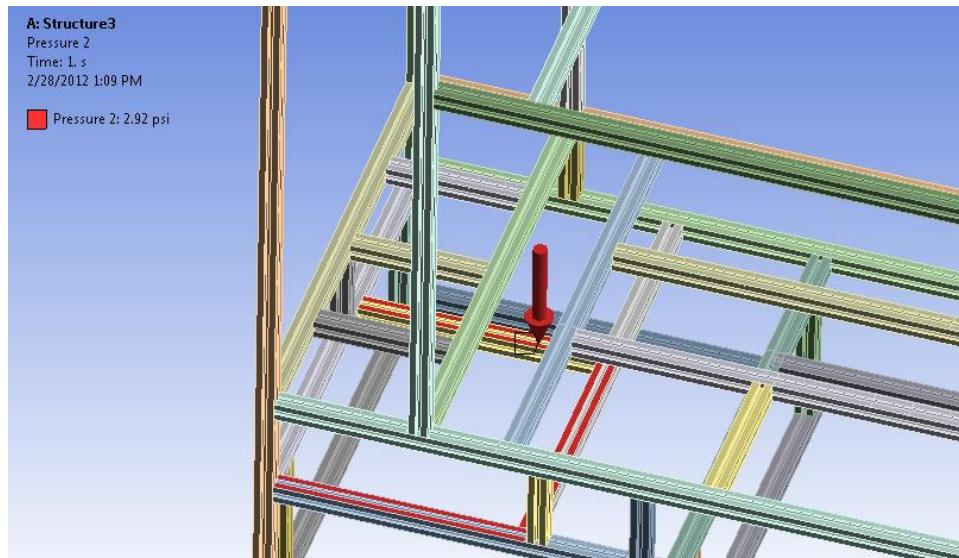


Figure 25: Red shaded area shows the location of the CPU and its contact area with the extrusion

For the download force of 6g:

Bending Stress, $\sigma = 2970.4$ psi

Factor of safety, $FS = (35000/2970.4)-1 = 10.78$

For the lateral force of 2g (tensile stress):

Weight of CPU, $W = 7.32 \times 2 = 14.64$ lbs

Tensile force acting on each $\frac{1}{4}$ -20 fastener, $F = W / 10 = 1.464$ lbs

Tensile stress, $\sigma = \text{Force on each bolt} / \text{Bolt area} = 1.464 / 0.049 = 29.82$ psi

Tensile strength of bolt = 180000 psi

Factor of safety, $FS = \frac{\text{Max tensile strength}}{\text{Tensile stress}} - 1 = 6035.21$

For the forward force of 9g (Bending stress in the extrusion):

Weight of CPU, $W = 7.32 \times 9 = 65.88$ lbs

Force acting on one extrusion, $P = 65.88 / 2 = 32.94$ lbf

Length of extrusion, $L = 4.5$ in

Uniformly distributed load, $w = 7.32$ lb/in

The bending stress due to uniformly dist. load can be expressed as, $\sigma = \frac{wL^2}{12Z}$

Where, $Z = \text{Section modulus} = \frac{\text{Moment of Inertia, } I}{c} = \frac{0.0442 \text{ in}^4}{0.5 \text{ in}} = 0.0884 \text{ in}^3$

Bending Stress, $\sigma = 139.73$ psi

Factor of safety, $FS = (35000/139.73)-1 = 249.48$

LCD Monitor:

The monitor is supported on a 100 x 100mm VESA mount adapter which is fastened to a vertical t-slot extrusion using three $\frac{1}{4}$ -20 socket screws as shown in Figure 26.

The forward force of 9g induces a shear stress in the screws (larger than stress due to 6g).

Weight of the monitor at 9g, $W = 63.9$ lbs

Shear force acting on each screw, $F_s = 63.9 / 3 = 21.3$ lbs

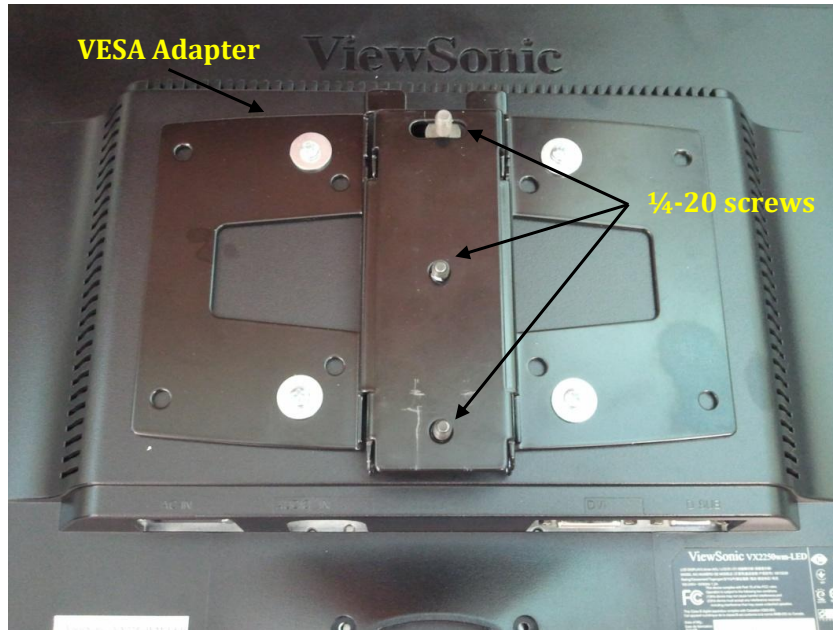


Figure 26: Backside of the LCD with the attached VESA adapter and mounting screws

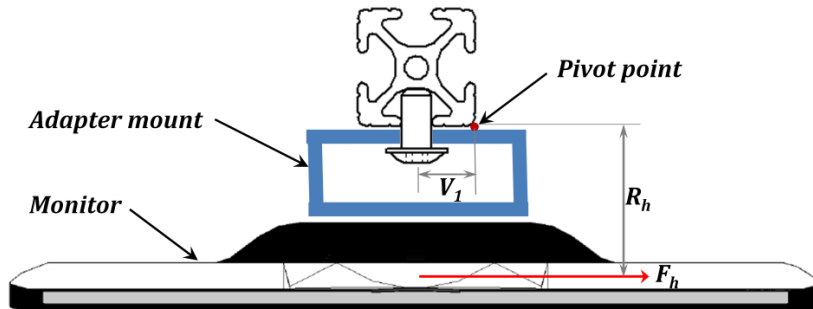


Figure 27: Schematic top view of the monitor assembly

Shear stress, $\tau = \text{Force on each bolt} / \text{Bolt area} = 21.3 / 0.049 = 434.69 \text{ psi}$

Tensile force on each bolt, $F_t = (F_h \times R_h) \cdot \frac{1}{V_1} = (21.3 \times 2.29) \cdot \frac{1}{0.5} = 97.55 \text{ lbs}$

Tensile stress on each bolt, $\sigma = F_t / A = 1990.0 / 0.049 = 1990.9 \text{ psi}$

Factor of safety for the combined loading of shear and tensile stress

$$FS = \frac{\text{Tensile strength}}{\sqrt{\sigma^2 + 4\tau^2}} = 82.85$$

Factor of safety for the bolt pull out

The factor of safety for the case of pull out of the bolt (1/4 -20) from the nut can be evaluated as,

$$FS = \frac{\text{Bolt pull out strength}}{\text{Tensile stress on each bolt}} - 1$$

In the case of t-slot extrusions, a load is fastened on to the t-slot in the frame due to the spring-locking action of the nut against the aluminum slot as the bolt is tightened. In this scenario, since the aluminum has lower yield strength than the steel fasteners, the aluminum slot will fail before the bolt pulls out of the nut. Hence, the bolt pull out strength is assumed to be yield strength of aluminum, 35000 psi.

$$FS = \frac{35000}{1990.9} - 1 = 16.58$$

High Speed Camera:

The camera and the lens are supported on two t-slot extrusion members. The t-slot extrusions are fixed at both the ends by a T-joining plate using five 1/4-20 bolts. For the analysis only the load on one of the extrusions will be considered.

For the download force of 6g acting on the extrusion:

Bending Stress, $\sigma = 4370.0$ psi

Factor of safety, $FS = (35000/ 4370.0)-1 = 7.00$

Shear stress due to 9g forward force:

The camera is held on to the camera plate using one 3/8-24 alloy steel fastener from the bottom of the camera plate. The maximum stress acting on the fasteners is due to the forward 9g force which induces a shear in the fastener. Hence the analysis is only performed for the worst case scenario of 9g force.

Weight of the camera assembly, $W = 17$ lbs

Force on the bolt due to 9g force, $F = (17 \times 9) = 153$ lbs

Bolt diameter = 0.375 in

Bolt max shear strength = 135,000 psi

Shear stress, $\tau = \text{Force on each bolt}/ \text{Bolt area} = 153/0.11 = 1390.91$ psi

Factor of safety, $FS = \frac{\text{Max shear strength}}{\text{Shear stress}} - 1 = 96.06$

Kill switch unit:

The kill switch box is supported on t-slot extrusions using four ¼-20 socket screws.

The forward force of 9g causes a shear force in the screws (significantly greater than 2g lateral force).

Weight of kill switch unit, W = 9.92 lbs

Shear force acting on each screw, $F_s = (9.92 \times 9)/4 = 22.32$ lbs

Shear stress, $\tau = \text{Force on each bolt} / \text{Bolt area} = 22.32/0.11 = 202.91$ psi

Factor of safety, $FS = \frac{\text{Max shear strength}}{\text{Shear stress}} - 1 = 664.32$

For the download force of 6g acting on the extrusion:

Bending Stress, $\sigma = 3496.2$ psi

Factor of safety, $FS = (35000 / 3496.2) - 1 = 9.01$

Floor attachment:

The frame is attached to the cabin floor using six floor attachment brackets. Since the structure is firmly mounted on the floor, only the forward acting 9g force is considered for the structural analysis which acts at the center of mass of the frame.

Total weight of the structure (without camera assembly) at 9g, $W = 187.61 \times 9 = 1688.49$ lb

Assuming the load acts equally on all the six brackets,

Load on each bracket = 281.42 lb

Bolt 3 - Shear stress

Shear stress acting on bolt 3 (3/8”) = $281.42/.11 = 2558.32$ psi

Factor of safety = $(135,000/2558.32) - 1 = 51.77$

Bolt 1, 2 - Tensile stress

Tensile force acting on a selected bolt, n, can be evaluated as,

$$F_{nt} = (F_v R_v + F_h R_h) \cdot V_n / (V_1^2 + V_2^2 + \dots + V_x^2)$$

For bolt 1, $F_{1t} = (281.42 \times 18.55) \times 4.25 / (2.75^2 + 4.25^2) = 865.81$ lbf

Tensile stress on bolt 1 = $865.81 / 0.049 = 17669.65$ psi

Tensile factor of safety = $(180,000/17669.65) - 1 = 9.19$

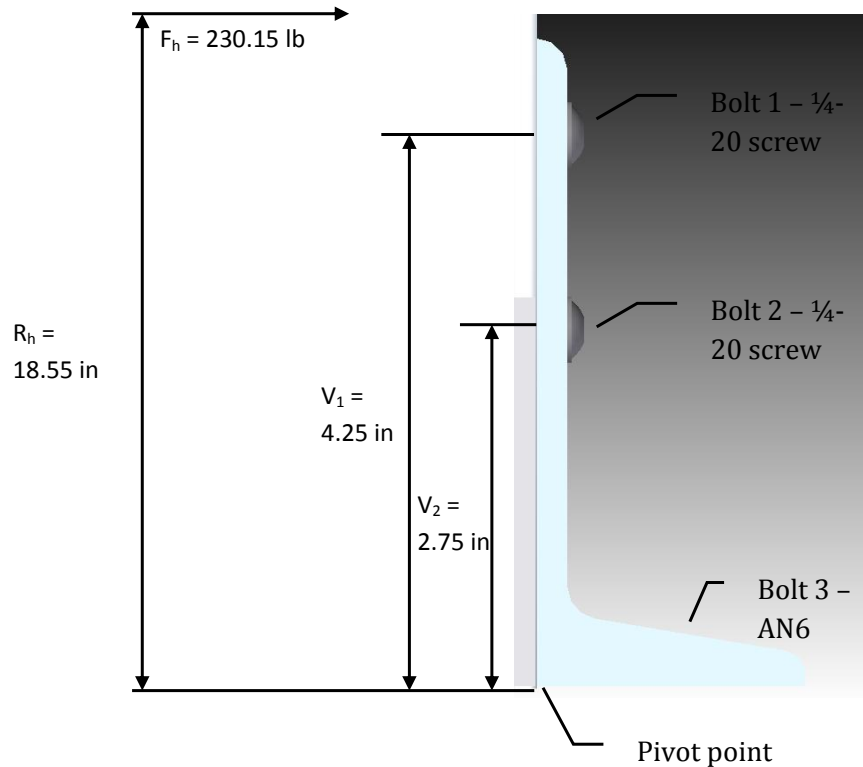


Figure 28: Schematic of the floor mounting bracket

For bolt 2, $F_{2t} = (281.42 \times 18.55) \times 2.75 / (2.75^2 + 4.25^2) = 560.23 \text{ lbf}$

Tensile stress on bolt 1 = $560.23 / 0.049 = 11433.3 \text{ psi}$

Tensile factor of safety = $(180,000/11433.3) - 1 = 14.74$

Data Acquisition (DAQ) Module:

The National Instruments DAQ module is attached to the extrusion using four $1/4$ -20 screws.

The forward force of 9g induces a shear stress in the screws (larger than stress due to 6g).

Weight of the module at 9g, $W = 2.26 \times 9 = 20.34 \text{ lbs}$

Shear force acting on each bolt, $F_s = 63.9/4 = 5.09 \text{ lbs}$

Shear stress, $\tau = \text{Force on each bolt} / \text{Bolt area} = 5.09/0.049 = 103.78 \text{ psi}$

Factor of safety

$$FS = \frac{\textit{Shear strength}}{\textit{Actual shear stress}} - 1 = 1299.88$$

Power Strip:

The 9 outlet power strip equipped with circuit breaker is fastened on to the extrusion using two ¼-20 screws as shown in Figure #.

The forward force of 9g induces a shear stress in the screws (larger than stress due to 6g).

Weight of power strip at 9g, $W = 1.45 \times 9 = 13.05$ lbs

Shear force acting on each bolt, $F_s = 13.05/2 = 6.53$ lbs

Shear stress, $\tau = \text{Force on each bolt} / \text{Bolt area} = 6.53/0.049 = 133.16$ psi

Factor of safety

$$FS = \frac{\textit{Shear strength}}{\textit{Actual shear stress}} - 1 = 1012.79$$

Keyboard tray:

The keyboard docking tray used to mount the keyboard during the flight is attached to the extrusion using a sliding bracket which is fastened using four ¼-20 screws.

The forward force of 9g induces a shear stress in the screws (larger than stress due to 6g).

Weight of the tray including the bracket at 9g, $W = 2.76 \times 9 = 24.84$ lbs

Shear force acting on each bolt, $F_s = 24.84/4 = 6.21$ lbs

Shear stress, $\tau = \text{Force on each bolt} / \text{Bolt area} = 6.21/0.049 = 126.73$ psi

Factor of safety

$$FS = \frac{\textit{Shear strength}}{\textit{Actual shear stress}} - 1 = 1064.22$$

6. ELECTRICAL ANALYSIS/VERIFICATION

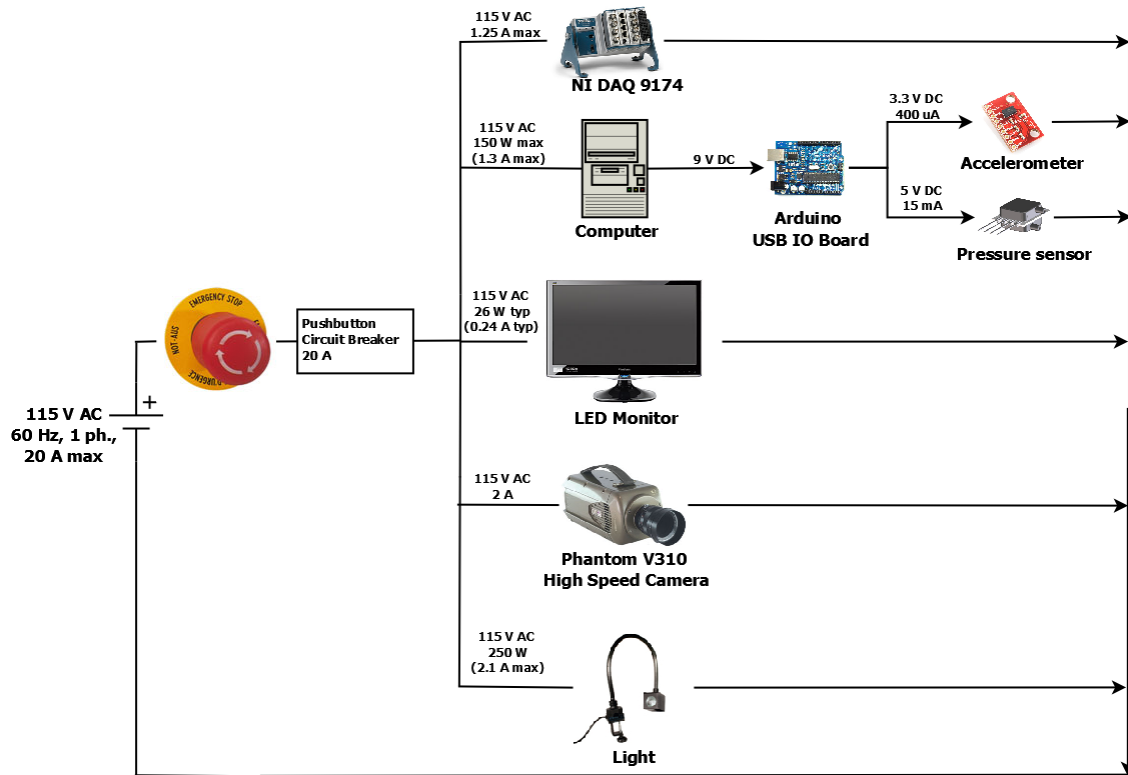


Figure 29: Electrical circuit diagram for components connected to 115 VAC

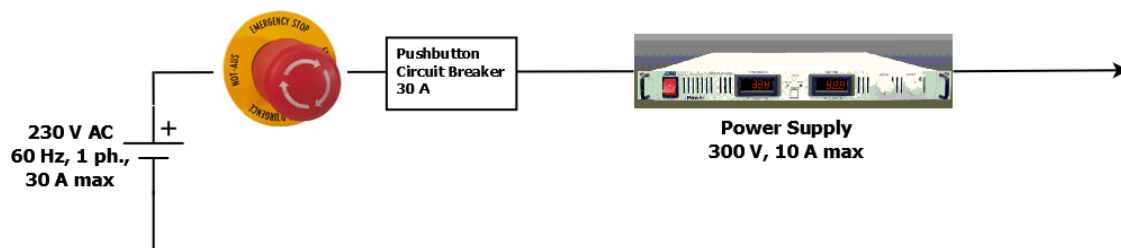


Figure 30: Electrical circuit diagram for components connected to 230 VAC

The experimental frame will be grounded to the aircraft frame using a 10 gage braided grounding strap. All the exposed metal surfaces will be connected to this strap.

(i) LOAD TABLES

Table 6: 115VAC Load Table

Power Source Details	Electronic Equipment	Current Drawn (A)
Name : Power Cord A Voltage : 115 VAC, 60 Hz Wire Gauge : 12 Max Outlet Current : 20 A	Data Acquisition	1.25
	Desktop Computer	1.3
	Monitor	0.24
	High Speed Camera	2.0
	Light	2.1
	Transformer – kill switch	1.29
	Total current draw (A)	8.18

Table 7: 220VAC Load Table

Power Source Details	Electronic Equipment	Current Drawn (A)
Name : Power Cord B Voltage : 230 VAC, 60 Hz Wire Gauge : 12 Max Outlet Current : 30 A	Power Supply	5
	Total current draw (A)	5

(ii) STORED ENERGY

No stored electrical energy.

(iii) ELECTRICAL KILL SWITCH

There is an electrical kill switch that will cut the power to all the electrical and electronic equipments. The electrical circuit for the kill switch circuit is shown in Figure 31. The kill switch, when pressed, de-energizes the contactor coil thereby losing contact with the components connected to the contactor. The contactor is energized using a 24 V ac transformer. Two contactors are used – one rated for 20A for components connected to 110 VAC and the other rated for 30A for the power supply connected to 230VAC. The kill

switch assembly also has a NEMA 5-20 R socket connecting a power strip, and a NEMA L14 20R socket for the power supply. Two wires from the kill switch terminate in plugs NEMA 5-20P and NEMA L14-20P to connect to the receptacles from the aircraft.

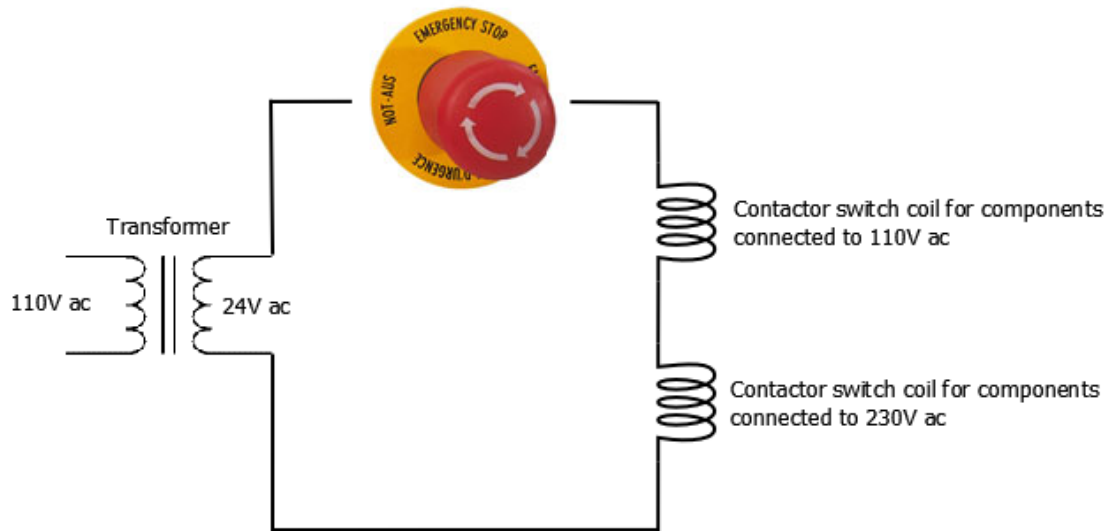


Figure 31: Electrical circuit for the emergency kill switch

(iv) ELECTRICAL SHUTDOWN PROCEDURE

- Verify that the test sequence has been completed.
- Turn off the camera and the lights.
- Set the voltage and current to 0Volts and 0 Amps respectively. Turn off the power supply.
- Monitor the temperature and pressure in the boiling chamber until they return to ambient conditions
- Turn off the data acquisition system
- Turn off the computer

(v) EMERGENCY SHUTDOWN PROCEDURE

Push the electrical kill switch button to kill the power supply to all the equipments. To return to normal operating conditions twist and release the emergency stop button and make sure the power supply returns to “zero” state.

(vi) LOSS OF ELECTRICAL POWER

In the event of electrical power loss, the experiment will fall to a safe position with the electrical power to the heaters set to zero. Upon the return of electrical power, the experiment will be in an idle state with the power to the heaters off.

7. PRESSURE VESSEL/SYSTEM

The boiling chamber used in the current experimental set up, as mentioned earlier, will be maintained at atmospheric pressure during the experiment. However, loss of flight cabin pressure might lead to a pressure differential of about 12 psia between the pressures inside and outside the tank. To test the structural integrity of the tank and the weld joints to withstand the pressure differential, a pressure test was conducted as shown in Figure 32.

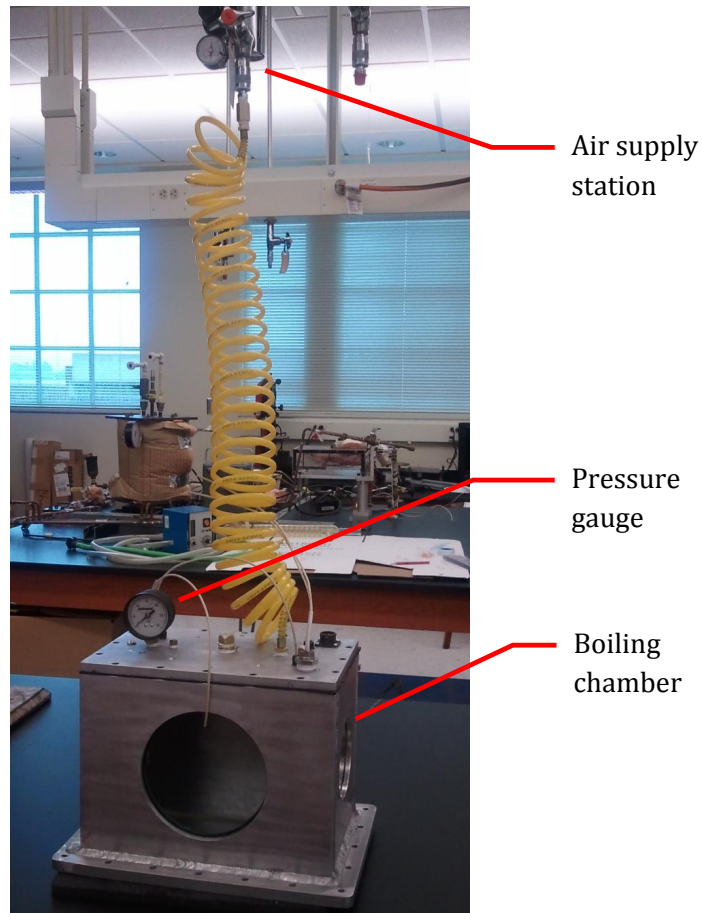


Figure 32: Pressure testing of boiling chamber

The tank was completely filled with water and air was supplied to the tank from an overhead supply station. A pressure gauge was used to monitor the pressure in the tank. The air supply valve was opened to increase the pressure up to 30 psia and no leaks were detected in the tank.

8. LASER CERTIFICATION

This experiment does not use a laser system

9. PARABOLA DETAILS AND GROUND CREW ASSISTANCE

Ground Crew Assistance: None Required

In flight crew assistance: None Required

Free floating requirements: None

10. INSTITUTIONAL REVIEW BOARD

This experiment does not use human, animal or any biological test specimen.

11. HAZARD ANALYSIS

Table 8: Hazard analysis prepared in accordance with JPR-1700.1

HAZARD	CAUSE	EFFECT	CONTROLS	VERIFICATION
Electrical Shock	Short circuit in test equipment	Burn, shock and/or death	All electrical circuits grounded	Review of Electrical drawing.
Hot surface burns	Cartridge heaters operate at more than 60°C	Burn	Isolated from operators	Review of Test Equipment.
Weight to be lifted (>40 lbs)	Test structure weighs more than 100 lbs	Physical injury	Handles and casters installed	More than 2 people to lift
Toxic gas	Decomposition of FC72 at temperatures greater than 200°C	Blindness. Tissue damage	Test section heater not designed to reach such high temperatures	Heater surface temperature will be monitored

HAZARD	CAUSE	EFFECT	CONTROLS	VERIFICATION
Pressure differential	Cabin pressure loss	Liquid leak	Secondary containment. Chamber has been pressure tested.	Monitor chamber pressure

12. TOOL REQUIREMENTS

The following tools will be required for ground operations. The tools will be brought by the investigators and no other special tools are required.

- Allen keys
- Phillips and slotted screw driver
- Adjustable crescent wrench
- Needle nose pliers

13. PHOTO REQUIREMENTS

No special photo or video supports equipments are required for this experiment.

14. AIRCRAFT LOADING

The aluminum structure is equipped with handles and wheels. The wheels will be disassembled before the flight and the assembly will be carried into the aircraft manually.

15. GROUND SUPPORT REQUIREMENTS

220 V and 115 V AC power outlets will be required on site in order to test the experimental setup and degas the fluid prior to the flight experiment.

16. HAZARDOUS MATERIALS

The working fluid used in this experiment, FC 72, decomposes into Hydrogen Fluoride and Perfluoroisobutylene (PFIB) at elevated temperatures - greater than 200 °C. However, in the current experimental setup the heater is not designed to reach such elevated temperatures. The supply current required to reach such high temperatures would cause electromigration in the heater leading to loss of electrical power supply. Also, the heater

temperature is continuously monitored in the experiment and in the event of any undesired temperature rise the power supply will be turned off manually.

17. MATERIAL SAFETY DATA SHEET

3M MATERIAL SAFETY DATA SHEET FC-72 FLUORINERT Brand Electronic Liquid 04/26/2005

SECTION 1: PRODUCT AND COMPANY IDENTIFICATION

PRODUCT NAME: FC-72 FLUORINERT Brand Electronic Liquid

MANUFACTURER: 3M

DIVISION: Electronics Markets Materials Division

ADDRESS: 3M Center, St. Paul, MN 55144-1000

EMERGENCY PHONE: 1-800-364-3577 or (651) 737-6501 (24 hours)

Issue Date: 04/26/2005

Supersedes Date: 03/09/2005

Document Group: 10-3789-4

Product Use:

Intended Use: For industrial use only. Not intended for use as a medical device or drug.

Specific Use: Testing Fluid or Heat Transfer Fluid for Electronics.

SECTION 2: INGREDIENTS

Ingredient C.A.S. No. % by Wt

PERFLUORO COMPOUNDS, (PRIMARILY COMPOUNDS WITH 6 CARBONS) 86508-42-1 100

SECTION 3: HAZARDS IDENTIFICATION

3.1 EMERGENCY OVERVIEW

Specific Physical Form: Liquid

Odor, Color, Grade: Colorless, odorless liquid.

General Physical Form: Liquid

Immediate health, physical, and environmental hazards: None known.

3.2 POTENTIAL HEALTH EFFECTS

Eye Contact:

Contact with the eyes during product use is not expected to result in significant irritation.

Skin Contact:

Contact with the skin during product use is not expected to result in significant irritation.

Inhalation: If thermal decomposition occurs: May be harmful if inhaled.

Ingestion: No health effects are expected.

3.3 POTENTIAL ENVIRONMENTAL EFFECTS

This compound is completely fluorinated (perfluorinated), or it contains perfluorinated portions.

Perfluoroalkyl groups resist degradation in most natural environments. This low-solubility substance has insignificant toxicity to aquatic organisms (Lowest LL50 or EL50 is >1000 mg/L). LL50 (Lethal Level) and EL50 are similar to LC50 and EC50, but tests the water phase from incompletely miscible mixtures. Take precautions to prevent direct release of this substance to the environment. **ATMOSPHERIC FATE:** Perfluoro compounds (PFCs) are photochemically stable and expected to persist in the atmosphere for more than 1000 years. PFCs have high global warming potentials (GWP), exceeding 5000 (100-yr-ITH). The Ozone Depletion Potential (ODP) is Zero.

SECTION 4: FIRST AID MEASURES

4.1 FIRST AID PROCEDURES

The following first aid recommendations are based on an assumption that appropriate personal and industrial hygiene practices are followed.

Eye Contact: Flush eyes with large amounts of water. If signs/symptoms persist, get medical attention.

Skin Contact: Wash affected area with soap and water. If signs/symptoms develop, get medical attention.

Inhalation: If signs/symptoms develop, remove person to fresh air. If signs/symptoms persist, get medical attention.

If Swallowed: No need for first aid is anticipated.

SECTION 5: FIRE FIGHTING MEASURES

5.1 FLAMMABLE PROPERTIES

Autoignition temperature *Not Applicable*

Flash Point *Not Applicable*

Flammable Limits - LEL [*Details: Nonflammable*]

Flammable Limits - UEL [*Details: Nonflammable*]

5.2 EXTINGUISHING MEDIA

Material will not burn.

3M MATERIAL SAFETY DATA SHEET FC-72 FLUORINERT Brand Electronic Liquid 04/26/2005

5.3 PROTECTION OF FIRE FIGHTERS

Special Fire Fighting Procedures: Wear full protective equipment (Bunker Gear) and a self-contained breathing apparatus (SCBA). Water may be used to blanket the fire. Exposure to extreme heat can give rise to thermal decomposition.

Unusual Fire and Explosion Hazards: No unusual fire or explosion hazards are anticipated. No unusual effects are anticipated during fire extinguishing operations. Avoid breathing the products and substances that may result from the thermal decomposition of the product or the other substances in the fire zone. Keep containers cool with water spray when exposed to fire to avoid rupture.

Note: See STABILITY AND REACTIVITY (SECTION 10) for hazardous combustion and thermal decomposition information.

SECTION 6: ACCIDENTAL RELEASE MEASURES

Accidental Release Measures: Observe precautions from other sections. Call 3M- HELPS line (1-800-364-3577) for more information on handling and managing the spill. Evacuate unprotected and untrained personnel from hazard area. The spill should be cleaned up by qualified personnel. Ventilate the area with fresh air. Contain spill. Working from around the edges of the spill inward, cover with bentonite, vermiculite, or commercially available inorganic absorbent material. Mix in sufficient absorbent until it appears dry. Collect as much of the spilled material as possible. Clean up residue with an appropriate organic solvent. Read and follow safety precautions on the solvent label and MSDS. Place in a metal container approved for transportation by appropriate authorities. Seal the container. Dispose of collected material as soon as possible.

In the event of a release of this material, the user should determine if the release qualifies as reportable according to local, state, and federal regulations.

SECTION 7: HANDLING AND STORAGE

7.1 HANDLING

Avoid skin contact with hot material. For industrial or professional use only. No smoking: Smoking while using this product can result in contamination of the tobacco and/or smoke and lead to the formation of the hazardous decomposition products mentioned in the Reactivity Data section of this MSDS. Store work clothes separately from other clothing, food and tobacco products. Use general dilution ventilation and/or local exhaust ventilation to control airborne exposures to below Occupational Exposure Limits. If ventilation is not adequate, use respiratory protection equipment.

7.2 STORAGE

Store away from heat. Keep container tightly closed. Keep container in well-ventilated area.

SECTION 8: EXPOSURE CONTROLS/PERSONAL PROTECTION

8.1 ENGINEERING CONTROLS

Provide appropriate local exhaust when product is heated. Provide appropriate local exhaust ventilation on open containers. For those situations where the fluid might be exposed to extreme overheating due to misuse or equipment failure, use with appropriate local exhaust ventilation sufficient to maintain levels of thermal decomposition products below their exposure guidelines.

8.2 PERSONAL PROTECTIVE EQUIPMENT (PPE)

8.2.1 Eye/Face Protection

Avoid eye contact.

The following eye protection(s) are recommended: Safety Glasses with side shields.

3M MATERIAL SAFETY DATA SHEET FC-72 FLUORINERT Brand Electronic Liquid 04/26/2005

8.2.2 Skin Protection

Avoid skin contact with hot material. Wear appropriate gloves, such as Nomex, when handling this material to prevent thermal burns. Avoid skin contact. Select and use gloves and/or protective clothing to prevent skin contact based on the results of an exposure assessment. Consult with your glove and/or protective clothing manufacturer for selection of appropriate compatible materials. Gloves made from the following material(s) are recommended: Nitrile Rubber.

8.2.3 Respiratory Protection

Under normal use conditions, airborne exposures are not expected to be significant enough to require respiratory protection. Avoid breathing of vapors, mists or spray. Select one of the following NIOSH approved respirators based on airborne concentration of contaminants and in accordance with OSHA regulations: Half facepiece or fullface air-purifying respirator with organic vapor cartridges. Consult the current 3M Respiratory Selection Guide for additional information or call 1-800-243-4630 for 3M technical assistance. If thermal degradation products are expected, use fullface supplied air respirator.

8.2.4 Prevention of Swallowing

Do not eat, drink or smoke when using this product. Wash exposed areas thoroughly with soap and water.

8.3 EXPOSURE GUIDELINES

None Established

SECTION 9: PHYSICAL AND CHEMICAL PROPERTIES

Specific Physical Form: Liquid

Odor, Color, Grade: Colorless, odorless liquid.

General Physical Form: Liquid

Autoignition temperature *Not Applicable*

Flash Point *Not Applicable*

Flammable Limits - LEL [*Details: Nonflammable*]

Flammable Limits - UEL [*Details: Nonflammable*]

Boiling point 50 - 60 °C

Density 1.7 g/ml

Vapor Density Approximately 11.7 [*@ 20 °C*] [*Ref Std: AIR=1*]

Vapor Pressure Approximately 232 mmHg [*@ 20 °C*]

Specific Gravity Approximately 1.7 [*Ref Std: WATER=1*]

pH *Not Applicable*

Melting point *Not Applicable*

Solubility in Water Nil

Evaporation rate > 1 [*Ref Std: BUOAC=1*]

Volatile Organic Compounds [*Details: Exempt*]

Percent volatile Approximately 100 %
VOC Less H2O & Exempt Solvents [Details: Exempt]
Viscosity Approximately 0.42 centistoke [@ 20 °C]

SECTION 10: STABILITY AND REACTIVITY

Stability: Stable.

Materials and Conditions to Avoid: Finely divided active metals; Alkali and alkaline earth metals; Heat(greater than 200 °C)

Hazardous Polymerization: Hazardous polymerization will not occur.

Hazardous Decomposition or By-Products

Substance Condition

Hydrogen Fluoride At Elevated Temperatures - greater than 200 °C

Perfluoroisobutylene (PFIB) At Elevated Temperatures - greater than 200 °C

Hazardous Decomposition: Hydrogen fluoride has an ACGIH Threshold Limit Value of 3 parts per million (as fluoride) as a Ceiling Limit and an OSHA PEL of 3 ppm of fluoride as an eight hour Time-Weighted Average and 6 ppm of fluoride as a Short Term Exposure Limit. The odor threshold for HF is 0.04 ppm, providing good warning properties for exposure.

SECTION 11: TOXICOLOGICAL INFORMATION

Product-Based Toxicology Information:

A Material Toxicity Summary Sheet (MTSS) has been developed for this product. Please contact the address listed on the first page of this MSDS to obtain a copy of the MTSS for this product. Please contact the address listed on the first page of the MSDS for Toxicological Information on this material and/or its components.

SECTION 12: ECOLOGICAL INFORMATION

ECOTOXICOLOGICAL INFORMATION

Test Organism Test Type Result

Fathead Minnow, Pimephales promelas 96 hours Lethal Concentration 50% >1000 mg/l

Water flea, Daphnia magna 48 hours Effect Concentration 50% >1500 mg/l

CHEMICAL FATE INFORMATION

Test Type Result Protocol

20 days Biological Oxygen Demand Nil

Chemical Oxygen Demand Nil

SECTION 13: DISPOSAL CONSIDERATIONS

Waste Disposal Method: Reclaim if feasible. As a disposal alternative, incinerate in an industrial or commercial facility in the presence of a combustible material. Combustion products will include HF. Facility must be capable of handling halogenated materials. To reclaim or return, check product label for contact.

EPA Hazardous Waste Number (RCRA): Not regulated

Since regulations vary, consult applicable regulations or authorities before disposal.

SECTION 14: TRANSPORT INFORMATION

ID Number(s):

98-0211-0216-9, 98-0211-0217-7, 98-0211-0267-2, 98-0211-1795-1, 98-0211-4860-0, 98-0211-5506-8, 98-0211-5533-2, 98-0211-7346-7, 98-0211-7992-8, ZF-0002-0305-7, ZF-0002-0321-4, ZF-0002-0354-5, ZF-0002-0802-3, ZF-0002-1162-1

Please contact the emergency numbers listed on the first page of the MSDS for Transportation Information for this material.

SECTION 15: REGULATORY INFORMATION

US FEDERAL REGULATIONS

Contact 3M for more information.

311/312 Hazard Categories:

Fire Hazard - No Pressure Hazard - No Reactivity Hazard - No Immediate Hazard - Yes Delayed Hazard - No

STATE REGULATIONS

Contact 3M for more information.

CHEMICAL INVENTORIES

The components of this product are in compliance with the chemical notification requirements of TSCA.

All applicable chemical ingredients in this material are listed on the European Inventory of Existing Chemical Substances (EINECS), or are exempt polymers whose monomers are listed on EINECS.

The components of this product are listed on the Canadian Domestic Substances List.

The components of this product are listed on the Australian Inventory of Chemical Substances.

The components of this product are listed on Japan's Chemical Substance Control Law List (also known as the Existing and New Chemical Substances List.)

Contact 3M for more information.

INTERNATIONAL REGULATIONS

Contact 3M for more information.

This MSDS has been prepared to meet the U.S. OSHA Hazard Communication Standard, 29 CFR 1910.1200.

SECTION 16: OTHER INFORMATION**NFPA Hazard Classification**

Health: 3 Flammability: 0 Reactivity: 0 Special Hazards: None

National Fire Protection Association (NFPA) hazard ratings are designed for use by emergency response personnel to address the hazards that are presented by short-term, acute exposure to a material under conditions of fire, spill, or similar emergencies. Hazard ratings are primarily based on the inherent physical and toxic properties of the material but also include the toxic properties of combustion or decomposition products that are known to be generated in significant quantities.

HMIS Hazard Classification

Health: 0 Flammability: 0 Reactivity: 0 Protection: X - See PPE section.

Hazardous Material Identification System (HMIS(r)) hazard ratings are designed to inform employees of chemical hazards in the workplace. These ratings are based on the inherent properties of the material under expected conditions of normal use and are not intended for use in emergency situations. HMIS(r) ratings are to be used with a fully implemented HMIS(r) program. HMIS(r) is a registered mark of the National Paint and Coatings Association (NPCA).

Revision Changes:

Section 16: HMIS hazard classification for health was modified.

Section 3: Potential effects from eye contact was modified.

Section 3: Potential effects from inhalation information was modified.

Section 4: First aid for inhalation - medical assistance - was modified.

Section 10: Hazardous decomposition or by-products phrase was added.

Section 10: Hazardous decomposition or by-products comment was deleted.

DISCLAIMER: The information in this Material Safety Data Sheet (MSDS) is believed to be correct as of the date issued. 3M MAKES NO WARRANTIES, EXPRESSED OR IMPLIED, INCLUDING, BUT NOT LIMITED TO, ANY IMPLIED WARRANTY OF MERCHANTABILITY OR FITNESS FOR A PARTICULAR PURPOSE OR COURSE OF PERFORMANCE OR USAGE OF TRADE. User is responsible for determining whether the 3M product is fit for a particular purpose and suitable for user's method of use or application. Given the variety of factors that can affect the use and application of a 3M product, some of which are uniquely within the user's knowledge and control, it is essential that the user evaluate the 3M product to determine whether it is fit for a particular purpose and suitable for user's method of use or application. 3M provides information in electronic form as a service to its customers. Due to the remote possibility that electronic transfer may have resulted in errors, omissions or alterations in this information, 3M makes no representations as to its completeness or accuracy.

In addition, information obtained from a database may not be as current as the information in the MSDS available directly from 3M.

18. EQUIPMENT PROCEDURE DOCUMENTATION

(i) EQUIPMENT SHIPMENT

The experimental equipments will be transported to the test site by the investigators.

(ii) GROUND OPERATIONS

A dry run of the experiment will be conducted on ground prior to the flight experiments and the fluid may also have to be degassed. These operations require both 115VAC and 220V AC power outlets.

(iii) LOADING/STOWING

The experiment support structure is equipped with handles and hence will be used to manually carry the structure into the aircraft.

(iv) PREFLIGHT

- Preflight operations include degassing the fluid to remove the dissolved gas content. 115VAC power outlets will be required for this operation.
- Heat the liquid to required temperature
- Charge the tank with fluid; compress the bellows and close the valve atop to maintain 1 atm pressure
- Set up camera and adjust focus and lighting requirements
- Turn on the computer to monitor data

(v) IN-FLIGHT CHECKLIST

Pre-parabola:

- Set required heat flux
- Monitor fluid temperature
- Check camera focus

Parabola:

- Record data at required g-force level
- Trigger high speed camera

Post-parabola:

- Change heat flux to test device
- Monitor fluid temperature

(vi) POST FLIGHT CHECKLIST

- Copy data from the computer hard drive to laptop for further analysis
- Change test section if required for the next experiment
- Charge the tank with more fluid if required

(vii) OFFLOADING OF EXPERIMENT

- Handles will be used to manually offload the experimental structure\

(viii) EMERGENCY PROCEDURES

- Power down the power supply unit in case of problems with boiling experiment
- Press the emergency stop button to kill the process and power down all electronic equipments

19. BIBLIOGRAPHY

[1] Yuan, H., and Prosperetti, A., 1999, "The Pumping Effect of growing and Collapsing Bubbles in a Tube", *J.Micromech. Microeng.* 9, pp. 402-413.

[2] T. Jun and C.J. Kim, "Micropumping of liquid by directional growth and selective venting of gas bubbles", *Proc. IEEE Solid-State Sensor Actuator Workshop*, pp. 144-147, 1996.

[3] Linke, H., Aleman, B., Melling, L., Taornima, M., Francis, M., Dow-Hygeland, C., Narayanan, V., Taylor, R. P., and Stout, A., 2006, "Self-propelled Liedenfrost Droplets", *Physical Review Letters*, Vol. 96, 154502.

[4] Nimkar, N.D., Bhavnani, S.H., Jaeger, R.C., 2006, "Effect of Nucleation Site Spacing on the Pool Boiling Characteristics of a Structured Surface", *International Journal of Heat and Mass Transfer*, Vol. 49, pp. 2829-2839.

[5] Thiagarajan, P., Kapsenberg, F., Narayanan, V., Bhavnani, S.H., Ellis, C.D., 2011, "Effect of Nucleation Site Spacing on the Pool Boiling Characteristics of a Structured Surface", *Interpack 2011, Portland, Oregon, 2011*.

[6] Zhang, H., Mudawar, I., Hasan, M.M., 2005, "Flow Boiling CHF in Microgravity", *International Journal of Heat and Mass Transfer* 48, pp. 3107 - 3118.

[7] Celata, G.P., 2007, "Flow Boiling Heat Transfer in Microgravity: Recent Results", *Microgravity Sci. Tech.* - 3/4.

Appendix G

Microgravity Experiments: Sample Calculations for the Bubble Velocity Model

This section provides the set of sample calculations to estimate bubble velocity for the 5.3 mm bubble shown in Fig. 4.9, which was experimentally estimated to be sliding at 27.4 mm/s.

Fluid properties are estimated at T_{sat} :

$$\mu = 4.5 \times 10^{-4} Nsm^{-2}; \sigma = 0.8273 \times 10^{-2} Nm^{-1}$$

Properties of liquid film between the saw tooth and the vapor: Thickness of film (H) will be assumed to be constant and same over both the long slope and short slope of the saw-teeth. Thickness (H) and length of the film (L) over the saw teeth were estimated from the bubble image.

$$L_{longslope} = 0.85mm; L_{shortslope} = 0.53mm$$

Fig. 4.10 shows bubble velocity values estimated for H values ranging from 1-25 μm . Sample calculations provided below are for a H value of 17 μm .

Vapor bubble properties:

$$r_1 = 0.26mm; r_2 = 0.35mm; D = 5.3mm$$

Pressure difference in the liquid film for the long slope of a single saw tooth is estimated as,

$$P_{1,l} - P_{2,l} = 2\sigma \left(\frac{1}{r_1} + \frac{1}{r_2} \right) = 110.91 \frac{N}{m^2}$$

$$\left(\frac{dP}{dx} \right)_{longslope} = - \left(\frac{P_{1,l} - P_{2,l}}{L_{longslope}} \right) = -130486.0 \frac{N}{m^3}$$

The same procedure is repeated for the short slope of the saw-tooth to calculate the pressure differential.

$$\left(\frac{dP}{dx} \right)_{shortslope} = - \left(\frac{P_{1,l} - P_{2,l}}{L_{shortslope}} \right) = -209269.0 \frac{N}{m^3}$$

The total force due to pressure differences in the liquid film in both short and long slopes of the saw teeth can be calculated using the equation below. For the bubble of diameter, ($D=5.3mm$), that is under analysis it is approximated to reside over 5 saw-teeth (5 long

slopes and 5 short slopes),

$$F_{\Delta P, tot} = \left\{ m \left[\left(\frac{\mu V}{H} + \frac{H}{2} \frac{\partial P}{\partial x} \right) LW \cos \theta \right]_{\text{long slope}} - n \left[\left(\frac{\mu V}{H} + \frac{H}{2} \frac{\partial P}{\partial x} \right) LW \sin \theta \right]_{\text{short slope}} \right\}$$

In the above equation, $\theta = 31^\circ$; m= number of long slopes; n = number of short slopes; W Diameter of bubble.

The Stokes drag due to inertia on the vapor bubble moving through the liquid is,

$$F_d = 4\pi\mu RV = 1.5 \times 10^{-5}V$$

The overall force balance can be expressed by,

$$m \left[\left(\frac{\mu V}{H} + \frac{H}{2} \frac{\partial P}{\partial x} \right) LW \cos \theta \right]_{\text{long slope}} - n \left[\left(\frac{\mu V}{H} + \frac{H}{2} \frac{\partial P}{\partial x} \right) LW \sin \theta \right]_{\text{short slope}} - 4\pi\mu RV = 0$$

Re-arranging the equation,

$$\begin{aligned} & \left[\left(m \frac{\mu}{H} LD \cos 31 \right) V + m \frac{H}{2} \frac{\partial P}{\partial x} LD \cos 31 \right]_{\text{longslope}} \\ & - \left[\left(n \frac{\mu}{H} LD \sin 31 \right) V + n \frac{H}{2} \frac{\partial P}{\partial x} LD \sin 31 \right]_{\text{shortslope}} \\ & - 1.5 \times 10^{-5}V = 0 \end{aligned}$$

Substituting the properties of fluids, liquid film thickness and length, and the vapor bubble parameters, the above equation can be simplified as,

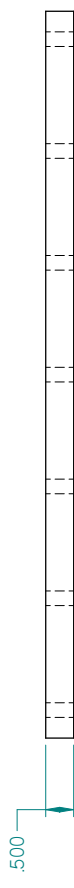
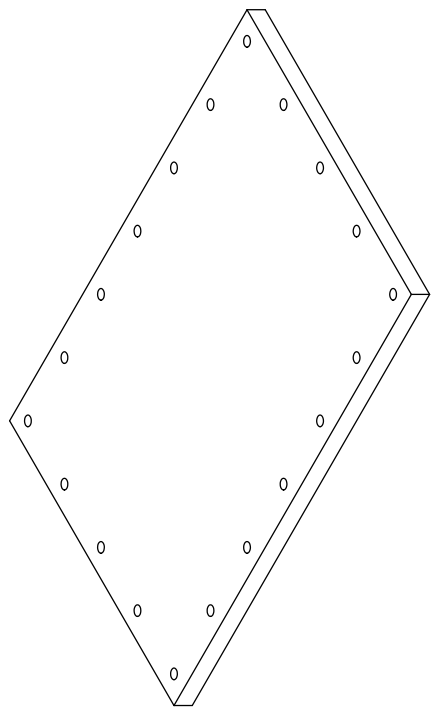
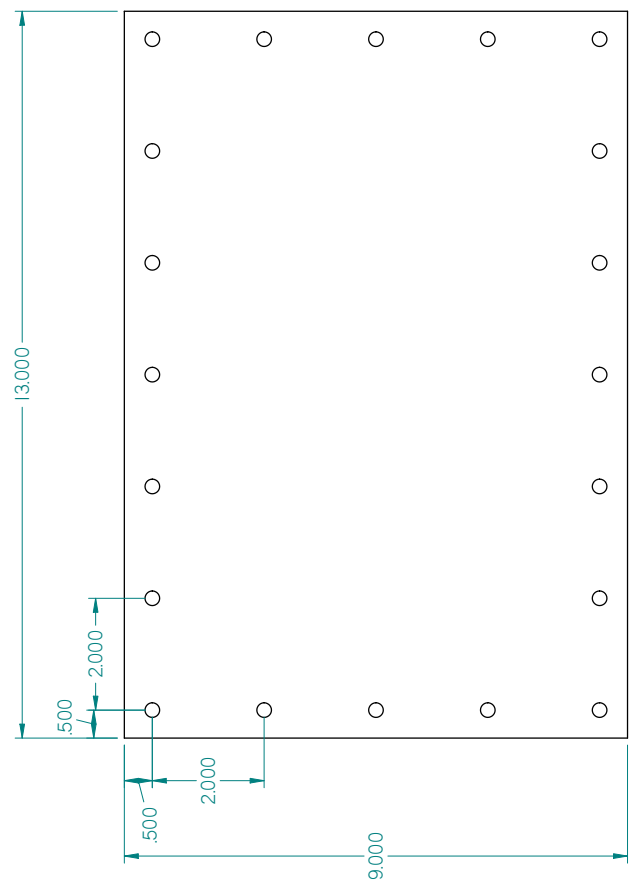
$$\begin{aligned} (5.11 \times 10^{-4} - 1.91 \times 10^{-4} - 1.5 \times 10^{-5}) V &= -1.3 \times 10^{-5} + 2.1 \times 10^{-5} \\ V &= 28.06 \text{ mm/s} \end{aligned}$$

Appendix H

Design Draft Files for Boiling Chamber Parts and Other Experimental Fixtures

REVISION HISTORY		DATE	APPROVED
REV	DESCRIPTION		

Boiling Chamber - Base

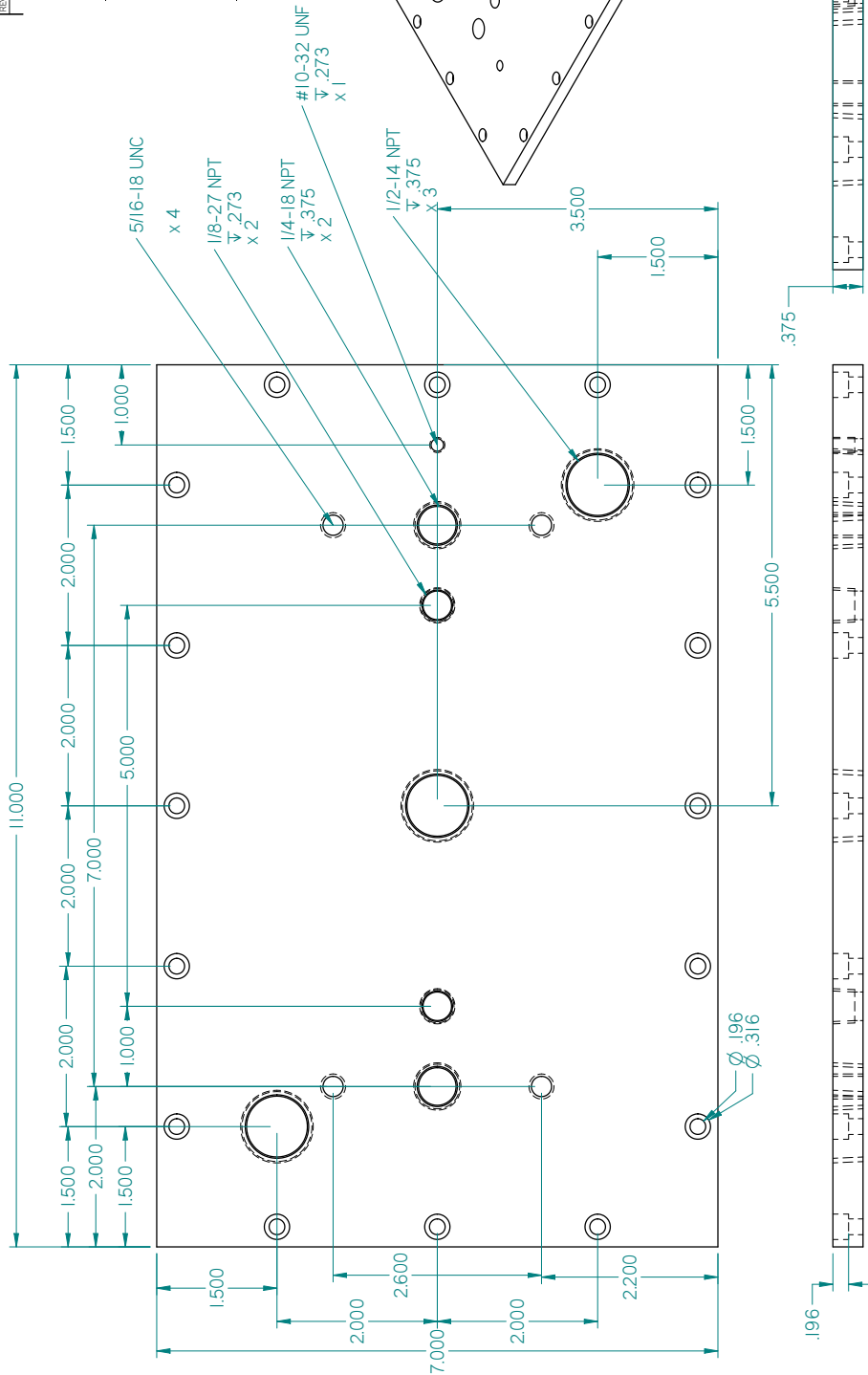


DRAWN	INCH	DATE	TITLE
ERIC APPER	QUZ/2013		Solid Edge
MARK APPER			
UNLESS OTHERWISE SPECIFIED DIMENSIONS ARE IN INCHES 2 PL. MAX PFA .000X			SCALE
FILE NAME: Bottom01			WEIGHT
SHEET 1 OF 1			

SOLID EDGE ACADEMIC COPY

REV	DESCRIPTION	DATE	APPROVED

Boiling Chamber - Lid

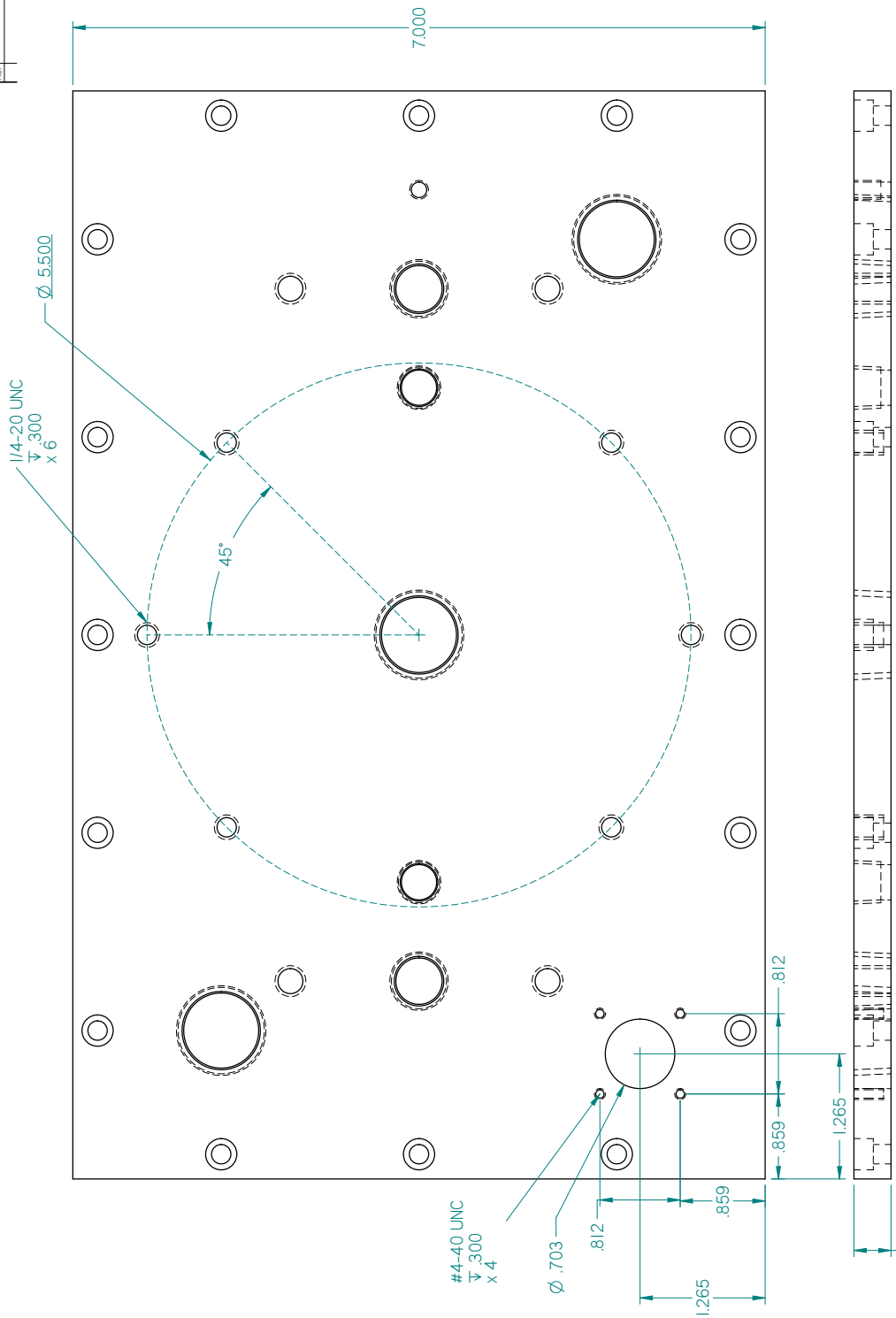


NAME	DATE	SCALE	WEIGHT	SHEET/PT

SOLID EDGE ACADEMIC COPY

REV	DESCRIPTION	DATE	APPROVED

**Lid -
Bellows
flange holes
& electrical
connector
holes**



DESIGN	NAME	DATE	TITLE

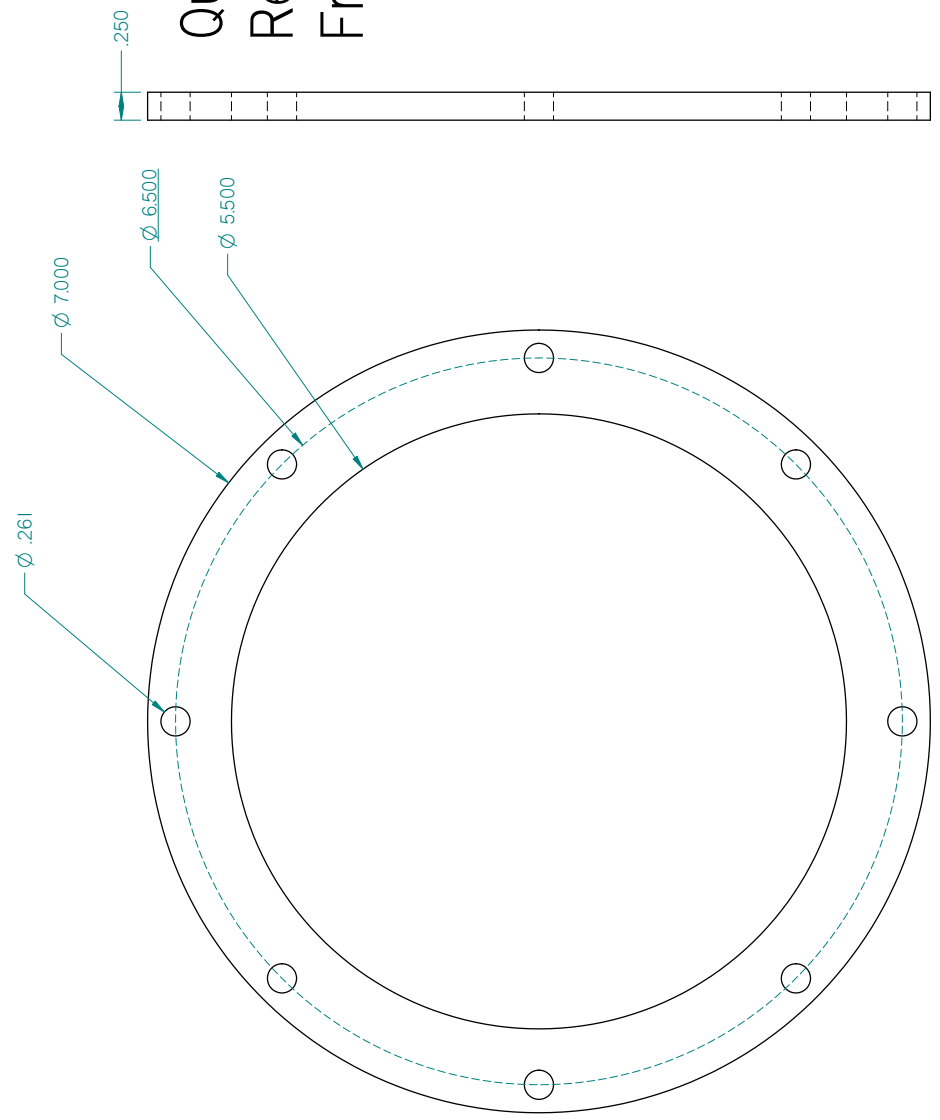
UNLESS OTHERWISE SPECIFIED
DIMENSIONS ARE IN INCHES
ANGLES IN DEGREES
SCALE: 2 PL. MAX. PPL. 4000X

FILE NAME	LOGICAL	SCALE	WEIGHT	SHEET	TOTAL

SOLID EDGE ACADEMIC COPY 11.000

REVISION HISTORY			
REV	DESCRIPTION	DATE	APPROVED

Quartz Window Retainer Ring 6"- Front Wall

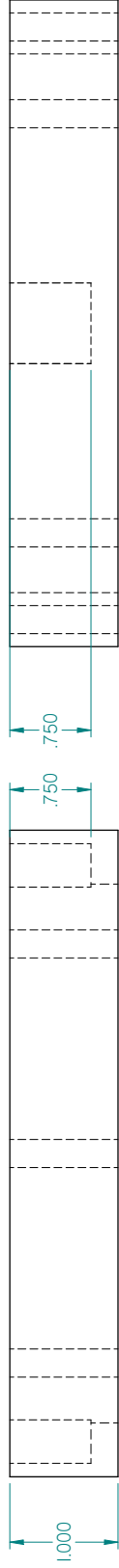
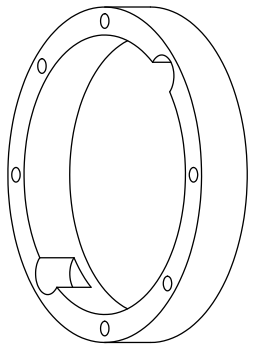
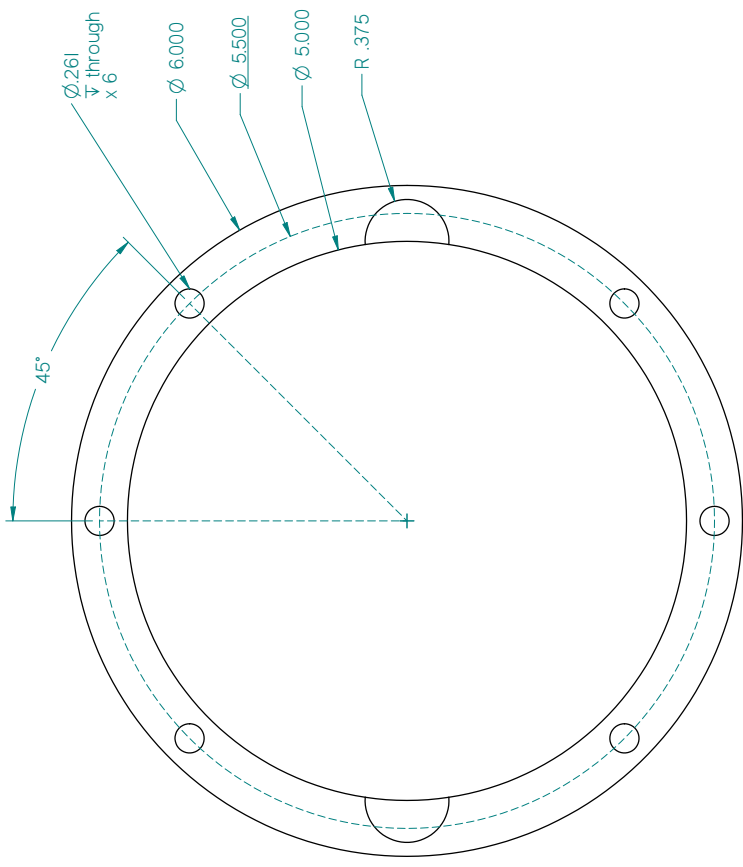


DESIGNER	NAME	DATE	Solid Edge	
DATE	REV	QUANTITY	TITLE	
SCALE	MARK APPR		FILE NAME	
			SCALE	
			WEIGHT	
			SHEET / OF 1	

SOLID EDGE ACADEMIC COPY

REV	DESCRIPTION	DATE	APPROVED

Bellows - Flange

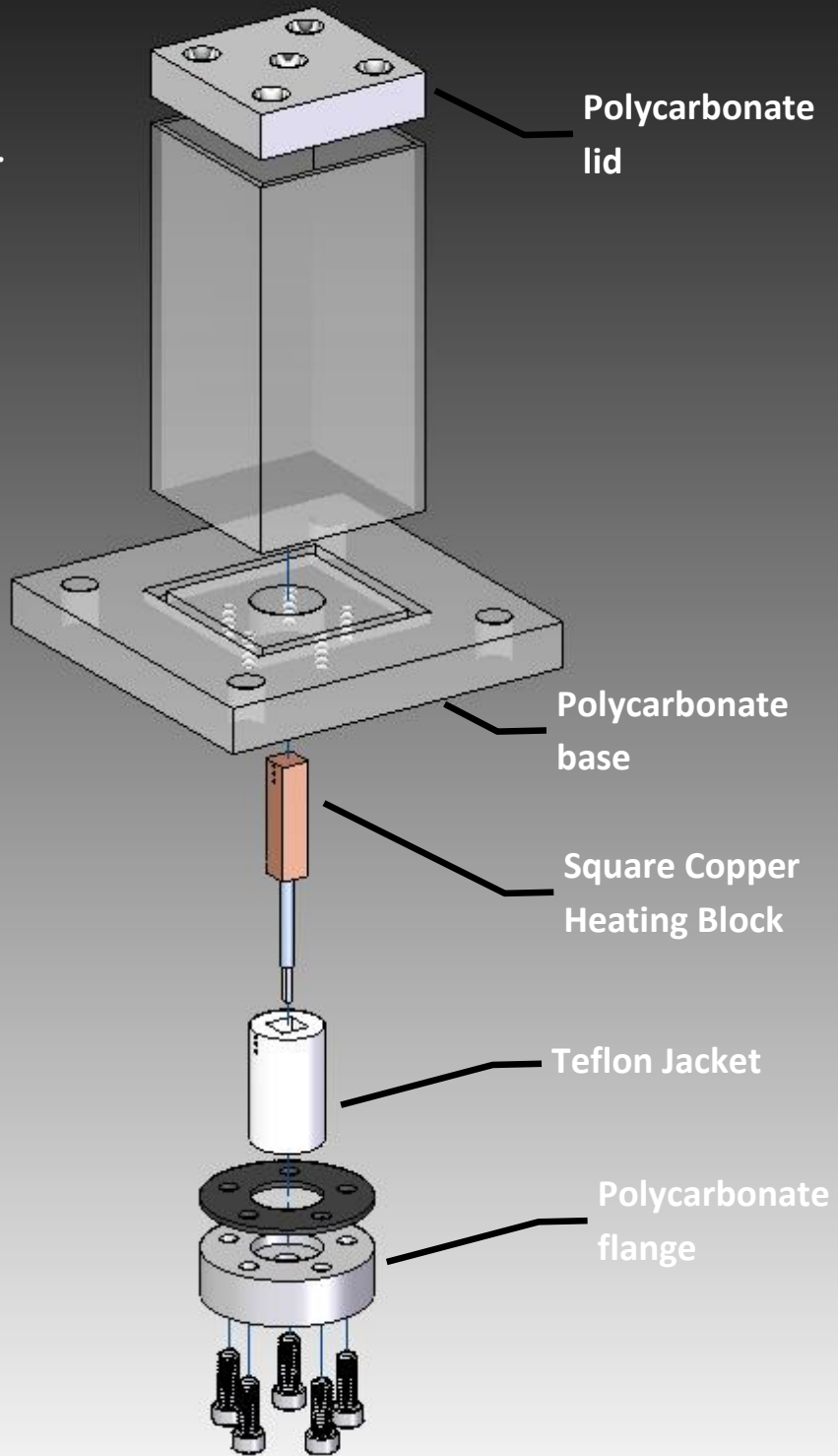


DRAWN	NAME	DATE	TITLE

SCALE	WEIGHT	SHEET	OF

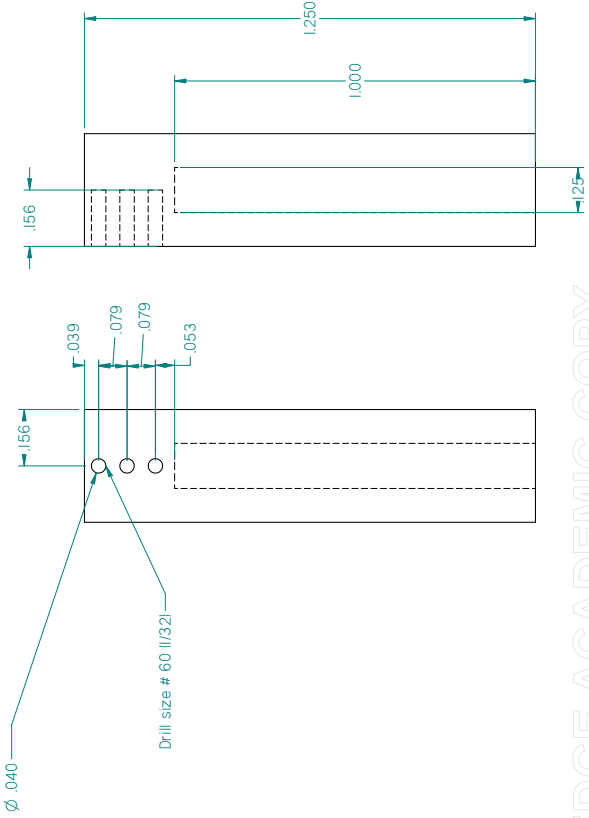
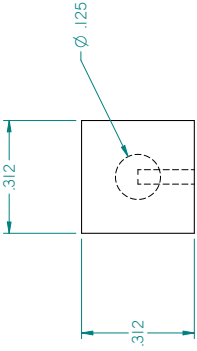
SOLID EDGE ACADEMIC COPY

Exoloded view of the
PIV boiling chamber



REV	DESCRIPTION	DATE	APPROVED

Copper heating block



NAME	DATE	TITLE

DESIGN	DATE	TITLE

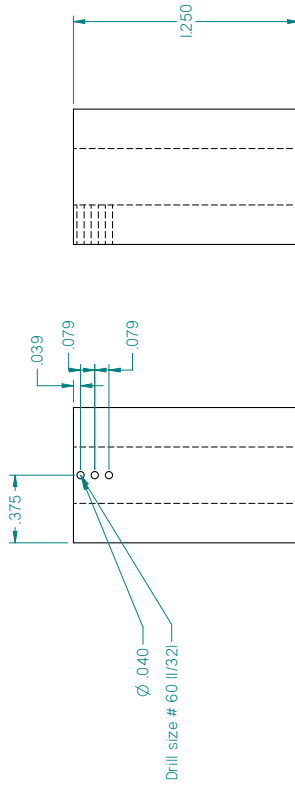
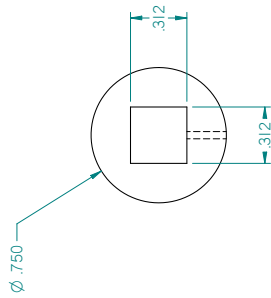
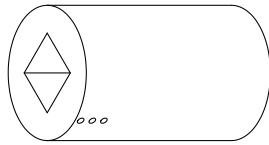
DESIGNER	DATE	TITLE

DATE	TITLE	SCALE	WEIGHT	SHEET	TOTAL

SOLID EDGE ACADEMIC COPY

REV	DESCRIPTION	DATE	APPROVED

Teflon Jacket



NAME	DATE	DATE	DATE	DATE

Solid Edge

UNLESS OTHERWISE SPECIFIED
DIMENSIONS ARE IN INCHES
TOLERANCES ARE:
FRACTIONS DECIMALS ANGLES 30°
2 P. 1003 P. 1000

SCALE: 1:1 SHEET NO. 1 OF 1

SOLID EDGE ACADEMIC COPY

